UAB

Universitat Autònoma de Barcelona

Bacterial Cellulose as a Scaffold for Electrode Materials in Electrochemical Energy Storage and Conversion

Wenhai Wang

Doctoral Thesis

Doctoral studies in Material Science

Supervisor: Dr. Dino Tonti

Institut de Ciència de Materials de Barcelona

July 2022

Declaration

Thesis submitted to aspire for the doctoral degree of Wenhai Wang.

Wenhai Wang

Supervisor's approval:

Dr. Dino Tonti
Tenured Scientist
Consejo Superior de Investigaciones Científicas
Institut de Ciència de Materials de Barcelona-CSIC

Bellaterra, 25 July 2022

Acknowledgments

Firstly, I would like to express my sincere gratitude to my supervisor Dr. Dino Tonti for offering me a chance to do research in ICMAB. Thanks for his patience, support and countless guidance for my research.

I would like to thank Dr. Anna Roig and Dr. Anna Laromaine from the Nanoparticles and Nanocomposites (NN) group in ICMAB for helping me revise and improve scientific papers. I would like to appreciate Soledad Roig-Sanchez for offering bacterial cellulose and revising papers. I am greatly grateful to Dr. Andrea Sorrentino, Dr. Vlad Martin-Diaconescu and Dr. Laura Simonelli for providing support in Alba.

I would express my thanks to these professional technicians in ICMAB: Anna Cresp, Joan. B. Esquius, Fco. Javier Campos (X-ray Diffraction Laboratory), Anna Esther Carrillo (Scanning Electron Microscope Service), Judith Oró Solé (Transmission Electron Microscopy Service), Julio Fraile (Surface Area Analysis Service), Roberta Ceravola (Thermal Analysis Service). I would also appreciate Guillaume Sauthier (Photoemission Spectroscopy Facility, ICN2) and Cristina Navarro Senent (Servei de Microscòpia, UAB).

I would like to thank Dr. Mara Olivares and Dr. Alvaro Yamil Tesio for their support.

I would appreciate all group members: Ashley Black, Rafael Trocoli, Eulalia Pujades, Marina Llenas, Marta Florensa, Victor Vallejo Exposito, Raúl Artal López, Jhonatan Ricardo Guarín, Juan Forero, Antonio Miguel Socías, Ruben García, Deyana Stoytcheva, Houdeville Raphaelle, Cheng Liu, Roberta Verrelli, Romain Dugas.

Finally, thank my families.

Abstract

Bacterial cellulose (BC) is a biopolymer with various outstanding properties, such as pure composition, nanosized fibers, and high water retention. Based on these properties, BC was employed in this thesis as a scaffold to process electrodes for electrochemical energy storage and conversion (EESC) applications. In general, the nanofibers allow high specific area and open porosity for optimal transport, but their insulating character prevents direct use. To obtain suitable conductivity, carbonization and metal coating were studied, respectively. Then, their electrochemical performance in EESC applications was investigated. The following main aspects of this work can be highlighted, each dedicated to the development of a novel material:

1. Carbons with appropriate porosity are ideal cathodes of $Li-O_2$ battery. Mesoporous carbons were obtained from carbonization of alcohol-treated BC. Soaking purified, wet BC in alcohol removes the initial water and prevents its collapse when drying. Compared with conventional methods, such as freeze-drying, or using templating agents, the proposed route to fabricate porous carbons is more convenient. In contrast with carbon derived from untreated BC that shows compact structure, carbon derived from 1-butanol treated BC presents to be porous, exhibits high capacity (5.6 mA h cm^{-2}) and has good cycle life

2. Manganese dioxide (MnO_2) is an interesting cathode for Zn ion battery (ZIB), while it suffers from poor conductivity, greatly impairing the electrochemical performance. N-doped carbon nanosheets derived from urea-soaked BC were utilized to improve the conductivity of MnO_2. BC possesses high water-absorbing capacity and it can absorb urea to obtain the nitrogen source. N-doped carbon nanosheet/MnO_2 as the cathode of ZIB shows a high capacity and long cycle life (114 mAh g^{-1} at 2 A g^{-1} after 1800 cycles).

3. Low-cost electrodes for hydrogen evolution reaction (HER) in neutral electrolytes usually show poor performance. A free-standing Ni-P/BC electrode was obtained, showing high conductivity and high HER activity at the same time. Ni-P was *in*

situ grown on BC by electroless deposition (ELD). The thin fibers of BC are beneficial to form small Ni-P particles, providing more catalytic sites. The obtained Ni-P/BC presents a small overpotential (141 mV dec^{-1}) and good stability in 1 M potassium phosphate-buffered saline (pH=7) electrolyte.

Abbreviations

3D	Three-dimensional
Ar	Argon
BC	Bacterial cellulose
BC-b	1-butanol treated BC
BC-e	Ethanol treated BC
BC-w	Untreated BC
BET	Brunauer-Emmett-Teller
Carbon-b	Carbon derived from BC-b
Carbon-e	Carbon derived from BC-e
Carbon-w	Carbon derived from BC-w
CBC	Carbonized BC
C_{dl}	Double-layer capacitance
CI	Crystallinity index
CNC	Cellulose nanocrystal
CNTs	Carbon nanotubes
CPE	Constant phase element
CV	cyclic voltammetry
DEGEME	Bis (2-methoxy ethyl) ether
DMAB	Dimethylamine-Borane
DSC	Differential Scanning Calorimetry
ECSA	Electrochemical surface area
EDS	Energy-dispersive spectroscopy
EESC	Energy storage and conversion
EIS	Electrochemical impedance spectroscopy
ELD	Electroless deposition
FP	Filter paper
FTIR	Fourier transform infrared

GFP	Glass fiber paper
HER	Hydrogen evolution reaction
LIB	Li ion battery
LSV	Linear sweep voltammetry
MOFs	Metal-organic frameworks
NC	Nanocellulose
NCS	N-doped carbon nanosheet
NFC	Nanofibrillated cellulose
Ni-P	Nickel-phosphorous
OER	Oxygen evolution reaction
ORR	Oxygen reduction reaction
PBS	Potassium phosphate-buffered saline
PP	Printer paper
PVDF	Polyvinylidene fluoride
R_{ct}	Charge-transfer resistance
R-GO	Grapheme oxides
SAED	Selected area electron diffraction
SEM	Scanning Electron Microscopy
TEGDME	Triethylene glycol monomethyl ether
TEM	Transmission electron microscopy
TGA	Thermogravimetric analysis
XAS	X-ray absorption spectroscopy
XPS	X-ray Photoelectron Spectroscopy
XRD	X-ray diffraction
ZIB	Zn ion battery

Table of Contents

Chapter 1 Introduction

1.1 Bacterial cellulose

With the constant development of society and economy, the demand for energy is rapidly growing, which is mainly satisfied by using fossil fuel including oil, coal, and natural gas (Figure 1.1). However, as the consumption of fossil fuel increases, environmental issues are becoming more and more serious. Besides, the shortage of fossil fuel is also attracting attention. Although wind, solar and tidal energy have been employed to relieve the demand on fossil sources to a certain extent [1], they still cannot solve the energy crisis in view of their non-constant supply and strong dependence on storage systems to manage energy delivery. Thus, it is crucial to develop substantial and sustainable storage systems to allow the establishment of renewable energy resources as well. Electrochemical energy storage and conversion (EESC) devices are outstanding, because of their high energy efficiency and environmental friendliness [2]. To realize the practical application of EESC devices, except for considering high performance and safety, it is also important to employ earth-abundant materials to reduce the cost of production and pressure on natural resources. Amid many options, the interest in cellulose-based materials has expanded strikingly in different EESC devices [3].
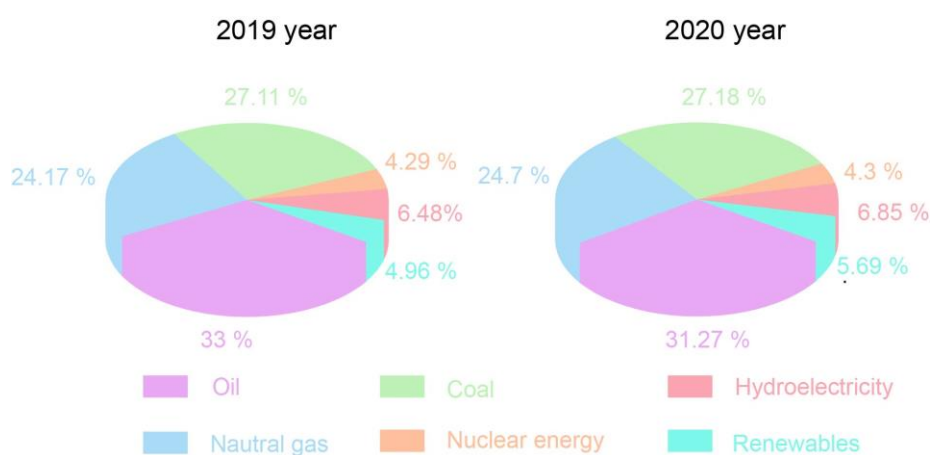

Figure 1.1. Shares of global primary energy of 2019 and 2020 (Data from Statistical Review of World Energy 2020).

Cellulose, as a common renewable biopolymer, is abundant and widely used, with a production estimated at about 7.5×10^{10} tons every year [4]. Compared with 3.3×10^9 tons of the worldwide oil consumed in 2018 [5], the value of 7.5×10^{10} tons is remarkable. Besides plants, bacteria also can be employed to obtain cellulose. Cellulose is a linear homopolymer (Figure 1.2), consisting of many D-glucose units linked together via ß-(1,4) glycosidic bonds [6]. These hydroxyl groups also can interact with hydroxyl groups from other neighboring cellulose chains and lead to the intramolecular hydrogen bonding, which is beneficial to the stabilization of the linear configuration [7].
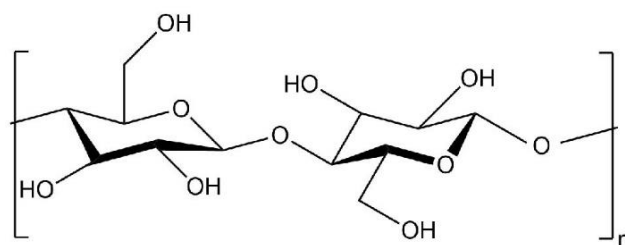
Figure 1.2. The chemical structure of cellulose.

Although cellulose is the main component (40-60 %) of plants, there are still hemicellulose (20-40 %) and lignin (10-25 %), other carbohydrate polymers that alter mechanical and chemical properties, being difficult for its processing [8]. Therefore, cellulose normally needs to be isolated from these components by various ways (such as steam explosion and chemical treatments etc.) [9]. The fiber of plant cellulose is composed of numerous cellulose microfibrils. Cellulosic materials with fibers or particles that have diameters less than 100 nm are identified as nanocellulose (NC). NC is highly appealing for the components of EESC devices, not only because it holds the well-known properties including biodegradability and nontoxicity of cellulose, but also because it possesses unique characteristics including good mechanical properties, thermal stability, large specific surface area and tunable self-assembly [10-12]. NC can be extracted from various plants (wood, bamboo culm, cotton, corn-cobs, etc.) or produced biochemically as detailed below [13, 14]. Chiefly,

it can be subdivided into three categories (Figure 1.3): cellulose nanocrystal (CNC), nanofibrillated cellulose (NFC), and bacterial cellulose (BC). The sources and the production methods of these three types of NCs are various. The sources of CNC and CNF mainly come from plants and BC is produced from bacteria (Figure 1.4).
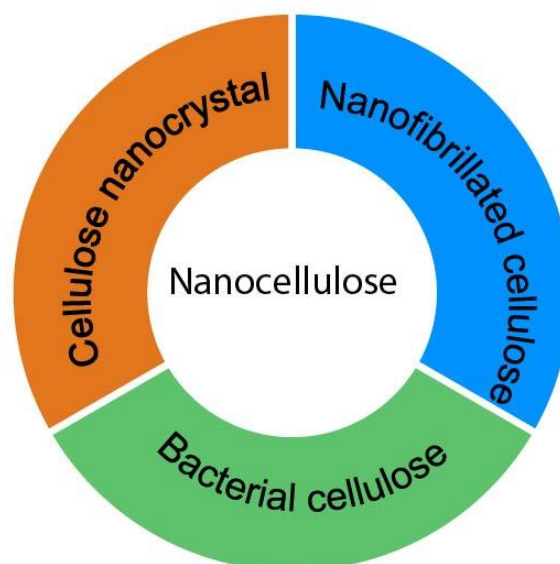
Figure 1.3. Categories of nanocellulose.

NFC can be obtained by mechanical approaches from plant cellulose, such as high-pressure homogenization, microfluidization, refining, ultrasonication, ball milling, and grinding [15]. With the mechanical force, the interfibrillar hydrogen bonds between cellulose microfibrils can be broken, leading to the generation of free individual NFC [16]. Although NFC can be successfully acquired from these mechanical methods, they still have high energy consumption, and leave large amounts of residual hemicellulose and lignin. In addition, the nanofibrillation degree is low.
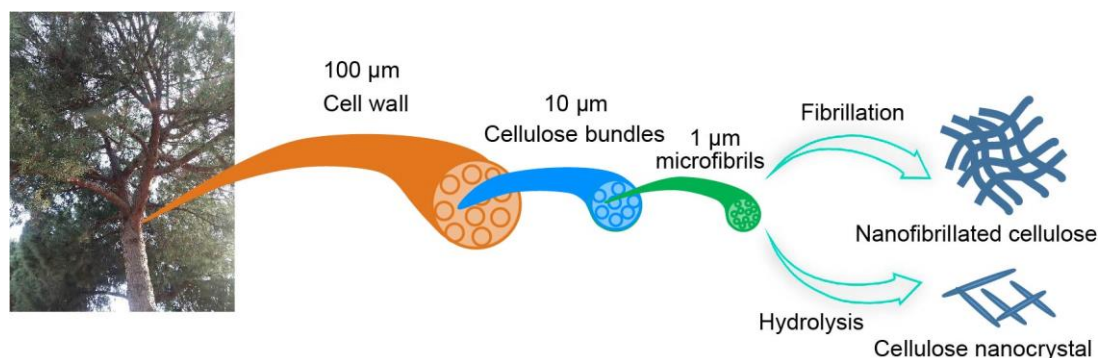
Figure 1.4. Extraction of cellulose nanocrystal and nanofibrillated cellulose from wood.

CNC can be produced from the acid hydrolysis of cellulose sources. The amorphous regions in the cellulose chain become unstable and can degrade easily under acid attack, whereas the hydrolysis barely affects the crystalline regions [17]. Thus, comparing with NFC, CNC shows relatively higher crystallinity. Typically, sulfuric acid is used for the hydrolysis, so that the obtained CNC can disperse well in water. This is because charged surface sulfate esters form, resulting from the reaction between sulfuric acid and hydroxyl groups on the surface of cellulose [18]. However, the yield of CNC is about 30-50 % and its thermal stability is also lower [19], because the thermal degradation can be accelerated with the sulfate groups on the surface [20]. Furthermore, the acid recovery is difficult and the treatment for neutralizing used acid produces large amounts of salts, which is an expensive waste to treat [21].

Different from CFC and CNC, BC is a nanocellulose directly obtained with a cellulose purity of almost 100 %. This obviates complex purification, simplifying the production processes and decreasing cost. In fact, BC can also be preferred as the raw material to prepare NFC and CNC [22].

As a popular Asian dessert known as "nata de coco", BC has already entered our lives. The price of *nata de coco* (Q-Phil Products International) in a Barcelona food store is about 1.6 €/g (dried weight). In comparison, the prices of CNC and NFC are about 3.6 €/g and 6 €/g from the company of Nanografi Nanotechnology, respectively. Therefore, in terms of the system cost, it is meaningful to construct BC-based materials in EESC devices.
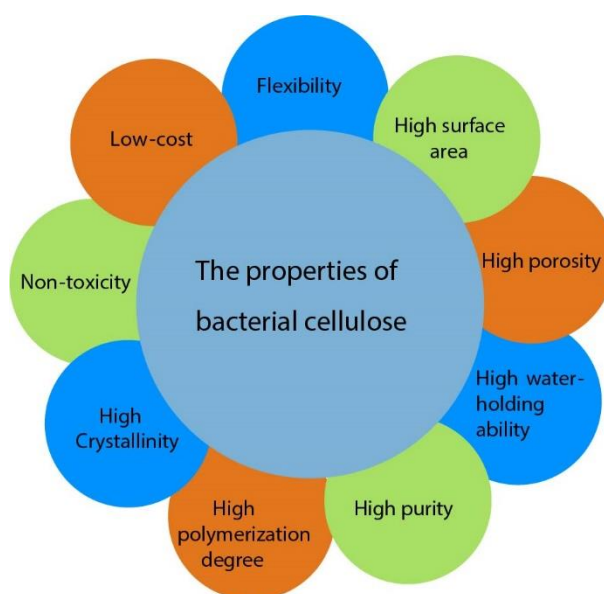
Figure 1.5. The properties of bacterial cellulose.

In addition to the economical one, BC also exhibits many remarkable advantages, summarized in Figure 1.5. The polymerization degree and the crystallinity of BC can respectively reach ~8000 and ~90 % [23]. BC possesses a three-dimensional (3D) structure consisting of cellulose nanofibers with the diameter of 10 to 100 nm, providing large specific surface area and high porosity [24]. BC displays a large capacity of water uptake (~400 times to its dried mass), which can be regarded as a promising type of hydrogels. What's more, BC shows excellent mechanical properties, reaching 20.8 GPa of tensile strength and 357.3 MPa of Young's modulus [25]. Due to these mechanical properties, the electrodes based on BC could be used as free-standing electrodes. BC presents optical transparency and excellent biocompatibility as well [26-29]. These distinguished features make BC widely used in many research fields covering optics, electronics, food industry, medical fields, and energy storage and conversion. The popularity of BC is also reflected by the steadily increasing number of scientific articles published between 2000 to 2021 (Figure 1.6).
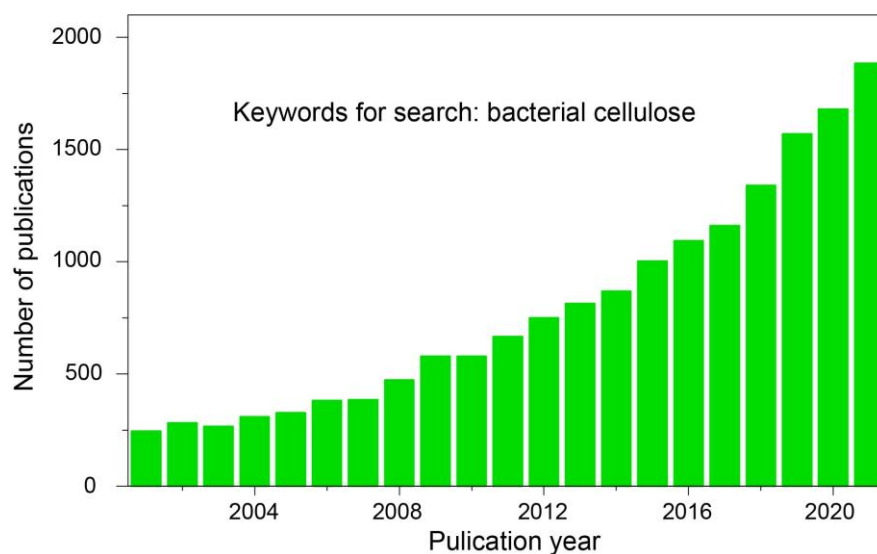
Figure 1.6. Number of publications about keywords of bacterial cellulose (Data derived from Web of Science)

BC is produced by a microbial fermentation (Figure 1.7). In 1886, Adrian Brown firstly reported that BC can be obtained from Acetobacter xylinum [30]. Then some studies revealed that BC also can be achieved from other bacteria, such as Rhizobium, Pseudomonas, Acetobacter Azotobacter, Salmonella, Sarcina ventriculi, Alcaligenes [31]. Although many bacteria can be used to prepare BC, only Acetobacter xylinum has been exploited commercially to produce BC owing to its high cellulose productivity [32].
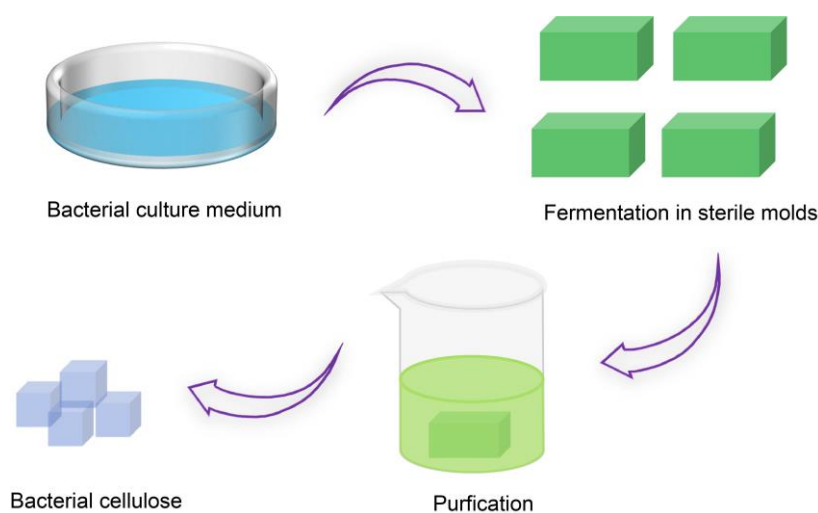
Figure 1.7. Scheme summarizing the production of bacterial cellulose. Bacterial cells are added in a culture medium consisting of carbon sources (such as organic acids,

oligosaccharides, monosaccharides, alcohols and agricultural wastes) and nitrogen sources (polypeptone, yeast extract and corn steep liquor); after 5-10 days the mixture is poured in sterile molds for fermenting and shaping; then harvested BC is washed to remove organic residues. Further specific processing is then applied to obtain food products.

1.2 Fabrication of BC-based electrodes

Abundant, sustainable, highly porous, lightweight materials with large surface area serving as conductive electrodes are largely demanded for EESC devices. Although BC possesses most mentioned properties, it is an insulating material, so it cannot be used as an electrode directly. There are two major strategies to fabricate conductive BC-based materials: (1) carbonize BC; (2) combine BC with conductive materials.

1.2.1 Carbonized BC

Converting BC into carbon can be an option for fabricating a conductive material. Since there is sufficient carbon content in BC, it is possible to manufacture carbon-based materials with BC as the precursors. Normally, carbonized BC (CBC) can be obtained by pyrolyzing BC in an inert atmosphere [33]. The process of pyrolysis is irreversible, producing great change in the physical state and the chemical composition. During the thermal decomposition process, BC is depolymerized and some volatile products are released, including water, carbon dioxide and monoxide, acetic acid, and different saccharides [34].

As is typical with biomass, the pyrolysis temperature of BC plays an important role in increasing the electrical conductivity of CBC. At higher treatment temperature the graphitization degree of carbonized BC becomes higher, resulting in the decrease of the electrical resistance [35]. Liang et al. developed a conductive CBC with 0.41 S cm^{-1}, which was obtained by pyrolyzing BC at 1450 °C [36]. The graphitization of CBC also can be accelerated by catalysts (Fe, Co, Ni) during the carbonization [37, 38]

and the electrical conductivity of CBC can be enhanced.

In addition, heteroatom doping, such as N, B, S, P, is of great interest for the remarkable improvement of the electrical conductivity of CBC [39]. Heteroatom doping has been achieved mainly by annealing the combination of heteroatom-containing compounds and BC or CBC. Lei et al. successfully prepared nitrogen-doped carbon nanofiber from BC/PPy composites (Figure 1.8) [40]. Pyrrole monomer was added in the BC suspension, and they combined with each other by hydrogen bond. The polymerization of pyrrole occurred with the aid of ferric chloride and then PPy uniformly generated on the surface of BC, giving place to 3D network of BC/PPy composites. Nitrogen-doped carbon nanofibers can be fabricated after annealing a 3D network of BC/PPy composites. Ma et al. fabricated S-doped carbon nanofibers by annealing a mixture of CBC and elemental sulfur [41]. The heteroatom doping of CBC also can be carried out by annealing BC or CBC in an atmosphere containing the heteroatom. For instance, Gao et al. prepared nitrogen-doped carbon nanofibers by a heat treatment of CBC in the ammonia atmosphere [42].
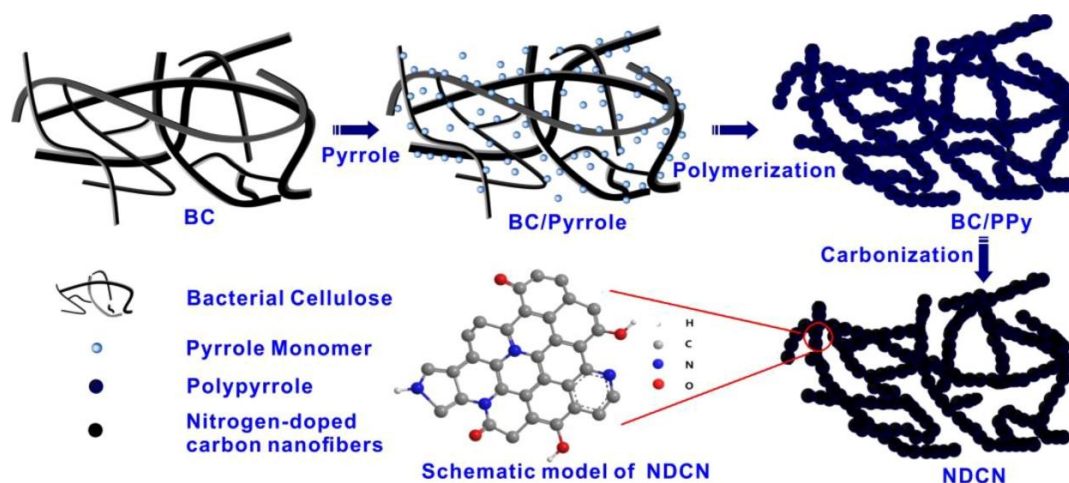
Figure 1.8. The preparation of nitrogen-doped carbon nanofiber from BC/PPy composites [40].

1.2.2 Combination with conductive materials

BC can be combined with conductive materials, for instance, carbons, conductive polymers, metallic particles, MXenes, through different ways to construct conductive composites (Figure 1.9) [43]. These BC-based hybrid composites can hold both properties of these conductive materials and BC. As it is arduous to dissolve BC, it is not easy to obtain good combinations between BC and conductive materials, and great efforts have been dedicated to construct conductive composites. Conductive materials can be coated on the surface of BC.
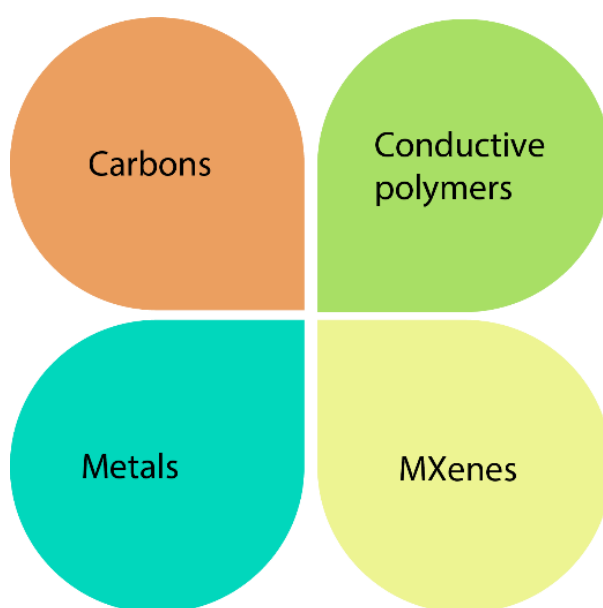
Figure 1.9. Classification of conductive materials used in BC composites.

Lv et al. successfully constructed conductive BC/Cu nanocomposites (Figure 1.10) [44]. In their method, Cu nanoparticles were coated on the surface of BC by magnetron sputtering. Compared with pristine BC, the conductivity of prepared BC/Cu nanocomposites increases largely from 1.14×10^{-10} S cm^{-1} to 2.6×10^{-4} S cm^{-1} [45].
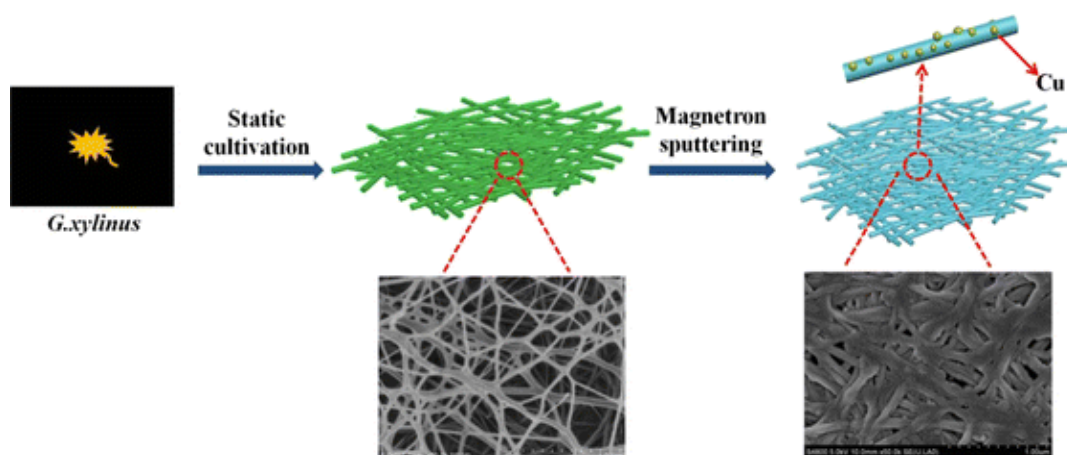
Figure 1.10. The sysnthesis of BC/Cu nanocomposites [44].

Conductive materials also can be incorporated inside BC with distinct strategies: blending, *in situ* polymerization, *in situ* bio-synthesization. Blending a BC membrane with a conductive material suspension, the conductive material can be transferred to BC, forming conductive hybrid materials [46]. For the in situ polymerization, BC is immersed in the monomer solution and enclosed BC/polymer matrix will be obtained with the help of an initiator [47]. In the *in situ* biosynthesized method, the conductive materials are dispersed in the culture medium of BC [48], so that BC is directly produced combined with conductive materials.

1.3 Batteries

The electrochemical storage of energy in a battery is accomplished by transforming chemical energy into electricity.

Generally speaking, a battery is composed of the following parts: anode, cathode, and electrolyte (Figure 1.11). The electrolyte works as a medium for transporting the electrolyte ions between the anode and the cathode. When the electrolyte is liquid, a separator is introduced to avoid direct contact between anode and cathode and thus prevent the short circuit. During discharge process, there is the occurrence of an oxidation reaction on the anode, which releases electrons. On the cathode, a reduction reaction takes place and consumes electrons that have traveled through an external circuit connecting it to the anode. If these reactions can reversely occur, the battery

can be recharged. Rechargeable batteries are called secondary batteries [49]. Conversely, batteries that do not possess the characteristic of rechargeability because reactions are irreversible, are termed as primary batteries. Primary batteries normally will be disposed after fully being used, causing detrimental effects on the environment and economy. Therefore, secondary batteries are highly demanded.
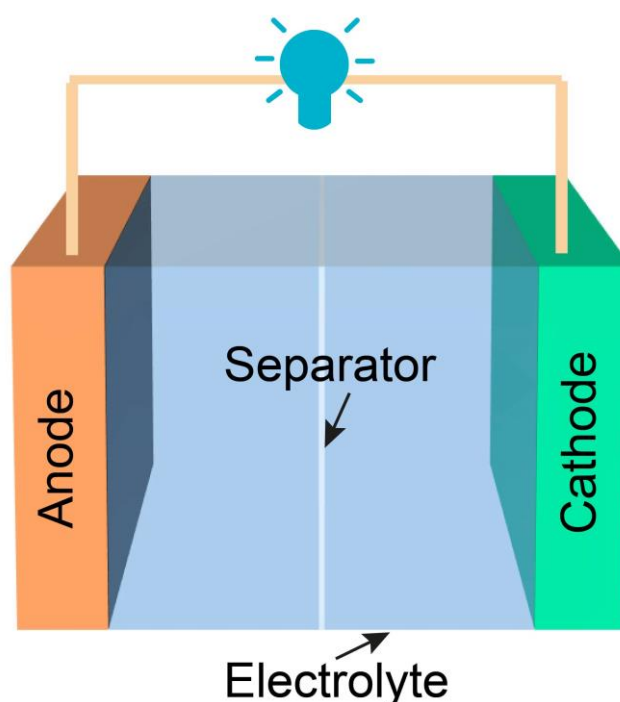
Figure 1.11. Schematic illustration of a typical battery.

Despite many kinds of battery chemistries have been invented (Figure 1.12), there are only a few secondary batteries have achieved wide commercialization, including lead-acid, nickel-metal hydride, nickel-cadmium, alkaline $Zn-MnO_2$ and lithium-ion batteries [50]. Among these secondary batteries, Li ion battery (LIB) is widely commercialized for the applications in portable devices, electric vehicles, and stationary storage, thanks to its high energy density and long cycle life [51, 52]. The high energy density can be ascribed to extremely low weight and reduction potential of lithium [53]. In addition, the storage mechanism of LIB is based on a reaction of intercalation/deintercalation of Li ions, which implies minimum electrode strains and mass rearrangements, favoring reversibility.
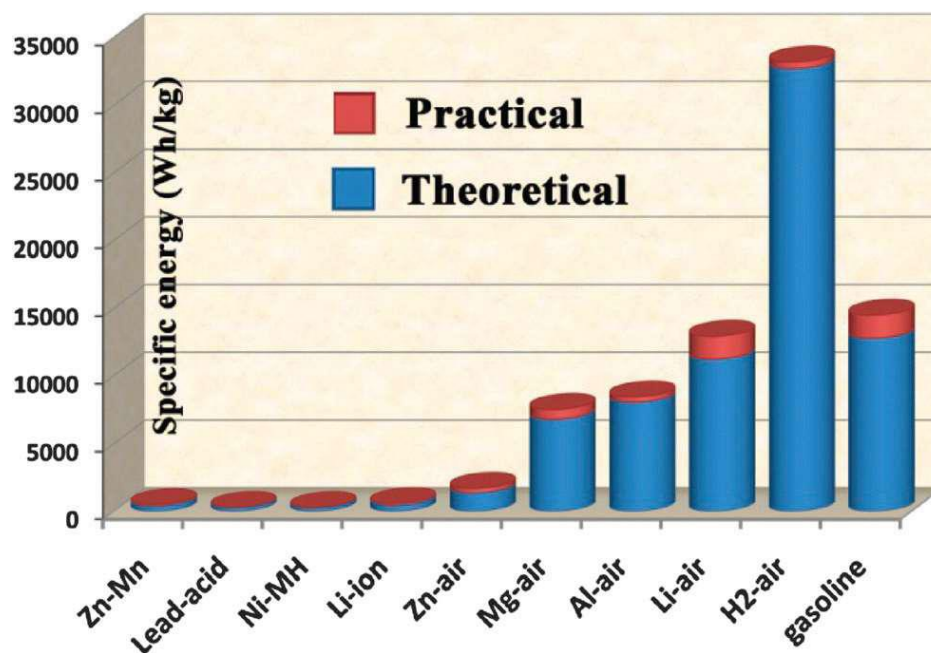
Figure 1.12 Comparison of the gravimetric energy density of batteries and gasoline [54].

The cost and theoretical energy density of LIB (100-265 Wh kg^{-1}) still hinder their wider applications in vehicles and large scale energy storage [55] , and it is not considered as the ideal technology that can satisfy the soaring demand of battery (Figure 1.13).
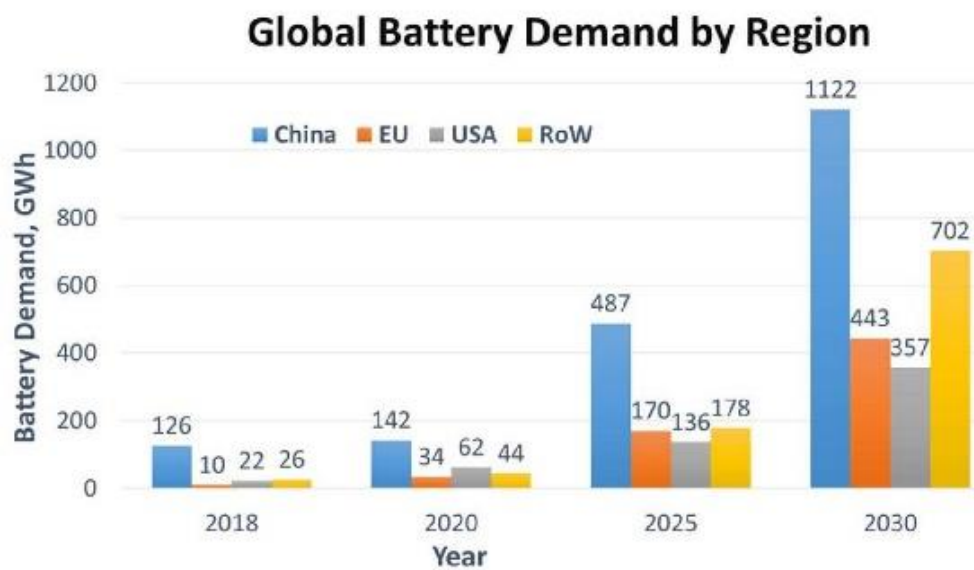
Figure 1.13. Global battery demand by region from 2018 to 2030 [56].

1.3.1 Li-O$_2$ battery

In comparison to LIB, Li-O$_2$ battery presents a much higher theoretical specific energy of 11700 Wh kg^{-1}, therefore it has received considerable attention [54]. The mechanism of Li-O$_2$ battery is based on the reversible formation/decomposition of the discharge product (Li$_2$O$_2$), which is different from that of Li-ion battery.

Typically, a Li-O$_2$ battery consists of four parts: Li metal anode, a separator, an electrolyte, and an O$_2$ cathode. The main electrochemical reaction of a Li-O$_2$ battery with aprotic electrolyte is $2Li+O_2 \rightleftharpoons Li_2O_2$ (Figure 1.14) [57]. During discharge, the Li metal is oxidized, generating dissolved Li ions and liberating electrons. O$_2$ receives the electrons released from the Li metal. The oxygen reduction reaction (ORR) takes place on the O$_2$ cathode and O$_2$ is reduced to form Li$_2$O$_2$. Upon charging, oxygen evolution reaction (OER) occurs and O$_2$ can be released. The O$_2$ cathode not only plays a significant role in transporting Li ions and O$_2$ [58], but also provides space for the deposition of Li$_2$O$_2$, and can even catalyze the reactions in some cases [59]. However, there are still several challenges for the O$_2$ cathode: (1) the sluggish kinetics of ORR and OER on the cathode results in high polarizations [60], (2) the accumulation of discharge products can easily induce the pore clogging and as a consequence the diffusion of Li$^+$/O$_2$ is blocked [61]. (3) several irreversible paths for side reactions are possible, sensibly limiting reversibility and cycle life. Thus, it is highly demanded to design suitable cathodes to address these issues for Li-O$_2$ battery. A good cathode should allow the diffusion of lithium ions and oxygen, and also favor the reversible Li$_2$O$_2$ formation and storage during the process of discharge [62, 63]. Noble metals or noble metal oxides are well-known for high catalytic activity, decreasing the polarizations. However, their high cost has limited the number of studies dedicated to their applications. In contrast to noble-metal, porous carbons are more advantageous [64, 65], as they generally offer good conductivity, light weight, large surface area, tunable porosity, low cost and abundant, often renewable, sources for its production [66, 67].
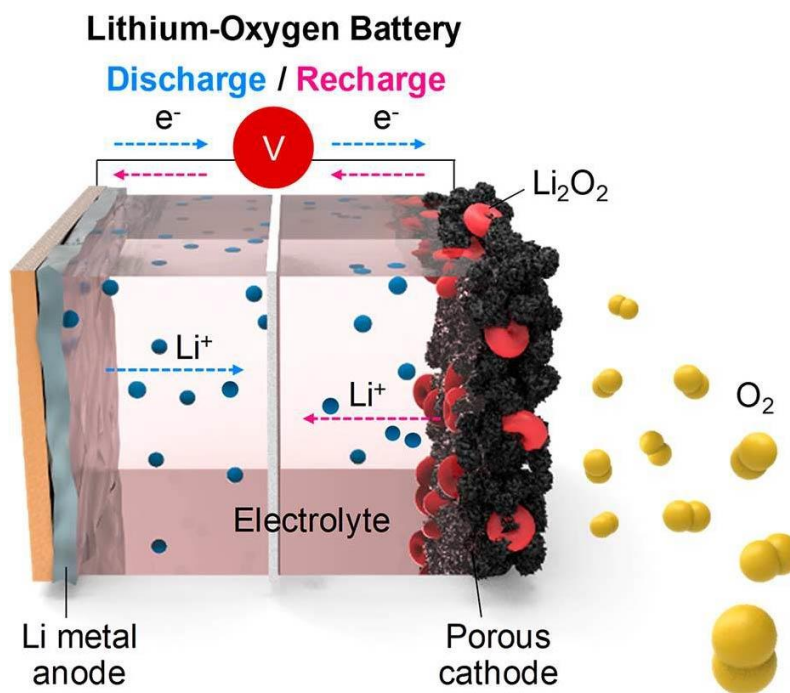
Figure 1.14. Schematic illustration of nonaqueous Li-O$_2$ battery [63].

1.3.2 Zn ion battery

Among alternative battery chemistries, rechargeable aqueous Zn ion battery (ZIB) has been seen as one of the most promising candidates because of the following merits:

(1) Zn is earth abundant and the price of Zn metal is much lower than Li metal (Table 1.1) [68]. Zn metal anode has a high theoretical capacity compared to the common Li-ion anode (graphite, 372 mAh g^{-1}) [69]. The relatively low redox potential of Zn (-0.76 V vs. standard hydrogen electrode (SHE)) makes it more stable in aqueous electrolytes than Li, Na, K, Ca and Al [70]. When avoiding using these metals directly as anodes and employing other anodes for the aqueous system, current collectors are still indispensable and most current collectors are more expensive than Zn metal (Table 1.2). What's more, these anodes need to be coated on current collectors, making the manufacturing processes more complex and further increasing the production cost.

Table 1.1. Comparison of different metals [71].

Element	Cost of metal ($/lb)	Potential vs SHE (V)	Crust abundance (ppm)	Ionic radius [Å]	Specific gravimetric capacity (mAh g^{-1})	Specific volumetric capacity (mAh cm^{-3})
Li	8-11	-3.04	17	0.76	3862	2062
Na	1.1-1.6	-2.71	23,000	1.02	1166	1128
K	3-9	-2.92	15,000	1.38	686	610
Zn	0.5-1.5	-0.76	79	0.74	820	5851
Mg	1-1.5	-2.36	29,000	0.72	2205	3833
Ca	/	-2.86	50,000	1.00	1340	2073
Al	0.5-1.5	-1.67	82,000	0.54	2980	8046

Table 1.2 The comparison of current collectors with the same thickness (0.125 mm) and the same size (50 x 50 mm). Data from Advent Research Materials Ltd. web page [72].

Current collector	Price ($/pc)
Zn foil	71
Cu foil	111
Ni foil	105
Ti foil	93
Steel foil	61

(2) The utilization of aqueous electrolytes can significantly improve the ionic conductivity and safety. In contrast, the ionic conductivity of organic electrolytes (10^{-2} to 10^{-3} S cm^{-1}) is two orders of magnitude lower than aqueous electrolytes (1 S cm^{-1}) [73]. In addition, the organic electrolytes are normally flammable and toxic, causing serious safety and environmental issues.

(3) In consideration of aqueous electrolytes and the stable Zn metal, the process

of assembling ZIB is much simpler, with no need for a glove box or dry room, resulting in potentially lower manufacturing cost.

Given these noticeable advantages of aqueous electrolytes and Zn metal, it is not surprising that Zn based batteries have the longest history among commercial batteries. Zn metal was firstly employed as the anode for Cu-Zn voltaic battery by Volta in 1799 [74]. Since then, however, alkaline Zn based batteries, with typically KOH aqueous solution that allow high conductivity and fast Zn dissolution kinetics have been preferred. Many alkaline primary Zn-based batteries were successfully obtained, such as $Zn-MnO_2$, Zn-Ni battery, Zn-Ag battery, Zn-air battery [75]. In the early 1970s, rechargeable alkaline Zn batteries were firstly invented by Carbide and Mallory [76]. Nevertheless, the problems of poor cycle life and coulombic efficiency have not been overcome [81], because the use of corrosive alkaline electrolytes can result in serious dendrite issues for Zn [77].
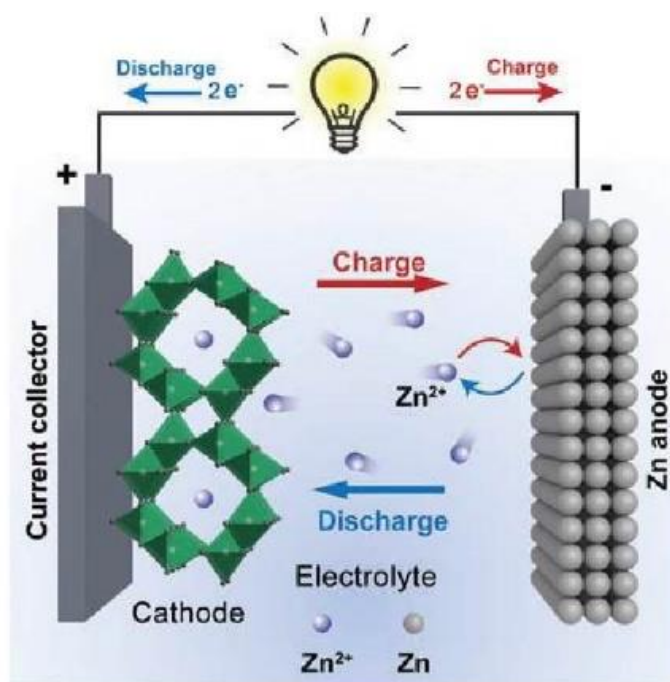

Figure 1.15. Schematic illustration of aqueous ZIB [78].

In ZIB, the mild electrolytes can alleviate zinc dendrites to a certain extent. The aqueous ZIB mainly consists of Zn metal anode, a separator, a nearly neutral (or slightly acidic) aqueous electrolyte containing Zn^{2+} and intercalation cathode material

for Zn ions (Figure 1.15). ZIB is different from traditional alkaline Zn based batteries, where the mechanism in the cathode is mainly based on chemical conversion reactions. Specifically, Zn-MnO_2: $MnO_2 + H_2O + e^- \rightarrow MnOOH + OH^-$; Zn-$O_2$ battery: $O_2 + 2H_2O + 4e^- \rightarrow 4OH^-$; Zn-Ni battery: $NiOOH + H_2O + e^- \rightarrow Ni(OH)_2 + OH^-$ [79-82]. With neutral electrolytes, the cathode mechanism is believed to involve Zn insertion/extraction [78]. Despite the ionic radius of Zn^{2+} (0.76 Å) is close to Li^+ (0.75 Å), the electrostatic interaction between cathode materials and Zn^{2+} is stronger than Li^+ because of its double charge [82], which largely hinders diffusion. Thus, there are a few cathode materials with satisfactory behavior that have been proved, including manganese-based oxides, Prussian blue analogs, V-based oxides and organic polymers [83]. Among them, MnO_2 has gained much interest, because of considerable capacity, decent voltage, low-cost and rich abundance [84]. However, MnO_2 exhibits poor electrical conductivity, seriously undermining the electrochemical performance of ZIBs [85, 86].

1.4 Hydrogen evolution reaction

Hydrogen gas has been regarded as a promising energy vector owing to the high energy and environmental-friendly combustion products. There are three main methods to produce H_2 (Figure 1.16): coal gasification, steam methane reforming and water electrolysis [87, 88]. Coal gasification and steam methane reforming still take up the large parts of hydrogen production (>95 %)，while there is about 4 % of the produced hydrogen coming from water electrolysis [87]. In these two main approaches, it is indispensable to consume fossil fuels directly producing CO_2 [89], becoming useless to reduce pollution and relieve global warming. Furthermore, the purity of obtained H_2 is low (~50 %) [90], because of large amounts of secondary products, such as CO and CO_2 [91, 92]. What's more, the requirements of instruments used in these processes are high due to high temperature resistance and other factors [93].
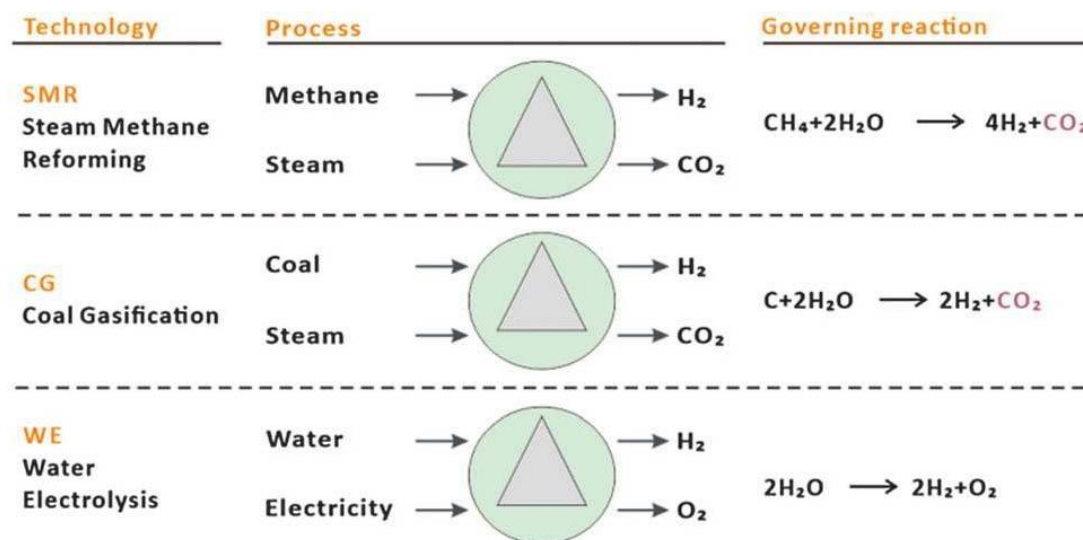
Figure 1.16. The three main methods of industrial hydrogen production [87].

In contrast, producing H_2 by electrochemical water splitting has raised tremendous attention. The source of this process is water, which is abundant, safe, and regenerated at the end of the process. Figure 1.17 shows the usual way of generating H_2 via electrochemical water electrolysis, where it just demands water and electricity without the need of high temperatures and pressure [94]. It also exhibits great advantages in terms of the rate of production and the purity (~99.999 %) of H_2 [95]. The reaction of hydrogen evolution reaction (HER) during water splitting depends on the electrolytes [96]:

acid electrolytes: $2H^+ + 2e^- \rightarrow H_2$;

alkaline/neutral electrolytes: $2H_2O + 2e^- \rightarrow H_2 + 2OH^-$.
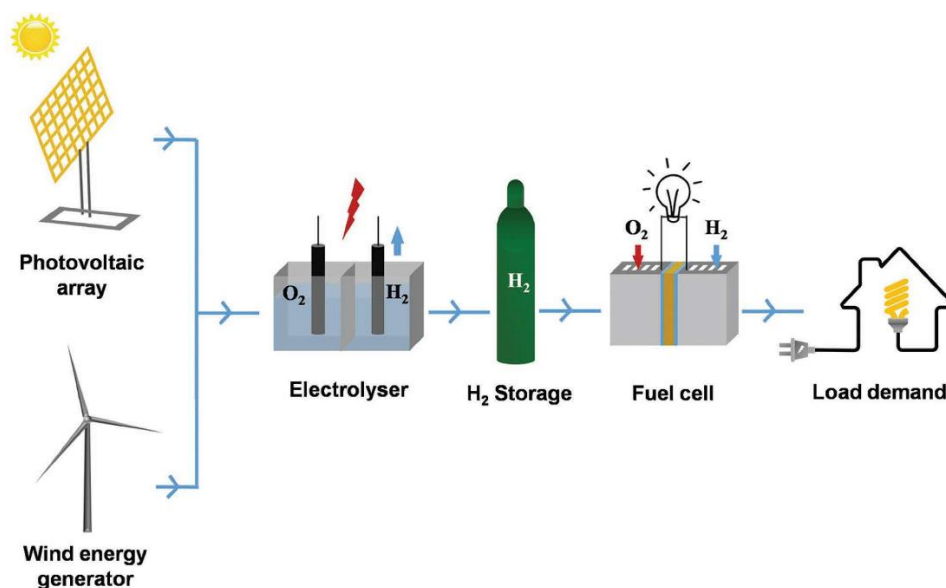
Figure 1.17. The production and the application of hydrogen energy [97].

However, the slow kinetics degrades the performance of HER [98, 99], requiring an appropriate catalyst. Presently, Pt-based materials are well-known for the superior HER activity [100]. However, the scarcity and the high cost of Pt hampers the wide applications. Immense efforts have been made to develop several classes of non-noble metal catalysts, such as metal phosphides, metal alloys, metal oxides, metal sulfides, metal nitrides and metal carbides [101].

Conventionally, the electrochemical HER is implemented in acid or alkaline electrolytes [102]. There are some serious issues for these electrolytes. Since the produced H_2 can be contaminated by acidic fogs, the facilities for H_2 production can be eroded by corrosive acid or alkaline medias [103]. These electrolytes can be also challenging for the stability of electrocatalysts, narrowing their choice. So, it is useful to investigate HER under neutral conditions, which is more environmentally friendly and likely to reduce the cost of H_2 production. Since the kinetics can be more sluggish in neutral medias than in acid and alkaline medias [104], developing highly performing catalysts becomes even more important in this case.

1.5 References

[1] S. Sanati, R. Abazari, J. Albero, A. Morsali, H. Garcia, Z. Liang, R. Zou, Metal-Organic Framework Derived Bimetallic Materials for Electrochemical Energy Storage, Angew. Chem. Int. Edit. 60(20) (2021) 11048-11067.

[2] J.B. Goodenough, Electrochemical energy storage in a sustainable modern society, Energy Environ. Sci. 7(1) (2014) 14-18.

[3] Z. Wang, Y.H. Lee, S.W. Kim, J.Y. Seo, S.Y. Lee, L. Nyholm, Why Cellulose-Based Electrochemical Energy Storage Devices?, Adv. Mater. 33(28) (2021) 2000892.

[4] B. Thomas, M.C. Raj, A.K. B, R.M. H, J. Joy, A. Moores, G.L. Drisko, C. Sanchez, Nanocellulose, a Versatile Green Platform: From Biosources to Materials and Their Applications, Chem. Rev. 118(24) (2018) 11575-11625.

[5] D.H. Vo, A.T. Vo, C.M. Ho, H.M. Nguyen, The role of renewable energy, alternative and nuclear energy in mitigating carbon emissions in the CPTPP countries, Renew. Energ. 161 (2020) 278-292.

[6] M.S. Singhvi, A.R. Deshmukh, B.S. Kim, Cellulase mimicking nanomaterial-assisted cellulose hydrolysis for enhanced bioethanol fermentation: an emerging sustainable approach, Green Chem. 23(14) (2021) 5064-5081.

[7] Z. Wang, P. Tammela, M. Strømme, L. Nyholm, Cellulose-based Supercapacitors: Material and Performance Considerations, Adv. Energy Mater. 7(18) (2017) 1700130.

[8] L. Lin, R. Yan, Y. Liu, W. Jiang, In-depth investigation of enzymatic hydrolysis of biomass wastes based on three major components: Cellulose, hemicellulose and lignin, Bioresour. Technol. 101(21) (2010) 8217-8223.

[9] G. Fan, M. Wang, C. Liao, T. Fang, J. Li, R. Zhou, Isolation of cellulose from rice straw and its conversion into cellulose acetate catalyzed by phosphotungstic acid, Carbohyd. Polym. 94(1) (2013) 71-76.

[10] J. Tao, R. Wang, H. Yu, L. Chen, D. Fang, Y. Tian, J. Xie, D. Jia, H. Liu, J. Wang, F. Tang, L. Song, H. Li, Highly Transparent, Highly Thermally Stable Nanocellulose/Polymer Hybrid Substrates for Flexible OLED Devices, ACS Appl.

Mater. Interfaces 12(8) (2020) 9701-9709.

[11] L. Zhu, L. Zong, X. Wu, M. Li, H. Wang, J. You, C. Li, Shapeable Fibrous Aerogels of Metal-Organic-Frameworks Templated with Nanocellulose for Rapid and Large-Capacity Adsorption, ACS Nano 12(5) (2018) 4462-4468.

[12] L. Wagberg, J. Erlandsson, The Use of Layer-by-Layer Self-Assembly and Nanocellulose to Prepare Advanced Functional Materials, Adv. Mater. 33(28) (2021) 2001474.

[13] V. Thakur, A. Guleria, S. Kumar, S. Sharma, K. Singh, Recent advances in nanocellulose processing, functionalization and applications: a review, Mater. Adv. 2(6) (2021) 1872-1895.

[14] Smalyukh, II, Thermal Management by Engineering the Alignment of Nanocellulose, Adv. Mater. 33(28) (2021) 2001228.

[15] S. Salimi, R. Sotudeh-Gharebagh, R. Zarghami, S.Y. Chan, K.H. Yuen, Production of Nanocellulose and Its Applications in Drug Delivery: A Critical Review, ACS Sustainable Chem. Eng. 7(19) (2019) 15800-15827.

[16] A. Isogai, Emerging Nanocellulose Technologies: Recent Developments, Adv. Mater. 33(28) (2021) 2000630.

[17] F.T. Seta, X. An, L. Liu, H. Zhang, J. Yang, W. Zhang, S. Nie, S. Yao, H. Cao, Q. Xu, Y. Bu, H. Liu, Preparation and characterization of high yield cellulose nanocrystals (CNC) derived from ball mill pretreatment and maleic acid hydrolysis, Carbohydr. Polym. 234 (2020) 115942.

[18] K. Sahlin, L. Forsgren, T. Moberg, D. Bernin, M. Rigdahl, G. Westman, Surface treatment of cellulose nanocrystals (CNC): effects on dispersion rheology, Cellulose 25(1) (2017) 331-345.

[19] L. Chen, J.Y. Zhu, C. Baez, P. Kitin, T. Elder, Highly thermal-stable and functional cellulose nanocrystals and nanofibrils produced using fully recyclable organic acids, Green Chem. 18(13) (2016) 3835-3843.

[20] H. Wang, H. Xie, H. Du, X. Wang, W. Liu, Y. Duan, X. Zhang, L. Sun, X. Zhang, C. Si, Highly Efficient Preparation of Functional and Thermostable Cellulose Nanocrystals via H_2SO_4 Intensified Acetic Acid Hydrolysis, Carbohyd. Polym. 239

(2020) 116233.

[21] H. Ji, Z. Xiang, H. Qi, T. Han, A. Pranovich, T. Song, Strategy towards one-step preparation of carboxylic cellulose nanocrystals and nanofibrils with high yield, carboxylation and highly stable dispersibility using innocuous citric acid, Green Chem. 21(8) (2019) 1956-1964.

[22] R.M. Viana, N. Sa, M.O. Barros, M.F. Borges, H.M.C. Azeredo, Nanofibrillated bacterial cellulose and pectin edible films added with fruit purees, Carbohydr. Polym. 196 (2018) 27-32.

[23] W. Chen, H. Yu, S.Y. Lee, T. Wei, J. Li, Z. Fan, Nanocellulose: a promising nanomaterial for advanced electrochemical energy storage, Chem. Soc. Rev. 47(8) (2018) 2837-2872.

[24] L. Liang, Z. Zhang, F. Song, W. Zhang, H. Li, J. Gu, Q. Liu, D. Zhang, Ultralight, flexible carbon hybrid aerogels from bacterial cellulose for strong microwave absorption, Carbon 162 (2020) 283-291.

[25] Q. Bai, Q. Xiong, C. Li, Y. Shen, H. Uyama, Hierarchical Porous Carbons from Poly(methyl methacrylate)/Bacterial Cellulose Composite Monolith for High-Performance Supercapacitor Electrodes, ACS Sustainable Chem. Eng. 5(10) (2017) 9390-9401.

[26] J. Caro-Astorga, K.T. Walker, N. Herrera, K.Y. Lee, T. Ellis, Bacterial cellulose spheroids as building blocks for 3D and patterned living materials and for regeneration, Nat. Commun. 12(1) (2021) 5027.

[27] J. Yang, L. Wang, W. Zhang, Z. Sun, Y. Li, M. Yang, D. Zeng, B. Peng, W. Zheng, X. Jiang, G. Yang, Reverse Reconstruction and Bioprinting of Bacterial Cellulose-Based Functional Total Intervertebral Disc for Therapeutic Implantation, Small 14(7) (2018) 1702582.

[28] M. Yan, W. Qu, Q. Su, S. Chen, Y. Xing, Y. Huang, N. Chen, Y. Li, L. Li, F. Wu, R. Chen, Biodegradable Bacterial Cellulose-Supported Quasi-Solid Electrolyte for Lithium Batteries, ACS Appl. Mater. Interfaces 12(12) (2020) 13950-13958.

[29] S. Tang, K. Chi, H. Xu, Q. Yong, J. Yang, J.M. Catchmark, A covalently cross-linked hyaluronic acid/bacterial cellulose composite hydrogel for potential

biological applications, Carbohydr. Polym. 252 (2021) 117123.

[30] B.A. J., On an acetic ferment which forms cellulose, J. Chem. Soc. 49 (1886) 432-439.

[31] J. Wang, J. Tavakoli, Y. Tang, Bacterial cellulose production, properties and applications with different culture methods - A review, Carbohydr. Polym. 219 (2019) 63-76.

[32] W. Liu, H. Du, M. Zhang, K. Liu, H. Liu, H. Xie, X. Zhang, C. Si, Bacterial Cellulose-Based Composite Scaffolds for Biomedical Applications: A Review, ACS Sustainable Chem. Eng. 8(20) (2020) 7536-7562.

[33] P. Bober, J. Kovářová, J. Pfleger, J. Stejskal, M. Trchová, I. Novák, D. Berek, Twin carbons: The carbonization of cellulose or carbonized cellulose coated with a conducting polymer, polyaniline, Carbon 109 (2016) 836-842.

[34] Z. Wang, B. Pecha, R.J.M. Westerhof, S.R.A. Kersten, C.-Z. Li, A.G. McDonald, M. Garcia-Perez, Effect of Cellulose Crystallinity on Solid/Liquid Phase Reactions Responsible for the Formation of Carbonaceous Residues during Pyrolysis, Ind. Eng. Chem. Res. 53(8) (2014) 2940-2955.

[35] R. Shi, C. Han, X. Xu, X. Qin, L. Xu, H. Li, J. Li, C.P. Wong, B. Li, Electrospun N-Doped Hierarchical Porous Carbon Nanofiber with Improved Degree of Graphitization for High-Performance Lithium Ion Capacitor, Chem. Eur. J. 24(41) (2018) 10460-10467.

[36] H.-W. Liang, Q.-F. Guan, Z. Zhu, L.-T. Song, H.-B. Yao, X. Lei, S.-H. Yu, Highly conductive and stretchable conductors fabricated from bacterial cellulose, NPG Asia Mater. 4(6) (2012) e19.

[37] M.P. Illa, C.S. Sharma, M. Khandelwal, Catalytic graphitization of bacterial cellulose-derived carbon nanofibers for stable and enhanced anodic performance of lithium-ion batteries, Mater. Today Chem. 20 (2021) 100439.

[38] C.J. Thambiliyagodage, S. Ulrich, P.T. Araujo, M.G. Bakker, Catalytic graphitization in nanocast carbon monoliths by iron, cobalt and nickel nanoparticles, Carbon 134 (2018) 452-463.

[39] S. Hong, J. Nam, S. Park, D. Lee, M. Park, D.S. Lee, N.D. Kim, D.-Y. Kim, B.-C.

Ku, Y.A. Kim, J.Y. Hwang, Carbon nanotube fibers with high specific electrical conductivity: Synergistic effect of heteroatom doping and densification, Carbon 184 (2021) 207-213.

[40] W. Lei, L. Han, C. Xuan, R. Lin, H. Liu, H.L. Xin, D. Wang, Nitrogen-doped carbon nanofibers derived from polypyrrole coated bacterial cellulose as high-performance electrode materials for supercapacitors and Li-ion batteries, Electrochim. Acta 210 (2016) 130-137.

[41] Q. Jin, W. Li, K. Wang, P. Feng, H. Li, T. Gu, M. Zhou, W. Wang, S. Cheng, K. Jiang, Experimental design and theoretical calculation for sulfur-doped carbon nanofibers as a high performance sodium-ion battery anode, J. Mater. Chem. A. 7(17) (2019) 10239-10245.

[42] Y. Gao, D. He, L. Wu, Z. Wang, Y. Yao, Z.-H. Huang, H. Yang, M.-X. Wang, Porous and ultrafine nitrogen-doped carbon nanofibers from bacterial cellulose with superior adsorption capacity for adsorption removal of low-concentration 4-chlorophenol, Chem. Eng. J. 420 (2021) 127411.

[43] R. Guo, L. Zhang, Y. Lu, X. Zhang, D. Yang, Research progress of nanocellulose for electrochemical energy storage: A review, J. Energy Chem. 51 (2020) 342-361.

[44] P. Lv, A. Wei, Y. Wang, D. Li, J. Zhang, L.A. Lucia, Q. Wei, Copper nanoparticles-sputtered bacterial cellulose nanocomposites displaying enhanced electromagnetic shielding, thermal, conduction, and mechanical properties, Cellulose 23(5) (2016) 3117-3127.

[45] Y. Wan, P. Xiong, J. Liu, F. Feng, X. Xun, F.M. Gama, Q. Zhang, F. Yao, Z. Yang, H. Luo, Y. Xu, Ultrathin, Strong, and Highly Flexible $Ti_3C_2T_x$ MXene/Bacterial Cellulose Composite Films for High-Performance Electromagnetic Interference Shielding, ACS Nano 15(5) (2021) 8439-8449.

[46] X. Zhang, X. Zhao, T. Xue, F. Yang, W. Fan, T. Liu, Bidirectional anisotropic polyimide/bacterial cellulose aerogels by freeze-drying for super-thermal insulation, Chem. Eng. J. 385 (2020) 123963.

[47] M. Mashkour, M. Rahimnejad, M. Mashkour, F. Soavi, Electro-polymerized polyaniline modified conductive bacterial cellulose anode for supercapacitive

microbial fuel cells and studying the role of anodic biofilm in the capacitive behavior, J. Power Sources 478 (2020) 228822.

[48] D. Abol-Fotouh, B. Dorling, O. Zapata-Arteaga, X. Rodriguez-Martinez, A. Gomez, J.S. Reparaz, A. Laromaine, A. Roig, M. Campoy-Quiles, Farming thermoelectric paper, Energy Environ. Sci. 12(2) (2019) 716-726.

[49] M.R. Palacin, Recent advances in rechargeable battery materials: a chemist's perspective, Chem. Soc. Rev. 38(9) (2009) 2565-2575.

[50] H. Jouhara, N. Khordehgah, N. Serey, S. Almahmoud, S.P. Lester, D. Machen, L. Wrobel, Applications and thermal management of rechargeable batteries for industrial applications, Energy 170 (2019) 849-861.

[51] A. Manthiram, A reflection on lithium-ion battery cathode chemistry, Nat. Commun. 11(1) (2020) 1550.

[52] T. Or, S.W.D. Gourley, K. Kaliyappan, A. Yu, Z. Chen, Recycling of mixed cathode lithium‐ion batteries for electric vehicles: Current status and future outlook, Carbon Energy 2(1) (2020) 6-43.

[53] N. Nitta, F. Wu, J.T. Lee, G. Yushin, Li-ion battery materials: present and future, Mater. Today 18(5) (2015) 252-264.

[54] F. Cheng, J. Chen, Metal-air batteries: from oxygen reduction electrochemistry to cathode catalysts, Chem. Soc. Rev. 41(6) (2012) 2172-2192.

[55] W. Wang, Y.-C. Lu, The Potassium–Air Battery: Far from a Practical Reality?, Acc. Mater. Res. 2(7) (2021) 515-525.

[56] Y. Zhao, O. Pohl, A.I. Bhatt, G.E. Collis, P.J. Mahon, T. Rüther, A.F. Hollenkamp, A Review on Battery Market Trends, Second-Life Reuse, and Recycling, Sustain. Chem. 2(1) (2021) 167-205.

[57] Z. Chang, J. Xu, X. Zhang, Recent Progress in Electrocatalyst for Li-O$_2$ Batteries, Adv. Energy Mater. 7(23) (2017) 1700875.

[58] H. Wang, X. Wang, M. Li, L. Zheng, D. Guan, X. Huang, J. Xu, J. Yu, Porous Materials Applied in Nonaqueous Li-O$_2$ Batteries: Status and Perspectives, Adv. Mater. 32(44) (2020) 2002559.

[59] D. Wang, X. Mu, P. He, H. Zhou, Materials for advanced Li-O$_2$ batteries: Explorations, challenges and prospects, Mater. Today 26 (2019) 87-99.

[60] L.-J. Zheng, F. Li, L.-N. Song, M.-L. Li, X.-X. Wang, J.-J. Xu, Localized surface plasmon resonance enhanced electrochemical kinetics and product selectivity in aprotic Li–O2 batteries, Energy Storage Mater. 42 (2021) 618-627.

[61] J. Li, S. Ding, S. Zhang, W. Yan, Z.-F. Ma, X. Yuan, L. Mai, J. Zhang, Catalytic redox mediators for non-aqueous Li-O$_2$ battery, Energy Storage Mater. 43 (2021) 97-119.

[62] J. Lu, Y.J. Lee, X. Luo, K.C. Lau, M. Asadi, H.H. Wang, S. Brombosz, J. Wen, D. Zhai, Z. Chen, D.J. Miller, Y.S. Jeong, J.B. Park, Z.Z. Fang, B. Kumar, A. Salehi-Khojin, Y.K. Sun, L.A. Curtiss, K. Amine, A lithium-oxygen battery based on lithium superoxide, Nature 529(7586) (2016) 377-382.

[63] W.J. Kwak, Rosy, D. Sharon, C. Xia, H. Kim, L.R. Johnson, P.G. Bruce, L.F. Nazar, Y.K. Sun, A.A. Frimer, M. Noked, S.A. Freunberger, D. Aurbach, Lithium-Oxygen Batteries and Related Systems: Potential, Status, and Future, Chem. Rev. 120 (2020) 6626-6683.

[64] M. Olivares-Marín, P. Palomino, J.M. Amarilla, E. Enciso, D. Tonti, Effects of architecture on the electrochemistry of binder-free inverse opal carbons as Li–air cathodes in an ionic liquid-based electrolyte, J. Mater. Chem. A. 1(45) (2013) 14270-14279.

[65] L. Ma, T. Yu, E. Tzoganakis, K. Amine, T. Wu, Z. Chen, J. Lu, Fundamental Understanding and Material Challenges in Rechargeable Nonaqueous Li-O$_2$ Batteries: Recent Progress and Perspective, Adv. Energy Mater. 8(22) (2018) 1800348.

[66] D.M. Itkis, D.A. Semenenko, E.Y. Kataev, A.I. Belova, V.S. Neudachina, A.P. Sirotina, M. Havecker, D. Teschner, A. Knop-Gericke, P. Dudin, A. Barinov, E.A. Goodilin, Y. Shao-Horn, L.V. Yashina, Reactivity of carbon in lithium-oxygen battery positive electrodes, Nano Lett. 13(10) (2013) 4697-4701.

[67] M. Kim, E. Yoo, W.-S. Ahn, S.E. Shim, Controlling porosity of porous carbon cathode for lithium oxygen batteries: Influence of micro and meso porosity, J. Power Sources 389 (2018) 20-27.

[68] B. Tang, L. Shan, S. Liang, J. Zhou, Issues and opportunities facing aqueous zinc-ion batteries, Energy Environ. Sci. 12(11) (2019) 3288-3304.

[69] M. Yan, C. Xu, Y. Sun, H. Pan, H. Li, Manipulating Zn anode reactions through salt anion involving hydrogen bonding network in aqueous electrolytes with PEO additive, Nano Energy 82 (2021).

[70] S. Zuo, X. Xu, S. Ji, Z. Wang, Z. Liu, J. Liu, Cathodes for Aqueous Zn-Ion Batteries: Materials, Mechanisms, and Kinetics, Chemistry- A European Journal 27(3) (2021) 830-860.

[71] X. Jia, C. Liu, Z.G. Neale, J. Yang, G. Cao, Active Materials for Aqueous Zinc Ion Batteries: Synthesis, Crystal Structure, Morphology, and Electrochemistry, Chem. Rev. 120(15) (2020) 7795-7866.

[72] A.R.M. Ltd, 2022. https://www.advent-rm.com/en-GB/. (Accessed July 25, 2022).

[73] L. Chen, Q. An, L. Mai, Recent Advances and Prospects of Cathode Materials for Rechargeable Aqueous Zinc-Ion Batteries, Advanced Materials Interfaces 6(17) (2019) 1900387.

[74] C.J.M. Melief, Smart delivery of vaccines, Nat. Mater. 17(6) (2018) 482-483.

[75] R.K. Ghavami, Z. Rafiei, S.M. Tabatabaei, Effects of cationic CTAB and anionic SDBS surfactants on the performance of $Zn-MnO_2$ alkaline batteries, J. Power Sources 164(2) (2007) 934-946.

[76] M. Yan, H. Ni, H. Pan, Rechargeable Mild Aqueous Zinc Batteries for Grid Storage, Adv. Energy Sustainability Res. 1(1) (2020) 2000026.

[77] H. Li, L. Ma, C. Han, Z. Wang, Z. Liu, Z. Tang, C. Zhi, Advanced rechargeable zinc-based batteries: Recent progress and future perspectives, Nano Energy 62 (2019) 550-587.

[78] N. Zhang, X. Chen, M. Yu, Z. Niu, F. Cheng, J. Chen, Materials chemistry for rechargeable zinc-ion batteries, Chem. Soc. Rev. 49 (2020) 4203-4219.

[79] D. Chen, M. Lu, D. Cai, H. Yang, W. Han, Recent advances in energy storage mechanism of aqueous zinc-ion batteries, J. Energy Chem. 54 (2021) 712-726.

[80] J.W. Gallaway, C.K. Erdonmez, Z. Zhong, M. Croft, L.A. Sviridov, T.Z.

Sholklapper, D.E. Turney, S. Banerjee, D.A. Steingart, Real-time materials evolution visualized within intact cycling alkaline batteries, J. Mater. Chem. A. 2(8) (2014) 2757-2764.

[81] F. Yang, X. Gao, J. Xie, X. Liu, J. Jiang, X. Lu, Cobalt‑Based Electrocatalysts as Air Cathodes in Rechargeable Zn-Air Batteries: Advances and Challenges, Small Struct. 2(12) (2021) 2100144.

[82] M. Song, H. Tan, D. Chao, H.J. Fan, Recent Advances in Zn-Ion Batteries, Adv. Funct. Mater. 28(41) (2018) 1802564.

[83] H. Jia, Z. Wang, B. Tawiah, Y. Wang, C.-Y. Chan, B. Fei, F. Pan, Recent advances in zinc anodes for high-performance aqueous Zn-ion batteries, Nano Energy 70 (2020) 104523.

[84] L.E. Blanc, D. Kundu, L.F. Nazar, Scientific Challenges for the Implementation of Zn-Ion Batteries, Joule 4(4) (2020) 771-799.

[85] Y. Liu, X. Chi, Q. Han, Y. Du, J. Huang, Y. Liu, J. Yang, α-MnO$_2$ nanofibers/carbon nanotubes hierarchically assembled microspheres: Approaching practical applications of high-performance aqueous Zn-ion batteries, J. Power Sources 443 (2019) 227244.

[86] Y. Zhao, Y. Zhu, X. Zhang, Challenges and perspectives for manganese‑based oxides for advanced aqueous zinc‑ion batteries, InfoMat 2(2) (2019) 237-260.

[87] X. Zou, Y. Zhang, Noble metal-free hydrogen evolution catalysts for water splitting, Chem. Soc. Rev. 44(15) (2015) 5148-80.

[88] S. Anantharaj, S.R. Ede, K. Karthick, S. Sam Sankar, K. Sangeetha, P.E. Karthik, S. Kundu, Precision and correctness in the evaluation of electrocatalytic water splitting: revisiting activity parameters with a critical assessment, Energy Environ. Sci. 11(4) (2018) 744-771.

[89] A. Chalgin, W. Chen, Q. Xiang, Y. Wu, F. Li, F. Shi, C. Song, P. Tao, W. Shang, J. Wu, Manipulation of Electron Transfer between Pd and TiO$_2$ for Improved Electrocatalytic Hydrogen Evolution Reaction Performance, ACS Appl. Mater. Interfaces 12(24) (2020) 27037-27044.

[90] N. Dat Vo, J.-H. Kang, M. Oh, C.-H. Lee, Dynamic model and performance of an integrated sorption-enhanced steam methane reforming process with separators for the simultaneous blue H_2 production and CO_2 capture, Chem. Eng. J. 423 (2021) 130004.

[91] Z. Chen, X. Duan, W. Wei, S. Wang, B.-J. Ni, Recent advances in transition metal-based electrocatalysts for alkaline hydrogen evolution, J. Mater. Chem. A. 7(25) (2019) 14971-15005.

[92] L. Barelli, G. Bidini, F. Gallorini, S. Servili, Hydrogen production through sorption-enhanced steam methane reforming and membrane technology: A review, Energy 33(4) (2008) 554-570.

[93] S. Anantharaj, V. Aravindan, Developments and Perspectives in 3d Transition-Metal-Based Electrocatalysts for Neutral and Near-Neutral Water Electrolysis, Adv. Energy Mater. 10(1) (2019) 1902666.

[94] S. Anantharaj, K. Karthick, S. Kundu, Evolution of layered double hydroxides (LDH) as high performance water oxidation electrocatalysts: A review with insights on structure, activity and mechanism, Mater. Today Energy 6 (2017) 1-26.

[95] S. Anantharaj, S. Kundu, S. Noda, Progress in nickel chalcogenide electrocatalyzed hydrogen evolution reaction, J. Mater. Chem. A. 8(8) (2020) 4174-4192.

[96] D. Strmcnik, P.P. Lopes, B. Genorio, V.R. Stamenkovic, N.M. Markovic, Design principles for hydrogen evolution reaction catalyst materials, Nano Energy 29 (2016) 29-36.

[97] J. Wang, F. Xu, H. Jin, Y. Chen, Y. Wang, Non-Noble Metal-based Carbon Composites in Hydrogen Evolution Reaction: Fundamentals to Applications, Adv. Mater. 29(14) (2017) 1605838.

[98] Z. Wang, B. Xiao, Z. Lin, Y. Xu, Y. Lin, F. Meng, Q. Zhang, L. Gu, B. Fang, S. Guo, W. Zhong, PtSe_2/Pt Heterointerface with Reduced Coordination for Boosted Hydrogen Evolution Reaction, Angew. Chem. Int. Edit. 60(43) (2021) 23388-23393.

[99] Z. Chen, X. Liu, T. Shen, C. Wu, L. Zu, L. Zhang, Porous NiFe alloys synthesized via freeze casting as bifunctional electrocatalysts for oxygen and

hydrogen evolution reaction, Int. J. Hydrogen. Energ 46(76) (2021) 37736-37745.

[100] C.-T. Dinh, A. Jain, F.P.G. de Arquer, P. De Luna, J. Li, N. Wang, X. Zheng, J. Cai, B.Z. Gregory, O. Voznyy, B. Zhang, M. Liu, D. Sinton, E.J. Crumlin, E.H. Sargent, Multi-site electrocatalysts for hydrogen evolution in neutral media by destabilization of water molecules, Nat. Energy 4(2) (2018) 107-114.

[101] R.Q. Yao, Y.T. Zhou, H. Shi, W.B. Wan, Q.H. Zhang, L. Gu, Y.F. Zhu, Z. Wen, X.Y. Lang, Q. Jiang, Nanoporous Surface High‐Entropy Alloys as Highly Efficient Multisite Electrocatalysts for Nonacidic Hydrogen Evolution Reaction, Adv. Funct. Mater. 31(10) (2020) 2009613.

[102] J. Mohammed-Ibrahim, X. Sun, Recent progress on earth abundant electrocatalysts for hydrogen evolution reaction (HER) in alkaline medium to achieve efficient water splitting-A review, J. Energy Chem. 34 (2019) 111-160.

[103] Z. Zhou, Z. Pei, L. Wei, S. Zhao, X. Jian, Y. Chen, Electrocatalytic hydrogen evolution under neutral pH conditions: current understandings, recent advances, and future prospects, Energy Environ. Sci. 13(10) (2020) 3185-3206.

[104] X. Zou, X. Huang, A. Goswami, R. Silva, B.R. Sathe, E. Mikmekova, T. Asefa, Cobalt-embedded nitrogen-rich carbon nanotubes efficiently catalyze hydrogen evolution reaction at all pH values, Angew. Chem. Int. Edit. 53(17) (2014) 4372-4376.

Chapter 2 Objectives

BC is a promising biomaterial possessing many outstanding features, such as low-cost, non-toxicity, high purity of cellulose, large surface area, high porosity, high water absorption capacity, and brilliant mechanical properties. These features make BC attractive for the fabrication of electrodes in EESC devices, requiring high electrochemically active area and open porosity for fast transport of electroactive species. The objectives of this thesis are developing suitable electrodes for $Li-O_2$ battery, ZIB and hydrogen production starting from BC, as specified below:

1. To evaluate the exchange of water for another solvent as a simple process to obtain suitable carbons from BC as the main component for $Li-O_2$ battery cathodes. To investigate the structures of the obtained carbons and assess their effects on the performance of $Li-O_2$ battery.

2. To take advantage of BC's strong water absorption capacity to introduce precursors for N-doped carbon. To evaluate the performance of obtained N-doped carbon/MnO_2 as the cathode for ZIB.

3. To make use of the excellent mechanical properties of pristine BC to support the growth of connected metallic Ni-P particles. To evaluate the performance of the obtained electrodes for HER in neutral electrolyte.

Chapter 3 Experimental

3.1 Materials

The specific experimental procedures for the preparation of the different materials are detailed in the respective chapters. Here, the general list of chemicals and materials, as well as the common procedures are provided.

3.1.1 Solvents

Product	Supplier
Methanol (99 %)	Scharlau
Ethanol (99 %)	Panreac
1-propanol (99.7 %)	Sigma Aldrich
1-butanol (99.5 %)	Labkem
1-hexanol (≥99.9 %)	Sigma Aldrich
1-octanol (≥99.9 %)	Sigma Aldrich
Acetone (≥99.9 %)	Panreac
Triethylene glycol monomethyl ether (≥97.0 %)	Sigma Aldrich
1-Methyl-2-pyrrolidone (≥99.8 %)	Sigma Aldrich
Lithium triflate (99.95 %)	Sigma Aldrich
Bis (2-methoxy ethyl) ether (99.95 %)	Sigma Aldrich

3.1.2 Metal salts

Product	Supplier
Nickel sulfate hexahydrate ($NiSO_4 \cdot 6H_2O$, 98 %)	Alfa Aesar
Tin chloride dehydrate ($SnCl_2 \cdot 2H_2O$, $\geqslant$99%)	Labkem
Palladium dichloride ($PdCl_2$, 99.9%)	Alfa Aesar
Sodium hypophosphite monohydrate ($NaH_2PO_2 \cdot H_2O$)	Acros Organincs
Sodium citrate dehydrate ($Na_3C_6H_5O_7 \cdot 2H_2O$, 99 %)	Alfa Aesar
Ammonium chloride (NH_4Cl, 99.5 %)	Sigma
Ammonia solution (NH_3, 30 %)	Panreac
Sodium borohydride ($NaBH_4$, 99 %)	Sigma Aldrich
Cobalt (II) sulfate heptahydrate ($CoSO_4 \cdot 5H_2O$, 99 %)	Sigma
Dipotassium hydrogenphosphate (K_2HPO_4, $\geqslant$99%)	Labkem
Potassium dihydrogen phosphate (KH_2PO_4, $\geqslant$99.5%)	Labkem
Sodium permanganate solution ($NaMnO_4$, 40 wt. % in H_2O)	Sigma-Aldrich
Commercial manganese dioxides (MnO_2, $\geqslant$99 %)	Sigma Aldrich
Zinc sulfate heptahydrate ($ZnSO_4 \cdot 7H_2O$, $\geqslant$99%)	Labkem
Manganese Sulfate Monohydrate ($MnSO_4 \cdot H_2O$, $\geqslant$99%)	Labkem

3.1.3 Others

Product	Supplier
Bacterial cellulose	Q-Phil Products International
Lithium foil (0.4 mm thickness)	Sigma-Aldrich
Zn foil (0.125 mm thickness)	Advent Research Materials Ltd
Super P	Timcal
Carbon paper (H2315, 210 um thickness)	Freudenberg
Polyvinylidene fluoride	Sigma-Aldrich
Glass fibre filter (270 μm thickness)	PRAT DUMAS
Pt/C (20 %)	QuinTech
Nafion 117 containing solution (5 %)	Sigma
Hydrogen chloride (HCl, 37 %)	Scharlab
Dimethylamine-Borane (DMAB, 97 %)	Alfa Aesar

3.2 BC processing

The Milli-Q water (18.2 MΩ cm^{-1}) was obtained from a Milli-Q system (Millipore, Billerica). Food-grade BC cubes (Q-Phil Products International, approx. size 15x15x15 mm^3) were placed in Milli-Q water with twice stirring for 3 h to remove the absorbed syrup. This step was repeated again with Milli-Q water for 12 h. Then, the BC cubes were autoclaved at 120 ℃ for 20 min. To replace water with other solvents, one piece of BC was pressed by a Teflon cylinder (150 g) for 10 min.

3.3 Characterization

FEI Quanta 200 FEG-ESEM equipment (15 kV Voltage) was used to obtain Scanning Electron Microscopy (SEM) images. Images were analyzed with ImageJ software to estimate fiber and particle diameters [1]. JEOL JEM1210 TEM (voltage 120 kV) and JEM-2011 TEM (voltage 200 kV) were carried out to obtain Transmission electron microscopy (TEM) images. Fourier transform infrared (FTIR)

spectra of samples were conducted by a Jasco 4700 Spectrophotometer. Raman spectra of samples were recorded by a Renishaw InVia Raman Microscope with 633 nm laser. Thermogravimetric analysis (TGA) was done by a NETZSCH STA 449 F1 Jupiter equipment under air atmosphere with 10 °C min^{-1} ramp. N_2 adsorption/desorption measurements were probed by Micromeritics ASAP 2020 equipment. X-ray Photoelectron Spectroscopy (XPS) measurements were taken by a SPECS EA10P hemispherical analyzer with a monochromatic Al Kα source. The X-ray absorption spectroscopy (XAS) data were obtained at the CLAESS beamline of the ALBA Synchrotron Light Source. The X-ray diffraction (XRD) patterns of all samples were performed by Siemens D-5000 equipment with Cu K$_\alpha$ radiation. Tests were carried out in a 2θ range of 10° to 90°. The crystallinity index (CI) of BCs was calculated by the following equation：

$$CI=(I_{110}-I_{am})/I_{110}$$

where I_{110} is the peak intensity at 22.5 ° for the crystalline part of cellulose type I, I_{am} is the peak intensity at about 18 ° for the amorphous part [2].

3.4 Electrochemical measurements

The cycle voltammetry (CV), linear sweep voltammetry (LSV) electrochemical impedance spectroscopy (EIS) and chronopotentiometry curves measurements were conducted by a Bio-logic VMP3 multichannel potentiostat. All LSV curves were corrected for iR drop. Galvanostatic discharge/charge tests were performed by battery cyclers, MTI BTS-5V100mA and LANHE M340A.

3.5 References

[1] C.A. Schneider, W.S. Rasband, K.W. Eliceiri, NIH Image to ImageJ: 25 years of image analysis, Nat. Methods 9(7) (2012) 671-675.

[2] E. Alonso, M. Faria, F. Mohammadkazemi, M. Resnik, A. Ferreira, N. Cordeiro, Conductive bacterial cellulose-polyaniline blends: Influence of the matrix and synthesis conditions, Carbohydr. Polym. 183 (2018) 254-262.

Chapter 4 Carbons Derived from Alcohol-Treated Bacterial Cellulose with Optimal Porosity for Li-O$_2$ Batteries

4.1 Summary

Considering that using compatible solvents with low surface tension, such as alcohols, to treat cellulose can relieve the occurrence of compacted structure [1, 2], here we show a facile and low-cost method to prepare porous carbons from alcohol-treated food store commercial BC. The obtained carbon microstructure is not a replica of the cellulose and suggests some intermediate melting step in the pyrolysis process. Nevertheless, carbon derived from alcohol treated BC has remarkable porosity, which is used as oxygen cathodes in Li-O$_2$ batteries, showing an outstanding capacity and good cycle life. This work not only proposed a more economic and sustainable route for the preparation of different porous carbons that hold various porosity and electrochemical performance because of the control to fiber aggregation of the same cellulose, but also provided an interesting insight in the carbonization process.

4.2 Introduction

Since biomass has been regarded as the fourth most widely used energy supply (after coal, oil, and natural gas) [3], it can be a great candidate for carbons. BC is a bio-based polymer produced from microbial fermentation process [4, 5], which is employed in a wide range of applications from health to electronics [6, 7]. BC as a carbon source has raised great attention, owing to its sustainability, low-cost, three-dimensional structure, high surface area and accessible porosity [8, 9], which are ideal for electrodes in energy storage devices.

As-prepared BC is in the form of a hydrogel, thus thermal carbonization requires

a drying step. The drying route applied modifies the morphology, surface area and porosity of BCs considerably, which can influence the properties of the resulting carbons [10, 11]. In fact, when the gel is dried by simple water evaporation in air or an oven, the strong capillary forces collapse the pores in the cellulose network, which induces fibril aggregation known as hornification, resulting in a low porosity material. Freeze-drying, spray-drying and supercritical drying are often used to hinder hornification [12, 13], increasing the surface area of cellulose and producing porous structures.

Such porous cellulose has been successfully employed by some research groups to produce carbons with a nanofibrous structure that replicate the nanocellulose network [8, 14]. However, the drying methods applied are generally time and energy consuming and require more expensive facilities than simple oven drying. Therefore these methods do not represent a remarkable advantage with respect to conventional methods to introduce and control porosity of carbons from biomass, as it is the case of chemical activation by corrosive compounds [15, 16], templating agents [17], or use hydrothermal synthesis [18].

As reported by previous literature [1, 2], alcohol treatments contribute to preserving porous structures in dried cellulose reducing the degree of hornification. We tested several solvents as water replacement of the bacterial cellulose hydrogel, focusing in particular on aliphatic alcohols of different chain lengths carbonized and tested as electrodes in $Li-O_2$ batteries.

4.3 Preparation of carbons

The preparation of carbons from never-dried, purified BC is schematized in Figure 4.1. The cleaned, cubic-shaped BC hydrogels were pressed to about 10 % of the original height to remove the majority of water. One pressed BC cube was then soaked in a beaker with 10 mL of a given solvent and stirred for 2 h at room temperature. Afterwards, the soaked BC was briefly drained of excess solvent and placed without pressing in an oven to dry (60 ºC, 24 h). Finally, dried BC was

carbonized in a tubular furnace under an Ar flow of 100 mL min^{-1} with a ramp of 10 ºC min^{-1} to 900 ºC and kept there for 1h.
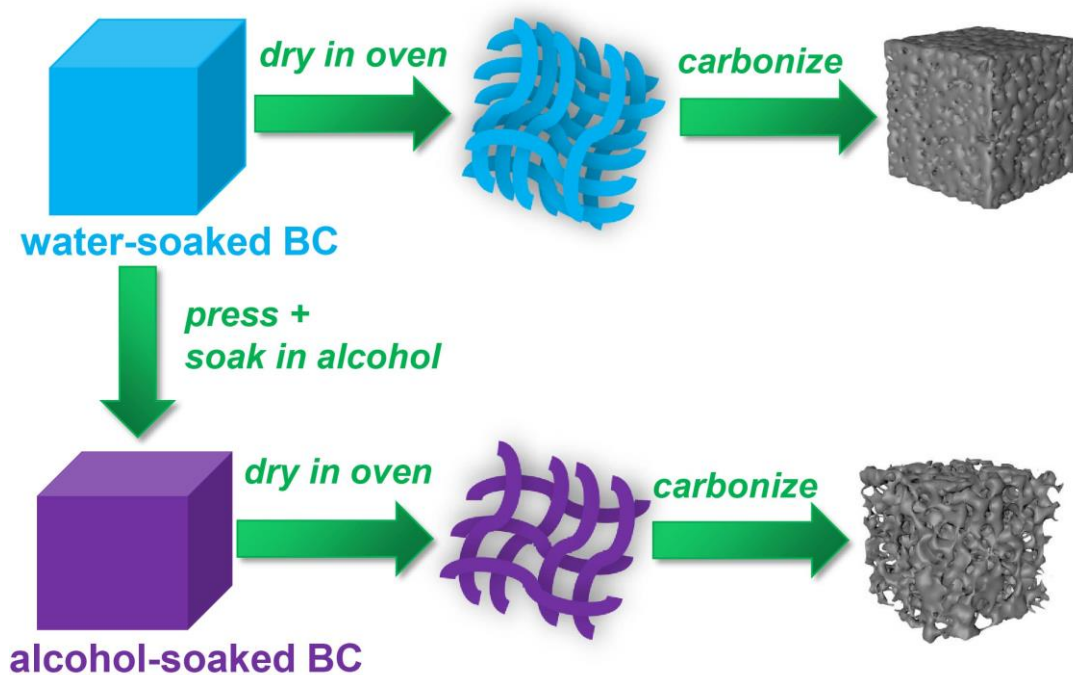

Figure 4.1. Schematic illustration of preparing carbons derived from BC.

Table 4.1 summarizes physical properties of the solvents that were tested. Water has the highest surface tension among these solvents. Other parameters, such as the solvent volatility may also play a role in the pore formation and could help explain differences between alcohols. To better understand the impact that the hydrogel water replacement for an organic solvent has on the obtained materials we focused on the characterization of the preparative steps of the carbons obtained from untreated (BC-w), and from two alcohols of different aliphatic chain length, ethanol (BC-e), and 1-butanol treated cellulose (BC-b).

The different solvents had different ability to swell BC. BC cubes swelled to recover more than 90 % of the original size in ethanol and more than 70 % in the case of 1-butanol.

Table 4.1. Boiling point and surface tension of solvents used in this study [19].

Solvents	Boiling point (°C)	Surface tension (20 °C) / (mN m^{-1})
water	100	72
methanol	64.51	22.50
ethanol	78.32	22.27
1-propanol	97.2	23.70
1-butanol	117.7	25.00
1-hexanol	157.1	24.48
1-octanol	195	26.71
ether	34.6	17.06
acetone	56.12	23.32
TEGDME	216	29.4

FTIR spectra of soaked BC are similar to those of the pure solvents, which is consistent with complete solvent substitution (Figure 4.2a and Figure 4.2c-d). The alcohol treatment does not chemically alter BCs, according to FTIR spectroscopy of dried BCs (Figure 4.2b and Figure 4.2c-d). In fact, dried BCs show typical cellulose peaks, which can respectively be ascribed to the stretching vibration of O-H (3350 cm^{-1}), H-C-H (2900 cm^{-1}), C-O-C (1427 cm^{-1}) [20], with no apparent difference between them, which also proves the quantitative solvent removal in the three cases.
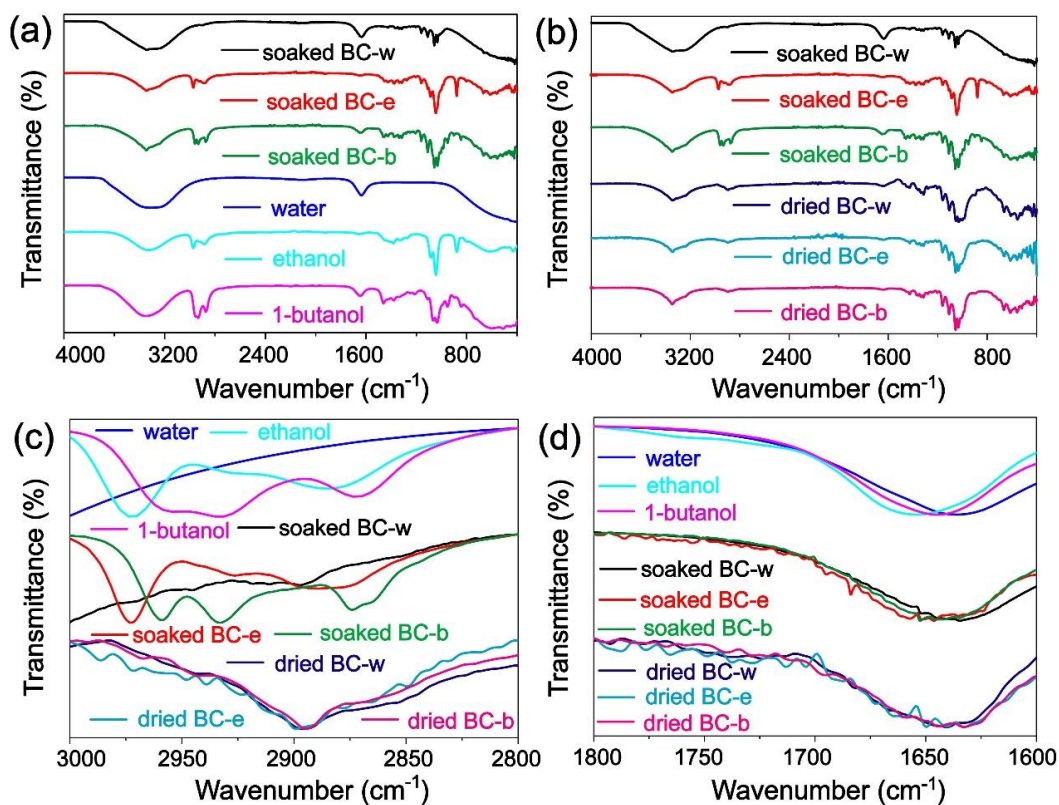
Figure 4.2. (a) FTIR of soaked BCs and pure solvents; (b) FTIR of soaked BCs and dried BCs; (c) FTIR (3000-2800 cm^{-1}) of samples; (d) FTIR (1800-1600 cm^{-1}) of samples.

At SEM images (Figure 4.3a-c), BC-w shows a smooth surface, which demonstrates that fibrils have compacted. The cross-section SEM images (Figure 4.3d-f) show that the layers of BC-w are more densified in comparison with BC-e and BC-b. This confirms that the treatment of ethanol and 1-butanol reduces interfibrillar contraction. The morphology differences between BC-w, BC-e can be attributed to the following factors. On the one hand, the much smaller surface tensions of ethanol and 1-butanol (Table 4.1) decrease the capillary force effects as compared to water during the solvent evaporation [1, 21]. Small surface tensions of ethanol and 1-butanol result in weaker capillary forces during the process of drying. In this case, fibrils move less than when water is removed, the distance between fibrils barely changes. On the other hand, ethanol and 1-butanol can attach to the surface of fibrils via hydrogen bonds [22, 23]. As a consequence, the self-association behaviors of fibrils can be hindered by the

chemical steric hindrance effect of ethanol and 1-butanol, impairing the cohesion among fibrils. Therefore, by treating wet BC with ethanol and 1-butanol highly porous structures can be achieved.
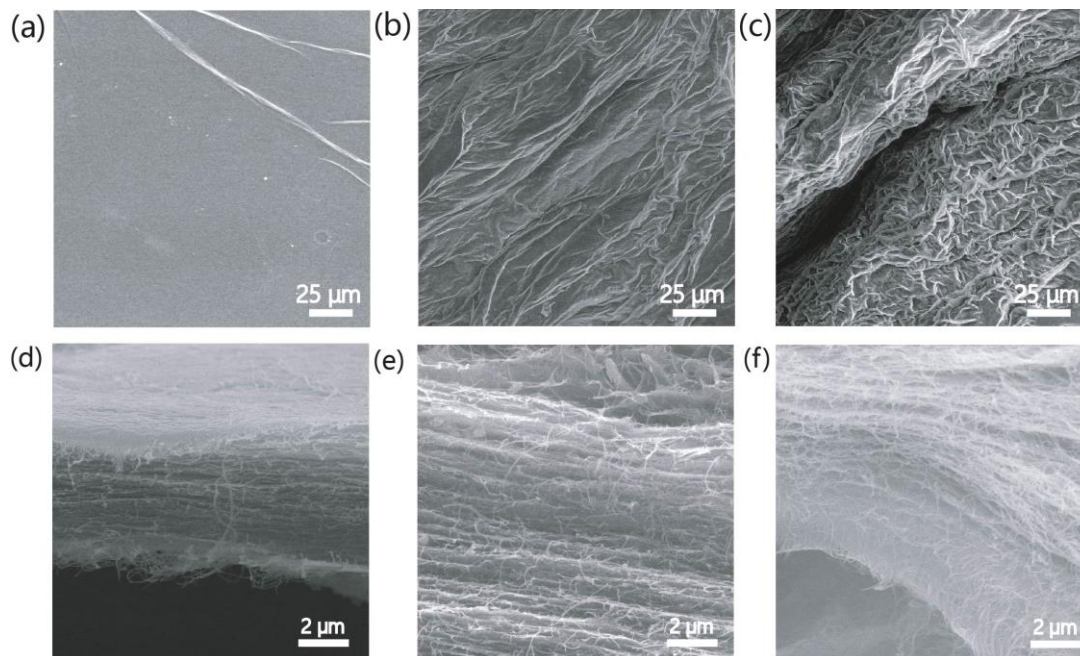

Figure 4.3. Characterization of different dried BCs. SEM surface images of dried (a) BC-w, (b) BC-e and (c) BC-b; cross-section images of (d) BC-w, (e) BC-e and (f) BC-b.

The porous structures of dried BCs were compared by nitrogen adsorption-desorption measurements (Figure 4.4). All three isotherms present hysteresis and could be considered of mixed type II and IV. Pore size distributions (Figure 4.4a) mainly range in the mesoporous region, with a macropore contribution in the case of alcohol-treated samples, while micropores are scarce in all three samples. Dried BC-w presents small area and porosity (BET specific surface area 21 m^2 g^{-1} and cumulative pore volume 0.11 cm^3 g^{-1}, Table 4.2). In contrast, BC-e and BC-b have respectively over four and five times larger surface areas and pore volumes. These increments agree with the textured structure observed by SEM in BC-e and BC-b. The pore size distributions (Figure 4.4b) of all dried BCs are dominated by mesopores, but BC-e and BC-b have larger predominant pore sizes than BC-w.
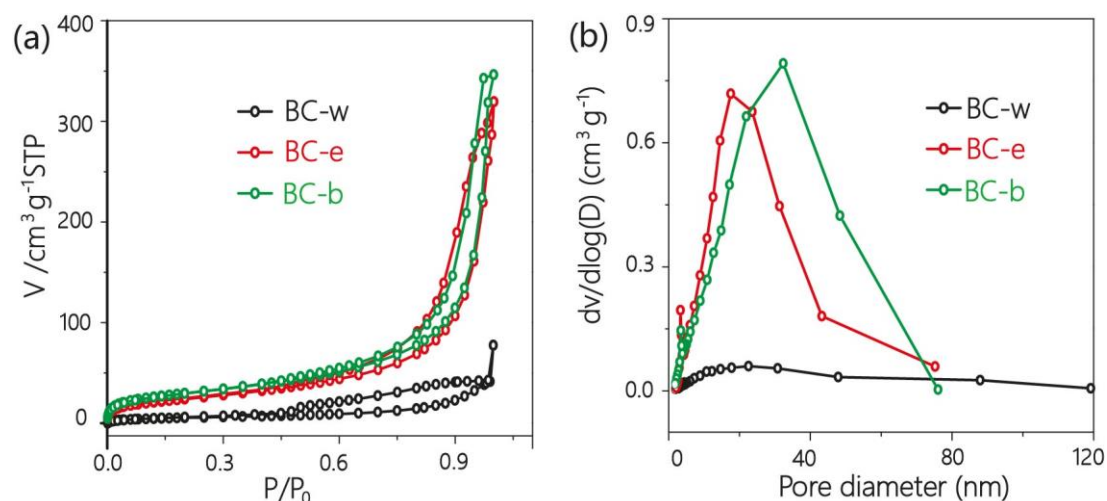
Figure 4.4. (a) Nitrogen adsorption-desorption isotherms of dried BCs; (b) pore size distribution.

Table 4.2. BET surface areas and pore volumes of dried BCs determined by N_2 absorption.

Samples	BET surface area ($m^2\ g^{-1}$)	Pore Volume ($cm^3\ g^{-1}$)	Pore Volume ($cm^3\ g^{-1}$)	Predominant pore size (nm)
BC-w	21	0.11	0.11	14
BC-e	88	0.44	0.44	17
BC-b	107	0.54	0.54	32

XRD was used to study the effect of alcohols on the crystallinity of BCs. Figure 4.5 depicts that all BCs show typical pattern peaks (14.5 ° and 22.5 °) of cellulose type I, which correspond to the (100) and (110) lattice planes respectively [24]. Compared with the crystallinity of BC-w (78 %), the crystallinity of BC-e (66 %) and BC-b (70 %) decreases slightly. The decrease in crystallinity suggests that the cellulose becomes more disordered and loosen, which can be attributed to the effect of dissociation of the hydrogen bonds between cellulose [25].
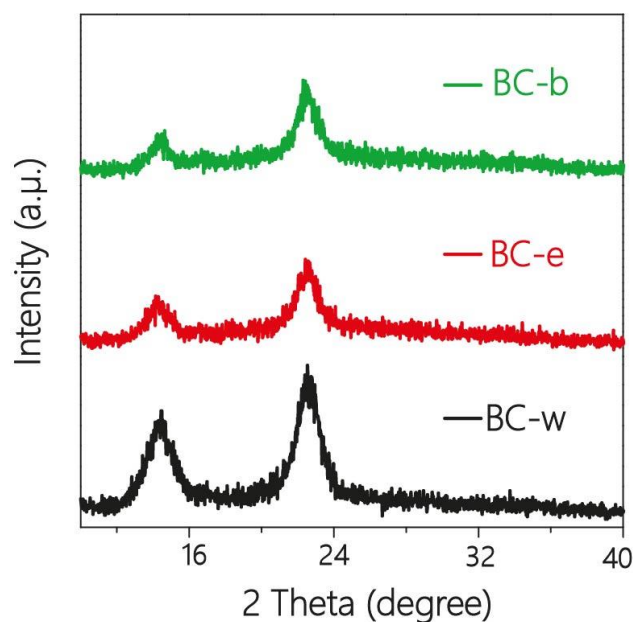
Figure 4.5 XRD of dried BCs.

To explore the effect of the fiber aggregation on the carbonization process, all dried BCs were subjected to TGA under Ar (Figure 4.6a). There are two major mass losses during the temperature ramp. The first small mass loss step (25-100 ℃) can be attributed to the evaporation of residual absorbed water [26]. The loss is larger for BC-w (2.5 %) than for alcohol treated samples (0.9 % for BC-e and 0.1 % for BC-b). This can be considered a proof that a large part of the most tightly bound water molecules was removed during the alcohol treatment. The second mass loss step occurred at 200-400 ℃, corresponding to BC decomposition and carbonization. During this step cellulose depolymerizes and fragments on variable molecular weight forms, giving place to char, tar, and volatile compounds (such as water, carbon dioxide and monoxide, acetic acid, and different saccharides) [27]. The yield of these solid, liquid and gaseous fractions has a strong influence on the subsequent carbonization process. The DSC curves (Figure 4.6b) indicated that the temperatures for the first major decomposition peaks of BC-e (286 ℃) and BC-b (297 ℃) are lower than BC-w (322 ℃). This can be related with the lower crystallinity of BC-e and BC-b, which can facilitate the degradation process of BCs [28]. In addition, carbon yields (Figure 4.6a) of BC-e (9 %) and BC-b (10 %) are lower than BC-w (14 %), probably because of the smaller pores of BC-w. These smaller pores retain more

strongly the pyrolysis liquid intermediates, which are also involved in cross-linking and char formation [29]. The impregnation of a less porous system implies a smaller liquid-gas interface and a stronger liquid-solid interaction, reducing the intermediate volatilization and increasing char production, resulting in a larger carbon yield [27, 29].
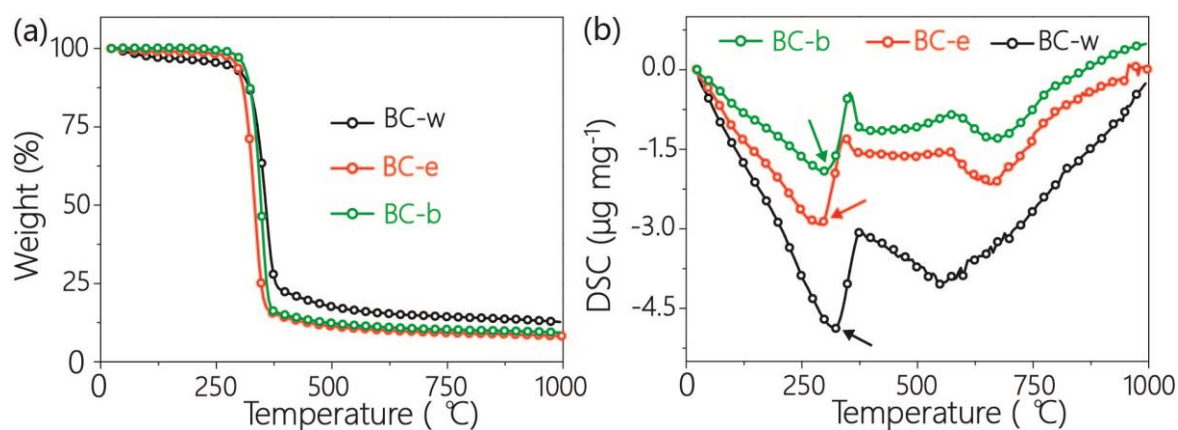

Figure 4.6. (a) TGA of dried BCs; (b) DSC of dried BCs.

The presence of liquid intermediates is evident from the textures observed after carbonizing dried BCs at 900 ℃ in Ar. Carbon originated from water-treated BC (carbon-w) presents a compact vitreous morphology (Figure 4.7a), which implies that their pores only correspond to narrow gaps between components of carbon-w. In contrast, carbons derived from ethanol (carbon-e) and 1-butanol (carbon-b) present evident porous structures (Figure 4.7b-c), although the original fibrous structure is not retained. The disappearance of fibrous structure probably can be ascribed to the melting of nanofibers during the high temperature treatment. The TEM images of carbons (Figure 4.7d-f) show that particularly carbon-b possesses more developed and open porous structures, while carbon-w appears denser than carbon-e and carbon-b. This indicates that ethanol and, particularly, 1-butanol treatments are beneficial to obtain porous carbons from BC.
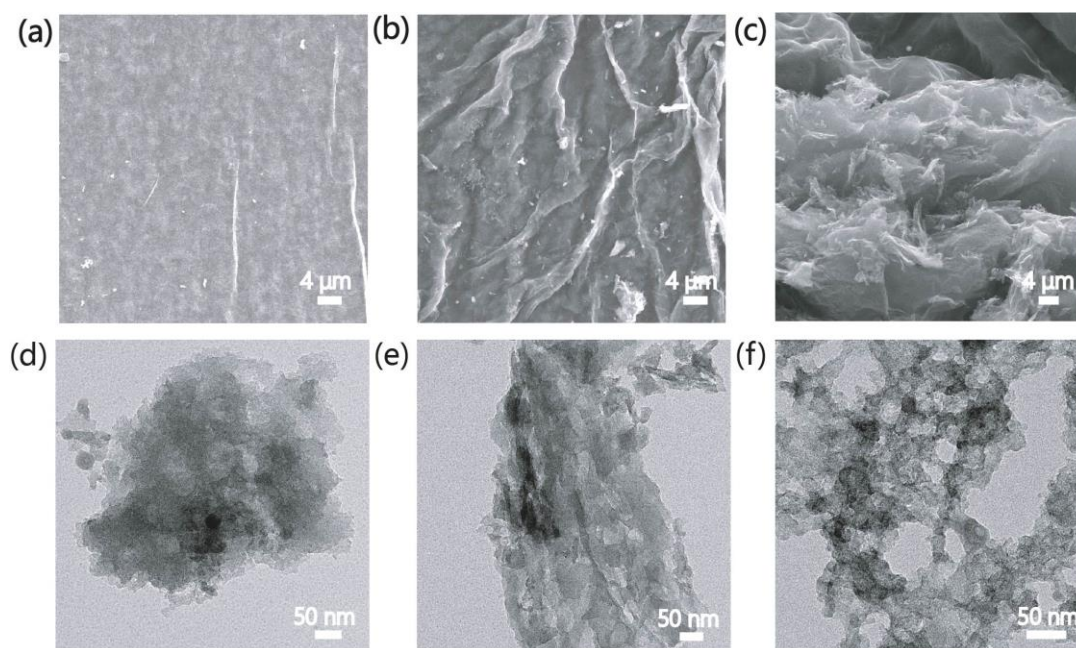
Figure 4.7. SEM images of (a) carbon-w, (b) carbon-e and carbon-b; TEM images of (d) carbon-w, (e) carbon-e and (f) carbon-b.

The porous structure properties of carbons were further studied by nitrogen adsorption-desorption measurements (Figure 4.8a and Table 4.3). Although the BET surface area of carbon-w results larger than other carbons, its pore structure mainly consists of micropores (Figure 4.8b). Instead, the pore structure of carbon-b is dominated by macropores and mesopores, resulting in a larger external area (surface area other than the inner surface of the micropores). Therefore, the more open structure of alcohol-dried BC-e and BC-b seems to be beneficial to the formation of a broader porous structure during pyrolysis.
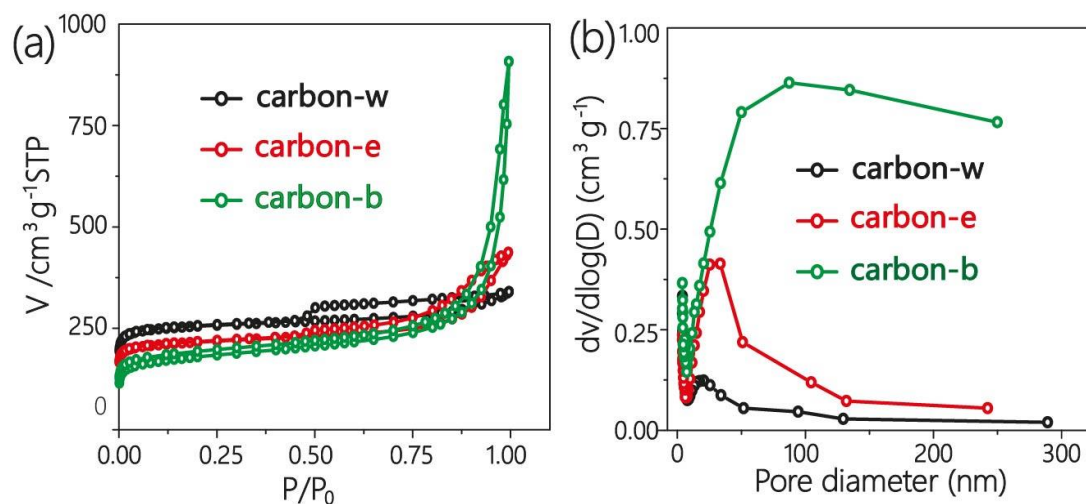
Figure 4.8. (a) Nitrogen adsorption-desorption; (b) pore size distribution.

Table 4.3. Textural data of samples and ECSAs of carbons.

Samples	BET surface area $(m^2\ g^{-1})$	External surface area $(m^2\ g^{-1})$	Pore Volume $(cm^3\ g^{-1})$	Predominant pore size (nm)
Carbon-w	1009	153.44	0.19	16
Carbon-e	848	142.26	0.41	27
Carbon-b	669	237.42	1.25	85
Super P[30]	67	70	0.14	40

The XRD patterns of carbons are shown in Figure 4.9. The broad peak at around 23° present in the three cases can be attributed to the (002) plane of graphitic carbon [31].

Figure 4.9. XRD of BC-derived carbons.

4.4 Electrochemical performance

To fabricate an air cathode, a slurry was prepared by mixing carbon samples and PVDF (8:2 carbon/PVDF w/w) in NMP and coated on a 10 mm diameter carbon paper (Freudenberg H2315). Then, the coated carbon paper was put in a vacuum oven at 80 ℃ for 24 h to remove NMP. The BC-derived carbon mass loading of the cathode is about 1 mg cm^{-2}. The Li-O$_2$ battery is composed of 3 part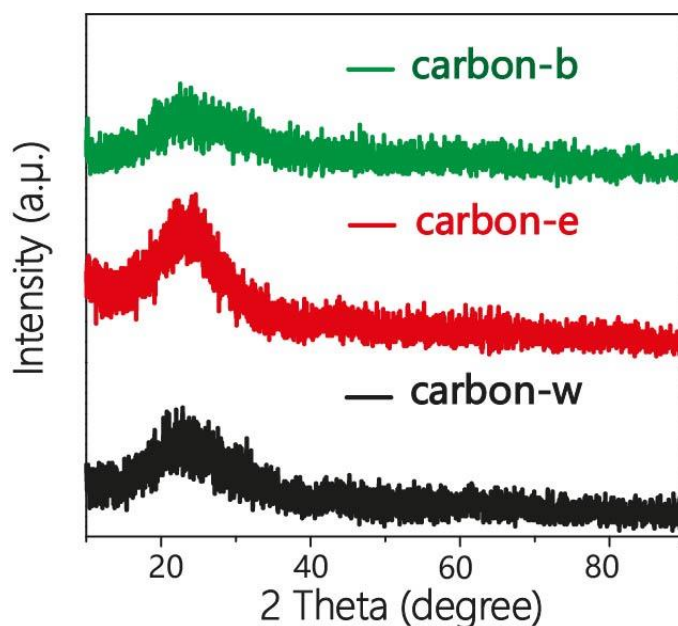s (carbon paper, glass fibre filter and Li foil). A 1 M lithium triflate solution in DEGDME was used as the electrolyte. Li-O$_2$ batteries were assembled in an Ar filled glove box (H$_2$O<0.1 ppm, O$_2$<0.1 ppm). All the tests were carried out in 1 atm dry O$_2$ to avoid the effect of CO$_2$ and humidity.

The estimation of the electrochemical surface area (ECSA) was based on the evaluation of the electrochemical double layer capacitance, and performed in a three-electrode system with a 1 M lithium triflate in DEGDME electrolyte after Ar bubbling. Carbon-coated carbon paper prepared as described above, with a mass loading of about 0.2 mg was used as the working electrode. Platinum wires were used as the counter and the reference electrode. The measurements were conducted at 2 mV s^{-1} in a narrow potential range. The electrochemical double layer capacitance

C_{EDL} was obtained by the following equation [32]:

$C_{EDL} = \int iVdV/(2\nu m\Delta V)$

where i is the current, V is the potential, m is the mass of carbons, ν is the scan rate, ΔV is the potential range.

The electrode architecture has a dramatic effect on the discharge capacity of Li-O_2 batteries, as shown by several previous studies [30, 33], which are useful to understand the behavior of our materials in this application. Therefore, the ECSA was determined to gain textural insights from the electrochemical point of view of the porous carbons [34, 35]. The ECSA is based on the formula (ECSA=C_{EDL}/C^*) [36], where C^* is the specific capacitance (F m^{-2}) of a bare glassy carbon electrode in the same electrolyte. The C^* value was determined by electrochemical impedance spectroscopy (Figure 4.10). The continuous line is the result of fitting data with the equivalent circuit shown in the insert (R is a resistor and CPE is a constant phase element), from which the parameters R=532 ohm, Q=1.57e-6 F·s$^{(\alpha-1)}$, α=0.939 were obtained. The effective capacitance of the constant phase element is given by $C_{eff} = (QR^{1-\alpha})^{1/\alpha}$ where α and Q as CPE parameters, R is the ohmic resistance [37, 38]. From this value we calculate the specific capacitance C*=C_{eff}/S_{GC}=14.06 μF cm^{-2}, where S_{GC}=0.07 cm^{-2} is the area of the glassy carbon electrode.
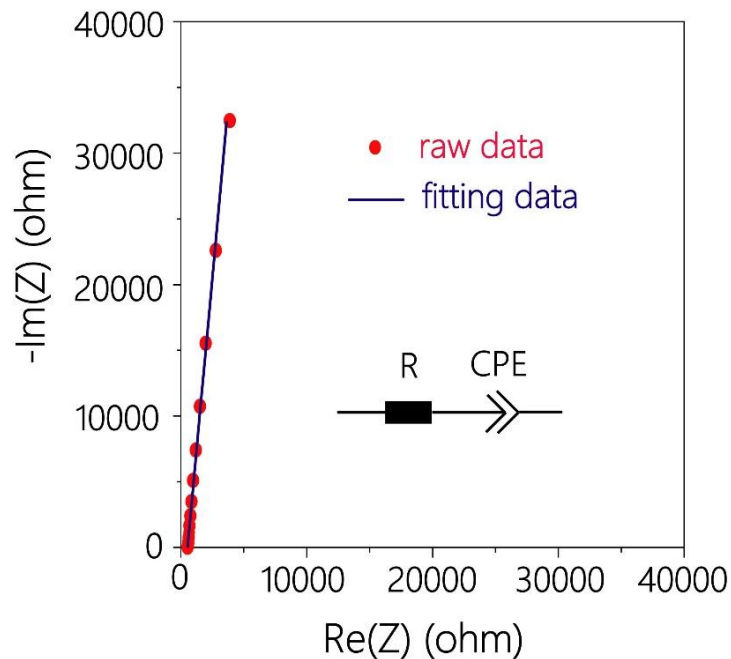

Figure 4.10. EIS of a bare glassy carbon electrode at the open circuit potential in 1 M

lithium triflate (DEGDME) with saturated Ar.

The values were obtained from capacitive currents in CV of the different carbons coated on a carbon paper support (Figure 4.11a). The ECSA of bare carbon paper is very small ($0.14 \ m^2 \ g^{-1}$), which means that its surface has little contribution to the electrochemical interface. The ECSA of carbon-b ($180 \ m^2 \ g^{-1}$) is the largest among the carbons derived from BCs, as carbon-e provided $99 \ m^2 \ g^{-1}$ and carbon-w $33 \ m^2 \ g^{-1}$ (Figure 4.11b). Thus, the largest BET area of BC-w translates into the smallest electrochemically effective area, showing that smallest micropores are not accessible to our electrolyte, similarly to what previously observed with ionic liquid electrolyte [33]. Instead, the larger pores of alcohol-treated carbons offer a better ion-accessible surface area, and show larger ECSA values. ECSA seems a more significant parameter to predict effectiveness as Li-O_2 cathode than BET area.
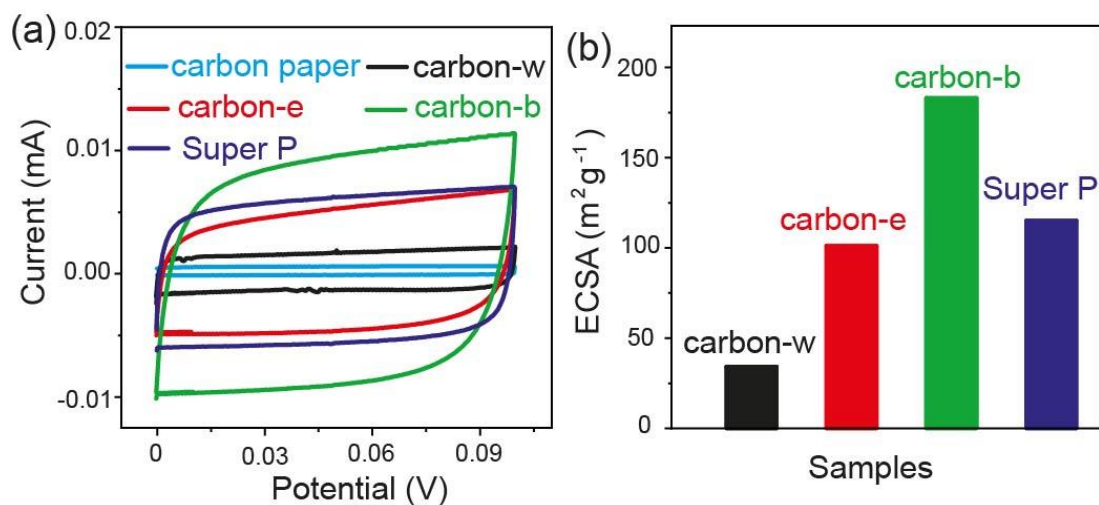
Figure 4.11. (a) CV curves of carbons in Ar-saturated 1 M lithium triflate in DEGDME; (b) comparison of ECSAs.

Figure 4.12 displays cyclic voltammetry curves of our carbons in the O_2 atmosphere at a scan rate of 20 mV s^{-1}. There are one reduction peak and one oxidation peak, which can be respectively ascribed to the formation of Li_2O_2 and the decomposition of Li_2O_2 [39]. Compared with carbon-w, alcohol-treated carbons display higher currents for both reduction and oxidation peaks. This shows that

carbon-e and carbon-b provide better oxygen redox activities thanks to their more suitable pore structure.
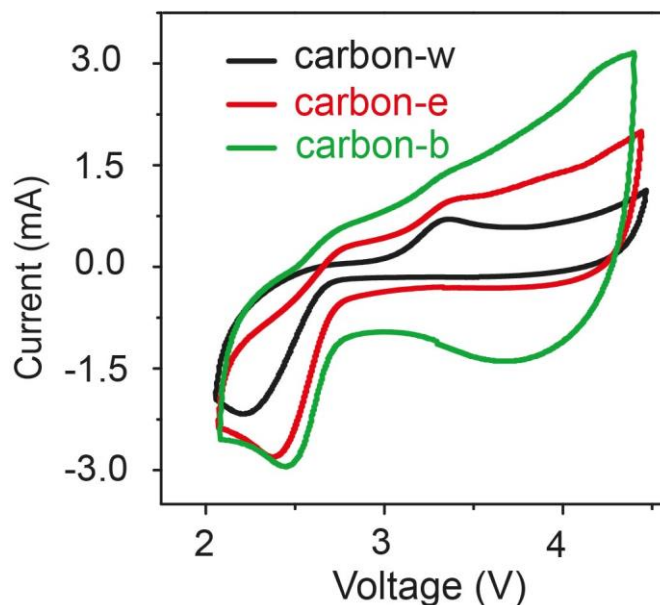
Figure 4.12. CV curves of Li-O_2 batteries with carbon cathodes (with a scan rate of 20 mV s^{-1} in the range of 2.0-4.5 V versus Li/Li$^+$).

Galvanostatic discharge-charge profiles of Li-O_2 batteries were operated at the current density of 0.1 mA cm^{-2} (Figure 4.13a). The contribution of bare carbon fiber support to this capacity is negligible (Figure 4.13b). Carbon-b and carbon-e provide discharge capacities of 5.58 and 1.36 mA h cm^{-2}, while carbon-w only gives capacity similar to that of the support alone (0.14 mA h cm^{-2}). Carbon-b also has the highest discharge voltage (~2.75 V), which can be attributed to its larger ECSA. The larger area significantly decreases overpotentials in Li-O_2 batteries and in effect, correlation between specific area and discharge potential has been shown previously [30, 40]. These capacities clearly show that not only the larger pore volume, but also the larger pore sizes favour more abundant discharge of Li$_2$O$_2$ [41]. The poor capacity of carbon-w can be attributed to its too small pore size. This is reflected by the low ECSA and is consistent with previous observation that only pores larger than a certain size, in the order of 10 nm, significantly contribute to the cathode capacity [33, 42]. In addition, small pores will be easily blocked, which hinders the diffusion of oxygen [43]. Instead, the other carbons show much more suitable pore structure, in particular

carbon-b, which even outperforms Super P, a carbon black with very open structure that typically offers large capacity [30, 42]. The capacity difference between carbon-b and Super P can be attributed to the different architecture of carbon-b which offers wider pores and larger surface area that allows for a better distribution of discharge products (Table 4.3).
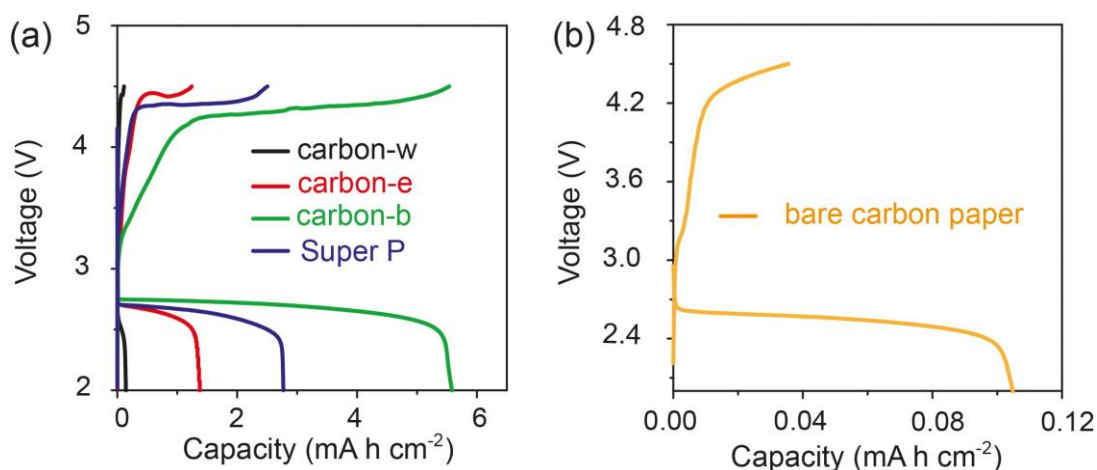
Figure 4.13. (a) Full discharge-charge profiles within the voltage range of 2.0-4.5 V at 0.1 mA cm^{-2}; (b) the full discharge-charge profile bare carbon paper at 0.1 mA cm^{-2}.

BC treated with 1-butanol for 24 hours showed similar morphologies and discharge capacities (Figure 4.14), confirming that two hours soaking is sufficient for quantitative water removal. Carbon-b exhibits outstanding discharge capacity also compared to other carbons reported in the literature, as it can be observed in Table 4.4.
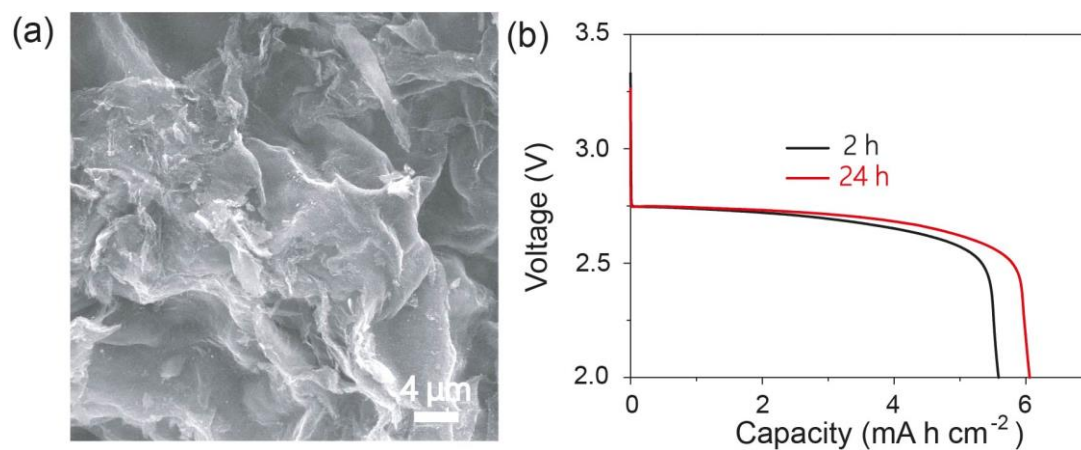
Figure 4.14. (a) SEM image of carbon derived from BC soaked 24 h in 1-butanol; (b)

comparison of full discharge profiles of carbons derived from BCs soaked in 1-butanol during different time at 0.1 mA cm^{-2}.

Table 4.4. Textural data of carbons and their discharge capacity for Li-O$_2$ batteries.

Carbon	BET surface area (m^2 g^{-1})	Pore volume (cm^3 g^{-1})	Predominant pore size (nm)	Discharge capacity (mA h cm^{-2})
Carbon-b	669	1.25	~85	5.58 (0.1 mA cm^{-2})
Hierarchical ordered macroporous/ultrathin mesoporous carbon [44]	451	1.9	~18.5	4.08 (0.1 mA cm^{-2})
Mesoporous carbon -3 [45]	789	1.18	~6	5 (0.1 mA cm^{-2})
rGO [43]	361	1.58	~17.5	4.71 (0.05 mA cm^{-2})
Carbon with steam activation [46]	1649	1.21	~8	1.2 (0.05mA cm^{-2})
Chemically obtained graphene [47]	535.3	0.41	~5	0.45 (0.075mA cm^{-2})
Activated tea leaves[48]	2868.4	1.16	<1	1.25 (0.1 mA cm^{-2})

The rate capabilities of carbon-b and Super P cathodes were compared at the increased current density of 0.4 mA cm^{-2} (Figure 4.15a). With the increment of the

current density, the discharge capacity descended, discharge voltage decreased and charge voltage increased in all cases, but more severely for Super P. This better rate capability can be attributed to larger ECSA, demonstrating again the optimal texture of alcohol-treated carbons as Li-O_2 cathodes. Carbon-b cathode displayed nearly 100 % coulomb efficiency at 0.1 mA cm^{-2}, and still 90 % at 0.4 mA cm^{-2}. However, due to the larger overpotentials, Super P exhibited poorer figures (92 % at 0.1 mA cm^{-2}, 43 % at 0.4 mA cm^{-2}). In line with this behavior, the cycling stability of carbon-b was far superior to that of Super P. In a test at 0.1 mA cm^{-2} with a capacity limitation of 0.5 mA h cm^{-2} (Figure 4.15b-d), the Super P electrode only sustained 4 cycles against more than 58 cycles for carbon-b. Table 4.5 depicts a comparison of the electrochemical performance for several reported cathodes. The outstanding number of cycles that carbon-b can withstand makes it an attractive material for Li-O_2 batteries.
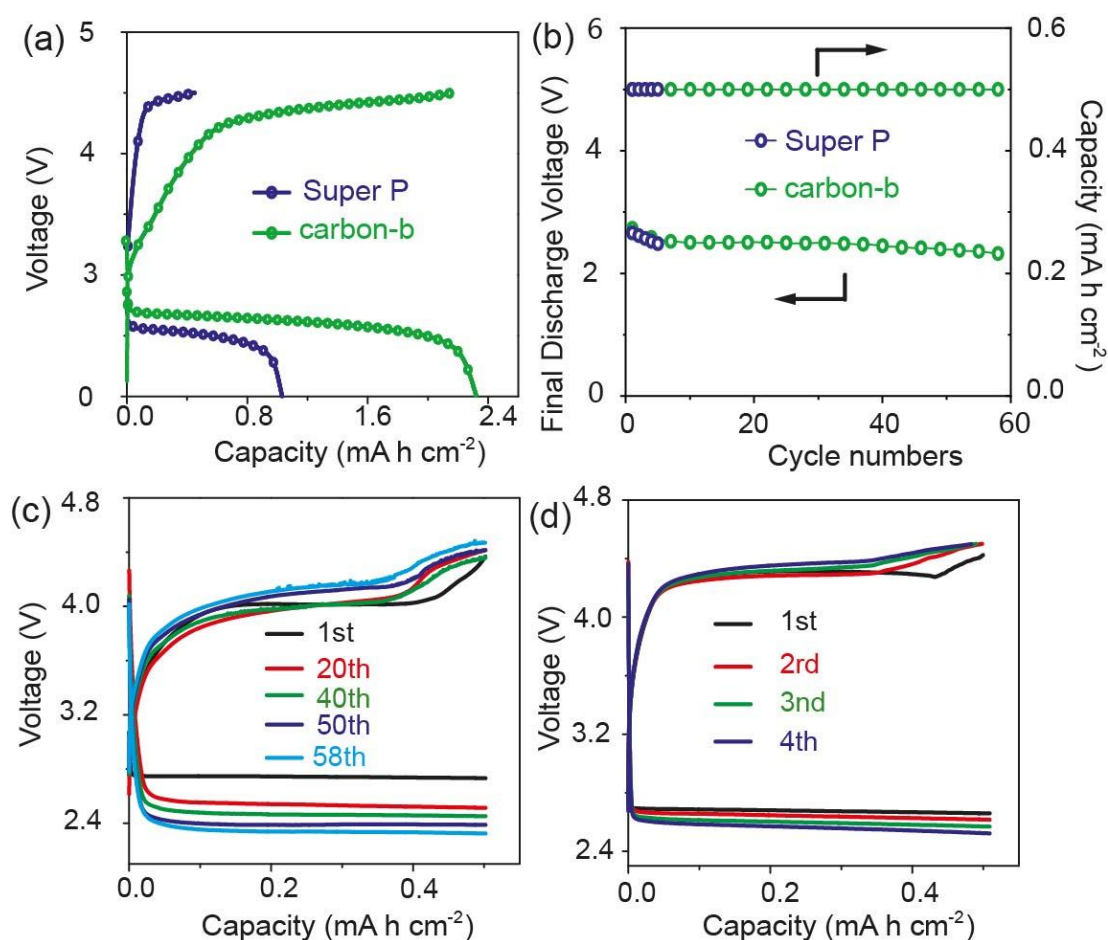

Figure 4.15. (a) Full discharge-charge profiles at 0.4 mA cm^{-2}; (b) cycle life of

carbon-b tested at 0.1 mA cm^{-2}; discharge-charge profiles of carbon-b (c) and Super P (d) at 0.1 mA cm^{-2}.

Table 4.5 Comparison of the cycle life carbon-b and values reported in literature for different Li-O$_2$ battery cathodes.

Sample	Current density (mA cm^{-2})	Capacity limitation (mA h cm^{-2})	Cycle number
Carbon-b	0.1	0.5	58
Carbon derived from [BMIm]Cl [49]	0.1	0.7	26
Graphene aerogel [50]	0.12	0.6	30
Mesoporous carbon-3 [45]	0.1	0.5	13
N-doped carbon [51]	0.08	1.5	20
Fe$_2$O$_3$/carbon [52]	0.1	0.48	30
Co@N-C microspheres [53]	0.1	0.5	40
MOF(Fe/Co)-CNTs [54]	0.1	0.6	40
Biphasic N-doped Co@graphene capsule [55]	0.1	1	30
NiFe$_2$O$_4$/C nanofibers [56]	0.1	0.44	40

To prove the specificity of the bacterial cellulose texture, cotton linters and agarose were also treated by water and 1-butanol. Cotton linters are made by much thicker cellulose fibers than those found in BC, while agarose is a gel with similar chemical properties to wet BC but with no fibers and homogeneous at the mesoscale.

1-butanol seems to reduce fiber agglomeration in cotton, and after carbonization some larger porosity is observed, but with micrometer-sized pores (Figure 4.16). No significant effect is instead visible in the microstructure of agarose after treatment in 1-butanol (Figure 4.17). In both cases, the capacity improvement from water to

1-butanol was not large (Figure 4.16 and Figure 4.17). This proves that the large mesoporosity is a specific effect of well-dispersed cellulose nanofibers, which can be obtained after drying from solvents such as alcohols, able to prevent their collapse.

Figure 4.16. SEM images of water (a) and 1-butanol (b) treated cotton linters; SEM images of carbons from water treated cotton linters (c) and 1-butanol treated cotton linters (d); (e) full discharge-charge profiles of carbons derived from water and

1-butanol-treated cotton linters at 0.1 mA cm^{-2}.

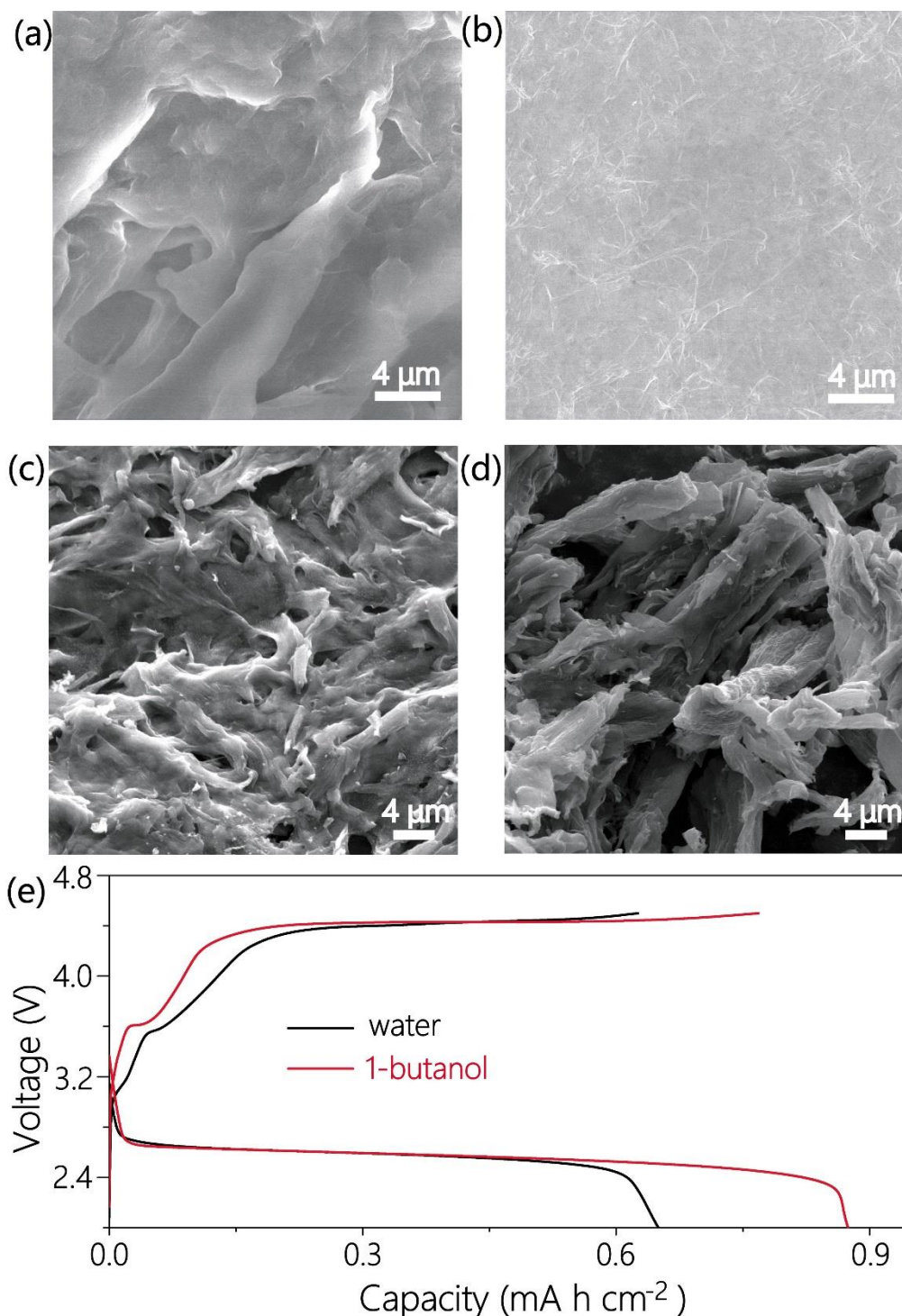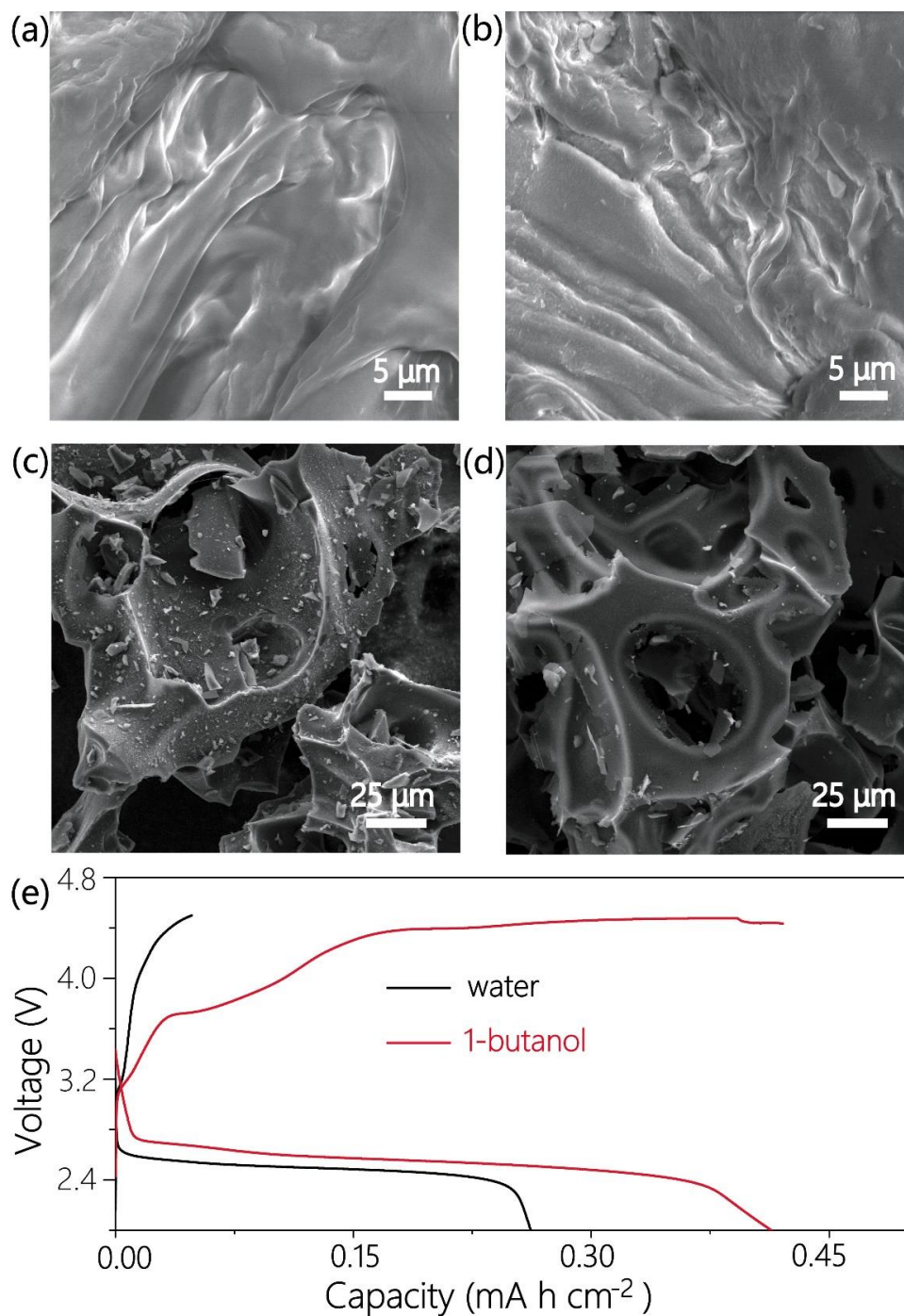**Figure 4.17.** SEM images of water (a) and 1-butanol (b) treated agarose; SEM images of carbons from water-treated agarose (c) and 1-butanol treated agarose (d); (e) full discharge-charge profiles of carbons derived from water and 1-butanol treated agarose at 0.1 mA cm^{-2}.

Other alcohols (such as methanol, 1-propanol, 1-hexanol and 1-octanol) and some non-alcohol solvents (acetone, ether and TEGDME) were also used to treat BCs with the same preparation method. All carbons derived from BCs treated with these solvents exhibit better capacities for Li-O$_2$ batteries than carbon-w (Figure 4.18 and Table 4.6) but lower than carbon-b. This shows that 1-butanol has optimal affinity for cellulose, probably due to its mixed hydrophobic-hydrophilic character [57, 58]. However, in general it can be affirmed that the treatment of solvents with low surface tensions on BCs can promote mesoporous carbons with excellent behavior as cathode for Li-O$_2$ batteries.

Figure 4.18. SEM images of carbons derived from methanol (a), 1-propanol (b), 1-hexanol (c), 1-octanol (d), acetone (e), ether (f) and TEGDME (g) treated BCs; (h) full discharge-charge profiles of carbons derived from different solvent-treated BCs.

Table 4.6 Discharge capacity at 0.1 mA cm^{-2} of carbons derived from different solvent-treated BCs.
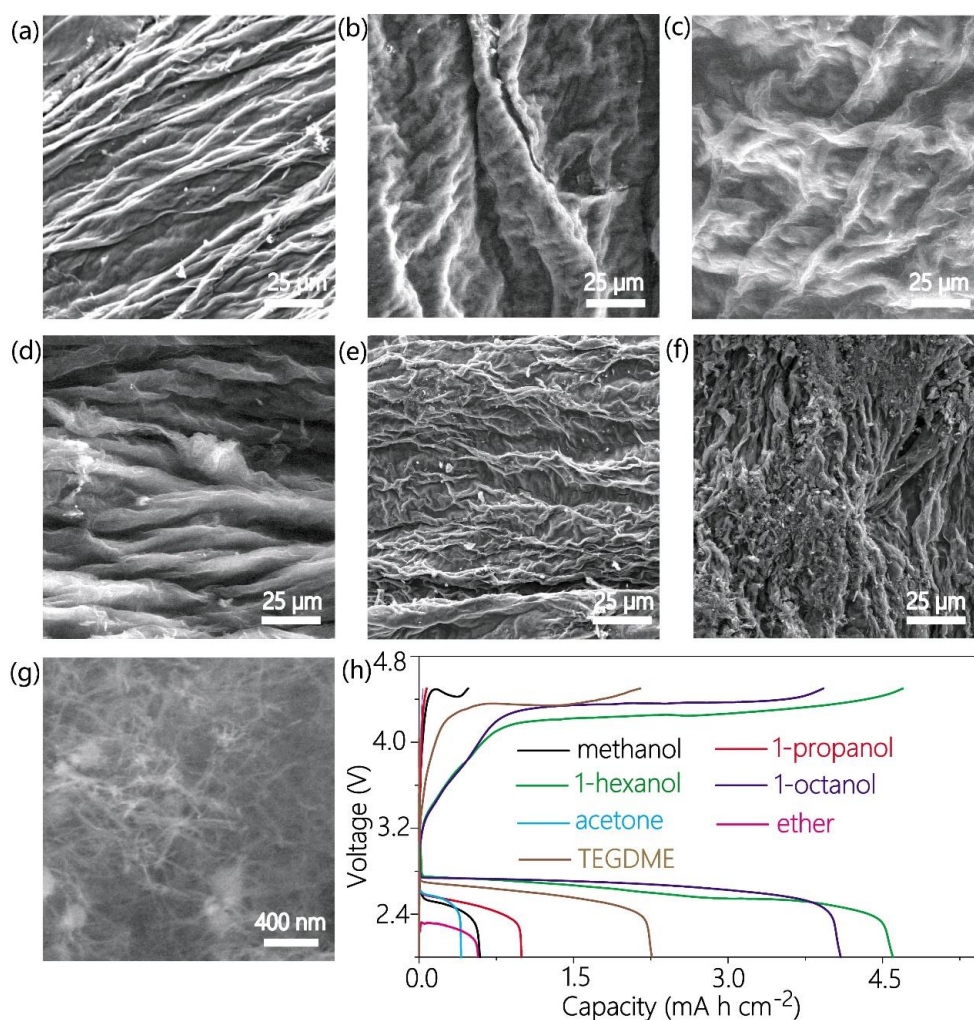
Solvent	Discharge capacity (mA h cm^{-2})
water	0.14
methanol	0.59
ethanol	1.36
1-propanol	0.99
1-butanol	5.58
1-hexanol	4.6
1-octanol	4.09
ether	0.57
acetone	0.4
TEGDME	2.25

4.5 Conclusions

Porous carbons employed as cathodes in Li-O$_2$ batteries have been successfully synthesized by using alcohols to treat BC. The much higher porosity compared to that of carbon originated from water-treated BC, seems to correspond to the more open structure of the intermediate dried cellulose, even if in all cases the fiber network is lost during carbonization. The structure obtained by treatment of BC with 1-butanol shows optimal properties as a cathode in a Li-O$_2$ battery, with much higher capacity (5.58 mA h cm^{-2}), lower overpotentials and longer cycling life than the water treated equivalent material. This performance is superior even to a reference commercial cathode material such as Super P, demonstrating a clear interest as a practical material for application in metal-air batteries, as well as metal-sulfur, supercapacitors and all systems that require efficient transport properties

4.6 References

[1] A. Tejado, W.C. Chen, M.N. Alam, T.G.M. van de Ven, Superhydrophobic foam-like cellulose made of hydrophobized cellulose fibres, Cellulose 21 (2014) 1735-1743.

[2] J. Li, T. Song, H. Xiu, M. Zhang, R. Cheng, Q. Liu, X. Zhang, E. Kozliak, Y. Ji, Foam materials with controllable pore structure prepared from nanofibrillated cellulose with addition of alcohols, Ind. Crop. Prod. 125 (2018) 314-322.

[3] F. Guo, X. Jia, S. Liang, N. Zhou, P. Chen, R. Ruan, Development of biochar-based nanocatalysts for tar cracking/reforming during biomass pyrolysis and gasification, Bioresource. Technol. 298 (2020) 122263.

[4] S. Roig-Sanchez, E. Jungstedt, I. Anton-Sales, D.C. Malaspina, J. Faraudo, L.A. Berglund, A. Laromaine, A. Roig, Nanocellulose films with multiple functional nanoparticles in confined spatial distribution, Nanoscale Horiz. 4(3) (2019) 634-641.

[5] A. Alonso-Díaz, J. Floriach-Clark, J. Fuentes, M. Capellades, N.S. Coll, A. Laromaine, Enhancing Localized Pesticide Action through Plant Foliage by Silver-Cellulose Hybrid Patches, ACS Biomater. Sci. Eng. 5(2) (2019) 413-419.

[6] G. Fei, Y. Wang, H. Wang, Y. Ma, Q. Guo, W. Huang, D. Yang, Y. Shao, Y. Ni, Fabrication of Bacterial Cellulose/Polyaniline Nanocomposite Paper with Excellent Conductivity, Strength, and Flexibility, ACS Sustainable Chem. Eng. 7(9) (2019) 8215-8225.

[7] D. Abol-Fotouh, B. Dorling, O. Zapata-Arteaga, X. Rodriguez-Martinez, A. Gomez, J.S. Reparaz, A. Laromaine, A. Roig, M. Campoy-Quiles, Farming thermoelectric paper, Energy Environ. Sci. 12(2) (2019) 716-726.

[8] X. Hao, J. Wang, B. Ding, Y. Wang, Z. Chang, H. Dou, X. Zhang, Bacterial-cellulose-derived interconnected meso-microporous carbon nanofiber networks as binder-free electrodes for high-performance supercapacitors, J. Power Sources 352 (2017) 34-41.

[9] L. Zuo, W. Fan, Y. Zhang, Y. Huang, W. Gao, T. Liu, Bacterial cellulose-based sheet-like carbon aerogels for the in situ growth of nickel sulfide as high performance

electrode materials for asymmetric supercapacitors, Nanoscale 9(13) (2017) 4445-4455.

[10] E. Jazaeri, L. Zhang, X. Wang, T. Tsuzuki, Fabrication of carbon nanofiber by pyrolysis of freeze-dried cellulose nanofiber, Cellulose 18(6) (2011) 1481-1485.

[11] N. Pircher, L. Carbajal, C. Schimper, M. Bacher, H. Rennhofer, J.M. Nedelec, H.C. Lichtenegger, T. Rosenau, F. Liebner, Impact of selected solvent systems on the pore and solid structure of cellulose aerogels, Cellulose 23(3) (2016) 1949-1966.

[12] Y. Peng, D.J. Gardner, Y. Han, Drying cellulose nanofibrils: in search of a suitable method, Cellulose 19(1) (2011) 91-102.

[13] A.A. Alhwaige, H. Ishida, S. Qutubuddin, Carbon Aerogels with Excellent CO_2 Adsorption Capacity Synthesized from Clay-Reinforced Biobased Chitosan-Polybenzoxazine Nanocomposites, ACS Sustainable Chem. Eng. 4(3) (2016) 1286-1295.

[14] Y. Li, Y. Liu, M. Wang, X. Xu, T. Lu, C.Q. Sun, L. Pan, Phosphorus-doped 3D carbon nanofiber aerogels derived from bacterial-cellulose for highly-efficient capacitive deionization, Carbon 130 (2018) 377-383.

[15] D.Y. Chung, Y.J. Son, J.M. Yoo, J.S. Kang, C.Y. Ahn, S. Park, Y.E. Sung, Coffee Waste-Derived Hierarchical Porous Carbon as a Highly Active and Durable Electrocatalyst for Electrochemical Energy Applications, ACS Appl. Mater. Interfaces 9(47) (2017) 41303-41313.

[16] C. Wang, D. Wu, H. Wang, Z. Gao, F. Xu, K. Jiang, A green and scalable route to yield porous carbon sheets from biomass for supercapacitors with high capacity, J. Mater. Chem. A. 6(3) (2018) 1244-1254.

[17] L. Hu, Q. Zhu, Q. Wu, D. Li, Z. An, B. Xu, Natural Biomass-Derived Hierarchical Porous Carbon Synthesized by an in Situ Hard Template Coupled with NaOH Activation for Ultrahigh Rate Supercapacitors, ACS Sustainable Chem. Eng. 6(11) (2018) 13949-13959.

[18] L. Zhang, T. You, T. Zhou, X. Zhou, F. Xu, Interconnected Hierarchical Porous Carbon from Lignin-Derived Byproducts of Bioethanol Production for Ultra-High Performance Supercapacitors, ACS Appl. Mater. Interfaces 8(22) (2016) 13918-25.

[19] N. Chen, Solvent Handbook, Chemical Industry Press, Beijing, 2002.

[20] H. Zhang, X. Sun, M.A. Hubbe, L. Pal, Highly conductive carbon nanotubes and flexible cellulose nanofibers composite membranes with semi-interpenetrating networks structure, Carbohydr. Polym. 222 (2019) 115013.

[21] Z. Hanif, H. Jeon, T.H. Tran, J. Jegal, S.-A. Park, S.-M. Kim, J. Park, S.Y. Hwang, D.X. Oh, Butanol-mediated oven-drying of nanocellulose with enhanced dehydration rate and aqueous re-dispersion, J. Polym. Res. 24(3) (2017) 191–201.

[22] Z. Lu, Z. Su, S. Song, Y. Zhao, S. Ma, M. Zhang, Toward high-performance fibrillated cellulose-based air filter via constructing spider-web-like structure with the aid of TBA during freeze-drying process, Cellulose 25(1) (2017) 619-629.

[23] J. Juntaro, S. Ummartyotin, M. Sain, H. Manuspiya, Bacterial cellulose reinforced polyurethane-based resin nanocomposite: A study of how ethanol and processing pressure affect physical, mechanical and dielectric properties, Carbohyd. Polym. 87(4) (2012) 2464-2469.

[24] M. Zeng, A. Laromaine, A. Roig, Bacterial cellulose films: influence of bacterial strain and drying route on film properties, Cellulose 21(6) (2014) 4455-4469.

[25] H. Chen, J. Chen, N. Teng, H. Na, J. Zhu, Controlling the status of corn cellulose solutions by ethanol to define fiber morphology during electrospinning, Cellulose 24(2) (2016) 863-870.

[26] L. Wang, M. Ago, M. Borghei, A. Ishaq, A.C. Papageorgiou, M. Lundahl, O.J. Rojas, Conductive Carbon Microfibers Derived from Wet-Spun Lignin/Nanocellulose Hydrogels, ACS Sustainable Chem. Eng. 7(6) (2019) 6013-6022.

[27] Z. Wang, B. Pecha, R.J.M. Westerhof, S.R.A. Kersten, C.-Z. Li, A.G. McDonald, M. Garcia-Perez, Effect of Cellulose Crystallinity on Solid/Liquid Phase Reactions Responsible for the Formation of Carbonaceous Residues during Pyrolysis, Ind. Eng. Chem. Res. 53(8) (2014) 2940-2955.

[28] Z. Wang, A.G. McDonald, R.J.M. Westerhof, S.R.A. Kersten, C.M. Cuba-Torres, S. Ha, B. Pecha, M. Garcia-Perez, Effect of cellulose crystallinity on the formation of a liquid intermediate and on product distribution during pyrolysis, J. Anal. Appl. Pyrol. 100 (2013) 56-66.

[29] P.C. Lewellen, W.A. Peters, J.B. Howard, Cellulose pyrolysis kinetics and char formation mechanism, Symp. (Int.) Combust. 16(1) (1977) 1471-1480.

[30] M. Olivares-Marín, M. Aklalouch, D. Tonti, Combined Influence of Meso- and Macroporosity of Soft-Hard Templated Carbon Electrodes on the Performance of Li-O$_2$ Cells with Different Configurations, Nanomaterials 9(6) (2019) 810-822.

[31] P.P. Ghimire, M. Gao, M. Jaroniec, Amino acid-assisted synthesis of porous graphitic carbon spheres with highly dispersed Ni nanoparticles, Carbon 153 (2019) 206-216.

[32] L. Zhang, H. Gong, Improvement in flexibility and volumetric performance for supercapacitor application and the effect of Ni-Fe ratio on electrode behaviour, J. Mater. Chem. A. 3(14) (2015) 7607-7615.

[33] M. Olivares-Marín, P. Palomino, E. Enciso, D. Tonti, Simple Method to Relate Experimental Pore Size Distribution and Discharge Capacity in Cathodes for Li/O$_2$ Batteries, J. Phys. Chem. C 118(36) (2014) 20772-20783.

[34] H. Wang, J. Wang, Y. Pi, Q. Shao, Y. Tan, X. Huang, Double Perovskite LaFe$_x$Ni$_{1-x}$O$_3$ Nanorods Enable Efficient Oxygen Evolution Electrocatalysis, Angew. Chem. Int. Edit. 58(8) (2019) 2316-2320.

[35] S.D. Ghadge, O.I. Velikokhatnyi, M.K. Datta, P.M. Shanthi, S. Tan, K. Damodaran, P.N. Kumta, Experimental and Theoretical Validation of High Efficiency and Robust Electrocatalytic Response of One-Dimensional (1D) (Mn,Ir)O$_2$:10F Nanorods for the Oxygen Evolution Reaction in PEM-Based Water Electrolysis, ACS Catal. 9(3) (2019) 2134-2157.

[36] H. Peng, B. Yao, X. Wei, T. Liu, T. Kou, P. Xiao, Y. Zhang, Y. Li, Pore and Heteroatom Engineered Carbon Foams for Supercapacitors, Adv. Energy Mater. 9(19) (2019) 1803665.

[37] M.N. Kakaei, J. Neshati, A.R. Rezaierod, On the Extraction of the Effective Capacitance from Constant Phase Element Parameters, Protect. Met. Phys. Chem. Surface 54(3) (2018) 548-556.

[38] G.J. Brug, A.L.G. van den Eeden, M. Sluyters-Rehbach, J.H. Sluyters, The

analysis of electrode impedances complicated by the presence of a constant phase element, J. Electroanal. Chem. Interfacial Electrochem. 176 (1984) 275-296.

[39] P. Wang, C. Li, S. Dong, X. Ge, P. Zhang, X. Miao, Z. Zhang, C. Wang, L. Yin, One-Step Route Synthesized $Co_2P/Ru/N$-Doped Carbon Nanotube Hybrids as Bifunctional Electrocatalysts for High-Performance $Li-O_2$ Batteries, Small 15(30) (2019) 1900001.

[40] K.-H. Xue, T.-K. Nguyen, A.A. Franco, Impact of the Cathode Microstructure on the Discharge Performance of Lithium Air Batteries: A Multiscale Model, J. Electrochem. Soc. 161(8) (2014) E3028-E3035.

[41] M. Benoit, A. Rodrigues, K. De Oliveira Vigier, E. Fourré, J. Barrault, J.-M. Tatibouët, F. Jérôme, Combination of ball-milling and non-thermal atmospheric plasma as physical treatments for the saccharification of microcrystalline cellulose, Green Chem. 14(8) (2012) 2212-2215.

[42] M. Aklalouch, M. Olivares-Marin, R.C. Lee, P. Palomino, E. Enciso, D. Tonti, Mass-transport Control on the Discharge Mechanism in $Li-O_2$ Batteries Using Carbon Cathodes with Varied Porosity, ChemSusChem 8(20) (2015) 3465-3471.

[43] N. Ding, S.W. Chien, T.S.A. Hor, R. Lum, Y. Zong, Z. Liu, Influence of carbon pore size on the discharge capacity of $Li-O_2$ batteries, J. Mater. Chem. A 2(31) (2014) 12433-12441.

[44] W. Yang, Z. Qian, C. Du, C. Hua, P. Zuo, X. Cheng, Y. Ma, G. Yin, Hierarchical ordered macroporous/ultrathin mesoporous carbon architecture: A promising cathode scaffold with excellent rate performance for rechargeable $Li-O_2$ batteries, Carbon 118 (2017) 139-147.

[45] M. Kim, E. Yoo, W.-S. Ahn, S.E. Shim, Controlling porosity of porous carbon cathode for lithium oxygen batteries: Influence of micro and meso porosity, J. Power Sources 389 (2018) 20-27.

[46] G. Zhang, Y. Yao, T. Zhao, M. Wang, R. Chen, From Black Liquor to Green Energy Resource: Positive Electrode Materials for $Li-O_2$ Battery with High Capacity and Long Cycle Life, ACS Appl. Mater. Interfaces 12(14) (2020) 16521-16530.

[47] W. Zhou, H. Zhang, H. Nie, Y. Ma, Y. Zhang, H. Zhang, Hierarchical

micron-sized mesoporous/macroporous graphene with well-tuned surface oxygen chemistry for high capacity and cycling stability Li-O$_2$ battery, ACS Appl. Mater. Interfaces 7(5) (2015) 3389-3397.

[48] F. Wang, P.K. Kahol, R. Gupta, X. Li, Experimental Studies of Carbon Electrodes With Various Surface Area for Li-O$_2$ Batteries, J. Electrochem. Energy Convers. Storage 16(4) (2019) 041007.

[49] W. Ni, S. Liu, Y. Fei, Y. He, X. Ma, L. Lu, Y. Deng, CoO@Co and N-doped mesoporous carbon composites derived from ionic liquids as cathode catalysts for rechargeable lithium-oxygen batteries, J. Mater. Chem. A. 4(20) (2016) 7746-7753.

[50] C. Zhao, C. Yu, S. Liu, J. Yang, X. Fan, H. Huang, J. Qiu, 3D Porous N-Doped Graphene Frameworks Made of Interconnected Nanocages for Ultrahigh-Rate and Long-Life Li-O$_2$ Batteries, Adv. Funct. Mater. 25(44) (2015) 6913-6920.

[51] J. Luo, X. Yao, L. Yang, Y. Han, L. Chen, X. Geng, V. Vattipalli, Q. Dong, W. Fan, D. Wang, H. Zhu, Free-standing porous carbon electrodes derived from wood for high-performance Li-O$_2$ battery applications, Nano Res. 10(12) (2017) 4318-4326.

[52] W. Chen, Z. Zhang, W. Bao, Y. Lai, J. Li, Y. Gan, J. Wang, Hierarchical mesoporous γ-Fe$_2$O$_3$/carbon nanocomposites derived from metal organic frameworks as a cathode electrocatalyst for rechargeable Li-O$_2$ batteries, Electrochim. Acta 134 (2014) 293-301.

[53] J. Song, X. Lv, Y. Jiao, P. Wang, M. Xu, T. Li, X. Chen, J. Li, Z. Zhang, Catalyst nanoarchitecturing via functionally implanted cobalt nanoparticles in nitrogen doped carbon host for aprotic lithium-oxygen batteries, J. Power Sources 394 (2018) 122-130.

[54] H. Wang, F. Yin, P. Lv, T. Fan, X. He, B. Chen, Metal–organic-framework-derived FeCo alloy core@nitrogen-doped carbon shell nanoparticles anchored on carbon nanotubes for rechargeable Li-O$_2$ battery, Int. J. Hydrogen. Energ 42(4) (2017) 2127-2133.

[55] G. Tan, L. Chong, R. Amine, J. Lu, C. Liu, Y. Yuan, J. Wen, K. He, X. Bi, Y. Guo, H.H. Wang, R. Shahbazian-Yassar, S. Al Hallaj, D.J. Miller, D. Liu, K. Amine, Toward Highly Efficient Electrocatalyst for Li-O$_2$ Batteries Using Biphasic N-Doping

Cobalt@Graphene Multiple-Capsule Heterostructures, Nano Lett. 17(5) (2017) 2959-2966.

[56] X. Zhang, C. Wang, Y.-N. Chen, X.-G. Wang, Z. Xie, Z. Zhou, Binder-free NiFe$_2$O$_4$/C nanofibers as air cathodes for Li-O$_2$ batteries, J. Power Sources 377 (2018) 136-141.

[57] H.-M. Kao, C.-C. Cheng, C.-C. Ting, L.-Y. Hwang, Phase control of cubic SBA-1 mesostructures via alcohol-assisted synthesis, J. Mater. Chem. 15(29) (2005) 2989–2992.

[58] C. Calero, J. Faraudo, D. Bastos-Gonzalez, Interaction of monovalent ions with hydrophobic and hydrophilic colloids: charge inversion and ionic specificity, J. Am. Chem. Soc. 133(38) (2011) 15025-15035.

Chapter 5 High performance N-doped carbon nanosheet/MnO$_2$ cathode derived from bacterial cellulose for aqueous Zn-ion batteries

5.1 Summary

A simple, green and scalable fabrication process of porous N-doped carbon nanosheet/MnO$_2$ derived from BC was developed and the obtained material was used as the cathode for ZIBs. In this process, BC was soaked in a urea solution to obtain the nitrogen source. And then after carbonization, porous N-doped carbon nanosheet (NCS) was obtained. The MnO$_2$ deposition was achieved by a reaction between NCS and NaMnO$_4$. The absorbed urea can provide the N source. Meanwhile, the decomposition of absorbed urea on BC can create high porosity for NCS during the process of pyrolysis. Due to the resulting good conductive and high porosity of NCS, the resulting NCS/MnO$_2$ composite derived from BC shows a large capacity and long-term cyclability (114 mAh g^{-1} at 2 A g^{-1} after 1800 cycles), compared with commercial MnO$_2$ (37 mAh g^{-1}). Furthermore, the electrochemical mechanism of NCS/MnO$_2$ was further scrutinized by multiple analytical methods. The results reveal that the mechanism of NCS/MnO$_2$ involves not only MnO$_2$ dissolution/deposition mechanism but also the Zn^{2+} intercalation/deintercalation.

5.2 Introduction

MnO$_2$ is the most popular cathode material studied in Zn-ion batteries, because of its considerable capacity, decent voltage, low-cost and rich abundance [1]. However, MnO$_2$ exhibits poor electrical conductivity, seriously undermining the electrochemical performance of ZIBs [2, 3]. For this purpose, conductive polymers and carbon materials (graphene, CNT, N-doped carbon) have been integrated with MnO$_2$ to improve the electronic conductivity [4-7]. However, conductive polymers

tend to degrade induced by swelling and shrinkage during the cycling, which negatively affects the electrochemical performance [8, 9]. Instead, CNT and graphene are relatively high-cost, which restricts their commercial applications. N-doped carbon has emerged as an effective candidate thanks to lower cost, good electrical conductivity and good electrochemical properties [10]. In many reports, metal-organic frameworks (MOFs) were utilized as the sources of N-doped carbon [7, 11-13]. Nevertheless, MOFs are often difficult to prepare at a large-scale, and suffer poor chemical stability [14-16]. It is more appealing to fabricate N-doped carbons from biomass, which is usually facile, low-cost, ecofriendly and easy to scale up. BC has been exploited to develop N-doped carbons, by polymerization of polypyrrole, polyaniline, polyacrylonitrile on BC [17-19] or high temperature ammonia treatment [20] to introduce the nitrogen source. These routes are time-consuming, complicated or unsafe, thus their economic viability remains limited. BC possesses a high water-absorption capacity, thus it can acquire the nitrogen source simply by absorbing urea solution. This avoids more complex and hazardous routes such as high temperature ammonia treatment, improving the experimental safety and simplifying the preparing processes.

5.3 Preparation of materials

Individual BC cubes were pressed by a ~150 g Teflon cylinder for 10 minutes to remove most water. The pressed BC was soaked in urea solution (0.1 g mL^{-1}) while stirring for 2 h. Then the soaked BC was extracted and dried in the oven at 60 °C for 24 h. The dried BC was carbonized in a tubular furnace under an Ar flow of 100 mL min^{-1} with a ramp of 10 °C min^{-1} to 900 °C and kept there for 1 h.

To prepare N-doped carbon/MnO_2 composite 24 mg carbon was added to a 35 mL solution containing 0.28 g $NaMnO_4$ and stirred for 4 h at room temperature. Then the product was washed by Milli-Q water several times and dried at 60 °C for 24 h.

Carbon-w was produced from simply carbonizing purified BC in the Ar atmosphere at 900 °C for 1 h, as in our previous chapter. C/MnO_2 is then obtained by

the reaction between carbon-w and $NaMnO_4$, which is in accordance with N-doped carbon/MnO_2.
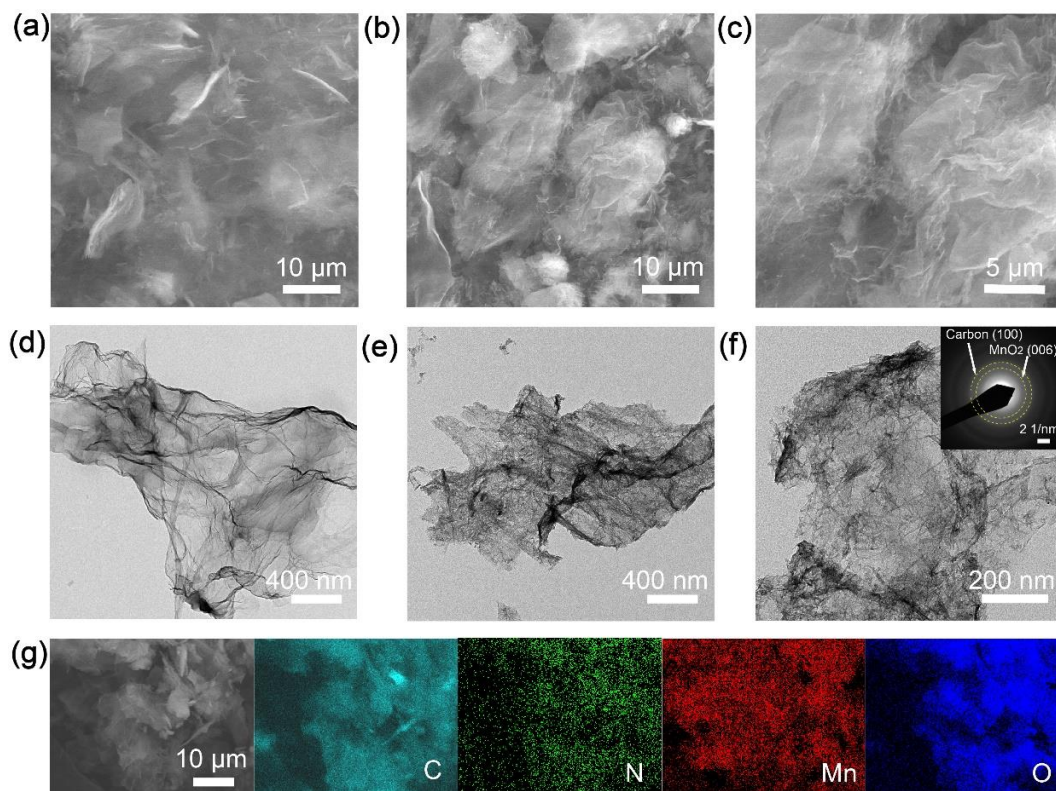

Figure 5.1. SEM images of (a) NCS, (b, c) NCS/MnO_2; TEM images of (d) NCS (e, f) NCS/MnO_2, (g) Element mapping of NCS/MnO_2

N-doped carbon was synthesized from the carbonization of urea-soaked BC and carbon-w was prepared from the pyrolysis of pure BC without urea. The morphologies and structure of prepared samples were compared by SEM and TEM. N-doped carbon displays nanosheet structure and high porosity (Figure 5.1a and Figure 5.1d), which is labeled as NCS. After NCS reacted with $NaMnO_4$, their morphologies barely changed (Figure 5.1a-c). TEM images further reveal some nanorods on NCS (Figure 5.1e-f), which can be attributed to the formation of MnO_2 according to the selected area electron diffraction (SAED) patterns. Energy-dispersive spectroscopy (EDS) mapping images show that the elements C, N, Mn and O distribute uniformly in NCS/MnO_2 (Figure 5.1g).
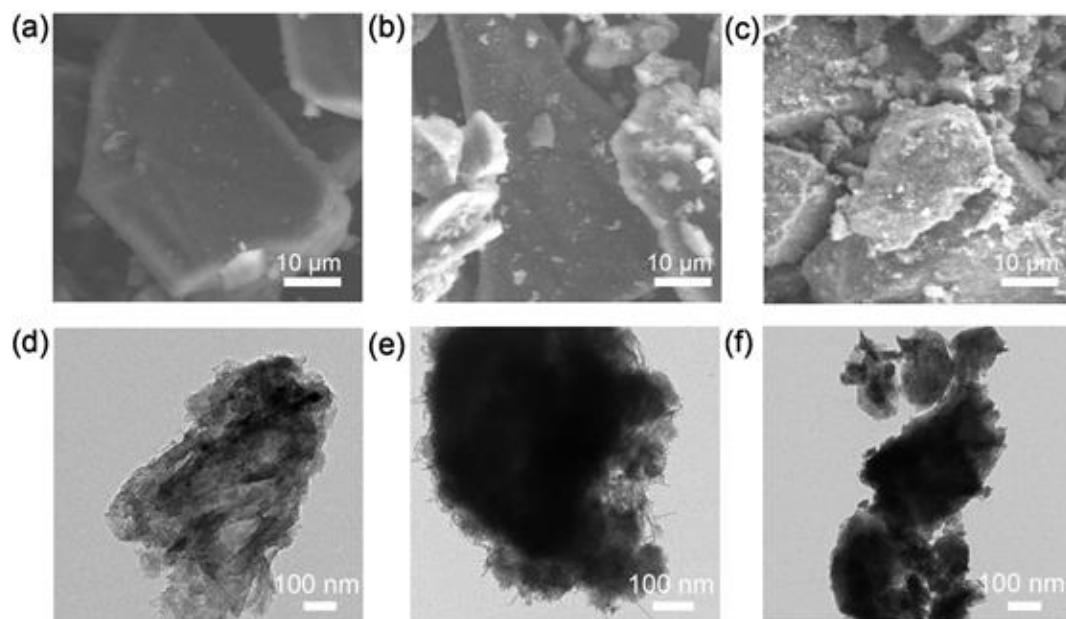
Figure 5.2. SEM images (a) Carbon-w, (b) C/MnO$_2$, (c) commercial MnO$_2$; TEM images (a) Carbon-w, (b) C/MnO$_2$, (c) commercial MnO$_2$.

In comparison, carbon-w shows more compact structure (Figure 5.2a and Figure 5.2c), implying that urea works as a porogen for carbon. There are also some MnO$_2$ nanorods on carbon-w after reacting with NaMnO$_4$ (Figure 5.2e). The morphology of commercial MnO$_2$ instead is dominated by large irregular particles of several tens micrometers along with smaller, of less than one micrometer (Figure 5.2c and Figure 5.2f).
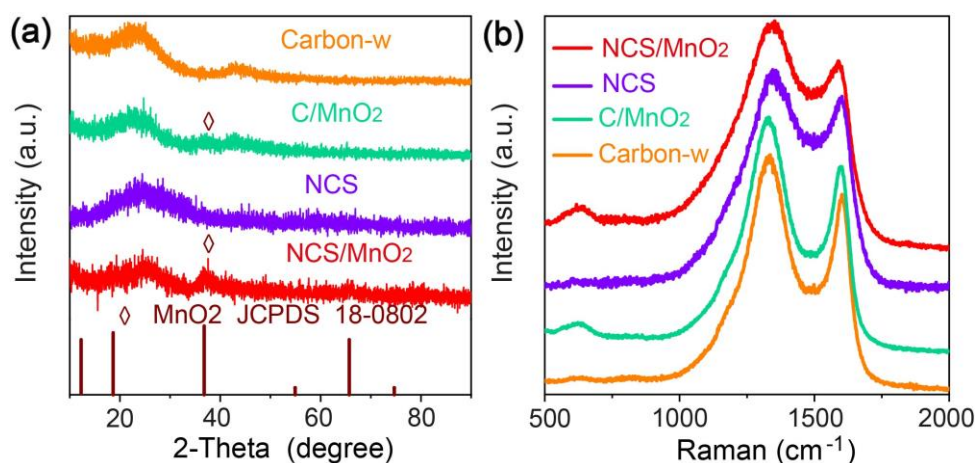

Figure 5.3. (a) XRD patterns and (b) Raman spectra of NCS, carbon-w, C/MnO$_2$ and NCS/MnO$_2$.

XRD measurements were carried out to investigate the phase structures of NCS, carbon-w, C/MnO_2 and NCS/MnO_2. As reported in Figure 5.3a, carbon-w and NCS show a broad peak at around 26°, belonging to the plane (002) of graphite carbon [21, 22]. Both C/MnO_2 and NCS/MnO_2 exhibit a weak and broad peak at 36°, which can be indexed to the plane (006) of birnessite-type MnO_2 [23]. Raman was used to quantify the graphitization degrees of carbon-w and NCS. There are in both samples two peaks located at 1350 cm^{-1} (D band) and 1600 cm^{-1} (G band), representing disordered and graphitized carbon (Figure 5.3b) [24]. The intensity ratio G to D band (I_D/I_G) is often used to evaluate the degree of graphitization. The value of I_D/I_G for NCS is 1.12, which is lower than for carbon-w (1.21). It implies that a higher graphitization can be obtained in presence of urea, which in addition is expected to infer better electron conduction [25]. After reacting with $NaMnO_4$, a new peak appearing at 640 cm^{-1} can be associated with the Mn-O stretching vibration of MnO_6 groups [26], demonstrating the formation of MnO_2 both on carbon-w and NCS. Compared with carbon-w and NCS, the ratios of I_D/I_G for NCS/MnO_2 (1.18) and C/MnO_2 (1.27) increase. This indicates that the introduction of MnO_2 causes more defects into carbon-w and NCS, leading to more defective graphitic structures or lower degree of graphitization [27, 28].

The porous structure of NCS was inspected by N_2 adsorption-desorption measurement (Figure 5.4a and Table 5.1). Although the surface area of NCS (431 m^2 g^{-1}) is not as high as that of carbon-w (1009 m^2 g^{-1}), its pore volume is much larger (0.86 vs. 0.19 cm^3 g^{-1}). The pore size distribution curves show that the pore structure of NCS is predominantly composed of mesopores and macropores (Figure 5.4b), leading to a high surface external area, while the pore structure of carbon-w mainly consists of micropores [29]. The high porosity of NCS can be attributed to the released ammonia and carbon dioxide gas from urea during cellulose carbonization [30, 31]. After MnO_2 formation, the surface area and pore volume of both carbons decrease (Figure 5.5a-b and Table 5.1). This is probably because some parts of NCS and carbon-w were consumed and the introduction of MnO_2 blocked pores to some extent, resulting in decreased surface areas and pore volumes, although trends are

similar to those found with carbon substrates. Although NCS/MnO$_2$ does not have a larger surface area (229 m^2 g^{-1}) than C/MnO$_2$ (401 m^2 g^{-1}), it exhibits a much larger pore volume (0.42 vs. 0.12 cm^3 g^{-1}). In addition, the porous structure of NCS/MnO$_2$ mainly consists of mesopores and macropores, while the pore structures of C/MnO$_2$ and commercial MnO$_2$ are dominated by micropores (Figure 5.5c). These results demonstrate that NCS/MnO$_2$ possesses higher porosity than C/MnO$_2$ and commercial MnO$_2$.
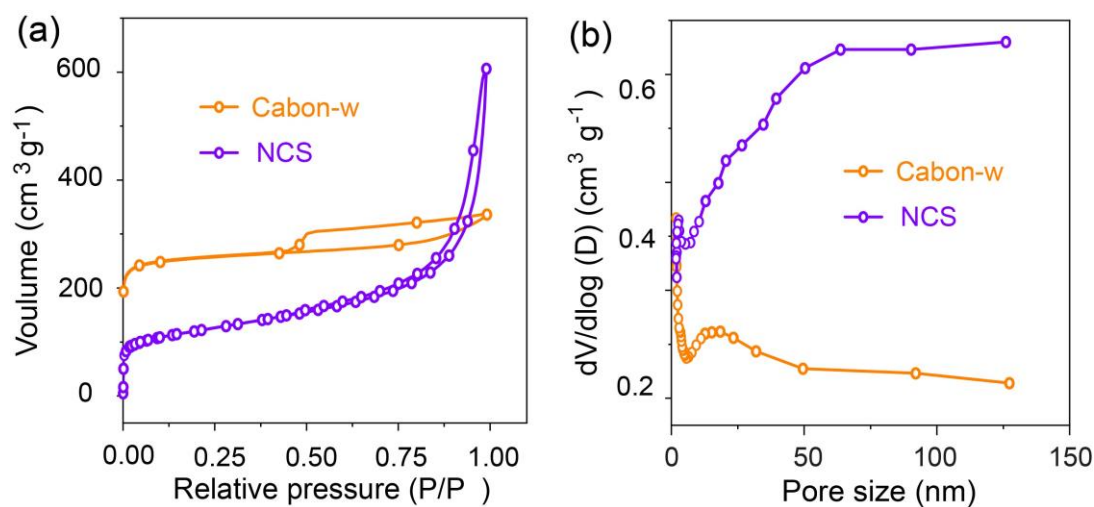

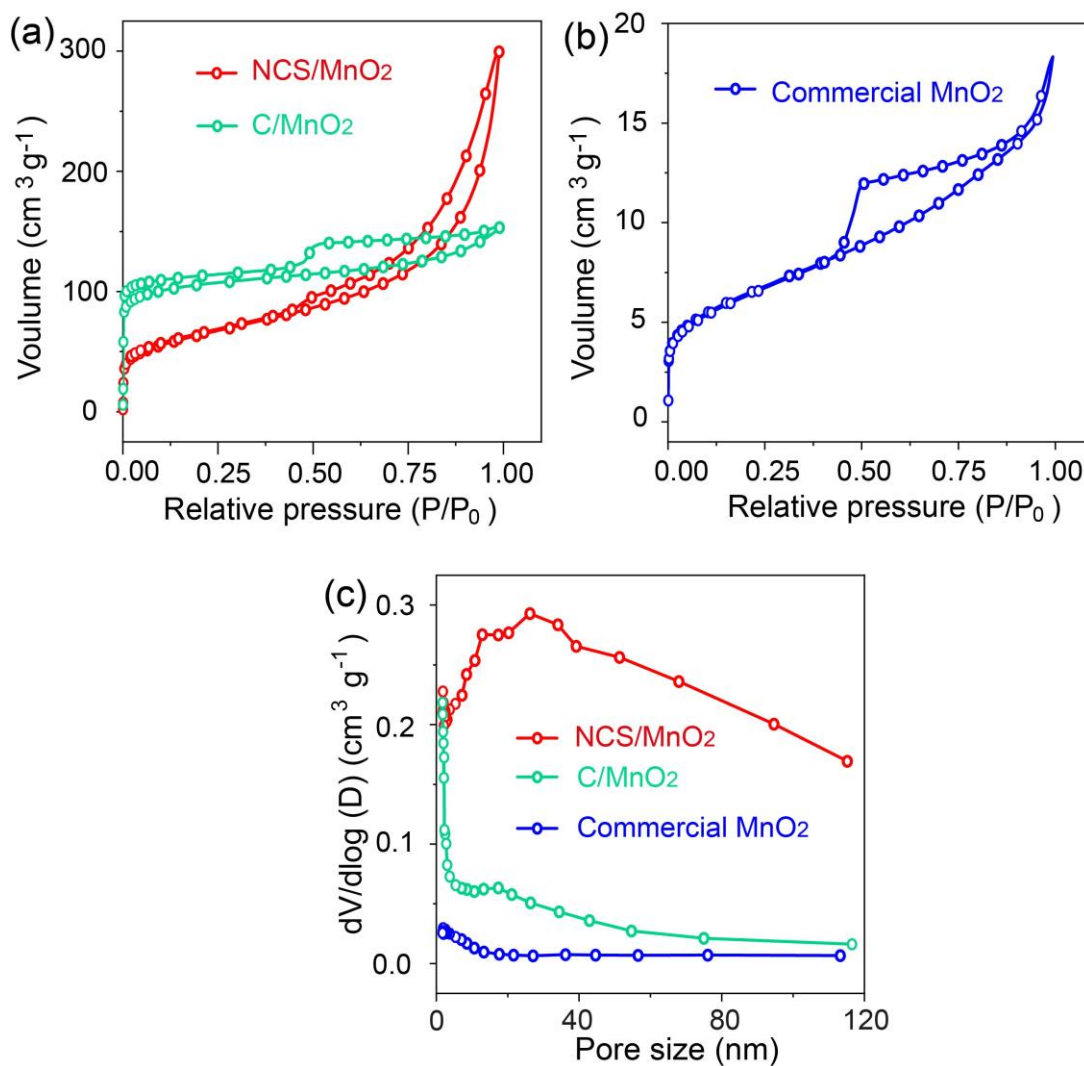**Figure 5.4.** (a) Nitrogen adsorption-desorption of NCS; (b) pore size distribution of NCS and carbon-w;

Figure 5.5. (a) Nitrogen adsorption-desorption of NCS/MnO$_2$ and C/MnO$_2$; (b) nitrogen adsorption-desorption of commercial MnO$_2$; (c) pore size distribution of MnO$_2$.

Table 5.1. Textural data of samples.

Carbon	BET surface area $(m^2\ g^{-1})$	External surface area $(m^2\ g^{-1})$	Pore volume $(cm^3\ g^{-1})$
Carbon-w[29]	1009	153	0.19
NCS	431	269	0.86
C/MnO$_2$	401	112	0.12
NCS/MnO$_2$	229	183	0.42
Commercial MnO$_2$	23	20	0.02

Electrodes of high porosity are more favorable for fast ion transfer, which can shorten the diffusion path [32, 33]. Porosity has an effect also on the content of MnO$_2$ in NCS/MnO$_2$, revealed by TGA, which is about 42 % (Figure 5.6), much higher than in C/MnO$_2$, about 11 %. The high porosity of NCS/MnO$_2$ favors the diffusion of NaMnO$_4$ into the bulk and the MnO$_2$ deposition can take place on the surface and inside of NCS at the same time [34, 35]. In contrast, the diffusion route of NaMnO$_4$ into carbon-w with low porosity is difficult and the reaction between carbon-w and NaMnO$_4$ mainly occurs on the surface of carbon-w. In fact, comparing pore volumes, the larger pore volume of NCS is better filled by MnO$_2$. As a consequence, the mass content of MnO$_2$ in NCS/MnO$_2$ is higher than C/MnO$_2$.
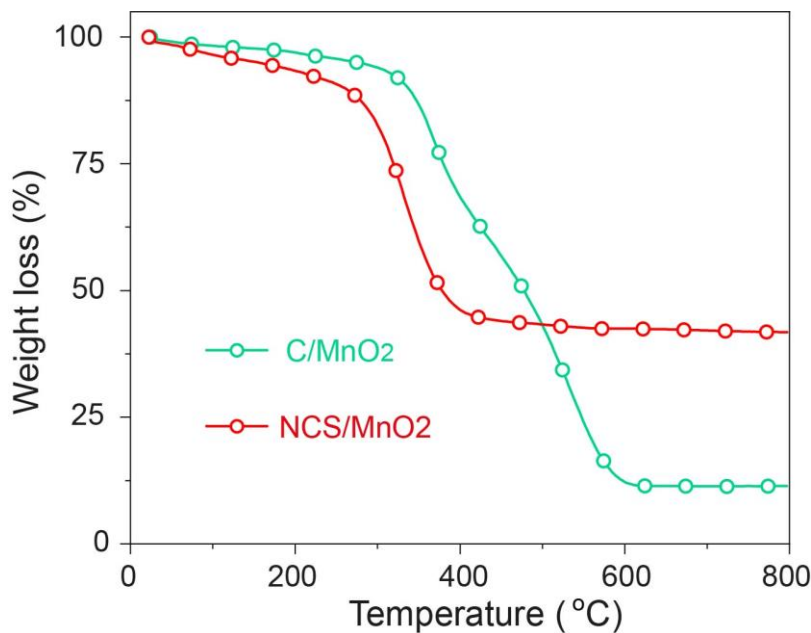
Figure 5.6. TGA curves of NCS/MnO$_2$ and C/MnO$_2$ in synthetic air flow.

To detect the surface chemical composition and chemical state of these samples, XPS was performed. N 1s peak is observed in the full spectrum of NCS (Figure 5.7a), indicating that N was successfully doped into carbon. The nitrogen content of NCS is 4.8 at.%. After NCS reacted with NaMnO$_4$, C 1s, N 1s, Mn 2p and O 1s peaks are obviously observed in the full spectrum of NCS/MnO$_2$ (Figure 5.7a). The C 1s spectrum of NCS/MnO$_2$ can be fitted into 4 peaks at 284.6, 285.2, 285.9, 288.3 and 292.5 eV (Figure 5.7b), belonging to C-C/C=C, C-N, C-O, C=O and O-C=O [36, 37]. The N 1s spectrum of NCS/MnO$_2$ can be divided into three peaks (Figure 5.7c), attributed to pyridinic-N (398.6 eV), pyrrolic-N (399.7eV) and graphitic-N (400.9 eV) [38]. It has been shown that pyridinic-N and pyrrolic-N can enhance the electronic conductivity of carbon and hence promote the battery performance [39, 40]. The binding energy of Mn 2p of C/MnO$_2$ and NCS/MnO$_2$ are similar to commercial MnO$_2$ (Table 5.2), confirming the presence of MnO$_2$ in C/MnO$_2$ and NCS/MnO$_2$. Mn 2p peaks can be deconvoluted into two peaks (Figure 5.7d), which can be assigned to Mn^{4+} (2p$_{3/2}$: 642 eV; 2p$_{1/2}$: 653 eV) and Mn^{3+} (2p$_{3/2}$: 644 eV; 2p$_{1/2}$: 655 eV) [41]. There is no obvious difference of Mn^{4+}/Mn^{3+} ratio between these samples (Table 5.3), which indicates that the Mn valences of these samples are similar.
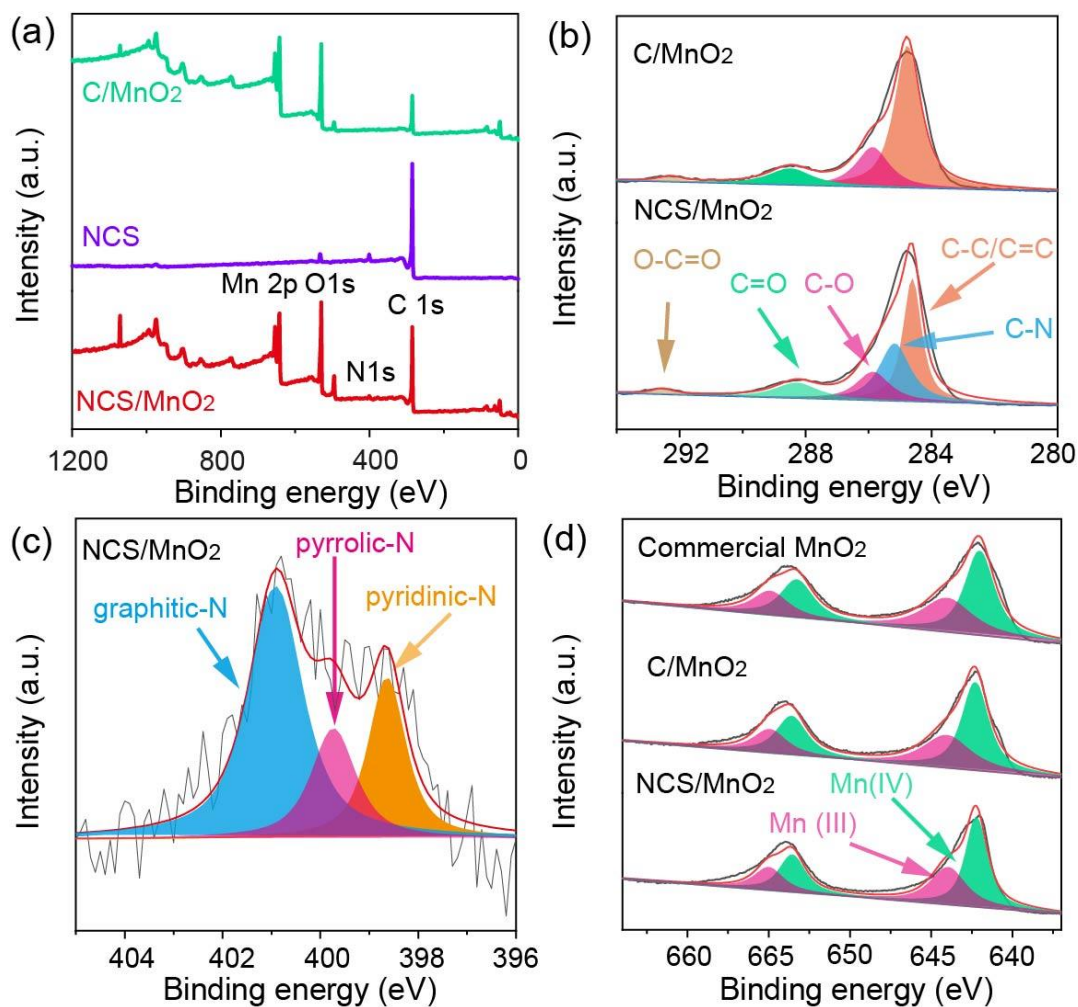
Figure 5.7. (a) full XPS spectra; XPS spectra (d) C 1s, (e) N 1s, (f) Mn 2p.

Table 5.2. Mn 2p binding energy values

Samples	$2p_{3/2}$ (eV)	$2p_{1/2}$ (eV)
NCS/MnO$_2$	654.0	642.2
C/MnO$_2$	653.8	642.0
Commercial MnO$_2$	653.8	642.0

Table 5.3. Mn valence related XPS information of samples

Samples	Mn^{4+}		Mn^{3+}		Mn^{4+}/Mn^{3+}
	2p$_{3/2}$	2p$_{1/2}$	2p$_{3/2}$	2p$_{1/2}$	
NCS/MnO$_2$	642.3	653.6	644.0	654.9	60.1%
C/MnO$_2$	642.0	653.3	644.0	654.9	59.2%
Commercial MnO$_2$	642.2	653.6	644.0	655.0	59.4%

5.4 Electrochemical performance

To prepare cathodes, MnO$_2$ based materials, Super P and PVDF were mixed at a weight ratio of 7:2:1 in 1-Methyl-2-pyrrolidone (NMP). Then the slurry was coated on a carbon paper and was dried in the oven (60 °C) for 24 h. The total loading on the carbon paper is about 1 mg cm^{-2}. The capacity is calculated by the mass of MnO$_2$/carbon composite. The Zn ion battery electrochemical performance of cathode materials was studied in Swagelok cells. The cells were assembled with Zn foil as the anode, glass fibre filter as the separator, 2 M ZnSO$_4$ with 0.2 M MnSO$_4$ aqueous electrolyte, and MnO$_2$ based materials as the cathode.

To evaluate the electrochemical performance of MnO$_2$ electrodes, full batteries with Zn foil anodes were assembled in Swagelok cells. As shown in Figure 5.8, CV curves of all three cathodes present two pairs of reduction/oxidation peaks, suggesting that they have similar redox reactions. But the currents of these peaks are larger for NCS/MnO$_2$ than C/MnO$_2$ and commercial MnO$_2$, demonstrating that NCS/MnO$_2$ possesses higher electrochemical activity and fast reaction kinetic [42].
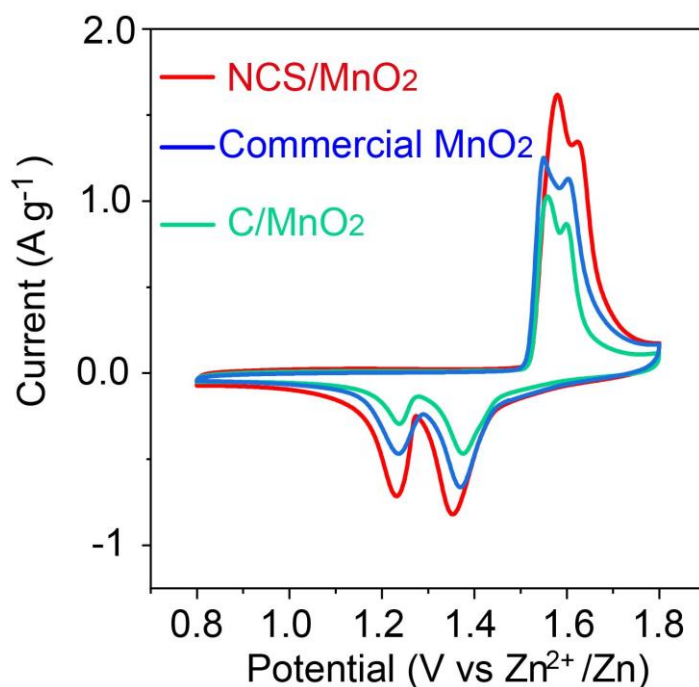
Figure 5.8. CV curves at a scan rate of 0.2 mV s^{-1};

The rate capabilities of cathodes were measured by applying different current densities (Figure 5.9a-d). NCS/MnO$_2$ presents 226 mA h g^{-1} at 0.1 A g^{-1}. Even at high current densities of 1 A g^{-1}, NCS/MnO$_2$ still can deliver 210 mA h g^{-1}. C/MnO$_2$ and commercial MnO$_2$ demonstrate much lower capacities. In particular, the capacities of commercial MnO$_2$ (from 187 mAh g^{-1} at 0.1 A g^{-1} to 127 mAh g^{-1} at 1 A g^{-1}) and C/MnO$_2$ (from 77 mAh g^{-1} at 0.1 A g^{-1} to 53 mAh g^{-1} at 1 A g^{-1}) decrease greatly with the increment of the current density. The capacity retentions at 1 vs. 0.1 A g^{-1} of commercial MnO$_2$ and C/MnO$_2$ are respectively 68 % and 69 %, considerably lower than NCS/MnO$_2$ (90 %). The lower capacities compared to NCS/MnO$_2$ can be explained with the lower MnO$_2$ content of C/MnO$_2$ (as determined by TGA), and with the large amount of coarse particles in the commercial MnO$_2$ sample. These results show that NCS/MnO$_2$ possesses an excellent rate performance.
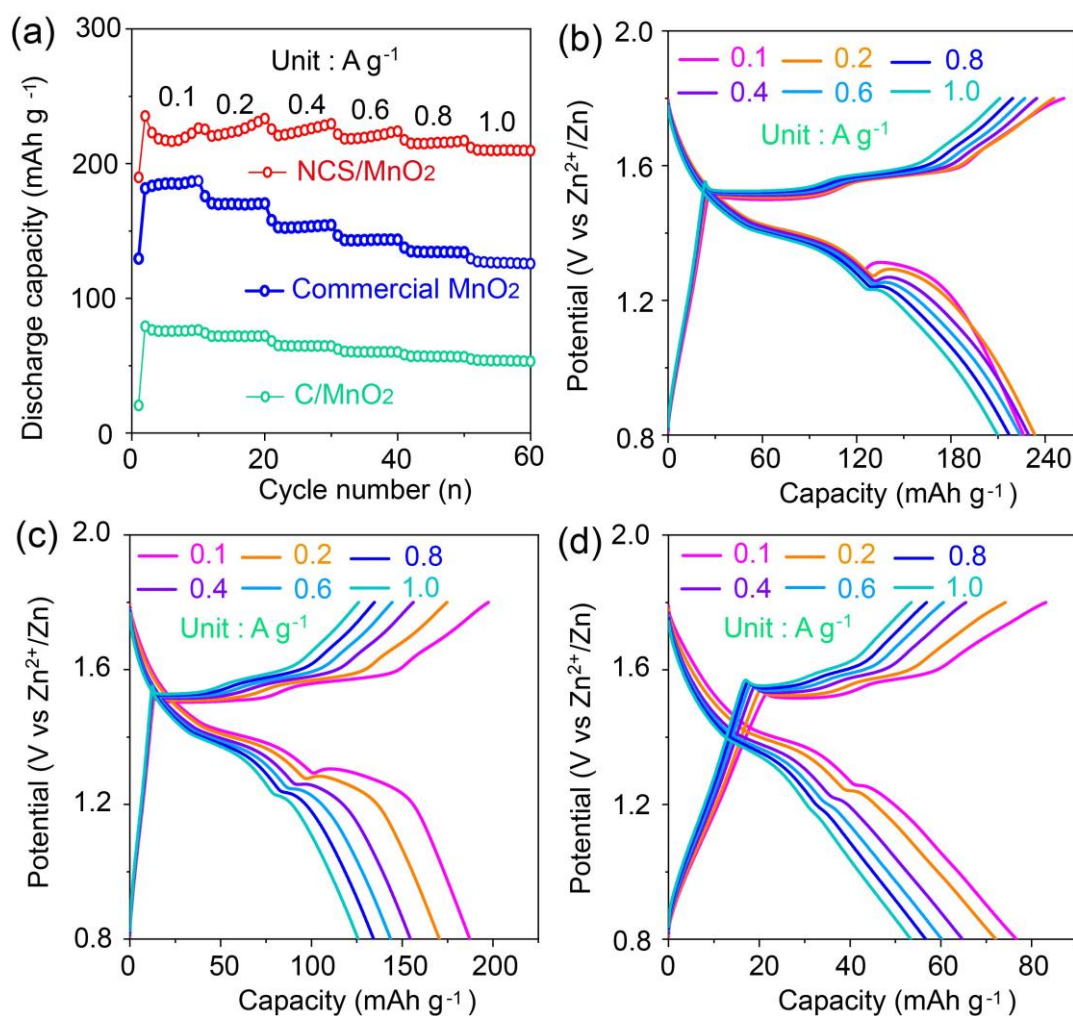
Figure 5.9. (a) Rate performance; galvanostatic discharge/charge profiles of NCS/MnO$_2$ (b), commercial MnO$_2$ (c) and C/MnO$_2$ (d) at different current densities.

To further evaluate the cycling stability, the electrodes were cycled at 0.2 A g^{-1} (Figure 5.10a). The discharge capacities gradually increase during the cycling, which can be associated with an electrochemical activation process also reported by other authors on ZIB systems [43]. The capacity of NCS/MnO$_2$ increased to a larger extent than C/MnO$_2$ and commercial MnO$_2$. Probably because of the high porosity of NCS/MnO$_2$, which can facilitate the deposition of MnO$_2$ during charge [44]. Among these electrodes, NCS/MnO$_2$ shows a higher capacity (358 mAh g^{-1}) than commercial MnO$_2$ (177 mAh g^{-1}) and C/MnO$_2$ (74 mAh g^{-1}) after 60 cycles. The capacity of NCS and carbon-w were also investigated (Figure 5.10b). The capacities of NCS (60 mAh g^{-1}) and carbon-w (48 mAh g^{-1}) are similar at 0.2 A g^{-1} after 60 cycles. This

phenomenon suggests NCS/MnO$_2$ and carbon-w end with a similar capacity without MnO$_2$ in the electrode. To evaluate the role of Mn^{2+} in the electrolyte, the Swagelok cell with NCS/MnO$_2$ as the cathode was assembled without using MnSO$_4$ additive under the same conditions (Figure 5.10c). The capacity of NCS/MnO$_2$ declines rapidly with cycle number. It is obvious that the addition of MnSO$_4$ can enhance the electrochemical reversibility. This confirms that the MnSO$_4$ additive can generate a proper equilibrium between Mn^{2+} dissolution and the re-oxidation of the Mn^{2+}, which improves the stability of the cathode [45].
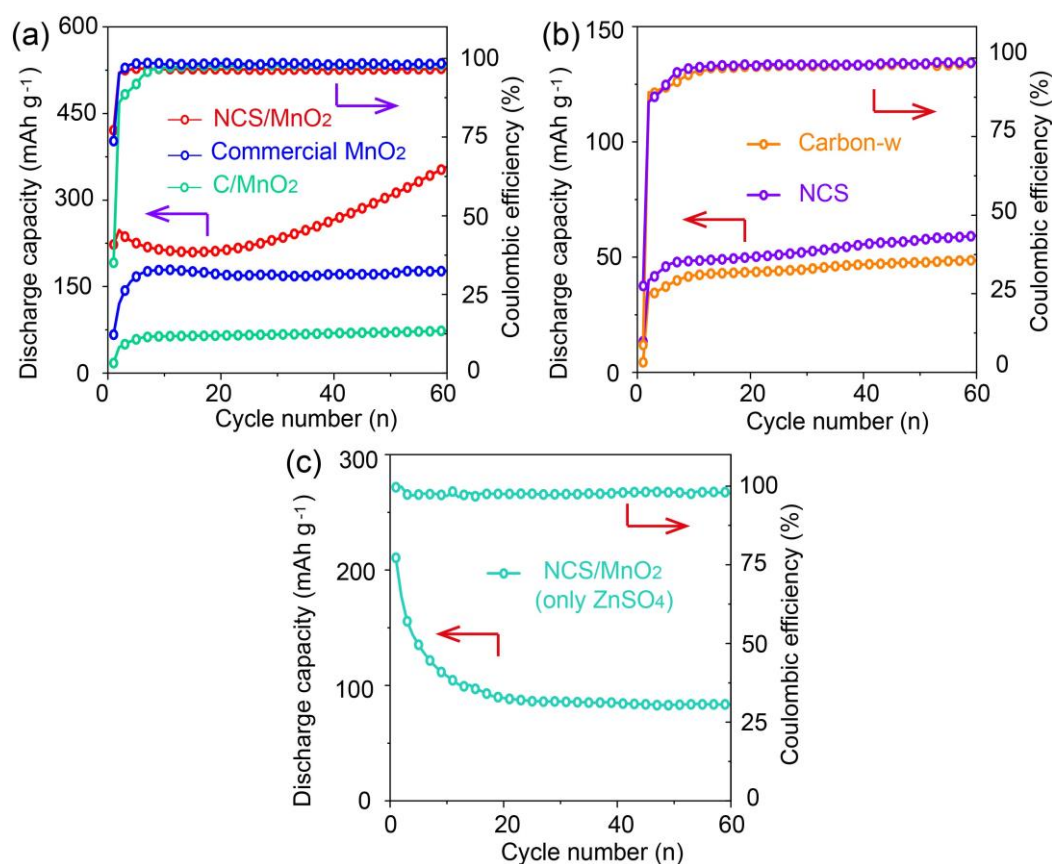

Figure 5.10. Cycling performance at 0.2 A g^{-1}: (a) NCS/MnO$_2$, commercial MnO$_2$ and C/MnO$_2$ (electrolyte: 2M ZnSO$_4$+0.2M MnSO$_4$); (b) NCS and carbon-w (electrolyte: 2M ZnSO$_4$+0.2M MnSO$_4$); (c) NCS/MnO$_2$ (electrolyte: 2M ZnSO$_4$).

The cycling stability of all electrodes were also investigated at a high current density of 2 A g^{-1}. As seen in Figure 5.11, the capacity of NCS/MnO$_2$ still can be

maintained at 114 mAh g^{-1} after 1800 cycles. For a comparison, low capacities are attained for C/MnO$_2$ (22 mAh g^{-1}) and commercial MnO$_2$ (37 mAh g^{-1}) after 1800 cycles. The excellent performance of NCS/MnO$_2$ is also superior to most of reported Mn-based cathodes (Table 5.4).
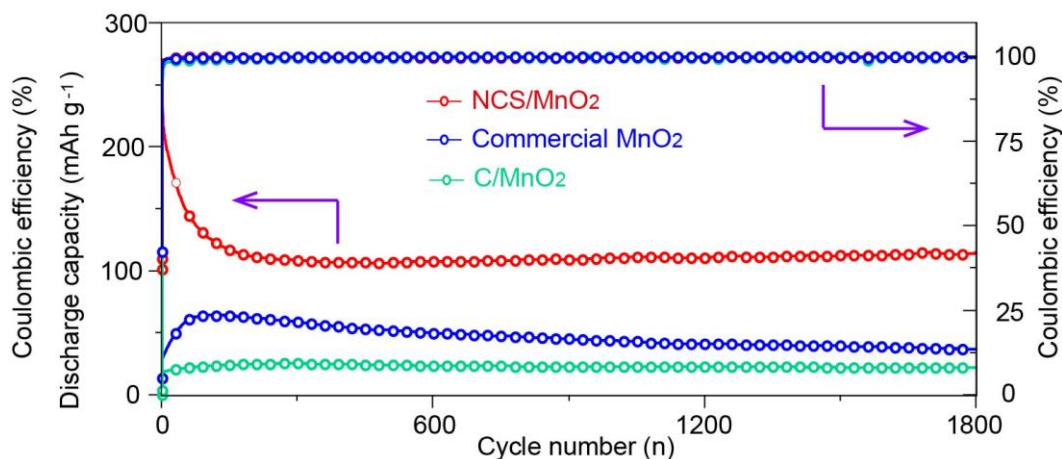

Figure 5.11. Cycling performance at 2 A g^{-1}.

Table 5.4. Comparison the cycling performance between NCS/MnO$_2$ and reported cathodes for aqueous zinc ion batteries.

Cathode	Cycling performance
NCS/MnO$_2$	114 mAh g-1 at 2 A g^{-1} after 1800 cycles
MnOx@N-C [7]	100 mAh g-1 at 2 A g^{-1} after 1600 cycles
carbon coated MnO [46]	116 mAh g−1 at 1 A g^{-1} after 1500 cycles
Co-Mn$_3$O$_4$/carbon nanosheet array [47]	103 mA h g-1 at 2 A g^{-1} after 1100 cycles
ZnMn$_2$O$_4$ microrods [48]	49 mAh g-1 at 2 A g^{-1} after 1000 cycles
MoS$_2$ [49]	102 mAh g-1 at 0.5A g^{-1} after 600 cycles
Ocu-Mn$_2$O$_3$ [50]	112 mA h at 1 A g-1 after 600 cycles
Na$_{0.44}$MnO$_2$ [51]	~37 mA h g-1 at 1 A g^{-1} after 800 cycles
Zn$_3$V$_2$O$_7$(OH)$_2$·2H$_2$O [52]	101 mAh g-1 at 0.2 A g^{-1} after 300 cycles
α-(Mn$_2$O$_3$−MnO$_2$)-500 [53]	95 mA h g−1 at 2 A g^{-1} after 800 cycles

To further assess the advantages of BC as a carbon source, filter paper (FP) and printer paper (PP) were also immersed in urea solution following the same protocol as BC. The FTIR spectra of dried urea/filter paper and dried urea/printer paper are similar to their corresponding pristine ones and just display a few weak peaks coming from urea (Figure 5.12), implying that urea is also absorbed on these papers, but the amount is very small. Conversely, the FTIR spectra of dried urea/BC is completely consistent with urea. As shown in Table 5.5, the mass of urea absorbed by filter paper and printer paper are respectively 0.004 and 0.005 g cm^{-2}, which is negligible in comparison with BC (0.15 g cm^{-2}). The mass ratio between absorbed urea and BC is 25, which is much higher than urea/FP (0.4) and urea/PP (0.6). These results clearly indicate the large BC water-absorbing capacity compared to regular microfibrous paper. This allows to incorporate large solute amounts that are retained and well distributed after drying. Given the small amount of added urea, there is no significant morphologic and performance difference between MnO_2 derived from papers exposed or not to urea (Figure 5.13 and Figure 5.14).
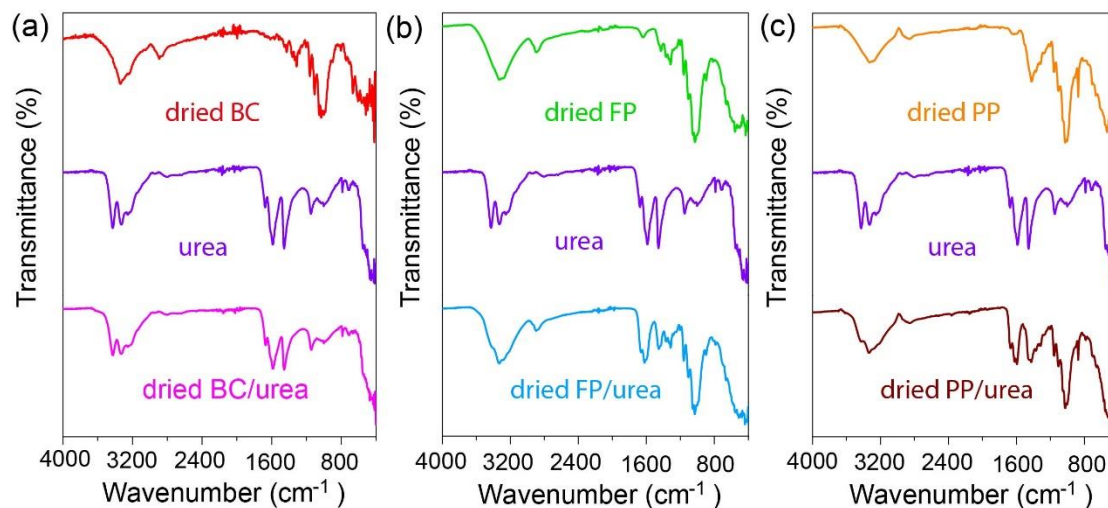

Figure 5.12. FTIR of (a) dried BC, urea and dried BC/urea (b) dried FP, urea and dried FP/urea, (b) dried PP, urea and dried PP/urea

Table 5.5. The mass of urea absorbed on substrates and substrates after drying.

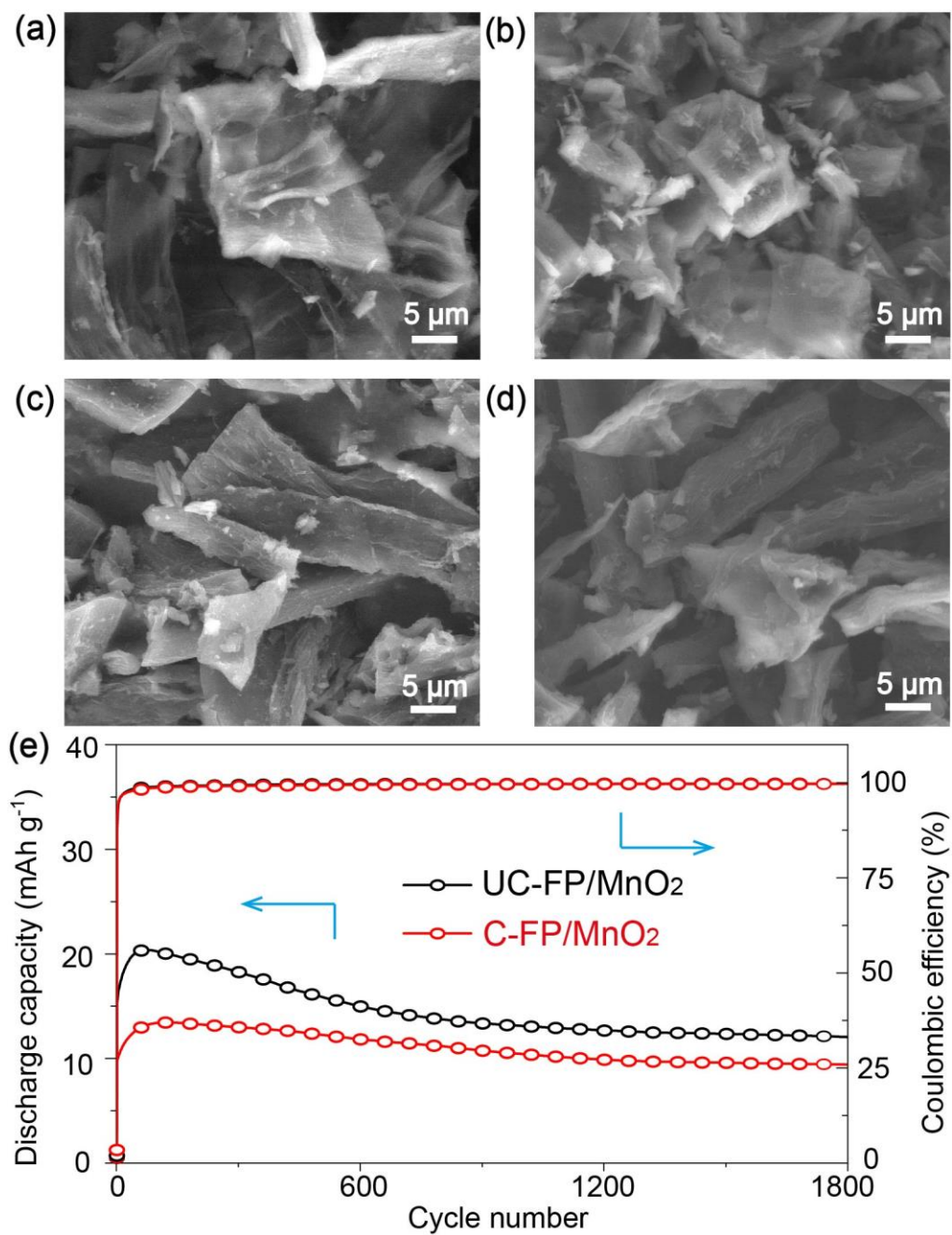| Substrate	BC	FP	PP
Absorbed Urea mass (g cm^{-2})	0.15	0.004	0.005
Bare substrates (g cm^{-2})	0.006	0.009	0.008
The mass ratio between the absorbed urea/the bare substrate	25	0.4	0.6

Figure 5.13. SEM images of (a) C-FP, (b) UC-FP, (c) C-FP/MnO$_2$ and (d) UC-FP/MnO$_2$. (e) Cycling performance of C-FP/MnO$_2$ and (d) UC-FP/MnO$_2$ at 2 A g^{-1}.
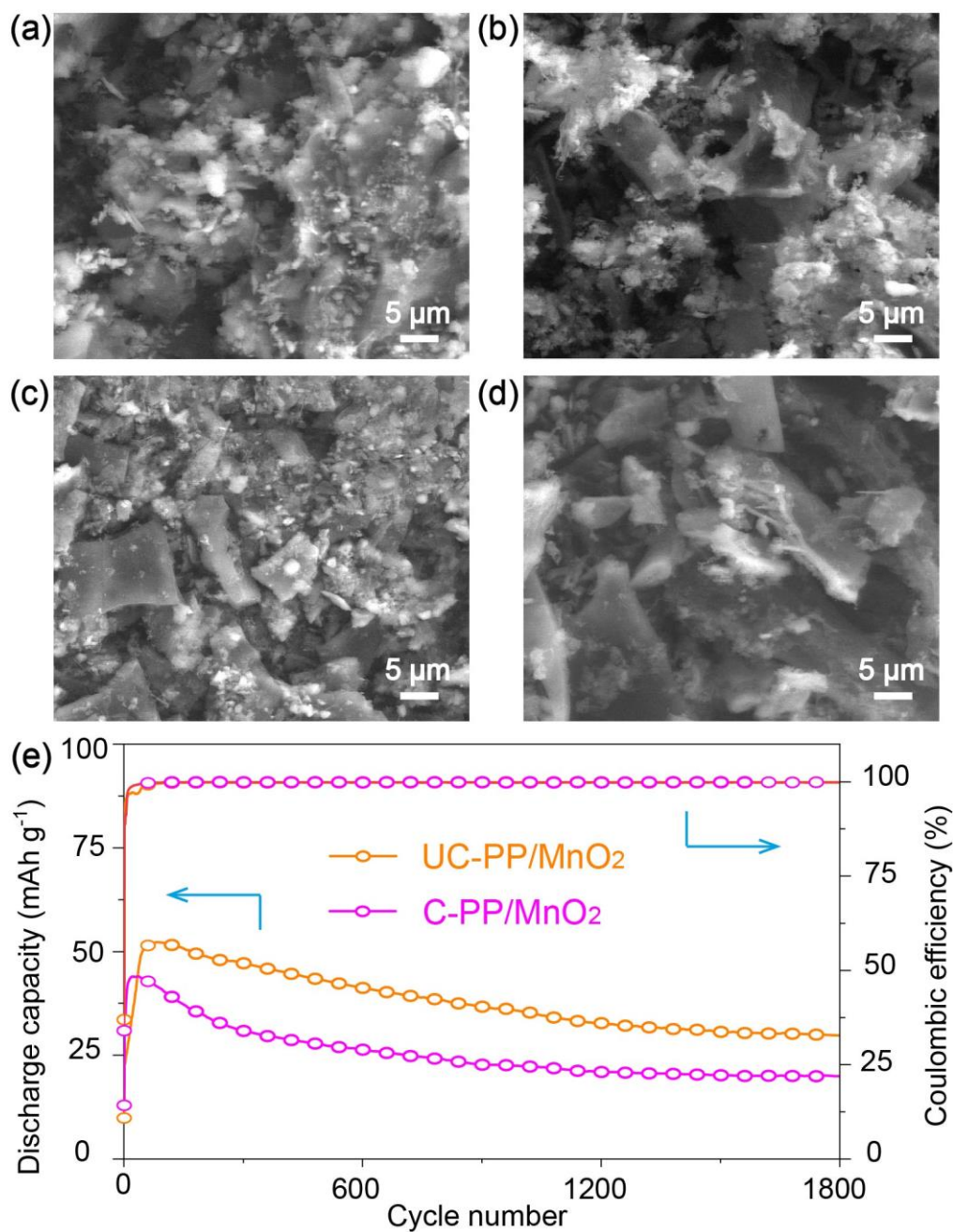
Figure 5.14. SEM images of (a) C-A4, (b) UC-A4, (c) C-A4/MnO$_2$ and (d) UC-A4/MnO$_2$. (e) Cycling performance of C-A4/MnO$_2$ and UC-A4/MnO$_2$ at 2 A g^{-1}.

Electrochemical impedance spectroscopy was conducted to further analyze the reaction kinetics of NCS/MnO$_2$, C/MnO$_2$ and commercial MnO$_2$ (Figure 5.15). The Nyquist plot is composed of one semicircle in the high frequency region and one straight line in the low frequency region. The semicircle is associated with charge-transfer resistance and the line is related to the ion diffusion process [54].

NCS/MnO_2 shows a smaller semicircle than other C/MnO_2 and commercial MnO_2, revealing a smaller charge transfer resistance for NCS/MnO_2. The diffusion coefficient of these electrodes can be reflected by the Warburg coefficient σ, which is inversely proportional to the diffusion coefficient [55]. The σ values of these electrodes can be obtained by fitting the linear relation between Z' and $\omega^{-1/2}$. The σ values of NCS/MnO_2, C/MnO_2 and commercial MnO_2 are respectively 26, 50, and 77 Ω s^{-1}. The σ values of C/MnO_2 and commercial MnO_2 are nearly 2-3 times higher than NCS/MnO_2, showing the fast ion diffusion for NCS/MnO_2. The fast charge transfer and the ion diffusion of NCS/MnO_2 can be attributed to the optimal architecture of NCS. N-doping can enhance the electronic conductivity of carbon [56, 57], which together with the high area increase the charge transfer rate, while the high porosity can offer numerous channels for transporting ions [58].
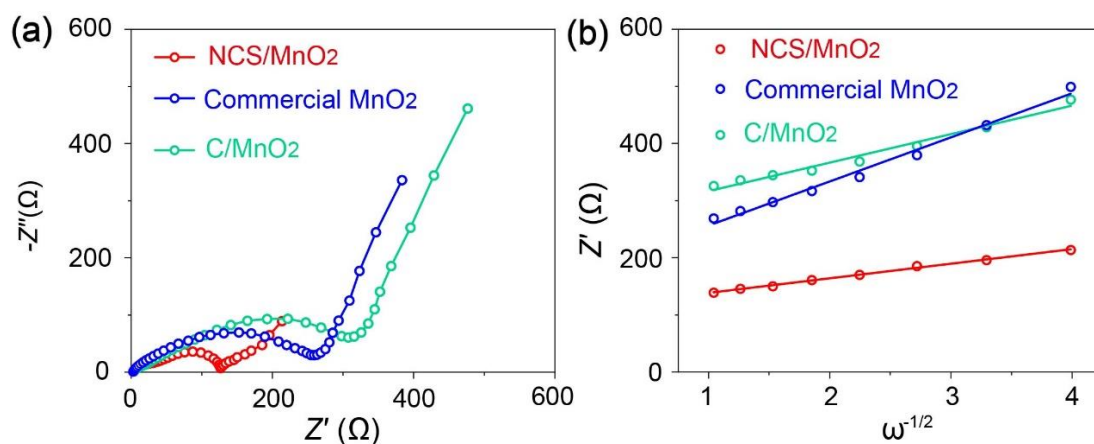

Figure 5.15. (a) Nyquist plots at the open circuit voltage and (b) the linear between Z' and w$^{-1/2}$ of NCS/MnO_2, NCS and C/MnO_2 and commercial MnO_2.

To better comprehend the electrochemical reaction mechanism of NCS/MnO_2, CV tests were conducted at different scan rates ranging from 0.2 to 1.0 mV s^{-1} (Figure 5.16a). The peaks slightly broaden without significant change of the CV. According to previous literature, the charge storage kinetics can be expressed by the following equation: $i = a \cdot v^b$ (*i*: peak current; *v*: scan rate; a, b: variable values). The b value can be calculated by the slopes of the fitting curves of log *i* versus log *v* (Figure 5.16b). b values of 1.0 and 0.5 respectively correspond to purely capacitive-like behavior and

diffusion-controlled process [59, 60]. The b values of these peaks separately are 0.74, 0.79, 0.63 and 0.7 (Figure 5.16c), suggesting that the electrochemical reactions mechanisms of NCS/MnO$_2$ contain both capacitive and diffusion-controlled processes.
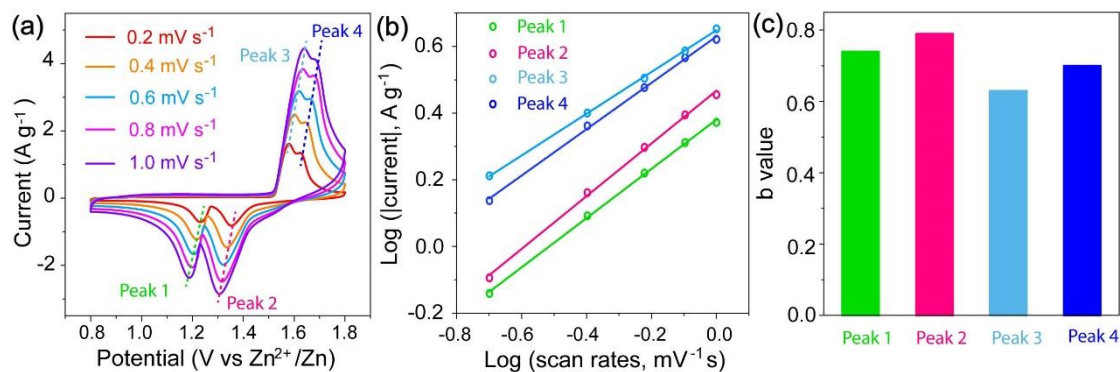

Figure 5.16. (a) CV curves of NCS/MnO$_2$ at various scan rates. (b) The relation between log i and log v. (c) the b-values of four peaks.

Based on the capacity measured on the basis of the MnO$_2$ content as determined by TGA, we estimate up to 558 mAh g(MnO$_2$)$^{-1}$ at 0.2 A g^{-1} after 1st discharge. This value is superior to the capacity expected for 1-electron reduction of MnO$_2$ (308 mAh/g$_{MnO2}$), and approaching a 2-electron reduction of MnO$_2$ to Mn^{2+} such as:

MnO$_2$ + 4H$^+$ + 2e $\rightleftharpoons$ Mn^{2+} + 2H$_2$O.
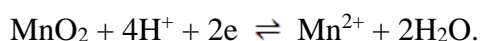
However, such a simple dissolution/precipitation mechanism is contradicted by the test reported above on the carbons without MnO$_2$ deposition. The very small capacity they exhibited demonstrates that only a small amount of MnO$_2$ forms on charge from Mn^{2+} in solution, while samples with a substantial initial MnO$_2$ loading have much larger capacity. Thus, the mechanism must be more complex.

To explore the structural evolution of NCS/MnO$_2$ during the process of discharge and charge, ex-situ SEM, TEM, XRD, XPS and XAS analyses were conducted at different charge points during the initial 2 cycles of galvanostatic discharge/charge of NCS/MnO$_2$ at 0.2 A g^{-1}. The points are marked on the profiles presented in Figure 5.17.
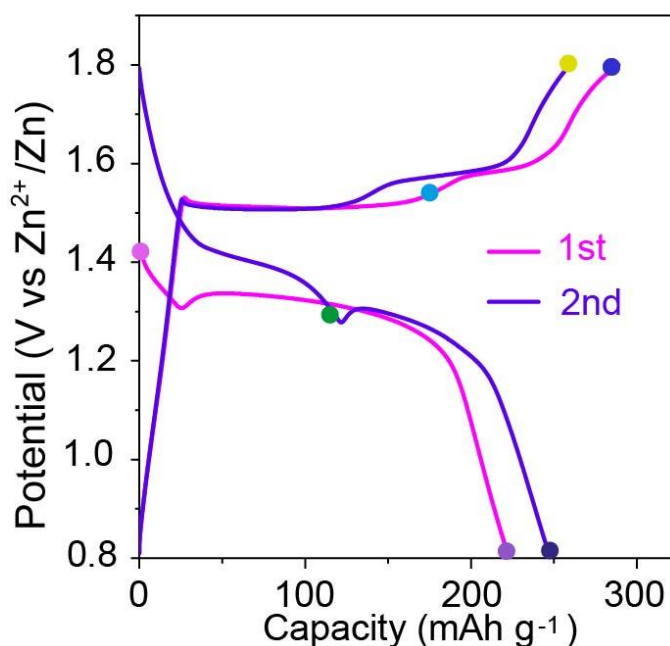
Figure 5.17. Galvanostatic discharge/charge profiles during initial 2 cycles at 0.2 A g^{-1}.

When 1st discharged to 0.8 V, compared with the XRD pattern of pristine NCS/MnO$_2$ electrode, there are new peaks located at 32.6° and 58.5° (Figure 5.18a), which are consistent with formation of zinc sulfate hydroxide hydrate (Zn$_4$(OH)$_6$SO$_4$·5H$_2$O, ZSH) [61]. SEM images show that large amounts of flakes emerge on the electrode of NCS/MnO$_2$ (Figure 5.19c and Figure 5.20b), thus these flakes can be assigned to ZSH [62]. The TEM image of NCS/MnO$_2$ cathode (1st discharged to 0.8 V) displays that there are no MnO$_2$ nanorods (seen on NCS, Figure 5.19d). There is no peak of Mn 2p in the XPS pattern after 1st discharge to 0.8 V (Figure 5.18b), demonstrating that MnO$_2$ actually dissolves during the discharge [61]. The generation of ZSH has been attributed to the dissolution reaction of MnO$_2$ into Mn^{2+}, which locally increases the pH, triggering the ZSH precipitation [63, 64]. Upon 1st charge to 1.8 V, these large ZSH flakes almost disappear (Figure 5.19g and Figure 5.20d) and many new nanosheets show up (Figure 5.19h). XPS and XAS analyses reveal that the energy positions of Mn peaks almost return to of the pristine state (Figure 5.18b-c), further suggesting that re-deposition of MnO$_2$ occurs. The formation of MnO$_2$ results from the reaction between ZSH and Mn^{2+} [64, 65].
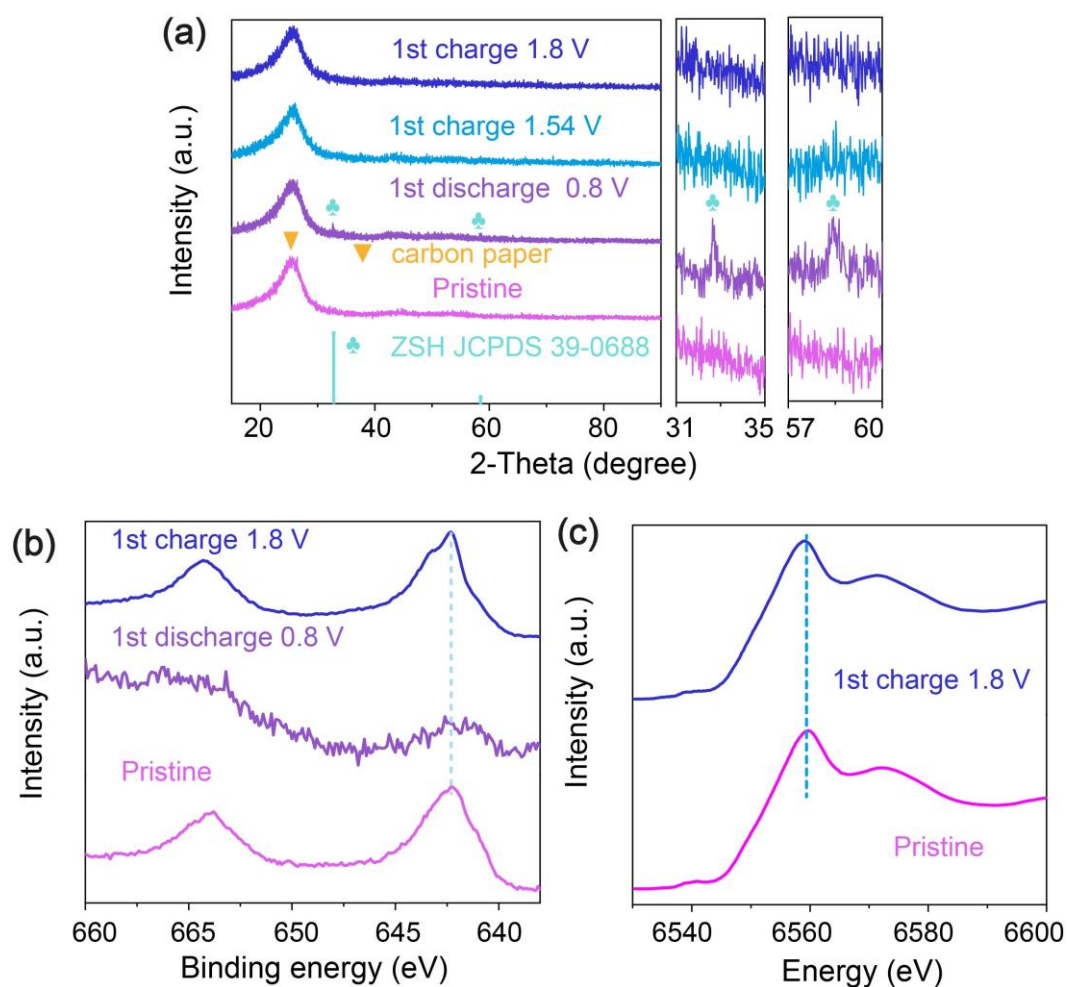
Figure 5.18. NCS/MnO₂ electrode 1st cycle: (a) XRD patterns; (b) XPS spectra Mn 2p; (c) ex-situ XAS.
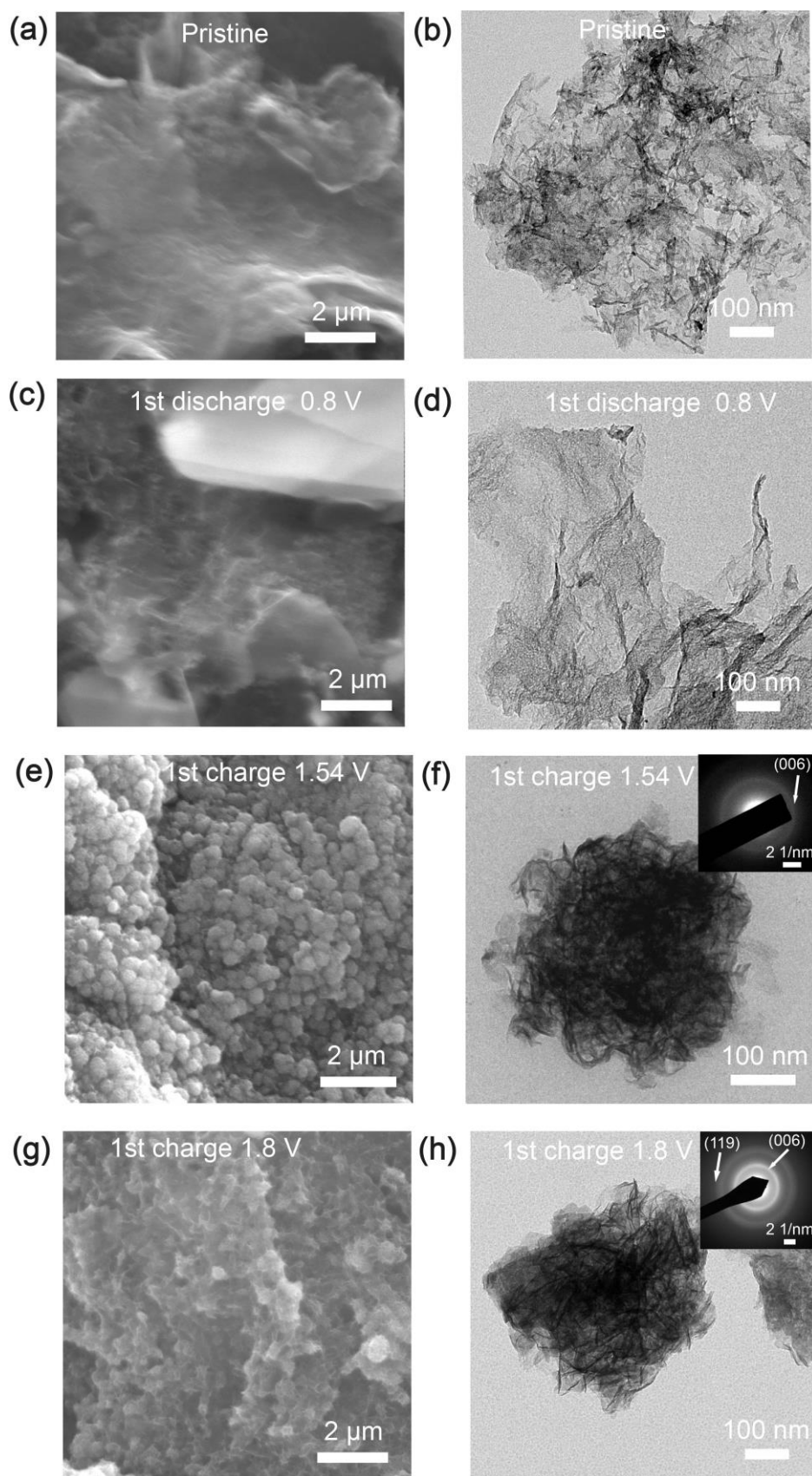
Figure 5.19. Morphological and Structural evolution of NCS/MnO$_2$ electrode (a), (c), (d) and (g) SEM images; (b), (d), (e) and (h) TEM images.
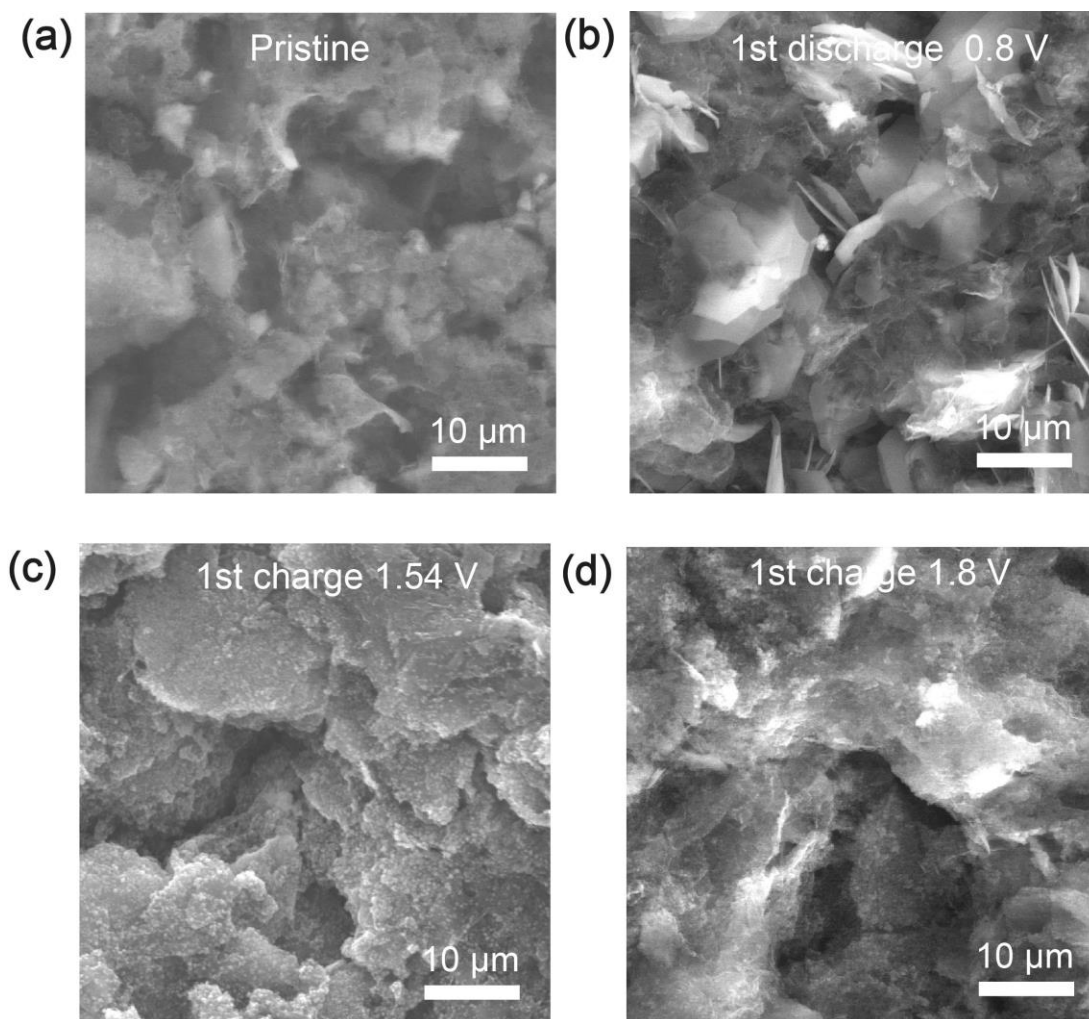
Figure 5.20. SEM images at a low manfication of NCS/MnO$_2$ during the 1st cycle at different states.

It is noteworthy that there are 2 plateaus (~1.5 V and ~1.6 V) during charge. To address the roles of ZSH and Mn^{2+} on the charge process, two NCS/MnO$_2$ cathodes (electrolyte: 2 M ZnSO$_4$ and 0.2 M MnSO$_4$) at the 1st full discharge were extracted from the cell. They were respectively removed of Mn^{2+} by washing, and of ZSH by acetic acid treatment (10 vol%). The processes are as follows: (1) one extracted NCS/MnO$_2$ electrode was dipped in Mili-Q water 3 times and then dried in the oven; (2) the other one extracted NCS/MnO$_2$ electrode was immersed in the acetic acid solution (10 vol%) for 5 minutes and then washed as the other electrode. The Mn^{2+}-free cathode was assembled with 2 M ZnSO$_4$ electrolyte. The ZSH-free cathode was assembled with the 2 M ZnSO$_4$ and 0.2 M MnSO$_4$ electrolyte. Then both cathodes were charged to 1.8 V. The charge capacities of both electrodes are small and

there are no obvious plateaus (Figure 5.21). So the occurrence of plateaus is related to the presence of both ZSH and Mn^{2+}. When charged to 1.54 V, ZSH already does not exist (Figure 5.18a, Figure 5.19e and Figure 5.20c), meaning that ZSH only involves the 1st plateau reaction and the product contributes to the 2nd plateau reaction. To determine this intermediate product, the charge states at 1.54 V and 1.8 V of NCS/MnO_2 were further investigated by TEM. The SAED patterns reveal that both products of charged states belong to birnessite-MnO_2 (Figure 5.19f and Figure 5.19h).
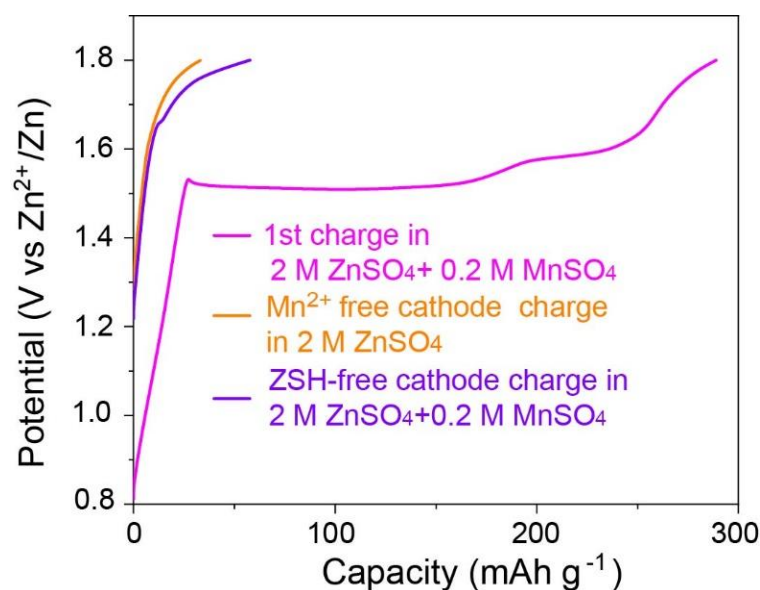
Figure 5.21. Charging curves of NCS/MnO2.

EDS results show that the Zn element content decreases greatly and the molar ratio of Mn/Zn increases from 1.0 to 4.6 when charged from 1.54 V to 1.8 V (Figure 5.22). This is compatible with a Zn_xMnO_2 product of the first charge plateau, so that the 2nd plateau reaction can be associated to Zn^{2+} deintercalation. Thus, during the 1st plateau reaction of the charge process, ZSH and Mn^{2+} react and generate Zn_xMnO_2.
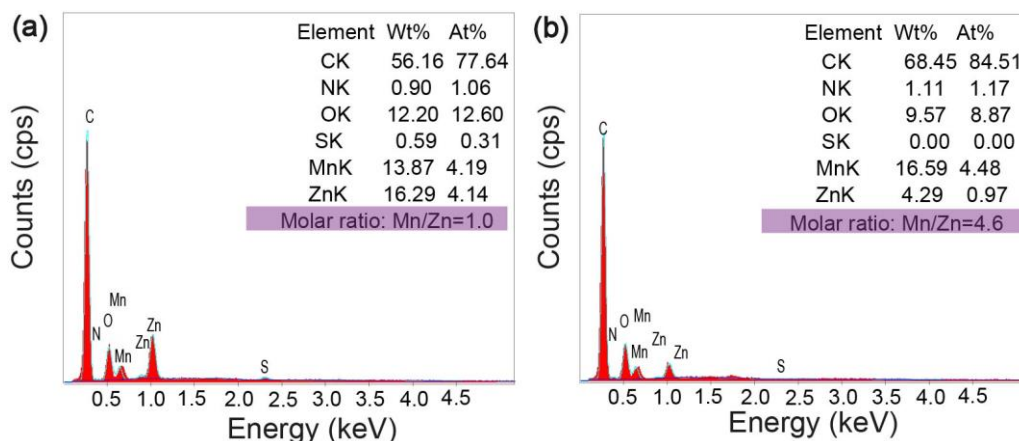
Figure 5.22. EDX spectra of NCS/MnO$_2$: (b) 1st charge to 1.54 V, (c) 1st charge to 1.80 V.

The 2nd cycle follows a similar mechanism as the 1st cycle (Figure 5.23-24). Instead, it is noteworthy that a new plateau (~1.4 V) appears at the 2nd discharge. We suggest that this first discharge plateau is the reverse of the second charge, i.e., Zn intercalation in MnO$_2$. Therefore, in the 2nd discharge there is no pH increase until 1.3 V, and no ZSH forms, so the discharged product at this state is still Zn$_x$MnO$_2$. In fact, the morphology of this state (the 2nd discharged 1.3 V) is coincident with the 1st charged 1.54 V state, demonstrating that the reaction of the 2nd discharge at high voltage (~1.4 V) and the reaction of the 1st charge at high voltage (~1.6 V) are inverse reactions to each other.
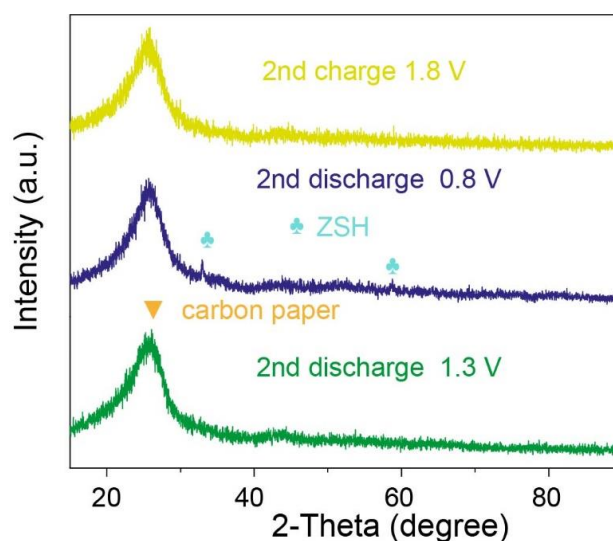
Figure 5.23. XRD patterns of the 2nd cycle for NCS/MnO$_2$ at 0.2 A g^{-1}.
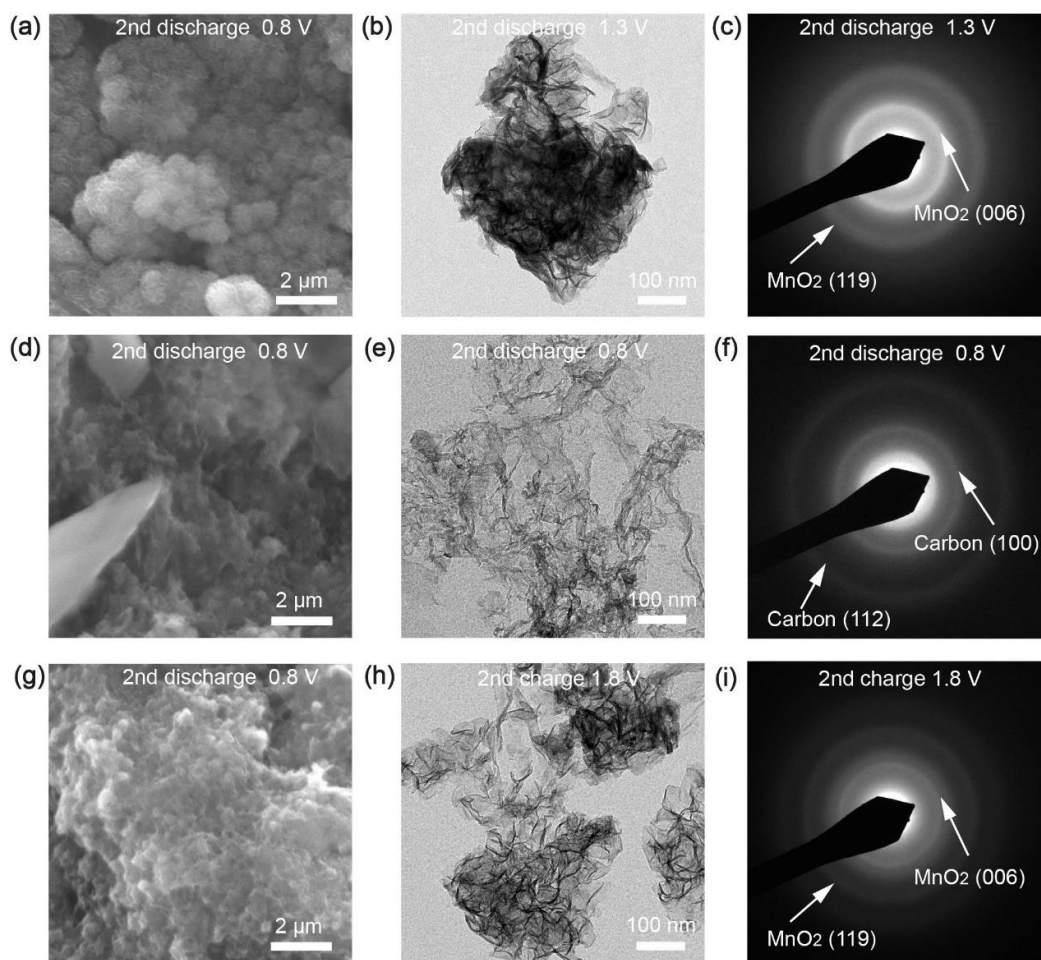
Figure 5.24. SEM, TEM and SAED images of NCS/MnO$_2$ during the 2nd cycle at different states.

In light of this possible mechanism, we relate the long lasting of the NCS/MnO$_2$ to its large area and high conductivity favoring optimal distribution of interfacial currents and dispersion of the precipitates.

5.5 Conclusions

In summary, porous N-doped carbon derived from BC is employed as a support for the growth of MnO$_2$. As prepared NCS/MnO$_2$ serves as a cathode in aqueous ZIBs and provides a superior performance (114 mAh g^{-1} at 2 A g^{-1} after 1800 cycles) compared to commercial MnO$_2$ and many cathodes reported in literature. With advantages of its nanosheet morphology providing highly porous and conductive carbon networks, NCS/MnO$_2$ exhibits remarkable capacity, excellent rate capability

and long cycle life. Besides, the charge storage mechanism and the corresponding phase transformation of NCS/MnO$_2$ were evaluated by multiple characterization methods, supporting a complex intercalation-dissolution mechanism that appears highly reversible thanks to the unique properties of this bacterial cellulose derived composite. Considering the simple, green and scalable fabrication, NCS/MnO$_2$ can be a promising cathode candidate for high-performance ZIBs.

5.6 References

[1] L.E. Blanc, D. Kundu, L.F. Nazar, Scientific Challenges for the Implementation of Zn-Ion Batteries, Joule 4(4) (2020) 771-799.

[2] Y. Liu, X. Chi, Q. Han, Y. Du, J. Huang, Y. Liu, J. Yang, α-MnO$_2$ nanofibers/carbon nanotubes hierarchically assembled microspheres: Approaching practical applications of high-performance aqueous Zn-ion batteries, J. Power Sources 443 (2019) 227244.

[3] Y. Zhao, Y. Zhu, X. Zhang, Challenges and perspectives for manganese-based oxides for advanced aqueous zinc-ion batteries, InfoMat 2(2) (2019) 237-260.

[4] J. Huang, Z. Wang, M. Hou, X. Dong, Y. Liu, Y. Wang, Y. Xia, Polyaniline-intercalated manganese dioxide nanolayers as a high-performance cathode material for an aqueous zinc-ion battery, Nat. Commun. 9(1) (2018) 2906.

[5] C. Wang, Y. Zeng, X. Xiao, S. Wu, G. Zhong, K. Xu, Z. Wei, W. Su, X. Lu, γ-MnO2 nanorods/graphene composite as efficient cathode for advanced rechargeable aqueous zinc-ion battery, J. Energy Chem. 43 (2020) 182-187.

[6] X. Shen, X. Wang, Y. Zhou, Y. Shi, L. Zhao, H. Jin, J. Di, Q. Li, Highly Reversible Aqueous Zn-MnO$_2$ Battery by Supplementing Mn^{2+}-Mediated MnO$_2$ Deposition and Dissolution, Adv. Funct. Mater. 31(27) (2021) 2101579.

[7] Y. Fu, Q. Wei, G. Zhang, X. Wang, J. Zhang, Y. Hu, D. Wang, L. Zuin, T. Zhou, Y. Wu, S. Sun, High-Performance Reversible Aqueous Zn-Ion Battery Based on Porous MnOx Nanorods Coated by MOF-Derived N-Doped Carbon, Adv. Energy Mater. 8(26) (2018) 1801445.

[8] C. Hu, Y. Lin, J.W. Connell, H.M. Cheng, Y. Gogotsi, M.M. Titirici, L. Dai, Carbon-Based Metal-Free Catalysts for Energy Storage and Environmental Remediation, Adv. Mater. 31(13) (2019) 1806128.

[9] H. Yu, G. Liu, M. Wang, R. Ren, G. Shim, J.Y. Kim, M.X. Tran, D. Byun, J.K. Lee, Plasma-Assisted Surface Modification on the Electrode Interface for Flexible Fiber-Shaped Zn-Polyaniline Batteries, ACS Appl. Mater. Interfaces 12(5) (2020) 5820-5830.

[10] D. Hursan, A.A. Samu, L. Janovak, K. Artyushkova, T. Asset, P. Atanassov, C. Janaky, Morphological Attributes Govern Carbon Dioxide Reduction on N-Doped Carbon Electrodes, Joule 3(7) (2019) 1719-1733.

[11] Z. Sheng, P. Qi, Y. Lu, G. Liu, M. Chen, X. Gan, Y. Qin, K. Hao, Y. Tang, Nitrogen-Doped Metallic MoS2 Derived from a Metal-Organic Framework for Aqueous Rechargeable Zinc-Ion Batteries, ACS Appl. Mater. Interfaces 13(29) (2021) 34495-34506.

[12] A. Samanta, B.K. Barman, S. Mallick, C.R. Raj, Three-Dimensional Nitrogen-Doped Graphitic Carbon-Encapsulated MnO-Co Heterostructure: A Bifunctional Energy Storage Material for Zn-Ion and Zn-Air Batteries, ACS Appl. Energy Mater. 3(10) (2020) 10108-10118.

[13] B. He, Z. Zhou, P. Man, Q. Zhang, C. Li, L. Xie, X. Wang, Q. Li, Y. Yao, V2O5 nanosheets supported on 3D N-doped carbon nanowall arrays as an advanced cathode for high energy and high power fiber-shaped zinc-ion batteries, J. Mater. Chem. A. 7(21) (2019) 12979-12986.

[14] S. Wang, C.M. McGuirk, A. d'Aquino, J.A. Mason, C.A. Mirkin, Metal-Organic Framework Nanoparticles, Adv. Mater. 30(37) (2018) 1800202.

[15] Z. Wang, J. Huang, J. Mao, Q. Guo, Z. Chen, Y. Lai, Metal-organic frameworks and their derivatives with graphene composites: preparation and applications in electrocatalysis and photocatalysis, J. Mater. Chem. A. 8(6) (2020) 2934-2961.

[16] S.M.J. Rogge, M. Waroquier, V. Van Speybroeck, Reliably Modeling the Mechanical Stability of Rigid and Flexible Metal-Organic Frameworks, Accounts. Chem. Res. 51(1) (2018) 138-148.

[17] J. Xu, J. Rong, F. Qiu, Y. Zhu, K. Mao, Y. Fang, D. Yang, T. Zhang, Highly dispersive NiCo2S4 nanoparticles anchored on nitrogen-doped carbon nanofibers for efficient hydrogen evolution reaction, J. Colloid Interf. Sci 555 (2019) 294-303.

[18] Y. Zhang, J. Tan, F. Wen, Z. Zhou, M. Zhu, S. Yin, H. Wang, Platinum nanoparticles deposited nitrogen-doped carbon nanofiber derived from bacterial cellulose for hydrogen evolution reaction, Int. J. Hydrogen. Energ 43(12) (2018) 6167-6176.

[19] A. Dobashi, J. Maruyama, Y. Shen, M. Nandi, H. Uyama, Activated carbon monoliths derived from bacterial cellulose/polyacrylonitrile composite as new generation electrode materials in EDLC, Carbohydr. Polym. 200 (2018) 381-390.

[20] Y. Gao, D. He, L. Wu, Z. Wang, Y. Yao, Z.-H. Huang, H. Yang, M.-X. Wang, Porous and ultrafine nitrogen-doped carbon nanofibers from bacterial cellulose with superior adsorption capacity for adsorption removal of low-concentration 4-chlorophenol, Chem. Eng. J. 420 (2021) 127411.

[21] Y. Zhang, Z. Wang, K. Hu, J. Ren, N. Yu, X. Liu, G. Wu, N. Liu, Anchoring silicon on the basal plane of graphite via a three-phase heterostructure for highly reversible lithium storage, Energy Storage Mater. 34 (2021) 311-319.

[22] H. Song, J. Su, C. Wang, Multi-Ions Electrolyte Enabled High Performance Voltage Tailorable Room-Temperature Ca-Metal Batteries, Adv. Energy Mater. 11(10) (2021) 2003685.

[23] J. Li, Y. Chen, J. Guo, F. Wang, H. Liu, Y. Li, Graphdiyne Oxide-Based High-Performance Rechargeable Aqueous Zn–MnO$_2$ Battery, Adv. Funct. Mater. 30(42) (2020) 2004115.

[24] H. Wang, F.X. Yin, N. Liu, R.H. Kou, X.B. He, C.J. Sun, B.H. Chen, D.J. Liu, H.Q. Yin, Engineering Fe-Fe$_3$C@Fe-N-C Active Sites and Hybrid Structures from Dual Metal-Organic Frameworks for Oxygen Reduction Reaction in H$_2$-O$_2$ Fuel Cell and Li-O$_2$ Battery, Adv. Funct. Mater. 29(23) (2019) 1901531.

[25] S. Li, Z. Lei, G. Yu, Q. Xu, W. Xu, R. Wu, M.K. Banks, Recycling the Catalyst of Atom Transfer Radical Polymerization to Prepare a Cu, N Codoped Mesoporous Carbon Electrocatalyst for Oxygen Reduction, ACS Sustainable Chem. Eng. 8(34) (2020) 12768-12774.

[26] M. Yuan, F. Luo, Y. Rao, J. Yu, Z. Wang, H. Li, X. Chen, SWCNT-bridged laser-induced graphene fibers decorated with MnO$_2$ nanoparticles for high-performance flexible micro-supercapacitors, Carbon 183 (2021) 128-137.

[27] K. Wang, Y. Chen, R. Tian, H. Li, Y. Zhou, H. Duan, H. Liu, Porous Co-C Core-Shell Nanocomposites Derived from Co-MOF-74 with Enhanced Electromagnetic Wave Absorption Performance, ACS Appl. Mater. Interfaces 10(13)

(2018) 11333-11342.

[28] R. Wang, M. He, Y. Zhou, S. Nie, Y. Wang, W. Liu, Q. He, W. Wu, X. Bu, X. Yang, Metal−organic frameworks self-templated cubic hollow Co/N/C@MnO_2 composites for electromagnetic wave absorption, Carbon 156 (2020) 378-388.

[29] W. Wang, S. Khabazian, S. Roig-Sanchez, A. Laromaine, A. Roig, D. Tonti, Carbons derived from alcohol-treated bacterial cellulose with optimal porosity for Li–O_2 batteries, Renew. Energ. 177 (2021) 209-215.

[30] Z. Weng, K. Zhang, Y. Qi, T. Zhang, M. Xia, F. Hu, S. Zhang, C. Liu, J. Wang, X. Jian, Scalable fabrication of heteroatom-doped versatile hierarchical porous carbons with an all-in-one phthalonitrile precursor and their applications, Carbon 159 (2020) 495-503.

[31] A. Eftekhari, Z. Fan, Ordered mesoporous carbon and its applications for electrochemical energy storage and conversion, Materials Chemistry Frontiers 1(6) (2017) 1001-1027.

[32] A.R. Selvaraj, A. Muthusamy, C. Inho, H.-J. Kim, K. Senthil, K. Prabakar, Ultrahigh surface area biomass derived 3D hierarchical porous carbon nanosheet electrodes for high energy density supercapacitors, Carbon 174 (2021) 463-474.

[33] L. Jin, X. Guo, R. Gong, J. Zheng, Z. Xiang, C. Zhang, J.P. Zheng, Target-oriented electrode constructions toward ultra-fast and ultra-stable all-graphene lithium ion capacitors, Energy Storage Mater. 23 (2019) 409-417.

[34] T. Le, Y. Yang, L. Yu, Z.H. Huang, F. Kang, In-situ growth of MnO_2 crystals under nanopore-constraint in carbon nanofibers and their electrochemical performance, Sci. Rep. 6 (2016) 37368.

[35] A.E. Fischer, K.A. Pettigrew, D.R. Rolison, R.M. Stroud, J.W. Long, Incorporation of Homogeneous, Nanoscale MnO_2 within Ultraporous Carbon Structures via Self-Limiting Electroless Deposition: Implications for Electrochemical Capacitors, Nano letter 7 (2007) 281-286.

[36] G. Li, J. Sun, W. Hou, S. Jiang, Y. Huang, J. Geng, Three-dimensional porous carbon composites containing high sulfur nanoparticle content for high-performance lithium-sulfur batteries, Nat. Commun. 7 (2016) 10601.

[37] J. Zhang, W. Zhu, Y. Pei, Y. Liu, Y. Qin, X. Zhang, Q. Wang, Y. Yin, M.D. Guiver, Hierarchically Porous Co-N-C Cathode Catalyst Layers for Anion Exchange Membrane Fuel Cells, ChemSusChem 12(18) (2019) 4165-4169.

[38] J. Wang, Z. Yang, Y. Li, X. Fan, F. Zhang, G. Zhang, W. Peng, S. Wang, Synthesis of porous nitrogen doped carbon cage from carbide for catalytic oxidation, Carbon 163 (2020) 43-55.

[39] F. Zheng, Y. Yang, Q. Chen, High lithium anodic performance of highly nitrogen-doped porous carbon prepared from a metal-organic framework, Nat. Commun. 5 (2014) 5261.

[40] H. Huang, R. Xu, Y. Feng, S. Zeng, Y. Jiang, H. Wang, W. Luo, Y. Yu, Sodium/Potassium-Ion Batteries: Boosting the Rate Capability and Cycle Life by Combining Morphology, Defect and Structure Engineering, Adv. Mater. 32(8) (2020) 1904320.

[41] S. Wang, Z. Yuan, X. Zhang, S. Bi, Z. Zhou, J. Tian, Q. Zhang, Z. Niu, Non-Metal Ion Co-Insertion Chemistry in Aqueous Zn/MnO_2 Batteries, Angew. Chem. Int. Edit. 60(13) (2021) 7056-7060.

[42] Y. Zhao, P. Zhang, J. Liang, X. Xia, L. Ren, L. Song, W. Liu, X. Sun, Uncovering sulfur doping effect in MnO_2 nanosheets as an efficient cathode for aqueous zinc ion battery, Energy Storage Mater. 47 (2022) 424-433.

[43] F. Tang, J. Gao, Q. Ruan, X. Wu, X. Wu, T. Zhang, Z. Liu, Y. Xiang, Z. He, X. Wu, Graphene-Wrapped MnO/C Composites by MOFs-Derived as Cathode Material for Aqueous Zinc ion Batteries, Electrochim. Acta 353 (2020) 136570.

[44] H. Moon, K.H. Ha, Y. Park, J. Lee, M.S. Kwon, J. Lim, M.H. Lee, D.H. Kim, J.H. Choi, J.H. Choi, K.T. Lee, Direct Proof of the Reversible Dissolution/Deposition of Mn^{2+}/Mn^{4+} for Mild-Acid $Zn-MnO_2$ Batteries with Porous Carbon Interlayers, Adv. Sci. 8(6) (2021) 2003714.

[45] H. Pan, Y. Shao, P. Yan, Y. Cheng, K.S. Han, Z. Nie, C. Wang, J. Yang, X. Li, P. Bhattacharya, K.T. Mueller, J. Liu, Reversible aqueous zinc/manganese oxide energy storage from conversion reactions, Nat. Energy 1(5) (2016) 16039.

[46] C. Zhu, G. Fang, S. Liang, Z. Chen, Z. Wang, J. Ma, H. Wang, B. Tang, X. Zheng,

J. Zhou, Electrochemically induced cationic defect in MnO intercalation cathode for aqueous zinc-ion battery, Energy Storage Mater. 24 (2020) 394-401.

[47] J. Ji, H. Wan, B. Zhang, C. Wang, Y. Gan, Q. Tan, N. Wang, J. Yao, Z. Zheng, P. Liang, J. Zhang, H. Wang, L. Tao, Y. Wang, D. Chao, H. Wang, $Co^{2+/3+/4+}$-Regulated Electron State of Mn-O for Superb Aqueous Zinc-Manganese Oxide Batteries, Adv. Energy Mater. 11(6) (2021) 2003203.

[48] V. Soundharrajan, B. Sambandam, S. Kim, S. Islam, J. Jo, S. Kim, V. Mathew, Y.-k. Sun, J. Kim, The dominant role of Mn^{2+} additive on the electrochemical reaction in $ZnMn_2O_4$ cathode for aqueous zinc-ion batteries, Energy Storage Mater. 28 (2020) 407-417.

[49] W. Xu, C. Sun, K. Zhao, X. Cheng, S. Rawal, Y. Xu, Y. Wang, Defect engineering activating (Boosting) zinc storage capacity of MoS_2, Energy Storage Mater. 16 (2019) 527-534.

[50] N. Liu, X. Wu, Y. Yin, A. Chen, C. Zhao, Z. Guo, L. Fan, N. Zhang, Constructing the Efficient Ion Diffusion Pathway by Introducing Oxygen Defects in Mn_2O_3 for High-Performance Aqueous Zinc-Ion Batteries, ACS Appl. Mater. Interfaces 12(25) (2020) 28199-28205.

[51] J. Li, L. Li, H. Shi, Z. Zhong, X. Niu, P. Zeng, Z. Long, X. Chen, J. Peng, Z. Luo, X. Wang, S. Liang, Electrochemical Energy Storage Behavior of $Na_{0.44}MnO_2$ in Aqueous Zinc-Ion Battery, ACS Sustainable Chem. Eng. 8 (2020) 10673-10681.

[52] C. Xia, J. Guo, Y. Lei, H. Liang, C. Zhao, H.N. Alshareef, Rechargeable Aqueous Zinc-Ion Battery Based on Porous Framework Zinc Pyrovanadate Intercalation Cathode, Adv. Mater. 30(5) (2018) 1705580.

[53] J. Long, F. Yang, J. Cuan, J. Wu, Z. Yang, H. Jiang, R. Song, W. Song, J. Mao, Z. Guo, Boosted Charge Transfer in Twinborn alpha-(Mn_2O_3-MnO_2) Heterostructures: Toward High-Rate and Ultralong-Life Zinc-Ion Batteries, ACS Appl. Mater. Interfaces 12(29) (2020) 32526-32535.

[54] R. Liang, J. Fu, Y.-P. Deng, Y. Pei, M. Zhang, A. Yu, Z. Chen, Parasitic electrodeposition in Zn-MnO2 batteries and its suppression for prolonged cyclability, Energy Storage Mater. 36 (2021) 478-484.

[55] B. Sambandam, S. Kim, D.T. Pham, V. Mathew, J. Lee, S. Lee, V. Soundharrajan, S. Kim, M.H. Alfaruqi, J.-Y. Hwang, J. Kim, Hyper oxidized $V_6O_{13+}\cdot nH_2O$ layered cathode for aqueous rechargeable Zn battery: Effect on dual carriers transportation and parasitic reactions, Energy Storage Mater. 35 (2021) 47-61.

[56] F. Wang, H. Zhao, Y. Ma, Y. Yang, B. Li, Y. Cui, Z. Guo, L. Wang, Core-shell-structured $Co@Co_4N$ nanoparticles encapsulated into MnO-modified porous N-doping carbon nanocubes as bifunctional catalysts for rechargeable Zn–air batteries, J. Energy Chem. 50 (2020) 52-62.

[57] H. He, D. Huang, Y. Tang, Q. Wang, X. Ji, H. Wang, Z. Guo, Tuning nitrogen species in three-dimensional porous carbon via phosphorus doping for ultra-fast potassium storage, Nano Energy 57 (2019) 728-736.

[58] M. Yang, Y. Wang, Z. Sun, H. Mi, S. Sun, D. Ma, P. Zhang, Anti-aggregation growth and hierarchical porous carbon encapsulation enables the $C@VO_2$ cathode with superior storage capability for aqueous zinc-ion batteries, J. Energy Chem. 67 (2022) 645-654.

[59] D. Chao, C.R. Zhu, M. Song, P. Liang, X. Zhang, N.H. Tiep, H. Zhao, J. Wang, R. Wang, H. Zhang, H.J. Fan, A High-Rate and Stable Quasi-Solid-State Zinc-Ion Battery with Novel 2D Layered Zinc Orthovanadate Array, Adv. Mater. 30(32) (2018) 1803181.

[60] G. Fang, C. Zhu, M. Chen, J. Zhou, B. Tang, X. Cao, X. Zheng, A. Pan, S. Liang, Suppressing Manganese Dissolution in Potassium Manganate with Rich Oxygen Defects Engaged High-Energy-Density and Durable Aqueous Zinc-Ion Battery, Adv. Funct. Mater. 29(15) (2019) 1808375.

[61] X. Zeng, J. Liu, J. Mao, J. Hao, Z. Wang, S. Zhou, C.D. Ling, Z. Guo, Toward a Reversible Mn^{4+}/Mn^{2+} Redox Reaction and Dendrite-Free Zn Anode in Near-Neutral Aqueous Zn/MnO_2 Batteries via Salt Anion Chemistry, Adv. Energy Mater. 10(32) (2020) 1904163.

[62] J. Zhou, M. Xie, F. Wu, Y. Mei, Y. Hao, L. Li, R. Chen, Encapsulation of Metallic Zn in a Hybrid MXene/Graphene Aerogel as a Stable Zn Anode for Foldable Zn-Ion Batteries, Adv. Mater. 34(1) (2022) 2106897.

[63] X. Xie, H. Fu, Y. Fang, B. Lu, J. Zhou, S. Liang, Manipulating Ion Concentration to Boost Two-Electron Mn^{4+}/Mn^{2+} Redox Kinetics through a Colloid Electrolyte for High-Capacity Zinc Batteries, Adv. Energy Mater. 12(5) (2022) 2102393.

[64] X. Guo, J. Zhou, C. Bai, X. Li, G. Fang, S. Liang, Zn/MnO_2 battery chemistry with dissolution-deposition mechanism, Mater. Today Energy 16 (2020) 100396.

[65] C. Li, X. Chi, J. Huang, J. Wu, Y. Liu, Reversible Transformation of a Zinc Salt-Boosted High Areal Capacity Manganese Dioxide Cathode for Energy-Dense and Stable Aqueous Zinc Batteries, ACS Appl. Energy Mater. 5 (2022) 1478-1486.

Chapter 6 Nickel-Phosphorous-coated Bacterial Cellulose as a Binder-Free Electrode for Efficient Hydrogen Evolution Reaction in Neutral Solution

6.1 Summary

A facile and low-cost method to fabricate a freestanding HER electrode was developed by in-situ growing Ni-P on BC through electroless deposition (ELD). The prepared Ni-P/BC possesses the properties of Ni-P and BC at the same time. Consequently, Ni-P/BC can be employed as a HER electrode directly. In addition, the method to *in situ* fabricate Ni-P on BC removes any need for binders. In comparison with some microfibrillated substrates, such as filter paper or glass fiber paper that can generate larger Ni-P particles, in this case, BC not only acts as a substrate for the growth of Ni-P particles, but also provide thin nanofibers with thickness of 20 to100 nm that are beneficial to form small particles, resulting in a large number of electrocatalytic active sites. Moreover, Ni-P/BC exhibits superior HER performance with a remarkably small overpotential of 161 mV at 10 mA cm^{-2} and a low Tafel slope (141 mV dec^{-1}) in a neutral solution. Besides, Ni-P/BC demonstrates stronger stability than commercial Pt/C. The mild experimental conditions, the straightforward fabrication and the excellent HER performance make Ni-P/BC electrode a strong candidate for practical applications.

6.2 Introduction

BC has been reported also for the preparation of HER catalysts. On account of the insulating character of BC, BC is usually carbonized to improve the electrode's conductivity [1-5]. Nevertheless, carbonized BC often loses its excellent mechanical properties and becomes fragile [6]. Hence, catalysts based on carbonized BC are usually immobilized on conductive substrates with the help of binders, impacting

negatively on the electrochemically active sites [7]. Therefore, it would be desirable to develop pristine BC-based electrodes with high HER performance.

Considering the high conductivity and the high HER activity of nickel-phosphorous (Ni-P) alloys [8, 9], pristine BC was integrated with Ni-P by ELD.

6.3 Electrode Preparations

To prepare metal-coated BC, dried and porous BC was used as support, exploiting the method based on alcohols described in Chapter 3. For this purpose, purified BC was squeezed under ~150 g Teflon cylinder for 10 min to remove most water and the pressed BC was placed in ethanol and kept stirring for 2 h at room temperature. Then the ethanol-treated BC was dried in an oven (60 °C, 24 h). The Ni-P/BC electrode was prepared as Figure 6.1. Dried BC was sensitized by immersing in an Sn^{2+} solution (0.05 M $SnCl_2$, 0.12 M HCl) for 30 min to absorb Sn^{2+} ions on the surface and washed in Milli-Q water 3 times. Next, BC was soaked in a Pd^{2+} solution (100 μg mL^{-1} $PdCl_2$, 0.03 M HCl) for 30 min and again rinsed in Milli-Q water 3 times. The reaction between Sn^{2+} and Pd^{2+} generates Pd particles that will catalyze the Ni deposition.[10] Finally, a 20 mL ELD solution (2 mmol $NiSO_4 \cdot 6H_2O$, 2 mmol $Na_3C_6H_5O_7 \cdot 2H_2O$, 2 mmol NaH_2PO_2 and 14 mmol NH_4Cl) was adjusted by ammonia solution to a pH of 8 and heated to 60 °C. The BC was dipped in the bath and kept for 10 min and after that, washed in Milli-Q water and ethanol 3 times. The washed BC was dried in the Ar atmosphere. The electrode was labeled as Ni-P/BC.
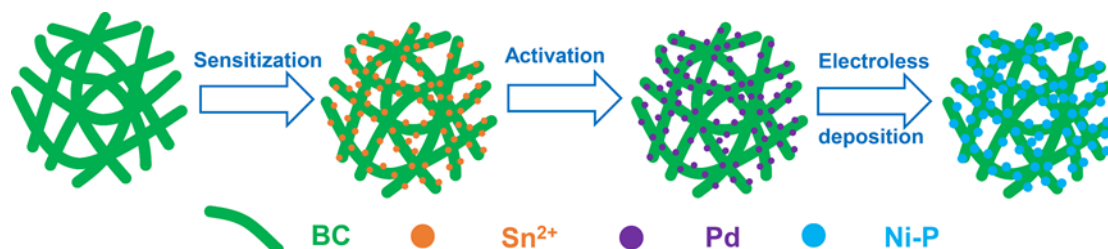

Figure 6.1. Schematic illustration of the synthesis routine of Ni-P/BC.

NaBH$_4$ and DMAB were also used as alternative Ni reducing agents. Due to the

strong reducing ability of NaBH$_4$, 5 mL fresh NaBH$_4$ solution was added dropwise to the ELD solution. DMAB was instead used in the same manner as NaH$_2$PO$_2$. The electrodes derived from NaBH$_4$ and DMAB were respectively labeled as Ni-B-1/BC and Ni-B-2/BC.

All three reducing agents, NaH$_2$PO$_2$, NaBH$_4$ and DMAB, produce spherical particles on BC surface (Figure 6.2a-c and Figure 6.2d-f). It can be seen that the particle size of Ni-B-2 (0.1-1 µm) is much larger than for Ni-B-1 (0.05-0.2 µm) and Ni-P (0.1-0.2 µm). Instead, the Ni mass loading using NaBH$_4$ is much lower (0.8 mg cm^{-2}) than the ones with NaH$_2$PO$_2$ (5.0 mg cm^{-2}) or DMAB (6.0 mg cm^{-2}). Probably because NaBH$_4$ is a stronger reducing agent and the Ni deposition took place preferentially in the solution rather than on the substrate [11]. In fact, in this case the plating solution turned dark quickly, contrasting with the other reducing agents where this happened only towards the end of the deposition time. The rings of SAED patterns for Ni-B-1 are more diffuse than Ni-B-2 and Ni-P (Figure 6.2g-i) indicating a weaker crystallinity of Ni-B-1.
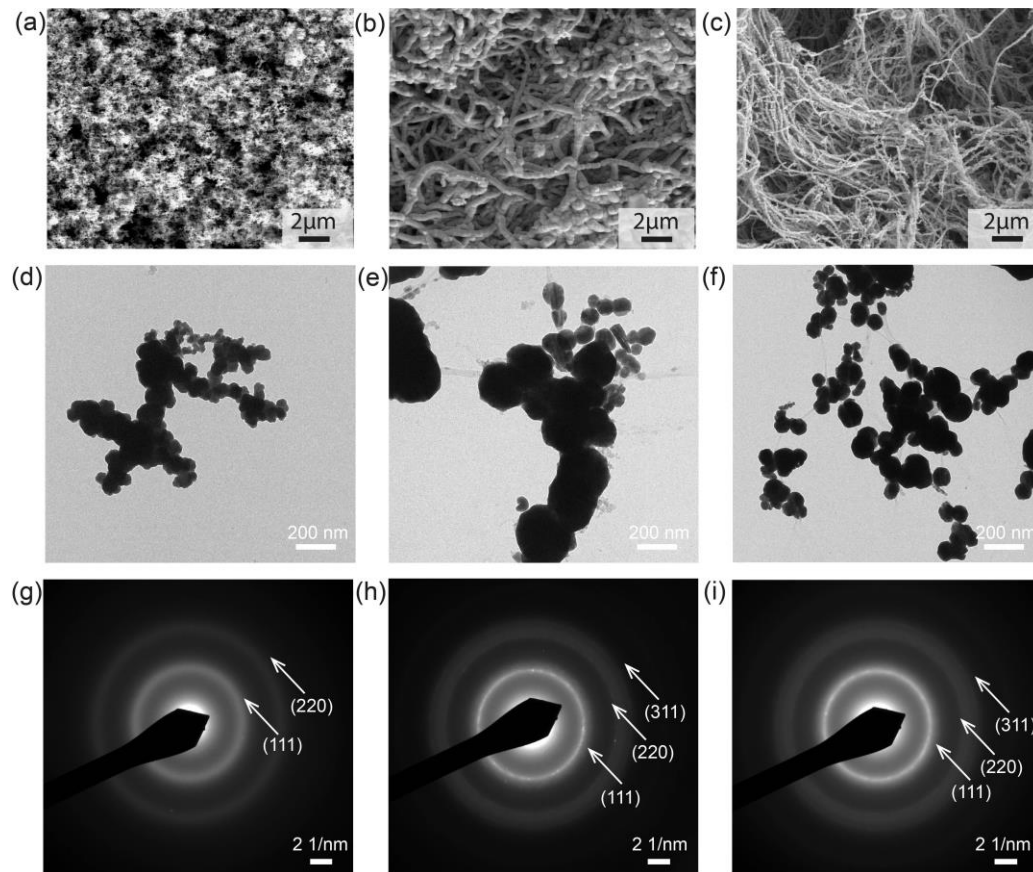

Figure 6.2. SEM images, TEM images and SAED patterns: (a), (d), (g) Ni-B-1/BC;

(b), (e), (h), Ni-B-2/BC; (c), (f), (i) Ni-P/BC.

EDS confirms the presence of Ni, P or B elements (Figure 6.3a-c). In addition, EDS mapping of Ni-P/BC further confirms that the Ni and P elements are uniformly distributed (Figure 6.3d).
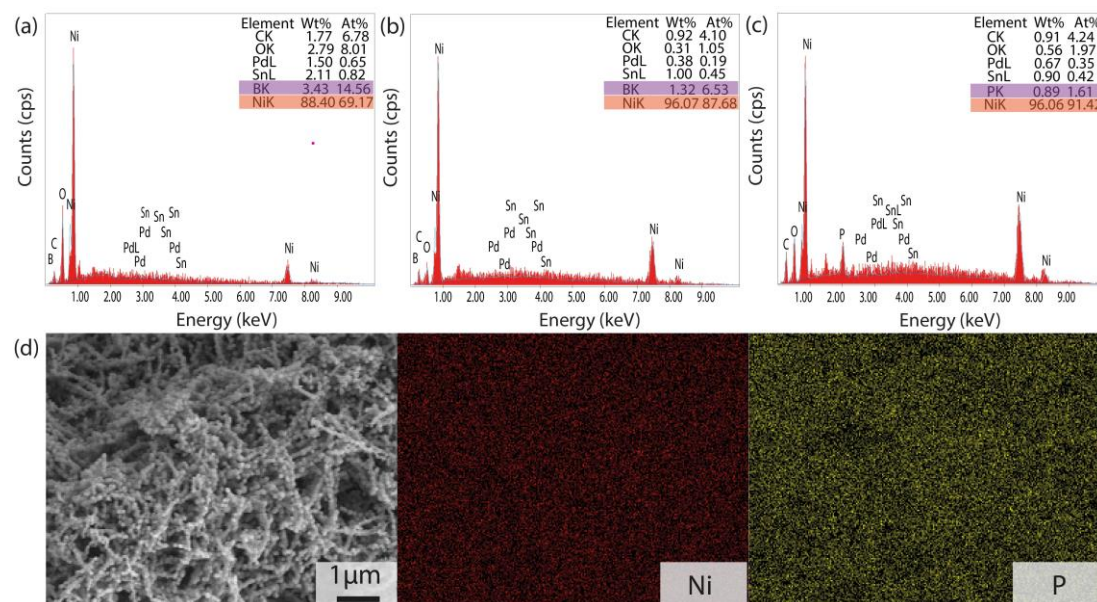

Figure 6.3. EDX spectra of (a) Ni-B-1/BC, (b) Ni-B-2/BC and (c) Ni-P/BC; (d) EDS mapping images of Ni-P/BC.

The phases and the crystal structures of these samples were evaluated by XRD. The diffraction peaks of bare BC centered at 14.5 ° and 22.5 ° belong to the (100) and (110) lattice planes of cellulose (Figure 6.4) [12]. For Ni-B-1/BC, only the cellulose peaks are observed, consistent with the low mass of Ni-B-1 on BC and the indication that electroless deposition barely occurred on the BC. In contrast, Ni-P/BC and Ni-B-2/BC present a diffraction peak at $2\Theta=45^{o}$, which can be assigned to the (111) plane of the Ni face-centered cubic structure (JCPDS 01-1260). Previous reports indicated that highly crystalline Ni tends to form when the content of B or P is low [13, 14].
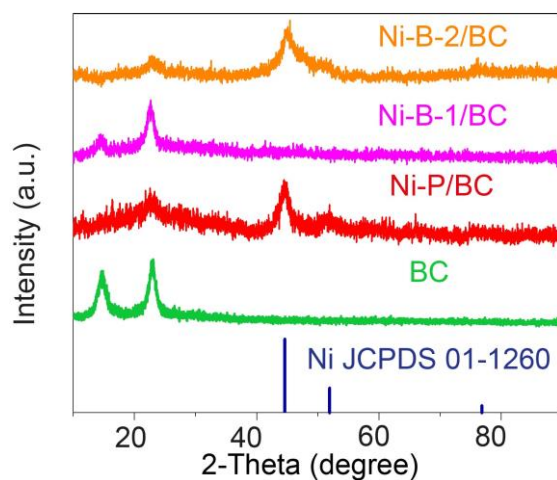
Figure 6.4. XRD patterns of samples and positions of Ni metal reference.

XPS confirms the presence of Ni, B or P elements on the surface of Ni-based BCs, in agreement with EDS results. The binding energies of Ni 2p spectra for all samples, at 870 eV and 853 eV, can be attributed to the $2p_{1/2}$ and $2p_{3/2}$ peaks of metallic Ni (Figure 6.5 and Table 6.1) [15, 16]. The peaks at 874 eV and 856 eV correspond to Ni^{2+}, which can be assigned to an oxidized state of Ni because of the air exposure [17].
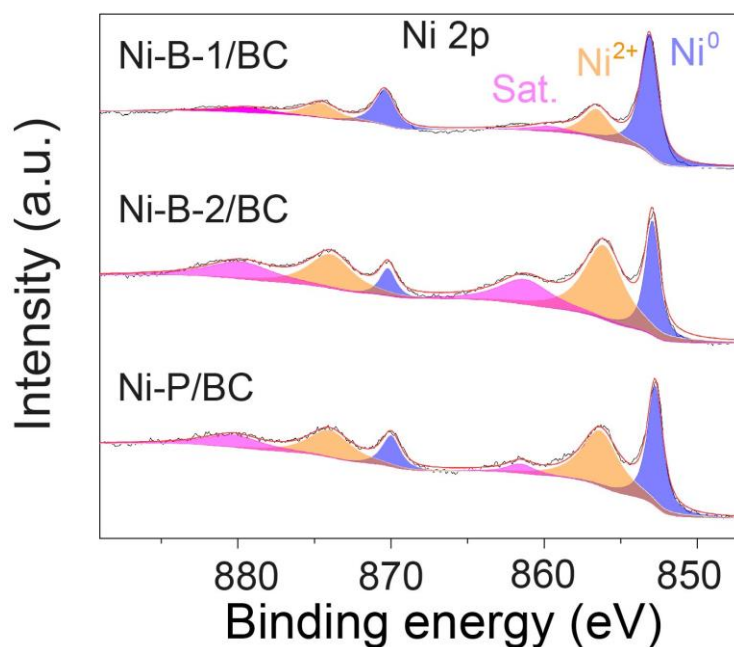

Figure 6.5. XPS spectra and fitting of Ni 2p.

Table 6.1 XPS binding energies of Ni 2p for Ni-B-1/BC, Ni-B-2/BC and Ni-P/BC.

Sample	2p$_{3/2}$			2p$_{1/2}$		
	Ni^0 (eV)	Ni^{2+} (eV)	Satellite (eV)	Ni^0 (eV)	Ni^{2+} (eV)	Satellite (eV)
Ni-B-1/BC	853.1	856.6	859.6	870.4	874.6	879.4
Ni-B-2/BC	852.9	856.1	861.3	870.2	874.0	879.8
Ni-P/BC	852.8	856.3	861.5	870.0	874.0	880.3

The other two peaks at 861 eV and 880 eV are satellite signals [18]. For Ni-B-1 and Ni-B-2, the deconvolution of B 1s spectrum exhibits two peaks at 188 eV and 192 eV (Figure 6.6a and Table 6.2), associated with zero valence B and oxidized B corresponding to surface B_2O_3 [19]. Compared with pure B (187.1 eV) [20], the binding energies of B change positively (Ni-B-1: 188.5 eV; Ni-B-2: 188.4 eV). This suggests some partial electron transfer from B^0 to Ni^0 clusters with consequent dipole formation. This agrees with literature showing that B tends to donate electrons to the metal atoms [21, 22]. It is worthy to note that compared with pure Ni (2p$_{3/2}$: 853.0 eV) [23], there is instead no significant shift of the Ni spectrum in the Ni-B/BC. This is probably because Ni is electrically connected to ground in the XPS spectrometer. This is probably because the Ni phase is electrically connected to ground in the XPS spectrometer and cannot actually be charged. B instead forms a dipole with respect to Ni. The P 2p spectra for Ni-P/BC could be deconvoluted into 3 peaks (Figure 6.6b). The two signals located at 130.4 eV and 129.9 eV can be ascribed to P 2p$_{1/2}$ and 2p$_{3/2}$ [24]. In comparison with pure P (2p$_{3/2}$: 30.2 eV), the binding energy of the P spectrum in this case shifts negatively, indicating that there is partial electron transfer from Ni to P [25]. The negatively charged P is beneficial to accept positively charged protons during the electrocatalytic process [26]. The last signal at about 133.4 eV is attributed to phosphate due to the atmospheric oxidation [27].
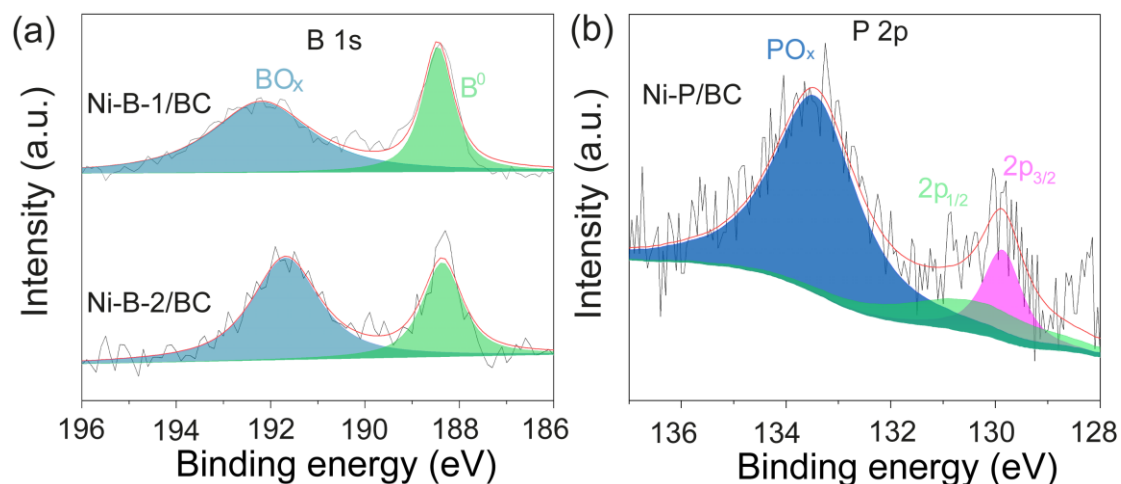
Figure 6.6. XPS spectra and fitting of B 1s (a), and P 2p (b).

Table 6.2 XPS binding energies BEs of B 1s for Ni-B-1/BC and Ni-B-2/BC.

Sample	BO_x (eV)	B^0 (eV)
Ni-B-1/BC	192.2	188.5
Ni-B-2/BC	191.7	188.4

FP and glass fiber paper (GFP) were also used as substrates to prepare Ni-P using the same method as with BC. The obtained electrodes were labeled as Ni-P/FP and Ni-P/GFP. To explore the influence of fiber's diameter on the produced Ni-P, FP and GFP were used as substrates. As shown in Figure 6.7, the fibers of BC (0.06±0.02 µm) are much thinner than those of FP (18.3 ±3.9 µm) and GFP (0.88±0.38 µm).
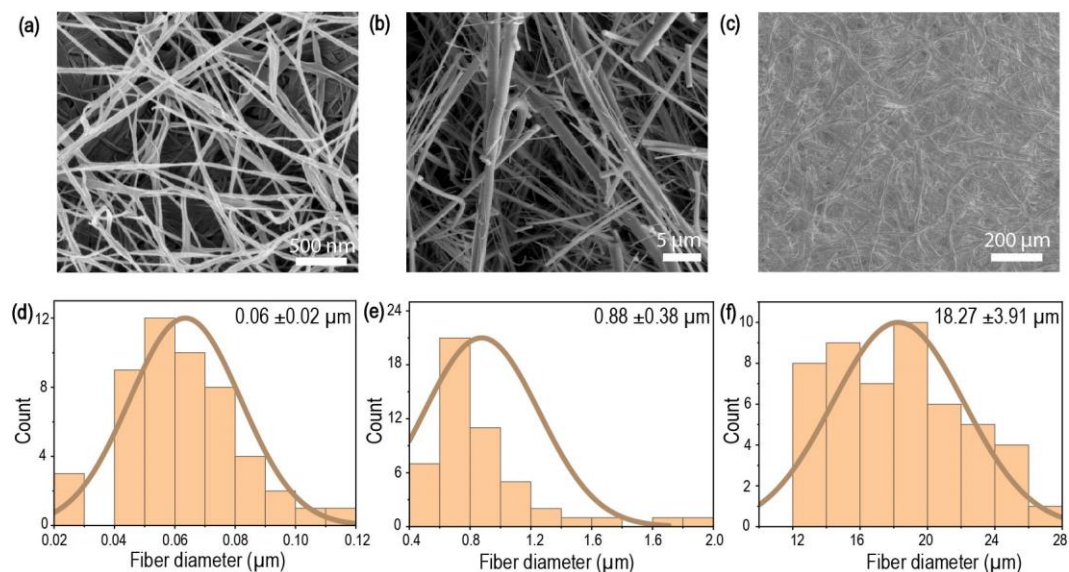
Figure 6.7. SEM images of (a) BC, (b) GFP and (c) FP. Fiber diameter histograms of (d) BC, (e) GFP and (f) FP obtained by manual measures on the images using the ImageJ software.

After ELD (Figure 6.8), the sizes of Ni-P particles on FP (0.80±0.12 µm) and GFP (0.55±0.17 µm) are much larger than Ni-P particles grown BC (0.18 ±0.04 µm). Besides, the aggregation of Ni-P particles is more critical on FP and GFP. This confirms that the thickness of fibers plays a significant role in the size of Ni-P particles [28].
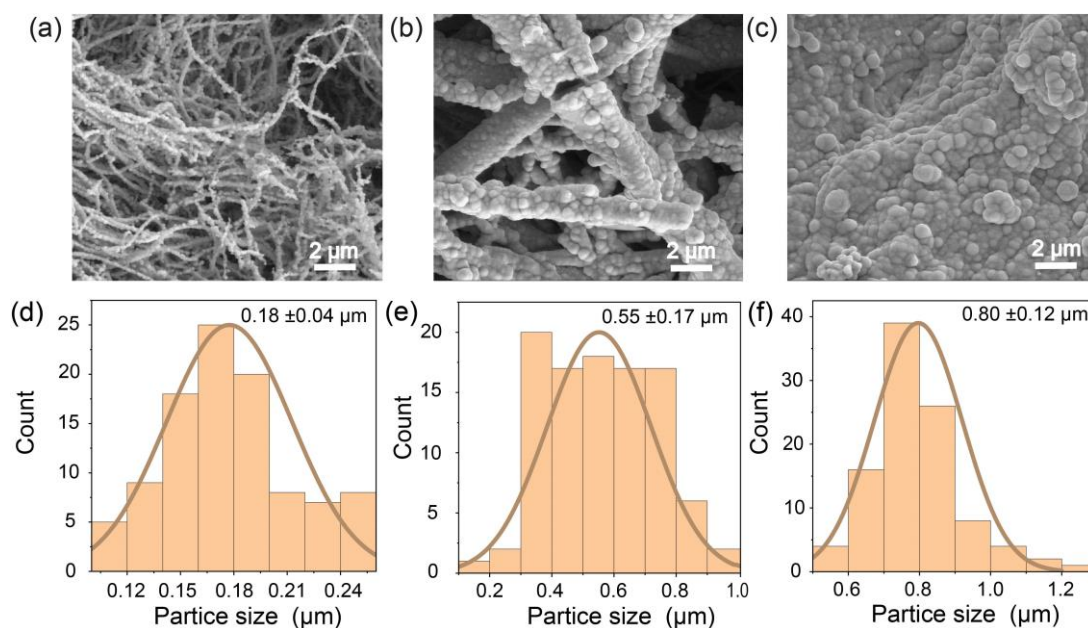

Figure 6.8. SEM images of (a) Ni-P/BC, (b) Ni-P/GFP and (c) Ni-P/FP; Ni-P particle

size histograms of (d) Ni-P/BC, (e) Ni-P/GFP and (f) Ni-P/FP obtained by manual measures on the images using the ImageJ software.

Despite different substrates and particle sizes, XRD and XPS show similar results (Figure 6.9 and Tables 6.3-4).
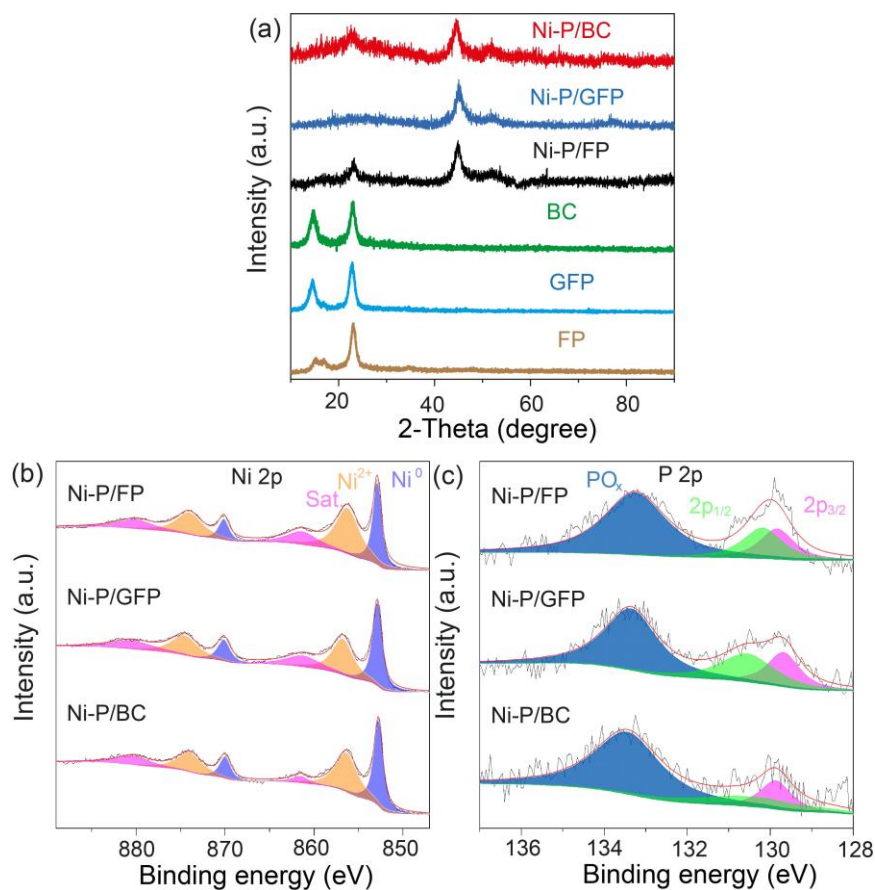
Figure 6.9. (a) XRD patterns; (b) XPS spectra of Ni 2p; (c) XPS spectra of P 2p.

Table 6.3 XPS binding energies of Ni 2p for Ni-P/BC, Ni-P/GFP and Ni-P/FP.

Sample	$2p_{3/2}$			$2p_{1/2}$		
	Ni^0 (eV)	Ni^{2+} (eV)	Satellite (eV)	Ni^0 (eV)	Ni^{2+} (eV)	Satellite (eV)
Ni-P/BC	852.8	856.3	861.5	870.0	874.0	880.3
Ni-P/GFP	852.9	856.8	861.2	870.1	874.6	880.5
Ni-P/FP	852.9	856.2	861.3	870.1	874.0	880.1

Table 6.4 XPS binding energies of P 2p for Ni-P/BC, Ni-P/GFP and Ni-P/FP.

Sample	P^0		PO$_x$ (eV)
	2p$_{1/2}$ (eV)	2p$_{3/2}$ (eV)	
Ni-P/BC	130.4	129.9	133.4
Ni-P/GFP	130.5	129.7	133.4
Ni-P/FP	130.2	129.8	133.3

A series of Ni-Co-P/BC electrodes were also synthesized by changing the molar ratios of Ni^{2+} and Co^{2+} (Ni/Co=8/2; 5/5; 2/8) in the electroless plating solution. The corresponding electrodes are separately denoted as Ni-Co-P-1/BC, Ni-Co-P-2/BC and Ni-Co-P-3/BC. Co-P/BC was obtained with 2 mmol CoSO$_4$·5H$_2$O in the same way as Ni-P/BC. With the increment of Co incorporation, the particle aggregation tends to be more obvious (Figure 6.10).

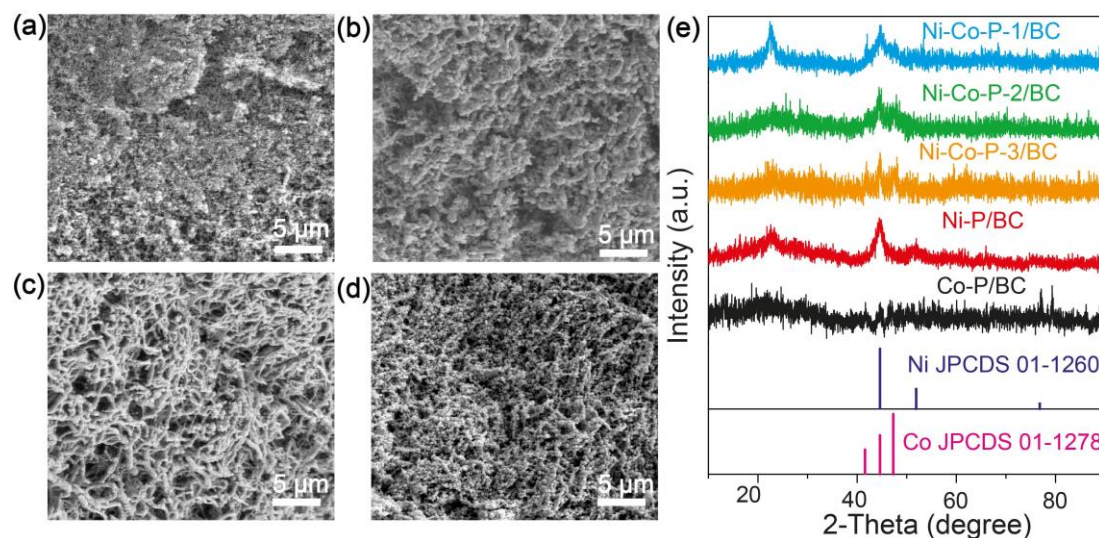**Figure 6.10.** SEM images of (a) Co-P/BC, (b) Ni-Co-P-3/BC, (c) Ni-Co-P-2/BC and Ni-Co-P-3/BC. (e) XRD patterns of samples.

For comparisons, a Pt/C electrode was prepared by dispersing 5 mg Pt/C (20 wt %) in the mixture made of 30 μL Nafion solution + 970 μL ethanol [29]. Then the dispersion was treated by ultrasound for 1 min to form an ink that was dropped on carbon paper to obtain a loading of 5.0 mg cm^{-2}.

6.4 Electrochemical measurements

The electrochemical measurements were carried out in a three-electrode cell. Graphite rod, Ag/AgCl electrode and prepared electrodes (1x1 cm) were respectively used as the counter electrode, the reference electrode and the working electrode. The potentials (V *vs* Ag/AgCl) measured in this work were converted to the potentials of reversible hydrogen electrode (RHE) according to the following equation $E_{RHE}=E_{Ag/AgCl}+0.197+0.059\cdot pH$ [30]. All electrochemical measurements were performed in N_2 saturated 1 M potassium phosphate-buffered saline (PBS, pH=7) electrolyte.

The electrochemical performance of these electrodes for HER was evaluated in 1 M PBS (pH=7) by a three-electrode system. Ni-B-1/BC shows a low reducing current (Figure 6.11a), demonstrating poor HER performance. It can be attributed to both the poor electric conductivity of Ni-B-1/BC and the low Ni loading of Ni-B-1. Ni-P/BC delivers a much lower overpotential (161 mV) than Ni-B-2/BC (269 mV) at 10 mA cm^{-2}. There are two main reasons behind it. On one hand, as already indicated by XPS results above, B partially transfers electrons to Ni, making the Ni atom in Ni-B-2/BC electron-rich compared to the Ni-P/BC. Electron-deficient Ni centers favor the hydrogen dissociative chemisorption better than electron-rich Ni ones [23]. On the other hand, the particle size of Ni-P (0.1-0.2 µm) is smaller than Ni-B-2 (0.1-1 µm), which can then provide a larger active surface area resulting in a larger number of active sites [31, 32]. HER kinetics of these electrodes were quantified by Tafel plots. As shown in Figure 6.11b, Ni-P/BC has a lower Tafel slope than Ni-B-1/BC and Ni-B-2/BC, revealing faster HER kinetics.
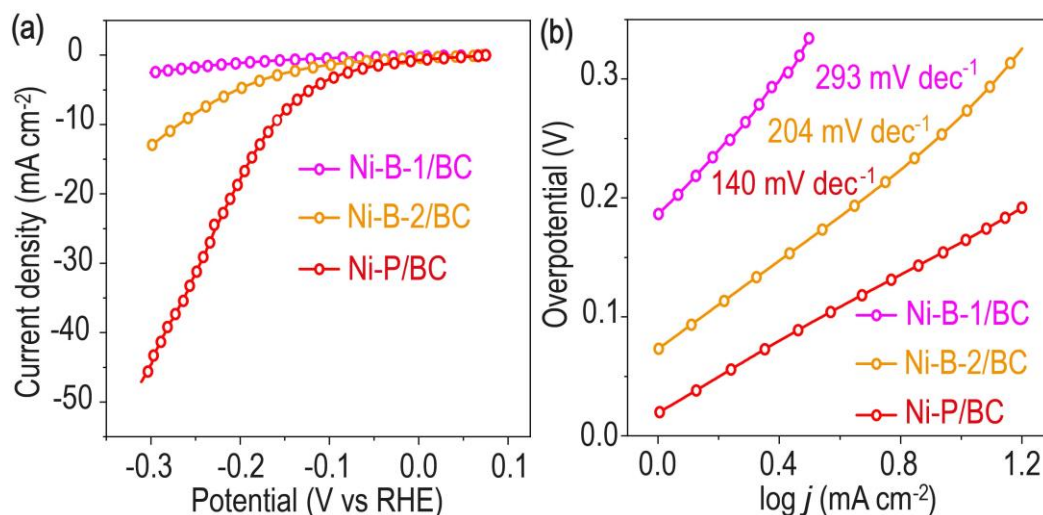
Figure 6.11. (a) HER polarization curves with a scan rate of 10 mV s^{-1} and (b) corresponding Tafel plots of electrodes in 1 M PBS.

EIS is also useful to evaluate the kinetics of these electrodes. The charge-transfer resistance (R_{ct}) is related to the HER kinetic rate and a lower value implies faster kinetics [33, 34]. Nyquist plots of electrochemical impedance for the three catalysts are presented in Figure 6.12. The semicircle diameter corresponds to R_{ct}, and clearly, Ni-P/BC exhibits a smaller R_{ct} than both Ni-B-1/BC and Ni-B-2/BC. This reflects a smaller charge-transfer resistance or a faster charge-transfer kinetics for Ni-P/BC. In addition, the onset on the real axis indicates a larger series resistance for Ni-B-1/BC (23.1 Ω) than Ni-B-2/BC (4.5 Ω) and Ni-P/BC (4.7 Ω), confirming the poor conductivity of Ni-B-1/BC.
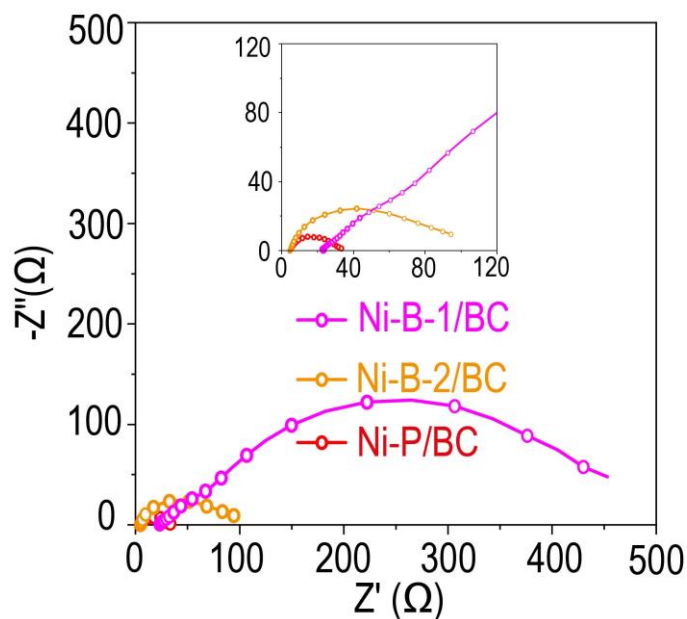
Figure 6.12. Electrochemical impedance spectra of electrodes for different reducing agents at 150 mV overpotential (the frequency range from 100 kHz to 0.01 Hz with 5 mV amplitude).

Next, the effect of Ni-P deposition time on the HER performance was also assessed. As the electroless deposition time extends, the size of Ni-P particles becomes larger (10 min: 0.1-0.2 µm; 20 min: 0.1-0.3 µm; 30 min: 0.2-0.7 µm) and the aggregation of Ni-P becomes more obvious (Figure 6.13a-c), leading to higher overpotentials (Figure 6.13d). Nevertheless, even if the particle size of Ni-P becomes comparable to Ni-B of Ni-B-2/BC, the overpotential remains smaller, confirming the important role of the P doping of Ni.
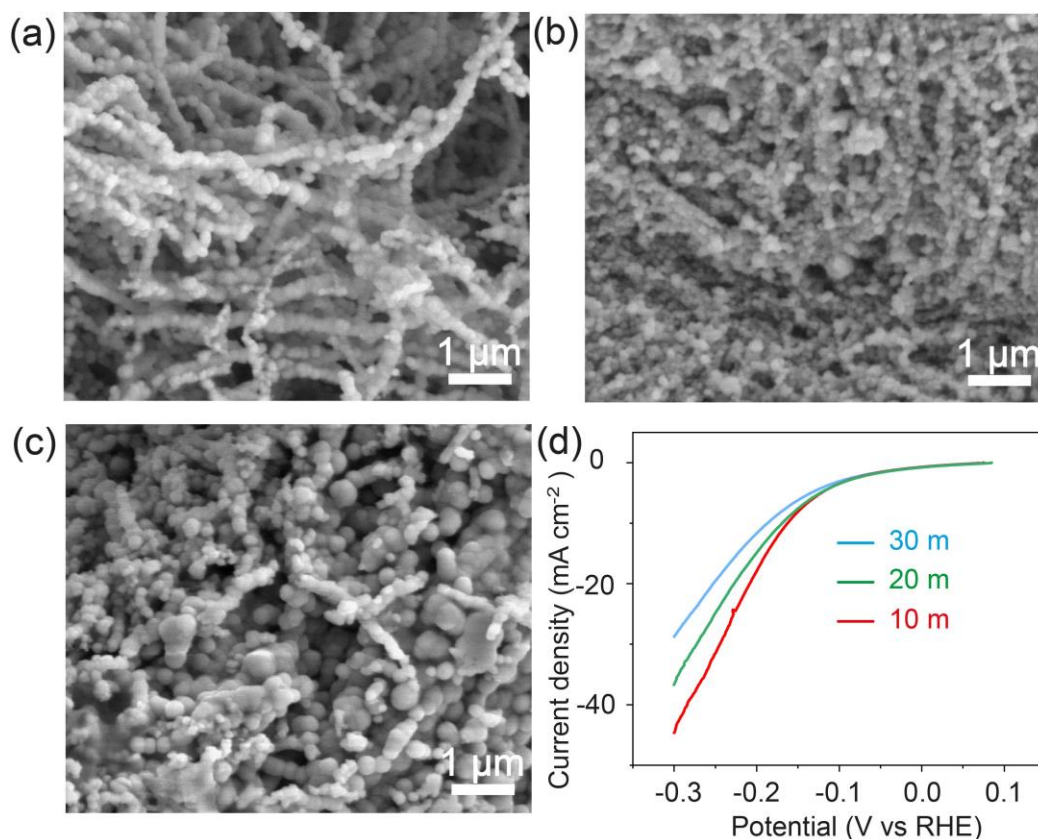
Figure 6.13. SEM images for different deposition times for Ni-P grown on BC: (a) 10 m, (b) 20 m and (c) 30 m; (d) HER polarization curves of different deposition time for Ni-P grown on BC.

The effect of particle size was studied by comparing Ni-P/BC with Ni-P deposited on filter paper (Ni-P/FP) and glass fibers (Ni-P/GFP). As shown in the HER polarization curves (Figure 6.14a), Ni-P/BC presents a lower overpotential (161 mV) than Ni-P/FP (252 mV) and Ni-P/GFP (201 mV) at 10 mA cm^{-2}, depicting the superior HER activity of Ni-P/BC. The Tafel slopes of Ni-P/FP and Ni-P/GFP are respectively 230 mV dec^{-1} and 194 mV dec^{-1} (Figure 6.14b), which indicates higher activation energy for HER [35]. Conversely Ni-P/BC possesses a lower Tafel slope (140 mV dec^{-1}). EIS also demonstrated faster charge transfer for Ni-P/BC, as indicated by its smaller semicircular diameter than Ni-P/FP and Ni-P/GGP in Figure 6.14c.

Figure 6.14. (a) HER polarization curves and (b) corresponding Tafel plots of electrodes in 1 M PBS. (c) Electrochemical impedance spectra of electrodes for different substrates at 150 mV overpotential.
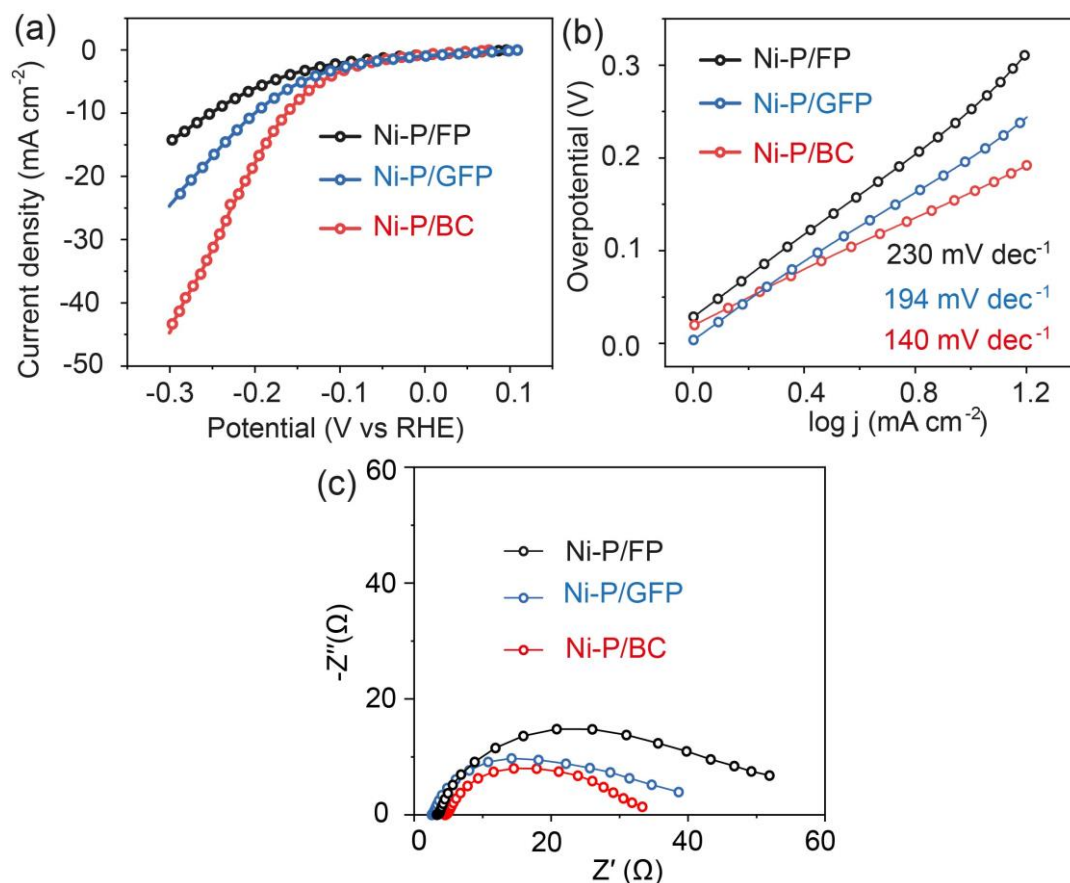
The ECSA reflects the number of active sites for catalysis and the value of ECSA is proportional to C_{dl} [36]. The C_{dl} values of these electrodes were investigated by CV at different scan rates (Figure 6.15). It is noticeable that compared with Ni-P/FP (3.9 mF cm^{-2}) and Ni-GFP (6.3 mF cm^{-2}), Ni-P/BC shows a larger C_{dl} (10.2 mF cm^{-2}), implying again more active sites in Ni-P/BC. Therefore, the remarkable HER activity of Ni-P/BC can be mainly attributed to the small size of Ni-P particles on BC, increasing substantially the active surface area [31, 32]. It is worth noting that Ni-P/BC also outperforms many reported non-precious metal HER electrodes (Table 6.5). As we can note in Table 6.5, the substrates of electrodes reported in the literature are conductive (such as glassy carbon, carbon paper, carbon cloth, F-doped tin oxide and Ni foam), most of which are less economical and environment-friendly than BC.

In addition, ex situ prepared catalysts usually need to be immobilized on conductive substrates with binders, which can impair the electrochemically active sites [7]. This makes the fabrication processes of electrodes more complex and expensive. Therefore, the binder-free Ni-P/BC electrode shows great advantages over these reported electrodes in terms of HER activity, cost, environment-friendliness and fabrication process.
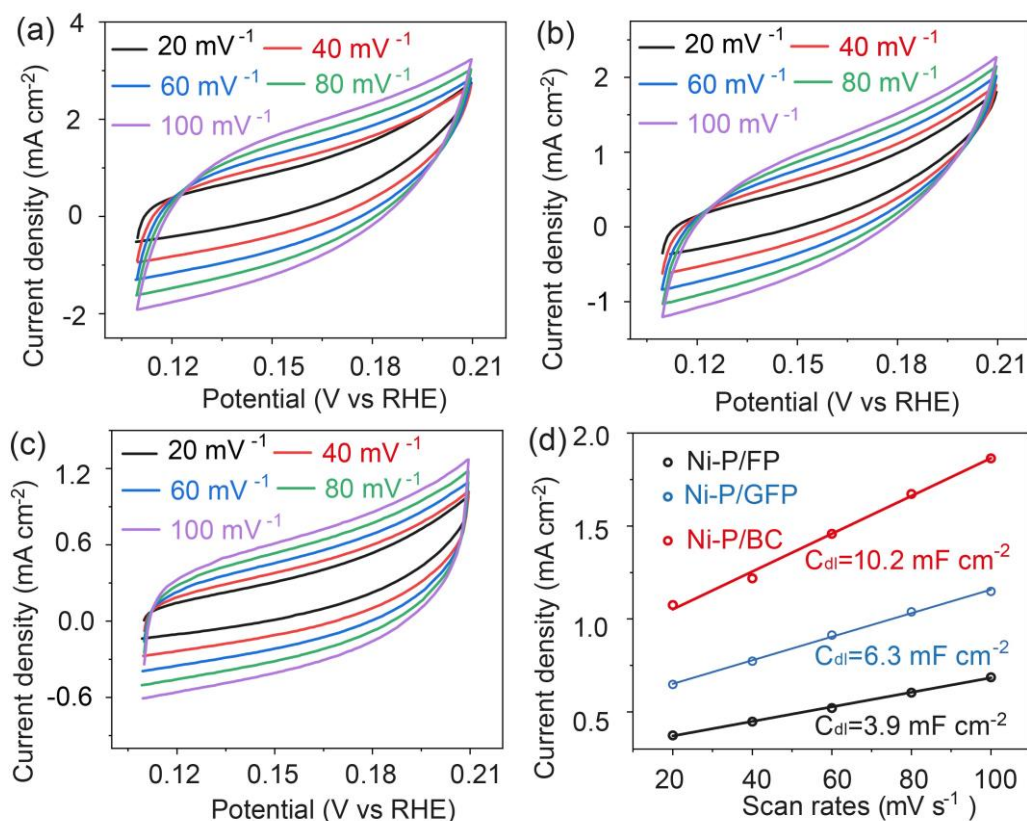
Figure 6.15. CV curves of (a) Ni-P/BC, (b) Ni-P/GFP and (c) Ni-P/FP at different scan rates; (d) capacitive currents at 0.16 V as a function of scan rate for electrodes.

Table 6.5 Comparison of the HER activity with other electrodes in 1 M PBS (pH=7).

Electrode	Substrate	Overpotential (mV at 10 mA cm^{-2})	Preparation method
Ni-P/BC	bacterial cellulose	161	electroless deposition
Ru single-atomic sites-Ni$_2$P [37]	glassy carbon	260	calcination
NiP$_x$ [38]	carbon cloth	230	electrochemical deposition
Ni$_2$P [39]	carbon paper	196	electrochemical deposition
NiP$_2$-carbon cloth nanohybrids [40]	carbon cloth	160	calcination
MoP nanosheet array/carbon cloth [41]	carbon cloth	187	calcination
CoS$_x$-(0.2-0.02) -12 [42]	FTO	168	electrochemical deposition
CoMoS$_4$ nanosheet array/carbon cloth [43]	carbon cloth	183	hydrothermal reaction
Ni$_3$S$_2$/Ni foam [44]	Ni foam	170	hydrothermal reaction
MoP700 [33]	glassy carbon	196	calcination
Ni/a-Ni(OH)$_2$ [45]	Ni foam	110	electrochemical deposition

Since bi-metallic transition metal-phosphorus also has been reported to show good HER performance [14, 46], Co was introduced into Ni-P/BC. The overpotential becomes larger with the increment of Co incorporation (Figure 6.16). Because the particles aggregate seriously after the introduction of Co. This effect seems dominating over possible tuning of the electronic structure.
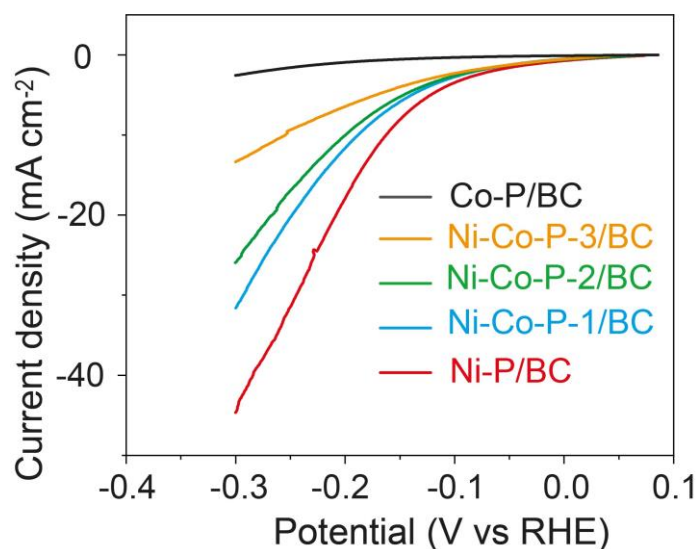
Figure 6.16. HER polarization curves of electrodes.

Finally, commercial Pt/C was also used as a comparison, coating it on carbon paper, since BC is not a conducting current collector. The overpotential of Ni-P/BC (161 mV) is indeed still higher than Pt/C (82 mV) at 10 mA cm^{-2} (Figure 6.17a). Although Pt/C shows better HER performance than Ni-P/BC, its durability is visibly poorer (Figure 6.17b), with a much more limited decrease of potential after 24 h operation for Ni-P/BC (~100 mV) than Pt/C (~310 mV). The cause of the dramatic deactivation of Pt/C is that phosphoric acid anions from PBS in the electrolyte can poison Pt [47]. Ni-P instead displays more robust in this neutral electrolyte.

Figure 6.17. (a) HER polarization curves of bare carbon paper and Pt/C. (b) Chronopotentiometry curves of Ni-P/BC and Pt/C at 10 mA cm^{-2}.

6.5 Conclusions

In summary, a highly active freestanding and binder-free Ni-P hydrogen evolution catalyst supported on BC was obtained by electroless deposition on BC. In terms of mechanical properties, pristine BC 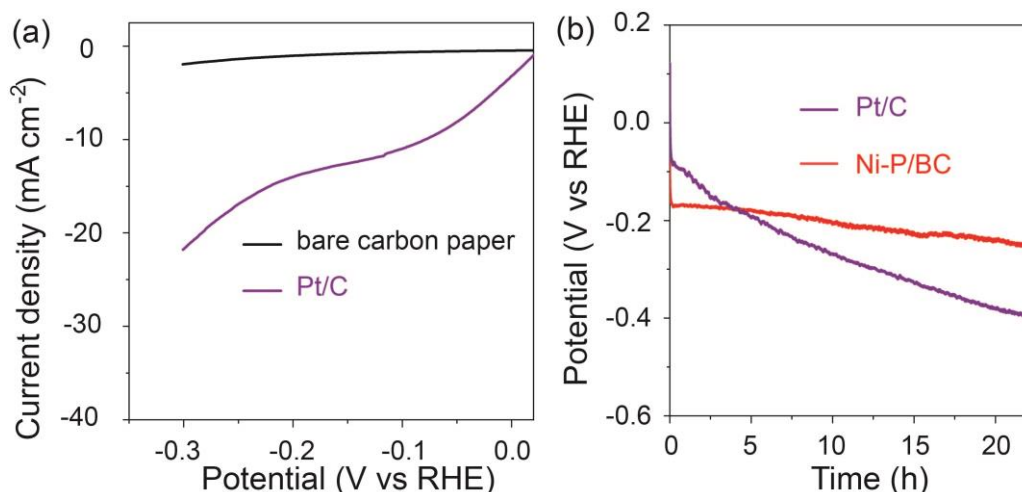presents fascinating outstanding performance advantages over carbonized BC. The deposition of Ni-P enables its use as an electrode substrate. It provides the required electric conductivity that is conventionally given by carbon supports or additives. This simple strategy based on pristine BC to obtain small particles is more convenient than traditional ways using end-capping reagents or expensive organic precursors [48-50]. This can simplify the electrode preparation and decrease its cost. Furthermore, Ni-P itself is a HER catalyst. Thus, *in situ* growth of Ni-P on BC not only offers advantages of both Ni-P and BC, but also casts off the reliance on binders. This novel Ni-P/BC catalyst working with a neutral electrolyte demonstrates superior HER efficiency with a lower overpotential (161 mV) as compared to using Ni-P on other substrates such as GFP (201 mV) or FP (252 mV) highlighting the relevance of the specific nanoarchitecture of BC. Fibers of small diameter are beneficial to form small-size particles leading to a more extended catalytic active area. However, the outstanding performance also relies on the electronic structure of the active sites. This is proven by the increased performance of

Ni-P, where a partial electron transfer from Ni to P occurs, compared with Ni-B, where the transfer is from B to Ni. In a neutral phosphate buffer, not only Ni-P/BC outperforms many reported non-precious metal HER electrodes, but it even shows better stability than Pt/C. Considering the texture and conductivity of Ni-P/BC, our strategy based on an electroless deposition process can also be promising in other energy conversion and storage applications, such as water splitting, metal-air batteries and supercapacitors.

6.6 References

[1] Q. Xie, Z. Wang, L. Lin, Y. Shu, J. Zhang, C. Li, Y. Shen, H. Uyama, Nanoscaled and Atomic Ruthenium Electrocatalysts Confined Inside Super-Hydrophilic Carbon Nanofibers for Efficient Hydrogen Evolution Reaction, Small 17(38) (2021) 2102160.

[2] X. Wang, Y. Fei, W. Zhao, Y. Sun, F. Dong, Tailoring unique neural-network-type carbon nanofibers inserted in CoP/NC polyhedra for robust hydrogen evolution reaction, Nanoscale 13(35) (2021) 14705-14712.

[3] Q. Kang, Y. Qin, Q. Lu, F. Gao, Waste leather-derived (Cr, N)-co-doped carbon cloth coupling with Mo2C nanoparticles as a self-supported electrode for highly active hydrogen evolution reaction performances, J. Power Sources 476 (2020) 228706.

[4] Q. Xiong, Y. Wang, P.F. Liu, L.R. Zheng, G. Wang, H.G. Yang, P.K. Wong, H. Zhang, H. Zhao, Cobalt Covalent Doping in MoS_2 to Induce Bifunctionality of Overall Water Splitting, Adv. Mater. 30 (2018) 1801450.

[5] S.-K. Park, J.K. Kim, Y.C. Kang, Amorphous Molybdenum Sulfide on Three-Dimensional Hierarchical Hollow Microspheres Comprising Bamboo-like N-Doped Carbon Nanotubes as a Highly Active Hydrogen Evolution Reaction Catalyst, ACS Sustainable Chem. Eng. 6(10) (2018) 12706-12715.

[6] M. Park, D. Lee, S. Shin, H.J. Kim, J. Hyun, Flexible conductive nanocellulose combined with silicon nanoparticles and polyaniline, Carbohydr. Polym. 140 (2016) 43-50.

[7] X. Huang, X. Xu, C. Li, D. Wu, D. Cheng, D. Cao, Vertical CoP Nanoarray Wrapped by N,P-Doped Carbon for Hydrogen Evolution Reaction in Both Acidic and Alkaline Conditions, Adv. Energy Mater. 9(22) (2019) 1803970.

[8] D. Shin, H.J. Kim, M. Kim, D. Shin, H. Kim, H. Song, S.-I. Choi, $Fe_xNi_{2-x}P$ Alloy Nanocatalysts with Electron-Deficient Phosphorus Enhancing the Hydrogen Evolution Reaction in Acidic Media, ACS Catal. 10(19) (2020) 11665-11673.

[9] B. Lu, Y. Wang, W. Li, S. Song, P. Tian, R. Li, X. Tian, X. Liu, J. Zang, Ni-P alloy@carbon nanotubes immobilized on the framework of Ni foam as a 3D

hierarchical porous self-supporting electrode for hydrogen evolution reaction, Int. J. Hydrogen. Energ 46(45) (2021) 23245-23253.

[10] L. Zhang, P. Zhu, F. Zhou, W. Zeng, H. Su, G. Li, J. Gao, R. Sun, C.P. Wong, Flexible Asymmetrical Solid-State Supercapacitors Based on Laboratory Filter Paper, ACS Nano 10(1) (2016) 1273-82.

[11] D. Wang, Y. Zhang, X. Lu, Z. Ma, C. Xie, Z. Zheng, Chemical formation of soft metal electrodes for flexible and wearable electronics, Chem. Soc. Rev. 47(12) (2018) 4611-4641.

[12] M. Zeng, A. Laromaine, A. Roig, Bacterial cellulose films: influence of bacterial strain and drying route on film properties, Cellulose 21(6) (2014) 4455-4469.

[13] Y. Yamauchi, T. Momma, T. Yokoshima, K. Kuroda, T. Osaka, Highly ordered mesostructured Ni particles prepared from lyotropic liquid crystals by electroless deposition: the effect of reducing agents on the ordering of mesostructure, J. Mater. Chem. 15(20) (2005) 1987-1994.

[14] Q. Yang, C. Lv, Z. Huang, C. Zhang, Amorphous film of ternary Ni-Co-P alloy on Ni foam for efficient hydrogen evolution by electroless deposition, Int. J. Hydrogen. Energ 43(16) (2018) 7872-7880.

[15] W. Hao, R. Wu, H. Huang, X. Ou, L. Wang, D. Sun, X. Ma, Y. Guo, Fabrication of practical catalytic electrodes using insulating and eco-friendly substrates for overall water splitting, Energy Environ. Sci. 13(1) (2020) 102-110.

[16] A. Sedighi, M. Montazer, S. Mazinani, Synthesis of wearable and flexible $NiP_{0.1}$-SnO_x/PANI/CuO/cotton towards a non-enzymatic glucose sensor, Biosens. Bioelectron. 135 (2019) 192-199.

[17] W. Tang, X. Liu, Y. Li, Y. Pu, Y. Lu, Z. Song, Q. Wang, R. Yu, J. Shui, Boosting electrocatalytic water splitting via metal-metalloid combined modulation in quaternary Ni-Fe-P-B amorphous compound, Nano Res. 13(2) (2020) 447-454.

[18] S. He, Z. Li, H. Mi, C. Ji, F. Guo, X. Zhang, Z. Li, Q. Du, J. Qiu, 3D nickel-cobalt phosphide heterostructure for high-performance solid-state hybrid supercapacitors, J. Power Sources 467 (2020) 228324.

[19] P. Zhang, M. Wang, Y. Yang, T. Yao, H. Han, L. Sun, Electroless plated Ni-B

films as highly active electrocatalysts for hydrogen production from water over a wide pH range, Nano Energy 19 (2016) 98-107.

[20] Y. Wei, P. Zou, Y. Yue, M. Wang, W. Fu, S. Si, L. Wei, X. Zhao, G. Hu, H.L. Xin, One-Pot Synthesis of B/P-Codoped Co-Mo Dual-Nanowafer Electrocatalysts for Overall Water Splitting, ACS Appl. Mater. Interfaces 13(17) (2021) 20024-20033.

[21] A. Chunduri, S. Gupta, O. Bapat, A. Bhide, R. Fernandes, M.K. Patel, V. Bambole, A. Miotello, N. Patel, A unique amorphous cobalt-phosphide-boride bifunctional electrocatalyst for enhanced alkaline water-splitting, Appl. Catal., B 259 (2019) 118051.

[22] Q. Liu, H. Zhao, M. Jiang, Q. Kang, W. Zhou, P. Wang, F. Zhou, Boron enhances oxygen evolution reaction activity over Ni foam-supported iron boride nanowires, J. Mater. Chem. A. 8(27) (2020) 13638-13645.

[23] H. Li, H. Li, W.-L. Dai, W. Wang, J.-F. Deng, XPS studies on surface electronic characteristics of Ni-B and Ni-P amorphous alloy and its correlation to their catalytic properties, Appl. Surf. Sci. 152 (1999) 25-34.

[24] L. Wan, Y. Wang, Y. Zhang, C. Du, J. Chen, Z. Tian, M. Xie, FeCoP nanosheets@Ni-Co carbonate hydroxide nanoneedles as free-standing electrode material for hybrid supercapacitors, Chem. Eng. J. 415 (2021) 128995.

[25] Q. Liu, J. Tian, W. Cui, P. Jiang, N. Cheng, A.M. Asiri, X. Sun, Carbon nanotubes decorated with CoP nanocrystals: a highly active non-noble-metal nanohybrid electrocatalyst for hydrogen evolution, Angew. Chem. Int. Edit. 53(26) (2014) 6710-4.

[26] K. Wang, K. Sun, T. Yu, X. Liu, G. Wang, L. Jiang, G. Xie, Facile synthesis of nanoporous Ni–Fe–P bifunctional catalysts with high performance for overall water splitting, J. Mater. Chem. A. 7(6) (2019) 2518-2523.

[27] F. Li, Y. Li, Q. Zhuo, D. Zhou, Y. Zhao, Z. Zhao, X. Wu, Y. Shan, L. Sun, Electroless Plating of NiFeP Alloy on the Surface of Silicon Photoanode for Efficient Photoelectrochemical Water Oxidation, ACS Appl. Mater. Interfaces 12(10) (2020) 11479-11488.

[28] X. Li, L. Zhang, Z. Wang, S. Wu, J. Ma, Cellulose controlled zinc oxide

nanoparticles with adjustable morphology and their photocatalytic performances, Carbohydr. Polym. 259 (2021) 117752.

[29] W. Hao, R. Wu, R. Zhang, Y. Ha, Z. Chen, L. Wang, Y. Yang, X. Ma, D. Sun, F. Fang, Y. Guo, Electroless Plating of Highly Efficient Bifunctional Boride-Based Electrodes toward Practical Overall Water Splitting, Adv. Energy Mater. 8(26) (2018) 1801372.

[30] J. Huang, Y. Su, Y. Zhang, W. Wu, C. Wu, Y. Sun, R. Lu, G. Zou, Y. Li, J. Xiong, FeOx/FeP hybrid nanorods neutral hydrogen evolution electrocatalysis: insight into interface, J. Mater. Chem. A. 6(20) (2018) 9467-9472.

[31] X. Chen, D. Wang, Z. Wang, P. Zhou, Z. Wu, F. Jiang, Molybdenum phosphide: a new highly efficient catalyst for the electrochemical hydrogen evolution reaction, Chem. Commun. 50(79) (2014) 11683-11685.

[32] D. Liu, X. Li, S. Chen, H. Yan, C. Wang, C. Wu, Y.A. Haleem, S. Duan, J. Lu, B. Ge, P.M. Ajayan, Y. Luo, J. Jiang, L. Song, Atomically dispersed platinum supported on curved carbon supports for efficient electrocatalytic hydrogen evolution, Nat. Energy 4(6) (2019) 512-518.

[33] X. Xie, M. Song, L. Wang, M.H. Engelhard, L. Luo, A. Miller, Y. Zhang, L. Du, H. Pan, Z. Nie, Y. Chu, L. Estevez, Z. Wei, H. Liu, C. Wang, D. Li, Y. Shao, Electrocatalytic Hydrogen Evolution in Neutral pH Solutions: Dual-Phase Synergy, ACS Catal. 9(9) (2019) 8712-8718.

[34] L. Ren, D. Yang, J.-H. Yang, Ruthenium-manganese phosphide nanohybrid supported on graphene for efficient hydrogen evolution reaction in acid and alkaline conditions, Int. J. Hydrogen. Energ 47(29) (2022) 13876-13886.

[35] H. Li, S. Lu, J. Sun, J. Pei, D. Liu, Y. Xue, J. Mao, W. Zhu, Z. Zhuang, Phase-Controlled Synthesis of Nickel Phosphide Nanocrystals and Their Electrocatalytic Performance for the Hydrogen Evolution Reaction, Chem. Eur. J. 24(45) (2018) 11748-11754.

[36] S. Shen, Z. Lin, K. Song, Z. Wang, L. Huang, L. Yan, F. Meng, Q. Zhang, L. Gu, W. Zhong, Reversed Active Sites Boost the Intrinsic Activity of Graphene-like Cobalt Selenide for Hydrogen Evolution, Angew. Chem. Int. Edit. 60(22) (2021)

12360-12365.

[37] K. Wu, K. Sun, S. Liu, W.-C. Cheong, Z. Chen, C. Zhang, Y. Pan, Y. Cheng, Z. Zhuang, X. Wei, Y. Wang, L. Zheng, Q. Zhang, D. Wang, Q. Peng, C. Chen, Y. Li, Atomically dispersed Ni-Ru-P interface sites for high-efficiency pH-universal electrocatalysis of hydrogen evolution, Nano Energy 80 (2021) 105467.

[38] M. Chen, J. Qi, W. Zhang, R. Cao, Electrosynthesis of NiP_x nanospheres for electrocatalytic hydrogen evolution from a neutral aqueous solution, Chem. Commun. 53(40) (2017) 5507-5510.

[39] R. Wu, B. Xiao, Q. Gao, Y.R. Zheng, X.S. Zheng, J.F. Zhu, M.R. Gao, S.H. Yu, A Janus Nickel Cobalt Phosphide Catalyst for High-Efficiency Neutral-pH Water Splitting, Angew. Chem. Int. Edit. 57(47) (2018) 15445-15449.

[40] Y. Ding, B.-Q. Miao, Y.-C. Jiang, H.-C. Yao, X.-F. Li, Y. Chen, Polyethylenimine-modified nickel phosphide nanosheets: interfacial protons boost the hydrogen evolution reaction, J. Mater. Chem. A. 7(22) (2019) 13770-13776.

[41] Z. Pu, S. Wei, Z. Chen, S. Mu, Flexible molybdenum phosphide nanosheet array electrodes for hydrogen evolution reaction in a wide pH range, Appl. Catal., B 196 (2016) 193-198.

[42] W. He, R. Ifraemov, A. Raslin, I. Hod, Room-Temperature Electrochemical Conversion of Metal-Organic Frameworks into Porous Amorphous Metal Sulfides with Tailored Composition and Hydrogen Evolution Activity, Adv. Funct. Mater. 28(18) (2018) 1707244.

[43] X. Ren, D. Wu, R. Ge, X. Sun, H. Ma, T. Yan, Y. Zhang, B. Du, Q. Wei, L. Chen, Self-supported $CoMoS_4$ nanosheet array as an efficient catalyst for hydrogen evolution reaction at neutral pH, Nano Res. 11(4) (2018) 2024-2033.

[44] L.L. Feng, G. Yu, Y. Wu, G.D. Li, H. Li, Y. Sun, T. Asefa, W. Chen, X. Zou, High-index faceted Ni_3S_2 nanosheet arrays as highly active and ultrastable electrocatalysts for water splitting, J. Am. Chem. Soc. 137(44) (2015) 14023-6.

[45] X. Gao, Y. Chen, T. Sun, J. Huang, W. Zhang, Q. Wang, R. Cao, Karst landform-featured monolithic electrode for water electrolysis in neutral media, Energy Environ. Sci. 13(1) (2020) 174-182.

[46] H. Liu, P. He, S. Wang, J. Gao, L. Zhou, C. Li, Y. Zhang, D. Yang, M. He, L. Jia, F. Dong, H. Liu, Facile one-step fabrication of bimetallic Co–Ni–P hollow nanospheres anchored on reduced graphene oxide as highly efficient electrocatalyst for hydrogen evolution reaction, Int. J. Hydrogen. Energ 44(44) (2019) 24140-24150.

[47] Y. Tan, M. Luo, P. Liu, C. Cheng, J. Han, K. Watanabe, M. Chen, Three-Dimensional Nanoporous $Co_9S_4P_4$ Pentlandite as a Bifunctional Electrocatalyst for Overall Neutral Water Splitting, ACS Appl. Mater. Interfaces 11(4) (2019) 3880-3888.

[48] D.-H. Ha, B. Han, M. Risch, L. Giordano, K.P.C. Yao, P. Karayaylali, Y. Shao-Horn, Activity and stability of cobalt phosphides for hydrogen evolution upon water splitting, Nano Energy 29 (2016) 37-45.

[49] T. Meng, Y.N. Hao, L. Zheng, M. Cao, Organophosphoric acid-derived CoP quantum dots@S,N-codoped graphite carbon as a trifunctional electrocatalyst for overall water splitting and Zn-air batteries, Nanoscale 10(30) (2018) 14613-14626.

[50] H. Li, P. Wen, D.S. Itanze, M.W. Kim, S. Adhikari, C. Lu, L. Jiang, Y. Qiu, S.M. Geyer, Phosphorus-Rich Colloidal Cobalt Diphosphide (CoP_2) Nanocrystals for Electrochemical and Photoelectrochemical Hydrogen Evolution, Adv. Mater. 31(24) (2019) 1900813.

Chapter 7 General conclusions and future prospects

7.1 General conclusions

This thesis mainly focuses on employing BC as a scaffold to fabricate electrodes for the application in electrochemical energy storage and conversion including $Li-O_2$ battery, Zn ion battery and hydrogen evolution reaction. The microstructure of BC is highly advantageous for these energy applications where high currents or low polarizations are required. This is essentially achieved by making well conducting electrodes with high area and good porosity allowing a fast transport of electroactive species and, when necessary (e.g., Li_2O_2 and MnO_2), a significant volume for their storage. Thus, the main challenge has been to transform the ideal nanofiber architecture into a still nanostructured material, but sufficiently conductive. Each obtained materials have been directed to specific applications:

1. A modified carbonization that obviates the densification usually occurring during drying, so that an open porous structure is still obtained. BC was treated with alcohol and a loose structure of BC can be obtained after oven drying, facilitating to produce carbons with high porosity. The high pore volume of 1-butanol-treated BC has been exploited for cathodes with high capacity in $Li-O_2$ battery.

2. A urea assisted carbonization that induces unexpected N doping carbon nanosheet and porous structure. Owing to the porous structure and conductivity of carbon, the obtained N-doped carbon nanosheet/MnO_2 demonstrates high performance of ZIB, greatly surpassing commercial MnO_2.

3. A metal coating process known in the industry. Robust HER electrodes made of nickel-phosphorous (Ni-P) with excellent conductivity and good HER performance were obtained from BC by electroless deposition. Ni-P/BC demonstrates outstanding HER activity with a low overpotential and good stability in neutral electrolyte.

These methods to obtain conductive BC-based electrodes are facile, sustainable

and economic, being viable for the application in electrochemical energy storage and conversion.

7.2 Future prospects

The simple and effective preparations that have been developed in this thesis, as well as the encouraging properties deserve further optimization and upscaling work to provide solutions with impact in the market and in society. Indeed, the applications of BC presented here represent just a tiny sample of the broad range of possibilities that BC has demonstrated in literature. There is still great potential for exploiting BC in many applications. For example:

1. The developed carbons can be exploited for Li-S batteries, supercapacitors and sensors. The porous structure of BC is beneficial to combine with active materials for fabricating sensing materials.

2. N-doped carbon nanosheets could be used to form composites with many other compounds to improve their electrical conductivity (such as Fe_3O_4, Co_3O_4, V_2O_5, $LiCoO_2$, $LiMn_2O_4$, etc.), which can be relevant in batteries, catalysis, and other applications.

3. Ni-P and other conductive materials that may be deposited on BC successfully can be used to fabricate binder-free electrodes for flexible energy storage devices and flexible electronics.

Appendix: publications

1. Nanoarchitectonics of bacterial cellulose with nickel-phosphorous alloy as a binder-free electrode for efficient hydrogen evolution reaction in neutral solution

Wenhai Wang, Siavash Khabazian, Marina Casas Papiol, Soledad Roig-Sanchez, Anna Laromaine, Anna Roig, Dino Tonti

International Journal of Hydrogen Energy, 2022, accepted.

2. Facile preparation of glycine-based mesoporous graphitic carbons with embedded cobalt nanoparticles,

Wenhai Wang, Alvaro Y. Tesio, Mara Olivares-Marín, Pedro Gómez Romero, Dino Tonti

Journal of Materials Science, 57 (2022) 13403-13413.

3. Carbons derived from alcohol-treated bacterial cellulose with optimal porosity for Li-O$_2$ batteries

Wenhai Wang, Siavash Khabazian, Marina Casas Papiol, Soledad Roig-Sanchez, Anna Laromaine, Anna Roig, Dino Tonti

Renewable Energy, 17 (2021) 209-215.

4. High performance N-doped carbon nanosheet/MnO$_2$ cathode derived from bacterial cellulose for aqueous Zn-ion batteries

Wenhai Wang, Ashley P. Black, Cheng Liu, Vlad Martin-Diaconescu, Laura Simonelli, Anna Laromaine, Anna Roig, Dino Tonti

In preparation.

Composites & nanocomposites

Facile preparation of glycine-based mesoporous graphitic carbons with embedded cobalt nanoparticles

Wenhai Wang[1], Alvaro Y. Tesio[2], Mara Olivares-Marín[3,*], Pedro Gómez Romero[4], and Dino Tonti[1,*]

[1] *Institut de Ciència de Materials de Barcelona (ICMAB), Consejo Superior de Investigaciones Científicas (CSIC), Campus UAB, 08193 Bellaterra, Barcelona, Spain*

[2] *Centro de Investigación y Desarrollo en Materiales Avanzados y Almacenamiento de Energía de Jujuy CIDMEJu (CONICET, Universidad Nacional de Jujuy), Centro de Desarrollo Tecnológico General Savio, 4612 Palpalá, Jujuy, Argentina*

[3] *Departamento de Ingeniería Mecánica, Energética y de los Materiales, Centro Universitario de Mérida, Universidad de Extremadura, 06800 Mérida, Spain*

[4] *Catalan Institute of Nanoscience and Nanotechnology (ICN2), The Barcelona Institute of Science and Technology (CSIC-BIST), Campus UAB, 08193 Bellaterra, Barcelona, Spain*

ABSTRACT

A simple route has been developed for the preparation of mesoporous graphitic carbons with embedded cobalt nanoparticles just using glycine as a nitrogen source, cobalt nitrate and distilled water. After heating the mixture to 300 °C under magnetic stirring, a dry solid product was obtained, which was then carbonized at 900 °C under argon atmosphere. Changing the glycine/Co molar ratio allowed controlling the size of the cobalt particles and their dispersion in the carbon matrix, the porosity of the carbon and its graphitic character. The carbon–metal composites obtained were tested as oxygen cathodes in Li–O$_2$ batteries. Cells assembled exhibited a full discharge capacity up to 2.19 mAh cm^{-2} at a current of 0.05 mA cm^{-2} and over 39 cycles at a cutoff capacity of 0.5 mAh cm^{-2}. This work provides a green, feasible and simple way to prepare mesoporous graphitic carbons with embedded cobalt nanoparticles without involving templates.

🙋 Springer

GRAPHICAL ABSTRACT
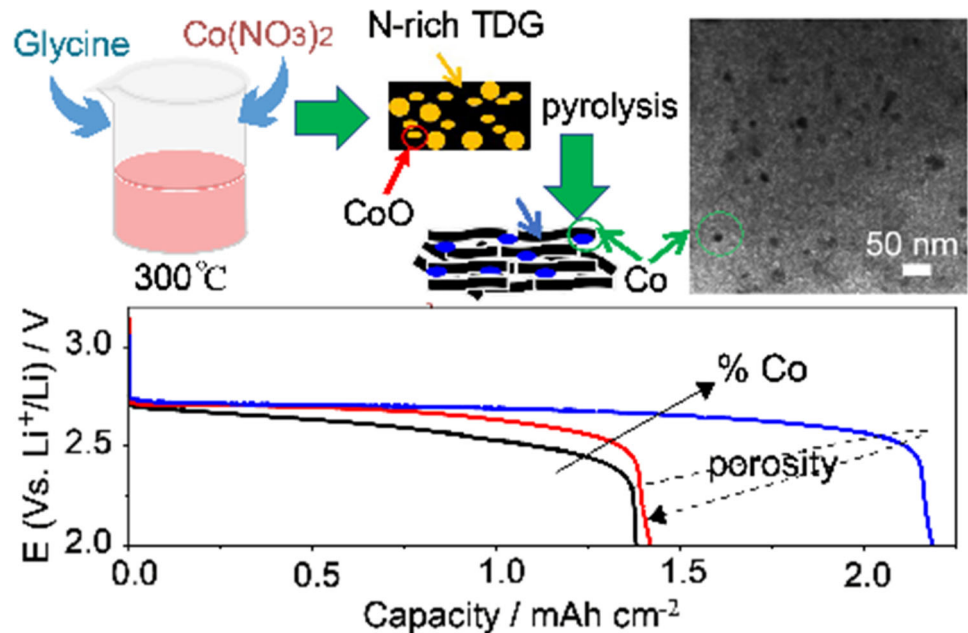
Introduction

In the global challenge of developing more efficient and ecofriendly energy systems, lithium-ion batteries have historically attracted the greatest interest, but today searching for higher energy density, a series of batteries known as "new generation batteries" are emerging. Among them lithium–oxygen battery (Li–O$_2$) stands out in terms of its energy density [1, 2]. In recent years, the study of various aspects of the non-aqueous Li–O$_2$ battery has been intensified, covering the stability of the electrolytes, solvents, cathode materials used and the problems derived from the charge/discharge reversibility of the battery (specially the oxidation of ORR products). During the discharge process, O$_2$ is reduced by a series of mechanisms strongly dependent on current density [3], solvent [4] and nature of the cathode [5] until it forms (mainly) insoluble and insulating Li$_2$O$_2$ [6]. However, the loss of capacity and the low cyclability that these batteries present is due to the oxygen species [7, 8] produced in the oxygen reduction and evolution reactions, which are highly reactive and

produce parasitic reactions, which decompose the components of the cell [9] such as the cathode [10] and the electrolyte [11].

Without any doubt, one of the most important aspects to developing a Li–O$_2$ battery is the oxygen cathode. For a Li–O$_2$ battery, this must fulfill a series of requirements, such as high oxygen permeability, excellent conductivity and catalysis of the oxygen redox reaction. Several non-carbonaceous materials are currently being studied to be used as cathodes [12, 13]. Nonetheless, carbon-based materials remain the most studied materials for cathode application in Li–O$_2$ batteries, in spite of having many known issues [5].

The known catalytic effect of cobalt has been introduced in Li–O$_2$ batteries as redox mediators [14, 15], carbon-free cathodes [16, 17] and carbon cathodes [18, 19]. Among the latter, porous carbons with embedded cobalt and cobalt oxide nanoparticles have been widely investigated in the field of energy conversion and storage: lithium-ion batteries [20, 21] lithium–sulfur batteries [22, 23] and Li–O$_2$ batteries [24, 25]; these last were mainly motivated by their ORR and OER catalytic activity [26]. In fact, it has

been reported that Co nanoparticles embedded in carbon nanostructures can reduce the charge and discharge polarization of Li–O_2 batteries extending its lifetime [27]. Indeed, it can also reduce the charge overvoltage by forming easily decomposable amorphous Li_2O_2 [27].

Several methods have been already proposed for synthesizing Co/porous carbons composites employing numerous carbon precursors, cobalt sources and experimental methods (see Table S1 in Supplementary material). Most of these methods suffer from need of expensive organic precursors (such as cobalt acetylacetonate and potassium hexacyanocobaltate), complicated processing (such as silica, or carbonates as templates) and careful washing. The table below summarizes the strategies used to obtain the Co-carbon composites used for oxygen redox.

Taking into account all the above, in search of a simpler and more sustainable route, we report herein a synthesis process to prepare mesoporous graphitic carbons with embedded cobalt particles to be used as cathodes in Li–O_2 batteries. The synthesis involved the use of commercial glycine, cobalt nitrate and distilled water. Glycine has been used elsewhere as a reducing fuel for the synthesis of ultraporous metals by a simple combustion reaction [28]. We performed an extensive composition and morphology characterization of these materials, named GX–Co–T (where X represents the glycine amount in the molar ratio G/CoN), and we studied the electrochemical properties. Both the morphological characteristics and the electrochemical behavior of the materials strongly varied depending on the preparation conditions and the amount of Co added. Cells assembled with G6–Co–T delivered a full discharge capacity up to 2.19 mAh cm^{-2} at a current of 0.05 mAh cm^{-2} over 39 cycles without any capacity loss at a cutoff capacity of 0.5 mAh cm^{-2}.

Experimental sections

Synthesis of MGC-Co

Mesoporous graphitic carbons with embedded cobalt nanoparticles (MGC–Co) were prepared by using a two-step simple method with commercial powdered glycine (glycine for synthesis, CAS number 56-40-6, Sigma-Aldrich) and cobalt (II) nitrate hexahydrate

(CoN, Co(NO$_3$)$_2$· 6H$_2$O, ACS reagent, ≥ 98%, CAS 10026–22-9, Sigma-Aldrich). The schematic illustration of the synthesis is shown in Scheme 1. Briefly, glycine powder was dissolved in deionized water under stirring using a PYREX® beaker. Subsequently, an amount of CoN was added to the previous solution until it was completely dissolved. Glycine/CoN molar ratios employed are shown in Table S2. Then, the solution was heated up to 300 °C within the same beaker on a digital hot plate stirrer until a brown dark residue was developed, and the release of vapors ended. This step ensured a good dispersion of nitrates in the matrix of the carbon precursor. The nitrogen-rich, thermally decomposed glycine (N-rich TDG) obtained was cooled at room temperature and subsequently carbonized in a tubular furnace at 900 °C under Ar atmosphere for 1 h using a heating rate of 10 °C/min. Before characterization, the carbonized products were grinded in an agate mortar and sieved through a 180-mesh. The average carbon yield was around 15 wt.% MGC-Co and was labeled as GX–Co–T, where X represents the glycine amount in the molar ratio G/CoN. For comparison purposes, carbonized glycine (G–T) at 900 °C was also prepared as a bare sample. An overview of the samples prepared is provided in Table S2, which also includes the respective Co contents calculated from the ash residues of thermal gravimetry in air (see below for conditions).

Materials characterization

Thermogravimetric analysis (TGA) was carried out with a simultaneous thermogravimetric analysis (TG)-differential scanning calorimetry/differential thermal analysis (heat flow DSC /DTA) system NETZSCH-STA 449 F1 Jupiter. The amount of cobalt incorporated in the carbon materials was analyzed by thermogravimetry from 25 to 900 °C at a heating rate of 5 °C/min under flowing air (80 mL/min). N$_2$ adsorption/desorption experiments were performed at − 196 °C using a Micromeritics ASAP 2020 equipment. Specific surface areas, S_{BET}, were determined by the Brunauer–Emmett–Teller (BET) method. Micropore volumes (V_{mi}) and external surface areas (S_{ext}) were determined by the t-plot method. Total pore volume (V_T) was estimated by the Gurvitsch's rule as the amount adsorbed at a relative pressure of $P/P_0 = 0.995$. Pore size distributions (PSDs) were estimated from the adsorption branches
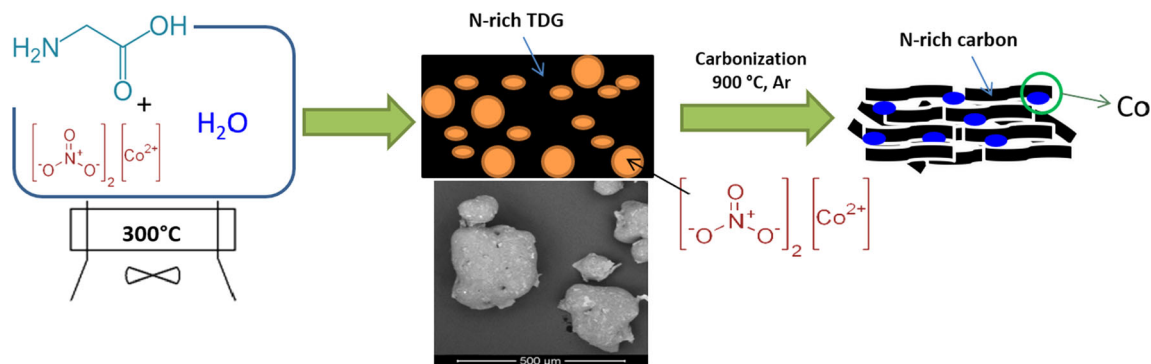
Scheme 1 Synthesis route scheme of mesoporous graphitic carbons with embedded cobalt nanoparticles (MGC-Co).

of the isotherms by the Barrett–Joyner–Halenda (BJH) model. TEM studies were performed with a JEOL (JEM1210) instrument, operating at 100 keV. Before examination, the samples were dispersed in anhydrous ethanol and deposited on a holey carbon film on a copper grid. X-ray diffraction (XRD) patterns at small and wide angles were obtained on a Siemens D5000 instrument operating at 40 kV and 20 mA, using Cu–Ka radiation ($l = 0.15406$ nm). X-ray photoelectron spectroscopy (XPS) measurements were carried out using a SPECS EA10P hemispherical analyzer using a 300 W non-monochromatic X-ray source (Al Kα line with a photon energy of 1486.6 eV).

Electrochemical measurements

As carbon powders, the different MGC-Co samples synthesized here were used after grinding in a mortar and sieving through a 180-mesh. The method used for the preparation of carbon − binder composite electrodes was based on the common procedure in which a carbon powder is mixed with polyvinylidene fluoride (PVDF, Sigma-Aldrich) as a binder and carbon black (Super P, TIMCAL) in the mass ratio of 4:4:2 in N-methyl-2-pyrrolidone (NMP, Sigma-Aldrich, $\geq$ 99.0%). The slurry obtained was used to impregnate a 10-mm-diameter carbon paper (Freudenberg H2315/H23) and finally dried at 80 °C for 25 h. The electrode loading was of the order of 1 mg ($\sim$ 1.3 mg cm^{-2}). Li–O$_2$ battery used consisted of a Teflon homemade cell based on the Giessen battery design [29]. The electrolyte was prepared in a glovebox without exposure to air: 1 M lithium triflate (LiTf, Sigma-Aldrich, 99.995%) dissolved in diethylene glycol dimethyl ether (DEGDME, Sigma-Aldrich, 99.5%). The separator was a 12-mm-diameter glass fiber filter (filterLab MFV1, 260 μm thick) soaked with $\sim$ 100 μl of electrolyte, the anode a 11-mm-diameter Li metal foil (Rockwood Lithium, 0.4 mm thick). All Li–O$_2$ cells were assembled in an argon-filled glove box. Once assembled, the cell was purged with dry pure oxygen for 60 s. Electrochemical tests, such as cyclic voltammetry and galvanostatic charge–discharge measurements, were performed using a MTI BST8-WA battery tester Biologic VMP3. All the tests were done at 25 °C.

Results and discussion

The literature data [30] indicate that glycine decomposes at temperatures between 220 and 280 °C into glycylglycine (dipeptide) and 2,5-piperazinedione. Among others, NH$_3$, H$_2$O and CO$_2$ gases evolve during the decomposition [30, 31]. At the same time, cobalt nitrate can be reduced to CoO, N$_2$O and H$_2$O at around 242 °C [30, 32]. According to that, after this first heating step, the dark product obtained presumably is composed of a complex mixture of glycylglycine (dipeptide), 2,5-piperazinedione and CoO. On the other hand, during the carbonization up to 900 °C, the obtained solid product can decompose releasing CO$_2$, HCNO, HCN [30] and NH$_3$ leading to a N-rich carbonaceous product at the end of the process. At the same time, the carbothermal reduction reaction of CoO to elemental metal occurs at temperatures higher than 800 °C [33] resulting in particles of cobalt embedded in the N-rich carbon matrix. Additionally, these metal particles that emerged could act as catalysts for the conversion of amorphous carbon into more ordered or graphitic carbon [34].

Figure 1 TEM images of G–T and G*X*–Co–T samples.
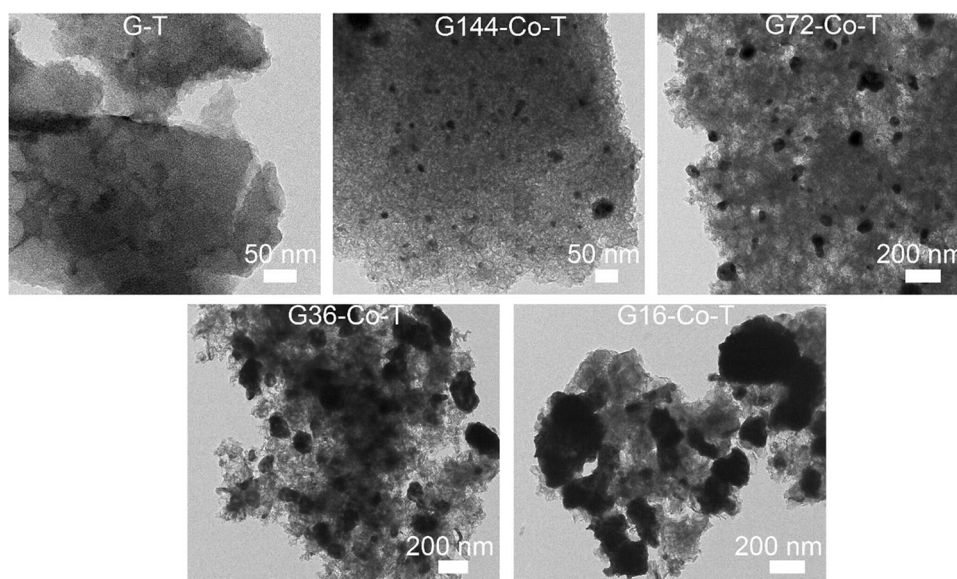
The morphology and structure of samples observed by TEM analysis are shown in Fig. 1. TEM image of carbonized glycine (G–T) revealed a carbonaceous material with a dense structure with low porosity. G*X*–Co-T samples showed clearly embedded cobalt particles within carbon matrix, the sizes and distributions of which are function of G/CoN molar ratio. In addition, all these samples revealed to have certain porosity which are also dependent on cobalt nitrate loading employed during synthesis. For lower G/CoN molar ratios (samples G144–Co–T and G72–Co–T), cobalt particles showed good dispersion and poor agglomeration in the carbon matrix, being the mean Co particle diameter in the range of 50–200 nm. On the other hand, TEM images of samples G36–Co–T, G16–Co–T and G6–Co–T revealed that an increase in the cobalt loading to values higher than 16 wt.% induced the formation of larger cobalt particles (up to about 500 nm) that did not disperse uniformly on the carbon matrix due to a clear agglomeration.

Figure 2a–b shows the N₂ sorption isotherms and the corresponding BJH pore size distributions (PSDs) of G*X*–Co–T samples. Pristine carbon obtained directly from the carbonization of glycine (G–T) was mainly a microporous carbon that shows a type I isotherm. Nevertheless, the addition of CoN influenced the mesostructuration of final products changing their isotherms shape to type II with associated H3-type hysteresis loop that according to the IUPAC classification indicates the presence of non-

rigid aggregates of plate-like particles or assemblies of slit-shaped mesopores [35].

According to textural data calculated from N₂ isotherms (see Table S3), a total pore volume (V_T) maximum is observed with the G36–Co–T (16 wt.% Co), with a V_T 2.3 times compared to pristine carbon G–T. For higher amounts of the experimentally determined Co (and thus of the porogen nitrate precursor), V_T gradually decreased, possibly associated with the high density of Co content and structural degradation (see Fig. 2c). Samples G6–Co–T and G36–Co–T showed clear mesoporous structures compared to pristine carbon. Ordered mesoporous carbons with embedded cobalt nanoparticles made by a novel one-pot laser-assisted approach were reported recently by Chimbeau et al. [35].

The structures of the pristine carbon (G–T) and Co-doped carbons were analyzed by XRD. XRD patterns of samples are shown in Fig. 2d. Sample G–T only presents a weak and broad reflection at around 24° corresponding to the (0 0 2) plane of carbon [36, 37], which indicates a still highly amorphous nature after the thermal treatment. On the other hand, samples prepared using cobalt nitrate showed a diffraction peak at $2\theta = 44.2°$ and $51.5°$ corresponding to (1 1 1) and (2 0 0) crystal planes of metallic cubic cobalt, respectively. On the other hand, traces of CoO can be also observed due to the oxidation of cobalt particles upon to exposure of air at room temperature [38]. In Fig. 2d, it can be appreciated how the (0 0 2) carbon peak becomes increasingly sharper even when the proportion of cobalt in the sample is small. These

Figure 2 **a** Nitrogen adsorption/desorption isotherms of G–T and GX–Co–T samples; **b** pore size distribution curves from the adsorption branches of the isotherms by BJH. **c** Total pore volume vs. experimentally determined Co content in G–T and GX–Co–T samples; **d** XRD patterns of samples G–T and Co-based samples.
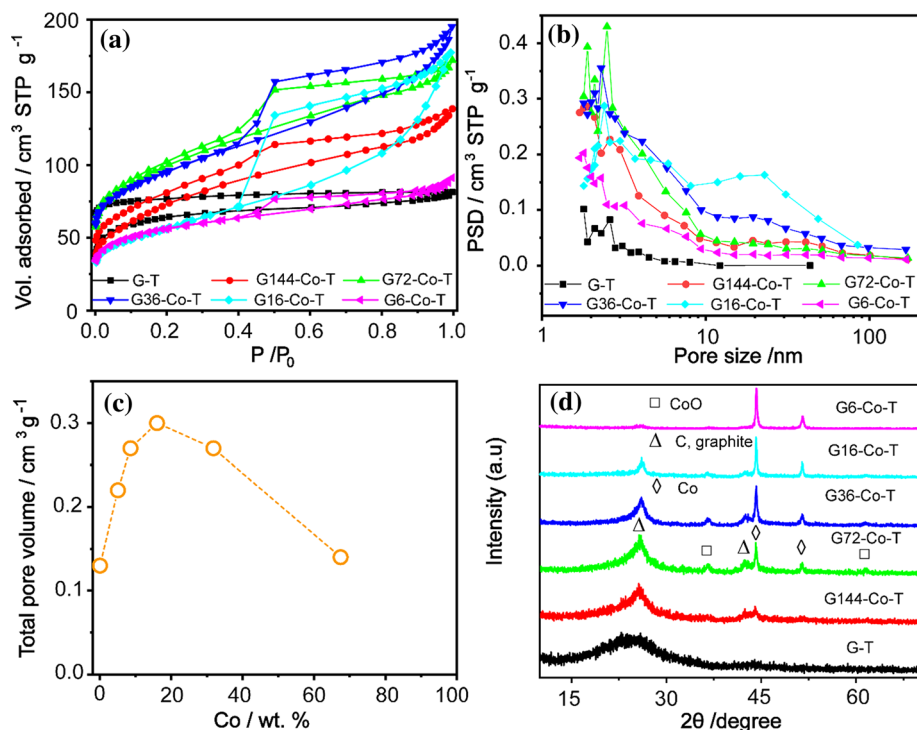
facts corroborate that, as previously reported [34], the formation of metal particles (e.g., Fe, Co and Ni) during carbonization can act as graphitization catalysts at relatively low temperatures. Note that in an uncatalyzed reaction the graphitization process occurs at temperatures above 2000 °C [39].

The XPS spectra in Figure S1 and Fig. 3 show the surface composition of representative samples, which can be qualitatively related to their bulk composition. GT pristine carbon presents a set of peaks corresponding to C 1s (285 eV), N 1s (401 eV) and O 1s (532 eV). Thus, the product obtained directly from the carbonization of glycine (at 900 °C) appears particularly N enriched. C 1 s spectrum can be mainly divided into C–C/C= C (284 eV), C–N (285 eV), C–O (286 eV) and O–C =O (289 eV) [40], which confirms that the carbon is bonded to nitrogen and some oxygen groups. Similarly, the high-resolution N 1 s spectrum can be deconvoluted into pyridinic-N (398 eV), Co–N$_x$ (399 eV), pyrrolic N (400 eV), graphitic N (401 eV) and oxidized N (402 eV) [41, 42]. It is known that pyridinic N and Co–N$_x$ species play an important role for ORR and OER [43]. The total of pyridinic N and Co–N$_x$ of G6–Co–T (37%) is higher than that of G–T (21%) or G36–Co–T (26%) (Table S4). Meanwhile, XPS spectra of samples obtained using cobalt nitrate exhibit in addition new peaks,

corresponding to Co(0), Co(II), Co–N$_x$ and the shake-up satellite peaks [44]. In addition, the O 1s spectra also prove the existence of cobalt oxide. The dominant existence of surface Co^{2+} oxides in the XPS analysis can be attributed to the thin CoO layer shell formed by the exposure of cobalt particles to ambient air [38] given the XPS surface sensitivity.

Cyclic voltammetry (CV) was applied to investigate the electrocatalytic activities of selected Co-based carbons and G–T within the voltage range of 2.0–4.5 V (Fig. 4a). All cathodes exhibit a reduction and an oxidation peak, respectively, ascribed to the formation of Li$_2$O$_2$ and the decomposition of Li$_2$O$_2$, respectively [45]. It is worth noticing that G6–Co–T shows larger ORR and OER peak current than G–T and G36–Co–T, implying its superior ORR and OER activity. Figure 6b shows discharge curves of Li–O$_2$ batteries at 0.05 mA cm^{-2}. The discharge capacity of G6–Co–T electrode (2.19 mAh cm^{-2}) is much higher than that of G–T electrode (1.38 mAh cm^{-2}) and G36–Co–T electrode (1.42 mAh cm^{-2}) consistent with what is expected from the results of the CV. The excellent performance of G6–Co–T electrode can be attributed to its higher pyridinic N and Co–N$_x$ content, providing more active sites for ORR [43], facilitating the formation and better distribution of the discharge products [46].

Figure 3 Deconvoluted XPS spectra C 1s (**a**), N 1s (**b**) Co 2p$_{3/2}$ (**c**) O 1s (**d**) of G–T, G36–Co–T and G6–Co–T.
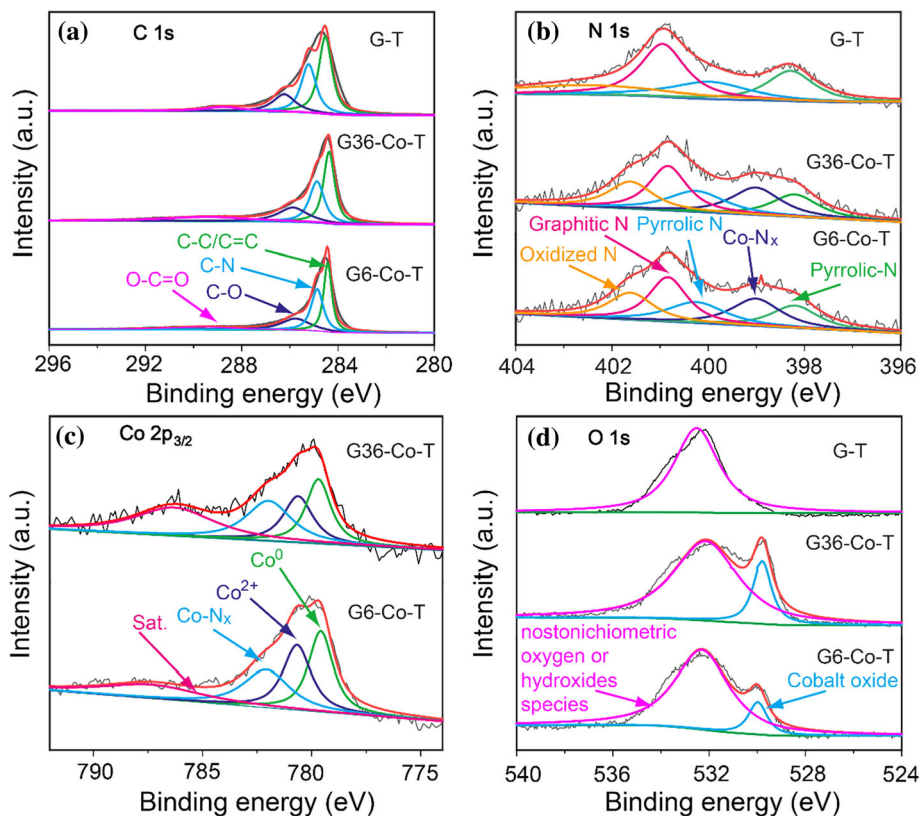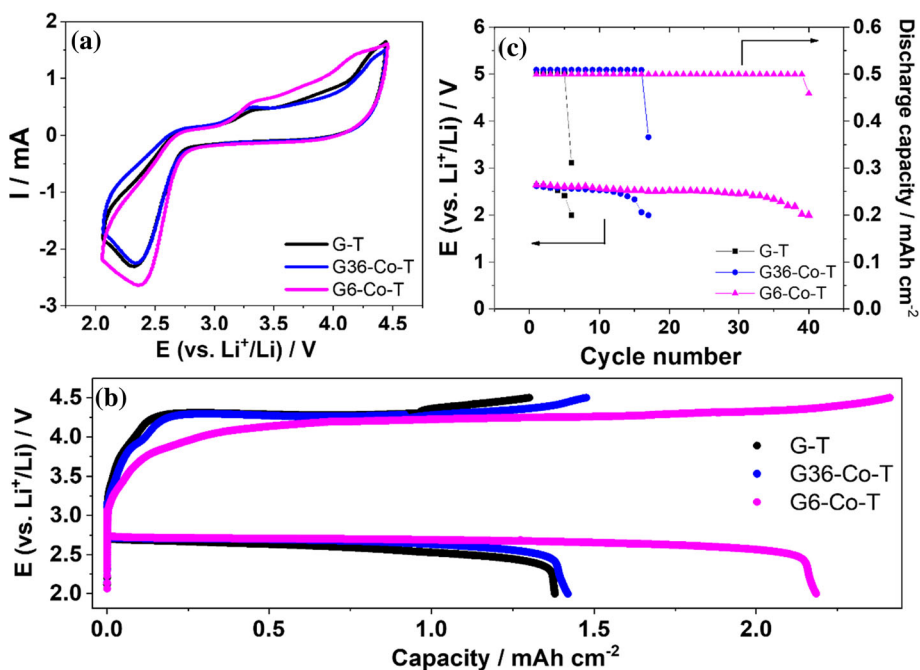

Figure 4 Electrochemical performance of Li –O$_2$ batteries in a 1 M LiTf dissolved in DEGDME electrolyte: **a** CV curves at a scan rate of 20 mV s^{-1}; **b** full discharge–charge profiles at 0.05 mA cm^{-2}; **c** cycling performance with both potential (2.0–4.5 V vs Li$^+$/Li) and capacity (0.5 mAh cm^{-2}) limitations, showing the terminal voltage and capacity for each cycle.

The cycling performance of the cathode with G-6, G6–Co–T and G36–Co–T was evaluated with the limited capacity of 0.5 mAh cm^{-2} at the current density 0.05 mA cm^{-2} (Fig. 4c). G6–Co–T cathode presents an improved cycle stability, proving once again the benefit of this over the other tested materials. There is an evident improvement on the discharge potential between GT and G36–Co–T. Here, the 2.3 times larger total pore volume may allow maintaining electrochemically active surface area, even though clogging occurs finally after discharging a similar capacity. However, when the percentage of Co increases to 67%, the increase in discharge capacity obtained is very evident (more than 50%). Note that in this case, the pore volume is approximately the same (0.13 ∼ 0.14 cm^3 g^{-1}), which justifies that the catalytic effect of the cobalt, together with pyridine nitrogen content added to the increase in the carbon graphitic character, has a more positive effect on the battery discharge than the total pore volume. This catalytic effect could imply a modified discharge mechanism that promotes a more homogeneous distribution of precipitate, which at the same time improves its removal, as confirmed by the enhanced anodic current above 3.2 V vs. Li (Fig. 4a), and by the improved cycle life. The discharge capacity and cycle life of G6–Co–T are comparable to several recently reported cathodes for Li–O$_2$ batteries (Table S5).

Conclusions

A novel and straightforward synthetic procedure is presented here allowing to produce N-enriched mesoporous graphitic carbon materials embedded with cobalt nanoparticles. This material makes use of the porous structure of a carbon with a high degree of graphitization and also takes the advantage of both catalytic effects of the N and the Co. Li–O$_2$ cells assembled with G6–Co–T electrode (Co = 67%) exhibited a full discharge capacity up to 2.19 mAh cm^{-2} at a current of 0.05 mAh cm^{-2} and cycle stability for over 39 cycles without capacity loss at a cutoff capacity of 0.5 mAh cm^{-2}.

The reported route is very simple and avoids the problem of residual templates after the reaction, consequently, eliminates the use of strong acids (i.e., HF) to remove the template. For the fact of not using even a wash of the final product, the waste generation is almost absent. In addition, glycine is an abundant and inexpensive raw material in the chemical industry. Carbon obtained directly from the carbonization of glycine was mainly a microporous carbon with low degree of graphitization but significant N content. However, the addition of cobalt nitrate influenced significantly the structure of final products turning it mesoporous. It is important to mention that even with a low proportion of cobalt a high degree of graphitization at low temperature could be reached. Both the porosity and the Co content could be adjusted with the initial ratio of the reagent concentration. For these reasons, this synthetic route can be considered not only economic but also green and eco-friendly.

Declarations

Conflict of interest The authors declared that they have no conflict of interest.

Supplementary Information: The online version contains supplementary material available at https://doi.org/10.1007/s10853-022-07421-3.

References

[1] Wang H, Wang X, Li M, Zheng L, Guan D, Huang X, Xu J, Yu J (2020) Porous materials applied in nonaqueous Li-O$_2$ batteries: status and perspectives. Adv Mater 32:2002559. https://doi.org/10.1002/adma.202002559

[2] Wang Y, Lu Y-C (2020) Nonaqueous lithium-oxygen batteries: Reaction mechanism and critical open questions. Energy Storage Mater 28:235. https://doi.org/10.1016/j.ensm.2020.03.007

[3] Adams BD, Radtke C, Black R, Trudeau ML, Zaghib K, Nazar LF (2013) Current density dependence of peroxide formation in the Li–O$_2$ battery and its effect on charge. Energy Environ Sci 6:1772. https://doi.org/10.1039/c3ee40697k

[4] Lai J, Liu H, Xing Y, Zhao L, Shang Y, Huang Y, Chen N, Li L, Wu F, Chen R (2021) Local strong solvation electrolyte trade-off between capacity and cycle life of Li-O$_2$ batteries. Adv Funct Mater 31:2101831. https://doi.org/10.1002/adfm.202101831

[5] Balaish M, Jung JW, Kim ID, Ein-Eli Y (2019) A critical review on functionalization of air-cathodes for nonaqueous Li-O$_2$ batteries. Adv Funct Mater 30:1808303. https://doi.org/10.1002/adfm.201808303

[6] Cao D, Yu F, Chen Y, Gao X (2021) Improving the true cycling of redox mediators-assisted Li-O$_2$ Batteries. Energy Environ Mater 4:201. https://doi.org/10.1002/eem2.12185

[7] Mourad E, Petit YK, Spezia R, Samojlov A, Summa FF, Prehal C, Leypold C, Mahne N, Slugovc C, Fontaine O, Brutti S, Freunberger SA (2019) Singlet oxygen from cation driven superoxide disproportionation and consequences for aprotic metal–O$_2$ batteries. Energy Environ Sci 12:2559. https://doi.org/10.1039/c9ee01453e

[8] Lee HW, Kim H, Jung HG, Sun YK, Kwak WJ (2021) Ambilaterality of redox mediators towards ^{1}O$_2$ in Li-O$_2$ batteries: trap and quencher. Adv Funct Mater 31:2002559. https://doi.org/10.1002/adfm.202102442

[9] Mozhzhukhina N, Marchini F, Torres WR, Tesio AY, Mendez De Leo LP, Williams FJ, Calvo EJ (2017) Insights into dimethyl sulfoxide decomposition in Li-O$_2$ battery: understanding carbon dioxide evolution. Electrochem Commun 80:16. https://doi.org/10.1016/j.elecom.2017.05.004

[10] Dong Q, Yao X, Zhao Y, Qi M, Zhang X, Sun H, He Y, Wang D (2018) Cathodically stable Li-O$_2$ battery operations using water-in-salt electrolyte. Chem 4:1345. https://doi.org/10.1016/j.chempr.2018.02.015

[11] Mehta MR, Knudsen KB, Bennett WR, McCloskey BD, Lawson JW (2021) Li-O$_2$ batteries for high specific power applications: a multiphysics simulation study for a single discharge. J Power Sources 484:229261. https://doi.org/10.1016/j.jpowsour.2020.229261

[12] X Lu, N Sakai, D Tang, X Li, T Taniguchi, R Ma, T Sasaki (2020) CoNiFe layered double hydroxide/RuO$_{2.1}$ nanosheet superlattice as carbon-free electrocatalysts for water splitting and Li-O$_2$ batteries. ACS Appl Mater Interfaces 12: 33083. https://doi.org/10.1021/acsami.0c07656

[13] Xing Y, Chen N, Luo M, Sun Y, Yang Y, Qian J, Li L, Guo S, Chen R, Wu F (2020) Long-life lithium-O$_2$ battery achieved by integrating quasi-solid electrolyte and highly active Pt$_3$Co nanowires catalyst. Energy Storage Mater 24:707. https://doi.org/10.1016/j.ensm.2019.06.008

[14] Blanchard R, Martin V, Mantoux A, Chatenet M (2018) Cobalt porphyrin and Salcomine as novel redox shuttle species to enhance the oxygen evolution reaction in Li O$_2$ batteries. Electrochim Acta 261:384. https://doi.org/10.1016/j.electacta.2017.12.129

[15] Li J, Ding S, Zhang S, Yan W, Ma Z-F, Yuan X, Mai L, Zhang J (2021) Catalytic redox mediators for non-aqueous Li-O$_2$ battery. Energy Storage Mater 43:97. https://doi.org/10.1016/j.ensm.2021.08.036

[16] Qiu X-y, Liu S-j, D-z Xu (2018) Yolk-shell structured Cu$_2$O as a high-performance cathode catalyst for the rechargeable Li-O$_2$ batteries. J Mater Sci 53:1318. https://doi.org/10.1007/s10853-017-1555-y

[17] Qian Z, Li X, Wang L, Wu T, Sun B, Du L, Ma Y, Du C, Zuo P, Yin G (2020) Enabling Highly stable Li–O$_2$ batteries with full discharge–charge capability: the porous binder- and carbon-free IrNi nanosheet cathode. ACS Sustainable Chem Eng 8:16115. https://doi.org/10.1021/acssuschemeng.0c02154

[18] Wang W, Khabazian S, Roig-Sanchez S, Laromaine A, Roig A, Tonti D (2021) Carbons derived from alcohol-treated bacterial cellulose with optimal porosity for Li–O₂ batteries. Renew Energ 177:209. https://doi.org/10.1016/j.renene.2021.05.059

[19] Zhao T, Yao Y, Yuan Y, Wang M, Wu F, Amine K, Lu J (2021) A universal method to fabricating porous carbon for Li-O₂ battery. Nano Energy 82:105782. https://doi.org/10.1016/j.nanoen.2021.105782

[20] Hong SH, Song MY (2018) Syntheses of nano-sized Co-based powders by carbothermal reduction for anode materials of lithium ion batteries. Ceram Int 44:4225. https://doi.org/10.1016/j.ceramint.2017.12.002

[21] Li Q, Wang Y, Yu J, Yuan M, Tan Q, Zhong Z, Su F (2022) High-performance Si-Containing anode materials in lithium-ion batteries: a superstructure of Si@Co–NC composite works effectively. Green Energy Environ 7:116. https://doi.org/10.1016/j.gee.2020.08.007

[22] Wang M, Zhou X, Cai X, Wang H, Fang Y, Zhong X (2020) Hierarchically porous, ultrathin N–doped carbon nanosheets embedded with highly dispersed cobalt nanoparticles as efficient sulfur host for stable lithium–sulfur batteries. J Energy Chem 50:106. https://doi.org/10.1016/j.jechem.2020.03.014

[23] Li J, Chen C, Qin F, Jiang Y, An H, Fang J, Zhang K, Lai Y (2018) Mesoporous Co–N–C composite as a sulfur host for high-capacity and long-life lithium–sulfur batteries. J Mater Sci 53:13143. https://doi.org/10.1007/s10853-018-2566-z

[24] Song J, Lv X, Jiao Y, Wang P, Xu M, Li T, Chen X, Li J, Zhang Z (2018) Catalyst nanoarchitecturing via functionally implanted cobalt nanoparticles in nitrogen doped carbon host for aprotic lithium-oxygen batteries. J Power Sources 394:122. https://doi.org/10.1016/j.jpowsour.2018.05.058

[25] Zhai Y, Wang J, Gao Q, Fan Y, Hou C, Hou Y, Liu H, Shao Q, Wu S, Zhao L, Ding T, Dang F, Guo Z (2019) Highly efficient cobalt nanoparticles anchored porous N-doped carbon nanosheets electrocatalysts for Li–O₂ batteries. J Catal 377:534. https://doi.org/10.1016/j.jcat.2019.07.055

[26] Zhang C, Shu J, Shi S, Nie J, Ma G (2020) Hemp derived N-doped highly porous carbon containing Co nanoparticles as electrocatalyst for oxygen reduction reaction. J Colloid Interface Sci 559:21. https://doi.org/10.1016/j.jcis.2019.09.064

[27] Kim YJ, Lee H, Lee DJ, Park JK, Kim HT (2015) Reduction of charge and discharge polarization by cobalt nanoparticles-embedded carbon nanofibers for Li–O₂ batteries. Chemsuschem 8:2496. https://doi.org/10.1002/cssc.201500520

[28] Gómez-Romero P, Fraile J, Ballesteros B (2013) Fractal porosity in metals synthesized by a simple combustion reaction. RSC Adv 3:2351. https://doi.org/10.1039/c2ra22441k

[29] Bender CL, Hartmann P, Vračar M, Adelhelm P, Janek J (2014) On the thermodynamics, the role of the carbon cathode, and the cycle life of the sodium superoxide (NaO₂) battery. Adv Energy Mater 4:1301863. https://doi.org/10.1002/aenm.201301863

[30] Manukyan KV, Cross A, Roslyakov S, Rouvimov S, Rogachev AS, Wolf EE, Mukasyan AS (2013) Solution combustion synthesis of nano-crystalline metallic materials: mechanistic studies. J Phys Chem C 117:24417. https://doi.org/10.1021/jp408260m

[31] Schaberg A, Wroblowski R, Goertz R (2018) Comparative study of the thermal decomposition behaviour of different amino acids and peptides. J Phys Confer Ser 1107:032013. https://doi.org/10.1088/1742-6596/1107/3/032013

[32] Yuvaraj S, Fan-Yuan L, Tsong-Huei C, Chuin-Tih Y (2003) Thermal decomposition of metal nitrates in air and hydrogen environments. J Phys Chem B 107:1044. https://doi.org/10.1021/jp026961c

[33] L'vov BV (2000) Mechanism of carbothermal reduction of iron, cobalt, nickel and copper oxides. Thermochim Acta 360:109. https://doi.org/10.1016/S0040-6031(00)00540-2

[34] Thambiliyagodage CJ, Ulrich S, Araujo PT, Bakker MG (2018) Catalytic graphitization in nanocast carbon monoliths by iron, cobalt and nickel nanoparticles. Carbon 134:452. https://doi.org/10.1016/j.carbon.2018.04.002

[35] Kim M-Z, Sharma P, Kim Y, Alam SF, Lee HR, Cho CH (2019) One-step template-free hydrothermal synthesis of partially Sr-incorporated hierarchical K-CHA zeolite microspheres. Micropor Mesopor Mat 286:65. https://doi.org/10.1016/j.micromeso.2019.05.007

[36] Yang X, Ding Y, Shen Z, Sun Q, Zheng F, Fong H, Zhu Z, Liu J, Liang J, Wang X (2019) High-strength electrospun carbon nanofibrous mats prepared via rapid stabilization as frameworks for Li-ion battery electrodes. J Mater Sci 54:11574. https://doi.org/10.1007/s10853-019-03698-z

[37] Li D, Han Z, Leng K, Ma S, Wang Y, Bai J (2021) Biomass wood-derived efficient Fe–N–C catalysts for oxygen reduction reaction. J Mater Sci 56:12764. https://doi.org/10.1007/s10853-021-06122-7

[38] Ding S, Xue M, Wu R, Lai Y, Men Y, Kong X, Han L, Han J, Yang W, Yang Y, Du H, Wang C, Yang J (2018) Electron beam reduction induced self-assembly growth of Co/CoO nanocomposite materials. J Alloy Compd 744:615. https://doi.org/10.1016/j.jallcom.2018.02.033

[39] Kinoshita K (1988) Carbon, Electrochemical and Physical Properties. John Wiley & Sons, Chichester, New York, Brisbane, Toronto. https://doi.org/10.1002/bbpc.198800269

[40] Zhang J, Zhu W, Pei Y, Liu Y, Qin Y, Zhang X, Wang Q, Yin Y, Guiver MD (2019) Hierarchically porous Co-N-C cathode catalyst layers for anion exchange membrane fuel cells. Chemsuschem 12:4165. https://doi.org/10.1002/cssc.201901668

[41] Jiang H, Liu Y, Hao J, Wang Y, Li W, Li J (2017) Self-Assembly synthesis of cobalt- and nitrogen-coembedded trumpet flower-like porous carbons for catalytic oxygen reduction in alkaline and acidic media. ACS Sustain Chem Eng 5:5341. https://doi.org/10.1021/acssuschemeng.7b00655

[42] Niu H-J, Wang A-J, Zhang L, Feng J-J (2020) Bioinspired one-step pyrolysis fabrication of 3D Porous Co, N, P-doped carbon nanosheets with enriched CoNx active sites as high-performance bifunctional oxygen electrocatalyst for rechargeable Zn–air battery. ACS Appl Energy Mater 3:2781. https://doi.org/10.1021/acsaem.9b02450

[43] Zhang M, Dai Q, Zheng H, Chen M, Dai L (2018) Novel MOF-derived Co@N-C bifunctional catalysts for highly efficient Zn-air batteries and water splitting. Adv Mater 30:1705431. https://doi.org/10.1002/adma.201705431

[44] Li Y, Mao Z, Wang Q, Li D, Wang R, He B, Gong Y, Wang H (2020) Hollow nanosheet array of phosphorus-anion-decorated cobalt disulfide as an efficient electrocatalyst for overall water splitting. Chem Eng J 390:124556. https://doi.org/10.1016/j.cej.2020.124556

[45] Wang H, Wang H, Huang J, Zhou X, Wu Q, Luo Z, Wang F (2019) Hierarchical mesoporous/macroporous Co-doped NiO nanosheet arrays as free-standing electrode materials for rechargeable Li-O$_2$ batteries. ACS Appl Mater Interfaces 11:44556. https://doi.org/10.1021/acsami.9b13329

[46] Li C, Liu D, Xiao Y, Liu Z, Song L, Zhang Z (2019) Mesoporous Co$_3$O$_4$-rods-entangled carbonized polyaniline nanotubes as an efficient cathode material toward stable lithium–air batteries. ACS Appl Energy Mater 2:2939. https://doi.org/10.1021/acsaem.9b00291
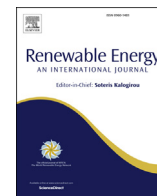
Carbons derived from alcohol-treated bacterial cellulose with optimal porosity for Li–O$_2$ batteries

Wenhai Wang [a], Siavash Khabazian [b], Soledad Roig-Sanchez [a], Anna Laromaine [a], Anna Roig [a], Dino Tonti [a, *]

[a] Institut de Ciència de Materials de Barcelona, ICMAB-CSIC, Campus UAB, 08193, Bellaterra, Spain
[b] Nanomaterials Group, Department of Materials Science and Engineering, Tarbiat Modares University, Tehran, Iran

A B S T R A C T

Porous carbons are important cathode materials for metal-air batteries, but the most usual methods to prepare these porous structures are complex and of high cost. We have prepared porous carbons from bacterial cellulose (BC) hydrogels by a simple water-alcohol solvent exchange before carbonization. Alcohol treatment facilitates looser and more open structures than untreated BC, resulting in porous carbon structures with high surface area, appropriate for electrochemical applications. Used as cathodes in lithium-oxygen batteries, the carbon derived from 1-butanol treated BC has excellent discharge capacity (5.6 mA h cm^{-2}) and good cycle life. This work presents a sustainable, straightforward and fast way to prepare porous carbon materials from BC.

© 2021 The Author(s). Published by Elsevier Ltd. This is an open access article under the CC BY license (http://creativecommons.org/licenses/by/4.0/).

1. Introduction

With the development of society, the demand for energy becomes an urgent need. Many aspects of energy-storage technologies have been explored to facilitate the use of sustainable energy sources [1,2]. Among these technologies, Li–O$_2$ battery has been regarded as one of the most promising, because of its high theoretical energy density of ~3500 Wh kg^{-1} [3]. But there are still numerous issues impeding the utilization of Li–O$_2$ batteries in practical use [4,5]. Owing to their sluggish kinetics, the oxygen reduction reaction (ORR) and the oxygen evolution reaction (OER) show large overpotentials, low energy and coulombic efficiency [6,7]. The performance of a Li–O$_2$ battery relies on the reaction between lithium ion and oxygen. A good cathode should allow the diffusion of lithium ions and oxygen, and also favor the reversible Li$_2$O$_2$ formation and storage during the process of discharge [8,9]. Porous carbons are the most widely used platform for air cathodes [10,11], as they generally offer good conductivity, light weight, large surface area, tunable porosity, and low cost and abundant, often renewable, sources for its production [12,13].

Bacterial cellulose (BC) is a bio-based polymer produced from a microbial fermentation process [14,15], which is employed in a wide range of applications from health to electronics [16,17]. BC as carbon source has raised great attention, owing it to its sustainability, relative low cost, three-dimensional structure, high surface area and accessible porosity [18,19], which are ideal for electrodes in energy storage devices. As-prepared BC is a hydrogel, thus thermal carbonization requires a drying step. The drying route applied considerably modifies the morphology, surface area and porosity of the BC, therefore it can influence the properties of the resulting carbons [20,21]. In fact, when the gel is dried by simple water evaporation in air at room or oven temperature, the strong capillary forces collapse the pores of the cellulose network, which induces fibril aggregation known as hornification, resulting in a low porosity material. Freeze-drying, spray-drying and supercritical drying are often used to hinder hornification [22,23], increasing the surface area of cellulose and producing porous structures.

Such porous cellulose has been successfully employed to produce carbons with a nanofibrous structure that replicates the nanocellulose network [18,24]. However, the drying methods applied are generally time- and energy-consuming and require expensive facilities than simple oven drying. Therefore these methods do not represent a remarkable advantage over more conventional methods to introduce and control porosity of

* Corresponding author.
  E-mail address: dino.t@csic.es (D. Tonti).

biomass-derived carbons, as it is the case of chemical activation by corrosive compounds [25,26], addition of templating agents [27], or hydrothermal synthesis [28]. On the other hand, some authors reported that using compatible solvents with low surface tension, such as alcohols, could relieve the occurrence of a compacted structure's cellulose [29,30].

We show here a facile and low-cost method to prepare porous carbons from food store commercial BC after a simple alcohol treatment. The obtained carbon microstructure is not a replica of the cellulose and suggests some intermediate melting step in the pyrolysis process. Nevertheless, the porosity of carbon derived from alcohol-treated BC is remarkable and used as oxygen cathodes in Li−O$_2$ batteries showed an outstanding capacity and good cycle life. These results not only show a more economic and sustainable route for the preparation of porous carbons, but the striking variations of carbon porosities and electrochemical performance obtained from the same cellulose modified just by controlling fiber aggregation also provide an interesting insight into the carbonization process.

2. Experimental

2.1. Materials

Bacterial cellulose (BC, Q-Phil Products International), methanol (Scharlau), ethanol (99%, Panreac), 1-propanol (99.7%, Sigma Aldrich), 1-butanol (99.5%, Labkem), 1-hexanol (≥99.9%, Sigma Aldrich), 1-octanol (≥99.9%, Sigma Aldrich), ether (≥99.9%, Sigma Aldrich), acetone (99%, Panreac), Tetraethylene glycol dimethyl ether ether (TEGDME, ≥97.0%, Sigma Aldrich), N-methyl-pyrrolidone (NMP, Sigma Aldrich), lithium triflate (99.95%, Sigma-Aldrich), bis(2-methoxy ethyl)ether (Diethylene glycol dimethyl ether, DEGDME, 99.95%, Sigma-Aldrich), polyvinylidene fluoride (PVDF, Sigma-Aldrich), carbon black (Super P, Timcal), lithium foil (Sigma-Aldrich, 0.4 mm thick), carbon paper (Freudenberg, H2315, 210 μm thick), glass fibre filter (PRAT DUMAS, 270 μm thick).

2.2. Preparation of carbons

BC processing: Food-grade BC was in the form of cubes (approx. size 15 × 15 × 15 mm^3) immersed in sucrose syrup. Cubes were drained and placed in Milli-Q water under stirring for 3 h, this process was repeated twice to remove the absorbed syrup and a final step of 12 h. Then, the BC cubes were autoclaved at 120 °C for 20 min. To replace water with other solvents, one piece of BC was pressed by a Teflon cylinder (150 g) for 10 min. The squeezed BC was then soaked in a beaker with 10 mL of a given solvent and stirred for 2 h at room temperature. Afterward, the soaked BC was briefly drained of excess solvent and placed without pressing in an oven to dry (60 °C, 24 h). Finally, dried BC was carbonized in a tubular furnace under an Ar flow of 100 mL min^{-1} with a ramp of 10 °C min^{-1} to 900 °C and kept there for 1 h.

2.3. Characterization

The water and alcohol-soaked BCs, were tested by Fourier transform infrared spectroscopy with attenuated total reflectance (FTIR-ATR). The measurements were carried out by Spectrophotometer Jasco 4700 equipment. The scan range was 400−4000 cm^{-1}. All scanning electron microscopy (SEM) images were obtained by FEI Quanta 200 FEG-ESEM equipment at 15 kV acceleration voltage, 10 mm working distance. Cross-sections were obtained by dipping samples in liquid nitrogen and then, cutting them with a blade. All samples were placed on an aluminum holder with adhesive carbon tape. For transmission electron microscopy (TEM) analysis, samples were sonicated in ethanol for a few

seconds and dropped on carbon-coated copper grids. TEM images were obtained by JEOL JEM1210 TEM with an ORIUS 831 SC 600 (Gatan camera) at 120 kV. N$_2$ adsorption/desorption measurements were conducted by Micromeritics ASAP 2020 equipment. The outgas conditions were at 120 °C for 12 h. The thermal properties of dried BCs were investigated by a TGA-DSC/DTA analyzer (NETZSCH STA 449 F1 Jupiter). The thermal conditions were 10 °C min^{-1} (ramp), 1000 °C (final temperature) and Ar atmosphere. The X-ray diffraction (XRD) patterns of all samples were performed by Siemens D-5000 equipment with Cu K$_α$ radiation. Tests were carried out in a 2θ range of 10−90°. The crystallinity index (CI) of BCs was calculated by the following equation:

CI=(I$_{110}$-I$_{am}$)/I$_{110}$ (1) where I$_{110}$ is the intensity of the peak at 22.5° for the crystalline part of cellulose type I and I$_{am}$ is the intensity of the peak at about 18° for the amorphous part [31].

2.4. Electrochemical performance

A slurry was prepared by gently grinding carbon samples in a mortar and mixing with PVDF (8:2 carbon/PVDF w/w) and few drops NMP. The slurry was then casted on a 10 mm diameter carbon paper (Freudenberg H2315). Then, the coated carbon paper was put in a vacuum oven at 80 °C for 24 h to remove NMP. The mass loading of air cathode is about 1 mg cm^{-2}. The Li−O$_2$ battery is composed of 3 parts, carbon paper, glass fibre filter and Li foil. A 1 M lithium triflate solution in DEGDME was used as the electrolyte. The Li−O$_2$ batteries were assembled in an Ar filled glove box (H$_2$O < 0.1 ppm, O$_2$ < 0.1 ppm). All the tests were carried out in 1 atm dry O$_2$ to avoid the effect of CO$_2$ and humidity. The cycle voltammetry measurements were conducted at a scan rate of 20 mV s^{-1} in the range of 2.0−4.5 V (versus Li/Li$^+$) by a Bio-logic VMP3 multichannel potentiostat. Galvanostatic discharge/charge tests were performed by a battery cycling equipment (MTI BST8-WA).

The estimation of the electrochemical surface area (ECSA) was based on the evaluation of the electrochemical double-layer capacitance and performed in a three-electrode system with a 1 M lithium triflate in DEGDME electrolyte after Ar bubbling. Carbon-coated carbon paper prepared as described above, with a mass loading of about 0.2 mg was used as the working electrode. Platinum wires were used as the counter and the reference electrode. The measurements were conducted at 2 mV s^{-1} in a narrow potential range. The electrochemical double-layer capacitance C$_{EDL}$ was obtained by the following equation [32]:

$$C_{EDL} = \int iVdV/(2vm \triangle V) \qquad (2)$$

where i is the current, V is the potential, m is the mass of carbons, v is the scan rate, ΔV is the potential range. The ECSA is given by the [33]:

ECSA = C$_{EDL}$/C* (3) where C* is the specific capacitance (F m^{-2}) of a bare glassy carbon electrode in the same electrolyte. A C* value of 14.06 μF cm^{-2} was determined by electrochemical impedance spectroscopy (EIS, Fig. S5).

3. Results and discussion

As reported by previous literature [29,30], alcohol treatments contribute to better preserve porous structures in dried cellulose reducing the degree of hornification. We tested several solvents as water replacement of the bacterial cellulose hydrogel, focusing in particular on aliphatic alcohols of different chain lengths, carbonized and tested as electrodes in Li/O$_2$ batteries. As summarized in Table S1, the poorest results are obtained with water, which seems

to confirm the effect of the high surface tension. Other parameters, such as solvent volatility may also play a role in the pore formation and could help explaining differences between alcohols. To better understand the impact that the replacement of water in the hydrogel for an organic solvent we focused on the characterization of the preparative steps of the carbons obtained from untreated (BC-w), ethanol (BC-e) as a reference alcohol treatment and 1-butanol treated cellulose (BC-b) which present the best electro-chemical results. The cleaned, cubic-shaped BC hydrogels were pressed to about 10% of the original height to remove the majority of the entrapped water. Pressed BCs were then soaked in the different alcohols and stirred for 2 h. During this time, the BC cubes swelled to recover more than 90% of the original size in ethanol and more than 70% in the case of 1-butanol. FTIR spectra of soaked BC are similar to those of the pure solvents, which is consistent with complete solvent substitution (Fig. S1a and Figure S1c-d). The alcohol treatment does not chemically alter BCs, according to FTIR spectroscopy of dried BCs (Fig. S1b and Fig. S1c-d). In fact, dried BCs show typical cellulose peaks, which can respectively be ascribed to the stretching vibration of O–H (3350 cm^{-1}), H–C–H (2900 cm^{-1}), C–O–C (1427 cm^{-1}) [34], with no apparent difference between them, which also proves the quantitative solvent removal in the three cases.

The SEM image (Fig. S2) of BC-w shows a smooth surface, which demonstrates that fibrils have compacted. The cross-section SEM images (Fig. 1a–c) show that the layers of BC-w are more densified in comparison with BC-e and BC-b. This confirms that the treatment of ethanol and 1-butanol reduce interfibrillar contraction. The morphology differences between BC-w, BC-e can be attributed to the following factors. On the one hand, the much smaller surface tensions of ethanol and 1-butanol (Table S1), which decrease the capillary force effects as compared to water during the solvent evaporation [29,35]. Low surface tensions of ethanol and 1-butanol

result in weaker capillary forces during the process of drying. The fibrils under weak capillary forces move less than under stronger capillary forces resulting from water, barely changing the distance between fibrils. On the other hand, ethanol and 1-butanol can attach to the surface of fibrils via hydrogen-bond [36,37]. As a consequence, the self-association behavior of fibrils can be limited by the steric hindrance of the aliphatic chains of ethanol and 1-butanol, which act as a spacer. Initially weaker and finally repulsive forces will be present among fibrils, preventing their cohesion. Therefore, highly porous structures can be achieved by ethanol and even more by 1-butanol treatment for BC.

The porous structures of dried BCs were further verified by nitrogen adsorption-desorption measurements (Fig. 1d). All three isotherms present hysteresis and could be considered of mixed type II and IV. Pore size distributions (Fig. 1e) mainly range in the mesoporous region, with a macropore contribution in the case of alcohol-treated samples, while micropores are scarce in all three samples. Dried BC-w presents small area and porosity (BET specific surface area 21 m^2 g^{-1} and cumulative pore volume 0.11 cm^3 g^{-1}, Table 1). In contrast, BC-e and BC-b have respectively over four and five times larger surface areas and pore volumes. These increments agree with the textured structure observed by SEM in BC-e and BC-b. The pore size distributions (Fig. 1e) of all dried BCs are dominated by mesopores, but BC-e and BC-b have larger predominant pore sizes than BC-w.

Powder X-ray diffraction (XRD) was used to study the effect of alcohols on the crystallinity of BCs. Fig. 1g depicts that all BCs show typical pattern peaks (14.5° and 22.5°) of cellulose type I, which correspond to the (100) and (110) lattice planes respectively [39]. Comparing with the crystallinity of BC-w (78%), the crystallinity of BC-e (66%) and BC-b (70%) decreases slightly. The decrease in crystallinity suggests that the cellulose becomes more disordered and loosen, which can be attributed to the effect of dissociation of
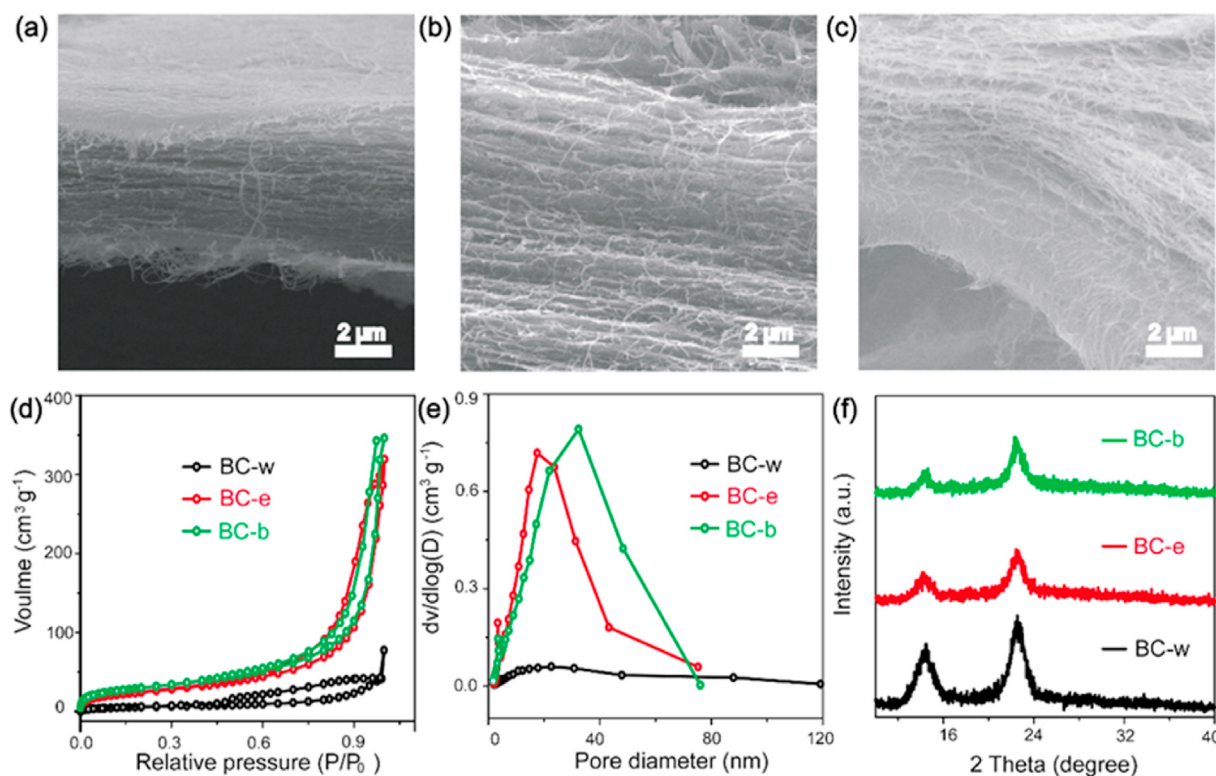

Fig. 1. Characterization of different dried BCs. SEM cross-section images of BC-w (a), BC-e (b) and BC-b (c), nitrogen adsorption–desorption of dried BCs (d), pore size distribution (e), XRD (f).

Table 1
Textural data of samples and the electrochemical surface area (ECSA) of carbons.

Samples	BET surface area (m² g⁻¹)	External surface area (m² g⁻¹)	Pore Volume (cm³ g⁻¹)	Predominant pore size (nm)	ECSA (m² g⁻¹)
Dried	21	18.29	0.11	14	/
BC-w					
Dried BC-e	88	91.83	0.44	17	/
Dried BC-b	107	102.51	0.54	32	/
Carbon-w	1009	153.44	0.19	16	33
Carbon-e	848	142.26	0.41	27	99
Carbon-b	669	237.42	1.25	85	180
Super P [38]	67	70	0.14	40	115

the hydrogen bonds between cellulose [40].

To explore the effect of the fiber aggregation on the carbonization process, all dried BCs were subjected to Thermogravimetric Analysis (TGA) under Ar (Fig. S3a). There are two major mass losses during the temperature ramp. The first small mass loss step (25−100 °C) can be attributed to the evaporation of residual absorbed water [41]. The loss is larger for BC-w (2.5%) than for alcohol-treated samples (0.9% for BC-e and 0.1% for BC-b). This can be considered a proof that a large part of the most tightly bound water molecules was removed during the alcohol treatment. The second mass loss step occurred at 200−400 °C, corresponding to BC decomposition and carbonization. During this step cellulose depolymerizes and fragments on variable molecular weight forms, giving place to char, tar, and volatile compounds (such as water, carbon dioxide and monoxide, acetic acid, and different saccharides) [42]. The yield of these solid, liquid and gaseous fractions has a strong influence on the subsequent carbonization process. The DSC curves (Fig. S3b) indicated that the temperatures for the first major decomposition peaks of BC-e (286 °C) and BC-b (297 °C) are lower than BC-w (322 °C). This can be related to the lower crystallinity of BC-e and BC-b, which can facilitate the degradation process of BCs [43]. In addition, carbon yields (Fig. S3a) of BC-e (9%) and BC-b (10%) are lower than BC-w (14%), probably because of the smaller pores of BC-w. These smaller pores retain more strongly the pyrolysis liquid intermediates, which are also involved in cross-linking and char formation [44]. The impregnation of a less porous system implies a smaller liquid-gas interface and a stronger liquid-solid interaction, reducing the intermediate volatilization and increasing char production, resulting in a larger carbon yield [42,44].

The presence of liquid intermediates is evident from the textures observed after carbonizing dried BCs at 900 °C in Ar. Carbon originated from water-treated BC (carbon-w) presents a compact vitreous morphology (Fig. 2a), which implies that their pores only correspond to narrow gaps between components of carbon-w. In contrast, carbons derived from ethanol (carbon-e) and 1-butanol (carbon-b) present evident porous structures (Fig. 2b and c), although the original fibrous structure is not retained. The disappearance of fibrous structure probably can be ascribed to the melting of nanofibers during the high temperature treatment. The TEM images of carbons (Fig. S4) show that particularly carbon-b possesses more developed and open porous structures, while carbon-w appears denser than carbon-e and carbon-b. This indicates that ethanol and, particularly, 1-butanol treatments are beneficial to obtain porous carbons from BC. The porous structure properties of carbons were further studied by nitrogen adsorption-desorption measurements (Fig. 2c and Table 1). Although the BET surface area of carbon-w results larger than other carbons, its pore structure mainly consists of micropores (Fig. 2d). Instead, the pore structure of carbon-b is dominated by macropores and mesopores, resulting in a larger external area. Therefore, the more open

structure of BC-e and BC-b seems to be beneficial for forming a broader porous structure during pyrolysis. The XRD patterns of carbons are shown in Fig. 2e. The broad peak at around 23° present in the three cases can be attributed to the (002) plane of graphitic carbon [45].

The electrode architecture has a dramatic effect on the discharge capacity of Li−O₂ batteries, as shown by several previous studies [38,46], which are useful to understand the behavior of our materials in this application. Therefore, the electrochemical surface area (ECSA) was determined to gain textural insights from the electrochemical point of view of the porous carbons [47,48], in the same electrolyte used in Li−O₂ battery tests. The values were obtained from capacitive currents in cyclic voltammetry (CV) of the different carbons coated on a carbon paper support (Fig. 3a). The ECSA of bare carbon paper is very small (0.14 m² g⁻¹), which means that it has little contribution to the electrochemical interface. The ECSA of carbon-b (180 m² g⁻¹) is the largest among the carbons derived from BCs, as carbon-e provided 99 m² g⁻¹ and carbon-w 33 m² g⁻¹ (Fig. 3b and Table 1). Thus, the largest BET area of BC-w translates into the smallest electrochemically effective area, showing that the smallest micropores are not accessible for our electrolyte, similarly to what we previously demonstrated with ionic liquid electrolytes [46]. Instead, the larger pores of alcohol-treated carbons offer a better ion-accessible surface area, and show larger ECSA values.

ECSA seems a more significant parameter to predict effectiveness as Li−O₂ cathode than BET area. Fig. 3c displays cyclic voltammetry curves of our carbons in O₂ atmosphere at a scan rate of 20 mV s⁻¹. There are one reduction peak and one oxidation peak, which can be respectively ascribed to the formation and the decomposition of Li₂O₂ [49]. Compared with carbon-w, alcohol-treated carbons display higher currents for both reduction and oxidation peaks. This shows that carbon-e and carbon-b provide better oxygen redox activities thanks to their more suitable pore structure. Galvanostatic discharge-charge profiles of Li−O₂ batteries were operated at the current density of 0.1 mA cm⁻² (Fig. 3d). The contribution of bare carbon fiber support is negligible (Fig. S6). Carbon-b and carbon-e provide discharge capacities of 5.58 and 1.36 mA h cm⁻², while carbon-w only gives capacity similar to that of the support alone (0.14 mA h cm⁻²). Carbon-b also has the highest discharge voltage (~2.75 V), which can be attributed to its larger ECSA. The larger area significantly decreases overpotentials in Li−O₂ batteries and in effect correlation between specific area and discharge potential has been shown previously [38,50]. These capacities clearly show that not only the larger pore volume, but also the larger pore sizes favor the more abundant discharge of Li₂O₂ [51]. The poor capacity of carbon-w can be attributed to its small pore size. This is reflected by the low ECSA and is consistent with our previous observation that only pores larger than a certain size, in the order of 10 nm, significantly contribute to the cathode capacity [46,52]. Besides, small pores will be easily blocked, which hinders the diffusion of oxygen [53]. Instead, the other carbons
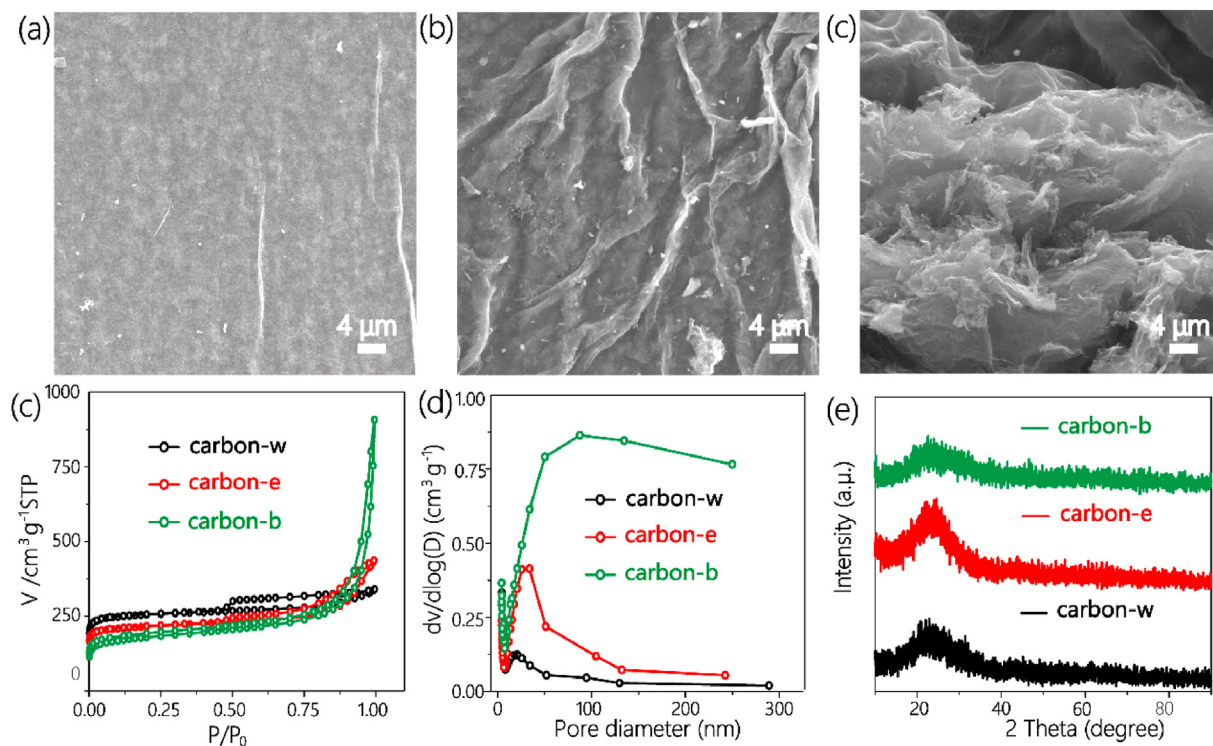
Fig. 2. SEM images of dried carbon-w (a), carbon-e (b) and carbon-b (c), nitrogen adsorption−desorption (c), pore size distribution (d), XRD (e) of carbons obtained from alcohol-treated bacterial cellulose.
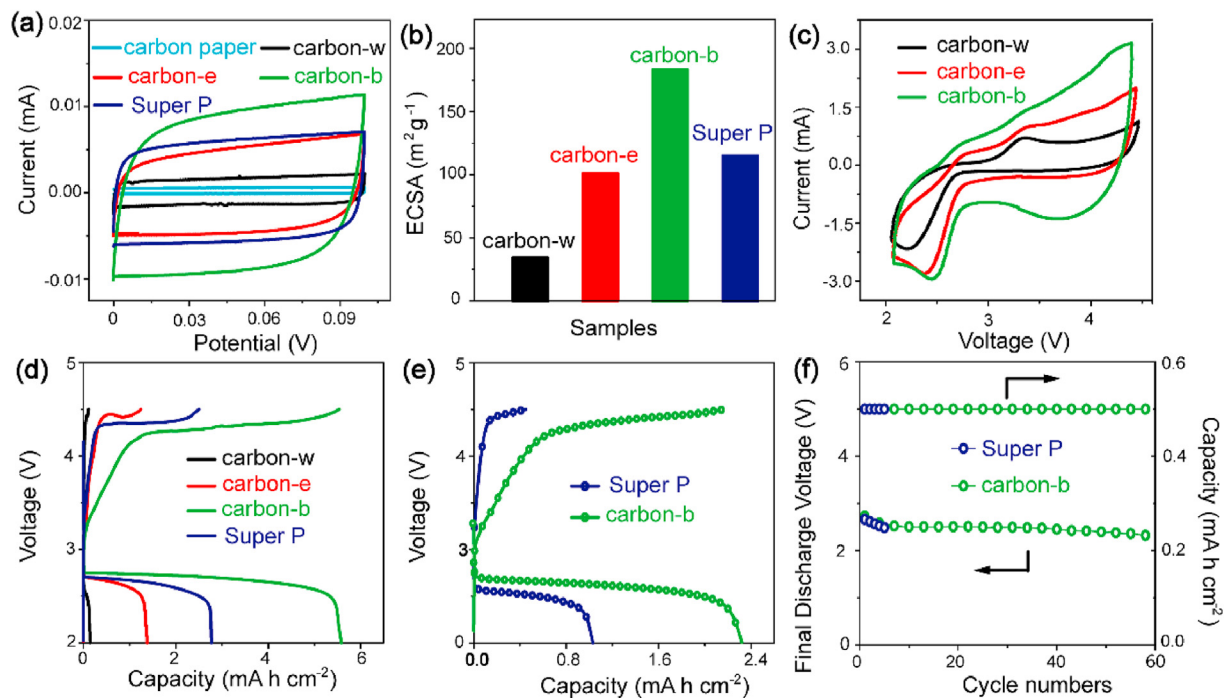

Fig. 3. Electrochemical properties of carbons: (a) CV curves of carbons in Ar-saturated 1 M lithium triflate in DEGDME; (b) comparison of ECSAs; (c) CV curves of Li−O₂ batteries with carbon cathodes; (d) full discharge-charge profiles within the voltage range of 2.0−4.5 V at 0.1 mA cm^{-2}; (e) full discharge-charge profiles at 0.4 mA cm^{-2}; (f) cycle life of carbon-b tested at 0.1 mA cm^{-2}.

show a much more suitable pore structure, in particular carbon-b which outperforms Super P, a carbon black with a very open structure that typically offers large capacity [38,52]. The capacity difference between carbon-b and Super P can be attributed to the

different architecture of carbon-b which offers wider pores and larger surface area that allows for a better distribution of discharge products (Table 1 and Table S2). In addition, BC treated with 1-butanol for 24 h showed similar morphologies and discharge

capacities (Fig. S7), confirming that 2 h soaking is sufficient for quantitative water removal. Compared to other reported carbons, carbon-b exhibits outstanding discharge capacity properties as it can be observed in Table S4.

The rate capabilities of carbon-b and Super P cathodes were compared at the increased current density of 0.4 mA cm^{-2} (Fig. 3e). With the increment of the current density, the discharge capacity descended, discharge voltage decreased and charge voltage increased in all cases, but more severely for Super P. This better rate capability can be attributed to larger ECSA, demonstrating again the optimal texture of alcohol-treated carbons as Li—O$_2$ cathodes. Carbon-b cathodes, displayed nearly 100% coulomb efficiency at 0.1 mA cm^{-2}, and still 90% at 0.4 mA cm^{-2}. However, due to the larger overpotentials, Super P exhibited poorer figures (92% at 0.1 mA cm^{-2}, 43% at 0.4 mA cm^{-2}). In line with this behavior, the cycling stability of carbon-b was far superior to that of Super P. In a test at 0.1 mA cm^{-2} with a capacity limitation of 0.5 mA h cm^{-2} (Fig. 3f and Fig. S8), the Super P electrode only sustained 4 cycles against more than 58 cycles for carbon-b. Table S3 depicts a comparison of the electrochemical performance for several reported cathodes. The outstanding number of cycles that carbon-b can withstand makes it an attractive material for Li—O$_2$ batteries.

To prove the specificity of the bacterial cellulose texture, cotton linters and agarose were also treated with water and 1-butanol, but the improvement from water to 1-butanol was not large (Fig. S9 and Fig. S10). This can be probably because the fibers of cotton linters and the bulk of agarose are much thicker and densified than the fiber structure of dried BCs. Other alcohols (such as methanol, 1-propanol, 1-hexanol and 1-octanol) and some non-alcohol solvents (acetone, ether and TEGDME) were also used to treat BCs with the same preparation method. All carbons derived from BCs treated with these solvents exhibit better capacities for Li—O$_2$ batteries than carbon-w (Fig. S11 and Table S1) but lower than carbon-b. This shows that 1-butanol has optimal affinity for cellulose, probably due to its mixed hydrophobic-hydrophilic character [54,55]. However, in general it can be affirmed that the treatment of solvents with low surface tensions on BCs can promote excellent carbons for Li—O$_2$ batteries.

4. Conclusions

Porous carbons employed as cathodes in Li—O$_2$ batteries have been successfully synthesized by using alcohols to treat BC. The much higher porosity compared to that of carbon originated from water-treated BC, seems to correspond to the more open structure of the intermediate dried cellulose, even if in all cases the fiber network is lost during carbonization. The structure obtained by treatment of BC with 1-butanol shows optimal properties as a cathode in a Li—O$_2$ battery, with much higher capacity (5.58 mA h cm^{-2}), lower overpotentials and longer cycling life than the water treated equivalent material. This performance is superior even to a reference commercial cathode material such as Super P, demonstrating a clear interest as a practical material for application in metal-air batteries, as well as metal-sulphur, supercapacitors and all systems that require efficient transport properties.

CRediT authorship contribution statement

Wenhai Wang: Conceptualization, Methodology, Investigation, Formal analysis, Writing — original draft. **Siavash Khabazian:** Methodology. **Soledad Roig-Sanchez:** Methodology, Writing — review & editing. **Anna Laromaine:** Writing — review & editing. **Anna Roig:** Writing — review & editing. **Dino Tonti:** Resources, Conceptualization, Writing — review & editing, Supervision.

Declaration of competing interest

The authors declare that they have no known competing financial interests or personal relationships that could have appeared to influence the work reported in this paper.

Acknowledgments

Appendix B. Supplementary data

Supplementary data to this article can be found online at https://doi.org/10.1016/j.renene.2021.05.059.

References

[1] C. Xia, C.Y. Kwok, L.F. Nazar, A high-energy-density lithium-oxygen battery based on a reversible four-electron conversion to lithium oxide, Science 361 (2018) 777—781.

[2] P. Salimi, O. Norouzi, S.E.M. Pourhoseini, P. Bartocci, A. Tavasoli, F. Di Maria, S.M. Pirbazari, G. Bidini, F. Fantozzi, Magnetic biochar obtained through catalytic pyrolysis of macroalgae: a promising anode material for Li-ion batteries, Renew. Energy 140 (2019) 704—714.

[3] J.J. Xu, Q.C. Liu, Y. Yu, J. Wang, J.M. Yan, X.B. Zhang, In situ construction of stable tissue-directed/reinforced bifunctional separator/protection film on lithium anode for lithium-oxygen batteries, Adv. Mater. 29 (24) (2017) 1606552.

[4] E. Wang, S. Dey, T. Liu, S. Menkin, C.P. Grey, Effects of atmospheric gases on Li metal cyclability and solid-electrolyte interphase formation, ACS Energy Lett 5 (4) (2020) 1088—1094.

[5] Y. Qiao, Q. Wang, X. Mu, H. Deng, P. He, J. Yu, H. Zhou, Advanced hybrid electrolyte Li-O$_2$ battery realized by dual superlyophobic membrane, Joule 3 (12) (2019) 2986—3001.

[6] C.M. Burke, R. Black, I.R. Kochetkov, V. Giordani, D. Addison, L.F. Nazar, B.D. McCloskey, Implications of 4 e$^-$ oxygen reduction via iodide redox mediation in Li—O$_2$ batteries, ACS Energy Lett 1 (4) (2016) 747—756.

[7] I. Landa-Medrano, I. Lozano, N. Ortiz-Vitoriano, I. Ruiz de Larramendi, T. Rojo, Redox mediators: a shuttle to efficacy in metal—O$_2$ batteries, J. Mater. Chem. A. 7 (2019) 8746—8764.

[8] J. Lu, Y.J. Lee, X. Luo, K.C. Lau, M. Asadi, H.H. Wang, S. Brombosz, J. Wen, D. Zhai, Z. Chen, D.J. Miller, Y.S. Jeong, J.B. Park, Z.Z. Fang, B. Kumar, A. Salehi-Khojin, Y.K. Sun, L.A. Curtiss, K. Amine, A lithium-oxygen battery based on lithium superoxide, Nature 529 (7586) (2016) 377—382.

[9] W.J. Kwak, Rosy, D. Sharon, C. Xia, H. Kim, L.R. Johnson, P.G. Bruce, L.F. Nazar, Y.K. Sun, A.A. Frimer, M. Noked, S.A. Freunberger, D. Aurbach, Lithium-oxygen batteries and related systems: potential, status, and future, Chem. Rev. 120 (2020) 6626—6683.

[10] M. Olivares-Marín, P. Palomino, J.M. Amarilla, E. Enciso, D. Tonti, Effects of architecture on the electrochemistry of binder-free inverse opal carbons as Li—air cathodes in an ionic liquid-based electrolyte, J. Mater. Chem. A. 1 (45) (2013) 14270—14279.

[11] L. Ma, T. Yu, E. Tzoganakis, K. Amine, T. Wu, Z. Chen, J. Lu, Fundamental understanding and material challenges in rechargeable nonaqueous Li-O$_2$ batteries: recent progress and perspective, Adv. Energy Mater. 8 (22) (2018) 1800348.

[12] D.M. Itkis, D.A. Semenenko, E.Y. Kataev, A.I. Belova, V.S. Neudachina, A.P. Sirotina, M. Havecker, D. Teschner, A. Knop-Gericke, P. Dudin, A. Barinov, E.A. Goodilin, Y. Shao-Horn, L.V. Yashina, Reactivity of carbon in lithium-oxygen battery positive electrodes, Nano Lett. 13 (10) (2013) 4697—4701.

[13] M. Kim, E. Yoo, W.-S. Ahn, S.E. Shim, Controlling porosity of porous carbon cathode for lithium oxygen batteries: influence of micro and meso porosity, J. Power Sources 389 (2018) 20—27.

[14] S. Roig-Sanchez, E. Jungstedt, I. Anton-Sales, D.C. Malaspina, J. Faraudo,

L.A. Berglund, A. Laromaine, A. Roig, Nanocellulose films with multiple functional nanoparticles in confined spatial distribution, Nanoscale Horiz 4 (3) (2019) 634—641.

[15] A. Alonso-Díaz, J. Floriach-Clark, J. Fuentes, M. Capellades, N.S. Coll, A. Laromaine, Enhancing localized pesticide action through plant foliage by silver-cellulose hybrid patches, ACS Biomater. Sci. Eng. 5 (2) (2019) 413—419.

[16] G. Fei, Y. Wang, H. Wang, Y. Ma, Q. Guo, W. Huang, D. Yang, Y. Shao, Y. Ni, Fabrication of bacterial cellulose/polyaniline nanocomposite paper with excellent conductivity, strength, and flexibility, ACS Sustain. Chem. Eng. 7 (9) (2019) 8215—8225.

[17] D. Abol-Fotouh, B. Dorling, O. Zapata-Arteaga, X. Rodriguez-Martinez, A. Gomez, J.S. Reparaz, A. Laromaine, A. Roig, M. Campoy-Quiles, Farming thermoelectric paper, Energy Environ. Sci. 12 (2) (2019) 716—726.

[18] X. Hao, J. Wang, B. Ding, Y. Wang, Z. Chang, H. Dou, X. Zhang, Bacterial-cellulose-derived interconnected meso-microporous carbon nanofiber networks as binder-free electrodes for high-performance supercapacitors, J. Power Sources 352 (2017) 34—41.

[19] L. Zuo, W. Fan, Y. Zhang, Y. Huang, W. Gao, T. Liu, Bacterial cellulose-based sheet-like carbon aerogels for the in situ growth of nickel sulfide as high performance electrode materials for asymmetric supercapacitors, Nanoscale 9 (13) (2017) 4445—4455.

[20] E. Jazaeri, L. Zhang, X. Wang, T. Tsuzuki, Fabrication of carbon nanofiber by pyrolysis of freeze-dried cellulose nanofiber, Cellulose 18 (6) (2011) 1481—1485.

[21] N. Pircher, L. Carbajal, C. Schimper, M. Bacher, H. Rennhofer, J.M. Nedelec, H.C. Lichtenegger, T. Rosenau, F. Liebner, Impact of selected solvent systems on the pore and solid structure of cellulose aerogels, Cellulose 23 (3) (2016) 1949—1966.

[22] Y. Peng, D.J. Gardner, Y. Han, Drying cellulose nanofibrils: in search of a suitable method, Cellulose 19 (1) (2011) 91—102.

[23] A.A. Alhwaige, H. Ishida, S. Qutubuddin, Carbon aerogels with excellent CO2 adsorption capacity synthesized from clay-reinforced biobased chitosan-polybenzoxazine nanocomposites, ACS Sustain. Chem. Eng. 4 (3) (2016) 1286—1295.

[24] Y. Li, Y. Liu, M. Wang, X. Xu, T. Lu, C.Q. Sun, L. Pan, Phosphorus-doped 3D carbon nanofiber aerogels derived from bacterial-cellulose for highly-efficient capacitive deionization, Carbon 130 (2018) 377—383.

[25] D.Y. Chung, Y.J. Son, J.M. Yoo, J.S. Kang, C.Y. Ahn, S. Park, Y.E. Sung, Coffee waste-derived hierarchical porous carbon as a highly active and durable electrocatalyst for electrochemical energy applications, ACS Appl. Mater. Interfaces 9 (47) (2017) 41303—41313.

[26] C. Wang, D. Wu, H. Wang, Z. Gao, F. Xu, K. Jiang, A green and scalable route to yield porous carbon sheets from biomass for supercapacitors with high capacity, J. Mater. Chem. A. 6 (3) (2018) 1244—1254.

[27] L. Hu, Q. Zhu, Q. Wu, D. Li, Z. An, B. Xu, Natural biomass-derived hierarchical porous carbon synthesized by an in situ hard template coupled with NaOH activation for ultrahigh rate supercapacitors, ACS Sustain. Chem. Eng. 6 (11) (2018) 13949—13959.

[28] L. Zhang, T. You, T. Zhou, X. Zhou, F. Xu, Interconnected hierarchical porous carbon from lignin-derived byproducts of bioethanol production for ultra-high performance supercapacitors, ACS Appl. Mater. Interfaces 8 (22) (2016) 13918—13925.

[29] A. Tejado, W.C. Chen, M.N. Alam, T.G.M. van de Ven, Superhydrophobic foam-like cellulose made of hydrophobized cellulose fibres, Cellulose 21 (2014) 1735—1743.

[30] J. Li, T. Song, H. Xiu, M. Zhang, R. Cheng, Q. Liu, X. Zhang, E. Kozliak, Y. Ji, Foam materials with controllable pore structure prepared from nanofibrillated cellulose with addition of alcohols, Ind. Crop. Prod. 125 (2018) 314—322.

[31] E. Alonso, M. Faria, F. Mohammadkazemi, M. Resnik, A. Ferreira, N. Cordeiro, Conductive bacterial cellulose-polyaniline blends: influence of the matrix and synthesis conditions, Carbohydr. Polym. 183 (2018) 254—262.

[32] L. Zhang, H. Gong, Improvement in flexibility and volumetric performance for supercapacitor application and the effect of Ni—Fe ratio on electrode behaviour, J. Mater. Chem. A. 3 (14) (2015) 7607—7615.

[33] H. Peng, B. Yao, X. Wei, T. Liu, T. Kou, P. Xiao, Y. Zhang, Y. Li, Pore and het-eroatom engineered carbon foams for supercapacitors, Adv. Energy Mater. 9 (19) (2019) 1803665.

[34] H. Zhang, X. Sun, M.A. Hubbe, L. Pal, Highly conductive carbon nanotubes and flexible cellulose nanofibers composite membranes with semi-interpenetrating networks structure, Carbohydr. Polym. 222 (2019) 115013.

[35] Z. Hanif, H. Jeon, T.H. Tran, J. Jegal, S.-A. Park, S.-M. Kim, J. Park, S.Y. Hwang, D.X. Oh, Butanol-mediated oven-drying of nanocellulose with enhanced dehydration rate and aqueous re-dispersion, J. Polym. Res. 24 (3) (2017) 191—201.

[36] Z. Lu, Z. Su, S. Song, Y. Zhao, S. Ma, M. Zhang, Toward high-performance fibrillated cellulose-based air filter via constructing spider-web-like structure with the aid of TBA during freeze-drying process, Cellulose 25 (1) (2017) 619—629.

[37] J. Juntaro, S. Ummartyotin, M. Sain, H. Manuspiya, Bacterial cellulose reinforced polyurethane-based resin nanocomposite: a study of how ethanol and processing pressure affect physical, mechanical and dielectric properties, Carbohydr. Polym. 87 (4) (2012) 2464—2469.

[38] M. Olivares-Marín, M. Aklalouch, D. Tonti, Combined influence of meso- and macroporosity of soft-hard templated carbon electrodes on the performance of Li-O2 cells with different configurations, Nanomaterials 9 (6) (2019) 810—822.

[39] M. Zeng, A. Laromaine, A. Roig, Bacterial cellulose films: influence of bacterial strain and drying route on film properties, Cellulose 21 (6) (2014) 4455—4469.

[40] H. Chen, J. Chen, N. Teng, H. Na, J. Zhu, Controlling the status of corn cellulose solutions by ethanol to define fiber morphology during electrospinning, Cellulose 24 (2) (2016) 863—870.

[41] L. Wang, M. Ago, M. Borghei, A. Ishaq, A.C. Papageorgiou, M. Lundahl, O.J. Rojas, Conductive carbon microfibers derived from wet-spun lignin/nanocellulose hydrogels, ACS Sustain. Chem. Eng. 7 (6) (2019) 6013—6022.

[42] Z. Wang, B. Pecha, R.J.M. Westerhof, S.R.A. Kersten, C.-Z. Li, A.G. McDonald, M. Garcia-Perez, Effect of cellulose crystallinity on solid/liquid phase reactions responsible for the formation of carbonaceous residues during pyrolysis, Ind. Eng. Chem. Res. 53 (8) (2014) 2940—2955.

[43] Z. Wang, A.G. McDonald, R.J.M. Westerhof, S.R.A. Kersten, C.M. Cuba-Torres, S. Ha, B. Pecha, M. Garcia-Perez, Effect of cellulose crystallinity on the formation of a liquid intermediate and on product distribution during pyrolysis, J. Anal. Appl. Pyrol. 100 (2013) 56—66.

[44] P.C. Lewellen, W.A. Peters, J.B. Howard, Cellulose pyrolysis kinetics and char formation mechanism, Symp. (Int.) Combust. 16 (1) (1977) 1471—1480.

[45] P.P. Ghimire, M. Gao, M. Jaroniec, Amino acid-assisted synthesis of porous graphitic carbon spheres with highly dispersed Ni nanoparticles, Carbon 153 (2019) 206—216.

[46] M. Olivares-Marín, P. Palomino, E. Enciso, D. Tonti, Simple method to relate experimental pore size distribution and discharge capacity in cathodes for Li/O2 batteries, J. Phys. Chem. C 118 (36) (2014) 20772—20783.

[47] H. Wang, J. Wang, Y. Pi, Q. Shao, Y. Tan, X. Huang, Double perovskite LaFe$_x$Ni$_{1-x}$O$_3$ nanorods enable efficient oxygen evolution electrocatalysis, Angew. Chem. Int. Ed. 58 (8) (2019) 2316—2320.

[48] S.D. Ghadge, O.I. Velikokhatnyi, M.K. Datta, P.M. Shanthi, S. Tan, K. Damodaran, P.N. Kumta, Experimental and theoretical validation of high efficiency and robust electrocatalytic response of one-dimensional (1D) (Mn,Ir)O$_2$:10F nanorods for the oxygen evolution reaction in PEM-based water electrolysis, ACS Catal. 9 (3) (2019) 2134—2157.

[49] P. Wang, C. Li, S. Dong, X. Ge, P. Zhang, X. Miao, Z. Zhang, C. Wang, L. Yin, One-step route synthesized Co$_2$P/Ru/N-doped carbon nanotube hybrids as bifunctional electrocatalysts for high-performance Li-O$_2$ batteries, Small 15 (30) (2019) 1900001.

[50] K.-H. Xue, T.-K. Nguyen, A.A. Franco, Impact of the cathode microstructure on the discharge performance of lithium air batteries: a multiscale model, J. Electrochem. Soc. 161 (8) (2014) E3028—E3035.

[51] M. Benoit, A. Rodrigues, K. De Oliveira Vigier, E. Fourré, J. Barrault, J.-M. Tatibouët, F. Jérôme, Combination of ball-milling and non-thermal atmospheric plasma as physical treatments for the saccharification of microcrystalline cellulose, Green Chem. 14 (8) (2012) 2212—2215.

[52] M. Aklalouch, M. Olivares-Marin, R.C. Lee, P. Palomino, E. Enciso, D. Tonti, Mass-transport control on the discharge mechanism in Li-O$_2$ batteries using carbon cathodes with varied porosity, ChemSusChem 8 (20) (2015) 3465—3471.

[53] N. Ding, S.W. Chien, T.S.A. Hor, R. Lum, Y. Zong, Z. Liu, Influence of carbon pore size on the discharge capacity of Li—O$_2$ batteries, J. Mater. Chem. 2 (31) (2014) 12433—12441.

[54] H.-M. Kao, C.-C. Cheng, C.-C. Ting, L.-Y. Hwang, Phase control of cubic SBA-1 mesostructures via alcohol-assisted synthesis, J. Mater. Chem. 15 (29) (2005) 2989—2992.

[55] C. Calero, J. Faraudo, D. Bastos-Gonzalez, Interaction of monovalent ions with hydrophobic and hydrophilic colloids: charge inversion and ionic specificity, J. Am. Chem. Soc. 133 (38) (2011) 15025—15035.